STRUCTURAL, OPTICAL AND ELECTRICAL PROPERTIES OF METAL OXIDE-2D MATERIAL BASED COMPOSITES FOR NON-VOLATILE RESISTIVE MEMORY DEVICE

THESIS

Submitted to

Delhi Technological University

in fulfilment of the requirements for the degree of

DOCTOR OF PHILOSOPHY
in
PHYSICS

by

KM. KOMAL
(2K18/PhD/AP/09)

Under the Supervisions of

DR. BHARTI SINGH
Supervisor

DR. MUKHTIYAR SINGH
Co-Supervisor

DEPARTMENT OF APPLIED PHYSICS
DELHI TECHNOLOGICAL UNIVERSITY
DELHI-110042, INDIA

MARCH 2024

Dedication

This dissertation honours my parents, Smt. Pushpa and Sh. Dayanand and my supervisor, Dr. Bharti Singh. Their unwavering love, encouragement, and support have helped me get through life.

DELHI TECHNOLOGICAL UNIVERSITY

(Govt. of National Capital Territory of Delhi)
Shahbad Daulatpur, Bawana Road, Delhi-110042

CERTIFICATE

This is to certify that the thesis entitled **"*Structural, optical and electrical properties of metal oxide-2D material based composites for non-volatile resistive memory device*"** submitted by **Ms. Km Komal (2K18/PhD/AP/09)** to Delhi Technological University (DTU), Delhi, India for the degree of Doctor of Philosophy, is a bonafide record of the research work carried out by her under my supervision and guidance. The work embodied in this thesis has been carried out in the Computational & Functional Materials Research Laboratory (CFMRL), Department of Applied Physics, Delhi Technological University (DTU), Delhi, India. The work of this thesis is original and has not been submitted in parts or fully to any other Institute or University for the award of any other degree or diploma.

Dr. Bharti Singh & Dr. Mukhtiyar Singh
Supervisor & Co-supervisor
Delhi Technological University
Delhi-110042, India

Prof. A.S. Rao
Head of the Department
Department of Applied Physics
Delhi Technological University

DELHI TECHNOLOGICAL UNIVERSITY

(Govt. of National Capital Territory of Delhi)
Shahbad Daulatpur, Bawana Road, Delhi-110042

CANDIDATE'S DECLARATION

I, **Ms. Km Komal**, hereby certify that the thesis entitled **"*Structural, optical and electrical properties of metal oxide-2D material based composites for non-volatile resistive memory device*"** submitted in the fulfilment of the requirements for the award of the degree of Doctor of Philosophy is an authentic record of my research work carried out under the supervision of **Dr. Bharti Singh** and Co-Supervision of **Dr. Mukhtiyar Singh**. This work in the same form or any other form has not been submitted by me or anyone else earlier for any purpose. Any material borrowed or referred to is duly acknowledged.

Km Komal
(2K18/PhD/AP/09)
Department of Applied Physics
Delhi Technological University
Delhi – 110042, India

ACKNOWLEDGEMENT

Above all, I want to express my heartfelt thanks to the Almighty for giving me the courage and patience to endure through these years of hard work.

First and foremost, I am thankful to almighty God for making me capable enough to reach this level of studies. Getting the right help at the required time has further enhanced my faith in God during my tenure of Ph.D. Researching at Delhi Technological University (DTU) has been a life-changing experience for me. I sincerely hope that this acknowledgement will be a little measure of my gratitude to everyone who has supported me along the way.

I am incredibly grateful to my supervisor, ***Dr. Bharti Singh****, for all of her advice, insight, and inspiration as well as for pushing me to boundaries I never thought I reach. Throughout the process of earning this degree, her excellent mentorship, motivation, patience, immense knowledge, enthusiasm, and continuous support kept me motivated. She is a constant source of inspiration for me, and her knowledge assisted me in understanding the art and science of thin films and nanotechnology while conducting research at the Computational & Functional Materials Research Laboratory at DTU, Delhi. Her dedication to completing the papers perfectly helped me understand the art of writing papers in a precise and brief manner. During my doctoral journey, she was a source of comfort for me when I was feeling uncertain and exhausted. Her wise counsel and kind words never failed to uplift my spirits. Her mentoring is a rare gem, and I feel fortunate to have had the opportunity to grow under her exceptional direction. She is much more than just an advisor; in the world of academia, she is a unique source of inspiration and guidance.*

I would like to thank my co-supervisor, ***Dr. Mukhtiyar Singh****, for his patience, enthusiasm, and extensive expertise. I am obliged to him for his unwavering support during my Ph.D. study and associated research. I was able to complete all of my research and write this thesis with his assistance. For my doctoral research, I could not have asked for a greater co-supervisor and mentor. Your guidance on my research and career has been priceless.*

My heartfelt gratitude also goes to ***Prof. Yogesh Singh****,* ***Prof. J. P. Saini****, and* ***Prof. S. Indu****, Ex-Hon'ble Vice-Chancellors of DTU,* ***Prof. Prateek Sharma****, Hon'ble Vice-Chancellor of DTU, and other authorities for their invaluable assistance and for giving enough facilities for this research. Additionally, I would like to express my gratitude to the DTU for covering the*

cost of my participation at the 11th International Conference on Materials for Advanced Technologies (IUMRS-ICAM & ICMAT 2023) which will take place on June 26-30, 2023.

I would also like to thank all of the teachers and staff at DTU, including ***Prof. Rinku Sharma****, Dean (Academic-PG), and* ***Prof. A.S. Rao****, Head of the Department of Applied Physics, for their assistance and collaboration during my research. I am grateful to the Delhi Technological University (DTU) Department of Applied Physics for providing the necessary workspace, allowing me to work as much as I want, within the allotted time.*

I am also appreciative of ***Prof. Nitin K. Puri*** *and* ***Dr. Amrish Panwar*** *for providing me with the facilities and research atmosphere. I appreciate their thoughtful conversation, helpful advice, and confidence during the research project.*

My sincere thanks and appreciation go to the SRC members, ***Dr. Govind Gupta*** *and* ***Dr. J. P. Singh*** *for their comments and constructive criticisms to enrich the quality of my doctoral work.*

It has been a wonderful experience to be a part of the Computational & Functional Materials Research Laboratory (CFMRL) Group, from which I have gained many experiences that I am confident will benefit me throughout my life. I am grateful to many people. I want to convey my heartfelt gratitude to my fellow labmates, ***Dr. Vishal Singh*** *and* ***Shilpa Rana****, for their constant help, continuous support, encouragement, timely advice, and all of the fun we had while on this difficult yet beautiful journey. The discussions that I had with them both regarding the work helped me improve my knowledge and enhance my experimental and analytical skills.*

I would especially want to thank all of my friends at DTU and beyond for helping to keep me sane. To my college friends: ***Jyoti, Priya, Durvesh, Megha Narwan, Kanika Sharma, Sunil, Hemant, Nikita Jain, Deepali, Naima, Anurag, Richa, Bhavya, Rajesh, Ramesh and Ankita,*** *you are all aware of my deep gratitude for you, and I cannot imagine my time at DTU without you all! I would especially like to thank* ***Rajeev*** *for helping me out at every turn over the years. Thank you for always being there for me,* ***Nitish Kumar, Sirtaz, Ali, Parth*** *and* ***Dr. Pardeep****! To* ***Anu, Sharad, Vinay, Jassveer, Shivani, Sangeeta, Ritu,*** *and* ***Vishakha****. As juniors, you have my sincere gratitude for your unwavering kindness and charming presence. I would like to express my heartfelt gratitude to* ***Dharam Pal*** *for helping me in my initial days of M.Sc. I will never forget the times I spent with them as priceless memories of my past.*

I would like to express my heartfelt gratitude to ***Dr. Priyanka Bamola,*** *Postdoctoral researcher, Renewable Energy Institute (IER), National Autonomous University of Mexico (UNAM), Temixco-62580, México for her always positive approach. I will always be indebted to her for the valuable time that she gave me for scientific and technical discussions.*

No study may be completed without appropriate funding from the paying agency. I am grateful to the financial agencies ***(Council of Scientific and Industrial Research, India)*** *for providing monetary support and a Senior Research Fellowship for this study.*

I would like to express my gratitude to my father, ***Mr. Dayanand****, and my mother,* ***Mrs. Pushpa,*** *for their continuous affection, steadfast support, and emotional assistance throughout my life. Over the years, my father has been the most significant source of support; he has devoted his time to assisting me in becoming a successful individual and has instilled in me the value of working outside my comfort zone. My parents constantly supported me and given me every chance to be here. The people who have supported and inspired me to do this thesis work are* ***Mr. Amit, Mr. Sumit Kumar,*** *and* ***Minakshi,*** *along with my younger brothers and sister. Their trust, faith, and confidence in me have always motivated me towards my objective. I truly value everything you have sacrificed for me throughout the years.*

Km. Komal

(March 2024)

Date: 24-03-2024

Place: New Delhi

ABSTRACT

Big data processing and storage are in high demand as human society moves into the big data era. One new gadget that has computation and memory built right in is the resistive switching memory device. As more and more conventional memory technologies, such SRAM, DRAM, and Flash, reaching the end of their useful lives, a novel idea known as "Universal Memory" emerges, fast speed (read and write), low power (access and standby), high density (low cost), non-volatility, random accessibility, and infinite durability are anticipated qualities of a universal memory. Magneto resistive memory (MRAM), phase change memory (PCM), and resistive memory (ReRAM) are a few possibilities for universal memory.

The increasing number of flexible, wearable, foldable, lightweight, and transparent electronic gadgets such as displays, RFID tags, sensors, mobile phones, and watches has recently increased demand for new types of memory devices. ReRAM development has received more attention in recent years because of its straightforward design, low power consumption, and quick performance. The non-volatile memory effect is caused by a systematic resistance change between the low resistance (R_{LRS}) and high resistance (R_{HRS}) states by varying the applied voltage bias to the cell. In order to produce resistive switching, or to cause HRS switched to LRS (set) and LRS switched to HRS (reset) transitions, different material combinations employed in MIM cells require different kinds of electrical stresses. Therefore, the resistive switching phenomenon can be divided into the following categories: i) unipolar and ii) bipolar resistive switching, which require the application of stresses with the same or opposite polarity to initiate the set and reset processes, respectively; iii) nonpolar resistive switching, which allow the application of stresses with any polarity to achieve the set and reset transitions; and iv) threshold resistive switching, which occur when the LRS is volatile and the reset process occurs automatically when the stress is turned off. Numerous inorganic and organic materials exhibit this resistive switching effect, including solid-state electrolytes, binary transition metal oxides, perovskites, organic donor-acceptor systems, and organic charge transfer complexes. However, recent developments in material science demonstrate that the organic-inorganic nanocomposite interface device has greater advantages than its inorganic and organic equivalents. Understanding the switching mechanism in ReRAM was particularly difficult because of the several events that coexisted when the ultimate electrical stress was applied. Many methods have been proposed to explain the resistive switching of ReRAM devices, including conductive filament generation, space-

charge-limited conduction, trap charging and discharge, Pool-Frenkel emission, and the Schottky emission. Size-dependent research and electrode material provide crucial hints for a clear grasp of the switching mechanism. Several methods, including X-ray photoelectron spectroscopy (XPS), Scanning electron microscopy (SEM) and high-resolution transmission electron microscopy (HRTEM), have been employed in this regard to comprehend the filament composition and, consequently, the underlying process.

The major objective of the present thesis is to examine the impact of different 2D materials (rGO, MoS_2, hBN) and SnO_2 as an active material deposited using spin-coating technique on the resistive switching phenomenon. Bipolar resistive switching is observed for SnO_2-2D material based film sandwiched between two different metal electrodes.

Firstly, the effects of pure reduced graphene oxide (rGO) inclusion on the resistive switching properties of tin oxide (SnO_2) based resistive memory device was studied. It has been demonstrated that the incorporation of rGO in SnO_2 nanocomposite induced bipolar resistance switching with enhanced ON/OFF ratio. Here, we have fabricated flexible resistive switching memory devices of pure SnO_2 and rGO-SnO_2 (5, 7, and 10 wt.%) nanocomposites. The resistive switching performance of the fabricated devices were compared and observed that the memory device with 7 wt. % of rGO in SnO_2 has a maximum ON/OFF ratio of ~ 70, in comparison to ~ 4 and ~ 3 for 5 and 10 wt. % sample respectively. The endurance and retention tests were performed on 7 wt. % rGO-SnO_2 composite film based memory device and the device shows no degradation in the memory window up to 100 cycles.

After incorporating conducting rGO, semiconducting molybdenum disulfide (MoS_2) was used for synthesizing tin oxide (SnO_2) based nanocomposite powder as a resistive switching material, where the effect of MoS_2 weight percentage (0, 5, 7, and 10 wt.%) have been evaluated in terms of the structural, optical, and electrical properties changes of resulting nanocomposite using X-ray diffraction, UV-Visible Spectroscopy, Scanning electron microscopy, and Transmission electron microscopy techniques. The nanocomposite samples were synthesized using a simple hydrothermal technique and are spin-coated on commercially available ITO-PET substrate. The top metallic electrode was deposited by thermally evaporating Aluminium through a shadow mask resulting in Al/SnO_2/ITO-PET and Al/MoS_2-SnO_2/ITO-PET (5%, 7%, 10%) based resistive memory devices. The measured current-voltage (I-V) characteristics over the fabricated devices having different MoS_2 wt. % showed the increase in I_{On}/I_{Off} ratio (3, 100, and 25) with an increase in MoS_2 concentration and is found

that device with 7wt % of MoS_2-SnO_2 has higher I_{On}/I_{Off} ratio (100) in comparison to 7 wt. % rGO-SnO_2 nanocomposite-based device. Additionally, a retention and endurance test was conducted to verify the fabricated devices stability and cyclic performance. The results showed that the 7%MoS_2-SnO_2 device maintained the HRS and LRS states for up to 2×10^3s and demonstrated stable performance for up to 100 switching cycles without much degradation, respectively. It is noteworthy that the currently suggested ReRAM technology, which is based on SnO_2 and MoS_2, has great potential for application in the wearable device market due to its flexible and low-power properties.

Further to increase the memory window, insulating hexagonal boron nitride (hBN) having wide band gap and tin oxide (SnO_2) based nanocomposite powder was synthesized hydrothermally for acting as switching material. X-ray diffraction and Raman spectroscopy methods were used to characterize the synthesized nanocomposite powder. The resistive switching performance of the fabricated devices were compared and observed that the memory device with 7 wt. % of hBN in SnO_2 has a maximum ON/OFF ratio of ~ 1000, in comparison to ~ 96 and ~10 for 5 and 10 wt. % sample respectively. The endurance and retention tests were also performed on 7 wt. % hBN-SnO_2 composite film based memory device and the device shows no degradation in the memory window up to 100 cycles. The present work demonstrates the systematic investigation of the effect of different ultrathin 2D layered nanomaterials and their concentration in metal oxide matrix for future flexible, reliable, and low-power non-volatile memory devices.

LIST OF PUBLICATIONS

Publications in Peer Reviewed Journals:

1. **Km Komal,** Govind Gupta, Mukhtiyar Singh, Bharti Singh, "*Improved resistive switching of RGO and SnO_2 based resistive memory device for non-volatile memory application*", Journal of Alloys and Compounds, Volume 923, 25 November 2022, 166196.

2. **K. Komal,** M. Singh, B. Singh, "*One step hydrothermal synthesis of MoS_2-SnO_2 nanocomposite for resistive switching memory application*", Journal of Materials Science: Materials in Electronics 34(17) (2023) 1351.

3. **Km Komal**, Mukhtiyar Singh, Bharti Singh, "*Flexible SnO_2-MoS_2 based memristive device exhibiting stable and enhanced memory phenomenon*", journal of Physics D: Applied Physics, 57 105107 (2024).

4. **Km Komal,** Mukhtiyar Singh, Bharti Singh, "*Effect of rGO weight percentage on structural, optical, and electrical properties of rGO-SnO_2 nanocomposite for memory device application*", Journal of Materials Science and Engineering: B, Volume 303, May 2024, 117274.

Accepted:

1. **Km Komal**, Mukhtiyar Singh, Bharti Singh, "*Two-dimensional (2D) hBN-SnO_2 based flexible memory device for enhanced resistive switching application*" (Accepted).

Communicated:

1. **Km Komal,** Priyanka Bamola, Bharti Singh, "SnO_2-2D materials based nanocomposite for improved visible light photocatalytic applications" in "**Applied Surface Science" (Communicated)**.

Conference Contributions-Poster and Oral Presentations:

1. Attended and Presented Poster presentation entitled **"*Synergistic Photocatalytic Enhancement: SnO_2-2D Nanocomposites for Sustainable Pollutant Degradation*"** at

sixth edition of International Conference on Atomic, Molecular, Material, Nano, and Optical Physics with Applications (ICAMNOP 2023), scheduled for December 20-22, 2023 at Delhi Technological University, Delhi, India.

2. Attended and Presented Poster presentation entitled **"*Two-dimensional (2D) hBN-SnO_2 based flexible memory device for resistive switching application*"** at 14th International Conference on "Recent Progress in Graphene and 2D Materials Research" (RPGR2023), held from 20-23 November 2023 in Bengaluru, India.

3. Attended and Presented Poster presentation entitled "***Structural, Optical and Electrical Properties of hBN-SnO_2 Nanocomposites as a Function of Varying hBN Weight Percentage***" at 11th International Conference on Materials for Advanced Technologies (IUMRS-ICAM & ICMAT 2023) which will be held in Singapore from 26th-30th June 2023.

4. Attended and Presented Poster presentation entitled "***Flexible MoS_2-SnO_2 Nanocomposite Based Resistive Memory Device for Non-Volatile Memory Applications***" at International Union of Materials Research Societies - International Conference in Asia - 2022(IUMRS-ICA, 2022) held at Indian Institute of Technology Jodhpur from December 19 to December 23, 2022.

5. Attended and Presented Poster presentation entitled "***Structural, optical and electrical properties of MoS_2-SnO_2 nanocomposites as a function of varying MoS_2 weight percentage***" at International Conference on Nanotechnology: Opportunities and Challenges (ICNOC- 2022) held at Jamia Millia Islamia (Central University), New Delhi November 28-29, 2022.

6. Attended and Presented Oral presentation entitled "***One-step hydrothermal synthesis of MoS_2-SnO_2 nanocomposite for improved resistive switching performance***" at International Conference on Recent Advancements in Chemical Sciences: Health, Environment and Society (ICRACS - 2022) held at Deshbandhu College, University of Delhi from 8th-9th April, 2022.

7. Attended and Presented Poster entitled "***Study of a non-volatile memory based on reduced graphene oxide and tin oxide nanocomposite***" at International Conference on Atomic, Molecular, Optical and Nano Physics with Application (CAMNP-2019) held at Delhi Technological University from 18th -20th December, 2019.

CONTENTS

LIST OF FIGURES

Figure No. **Page No.**

Chapter 1

Chapter 2

Chapter 3

Chapter 4

Chapter 5

LIST OF TABLES

LIST OF ABBREVIATIONS

Acronyms	Meaning
MoS_2	Molybdenum disulfide
rGO	Reduced graphene oxide
hBN	Hexagonal boron nitride
SnO_2	Tin oxide
Eg	Band gap
nm	Nanometre
cm	Centimetre
V	Volt
eV	Electron volt
Hz	Hertz
t(s)	Time in seconds
I	Current
PET	Polyethylene terephthalate
ITO	Indium tin oxide
rpm	Revolutions per minute
wt%	Weight percentage
λ	Wavelength of radiation
Å	Angstrom

mm	Millimeter
s	Second
d	Lattice spacing
h	Planck’s constant
°C	Degree Celsius
SEM	Scanning electron microscope
FE	Field emission
EDAX	Energy dispersive x-ray analysis
TEM	Transmission electron microscope
HRTEM	High resolution electron microscope
XPS	X-ray photoelectron
UHV	Ultra high vacuum
FWHM	Full width at half maxima
BE	Binding energy

CHAPTER 1

Introduction

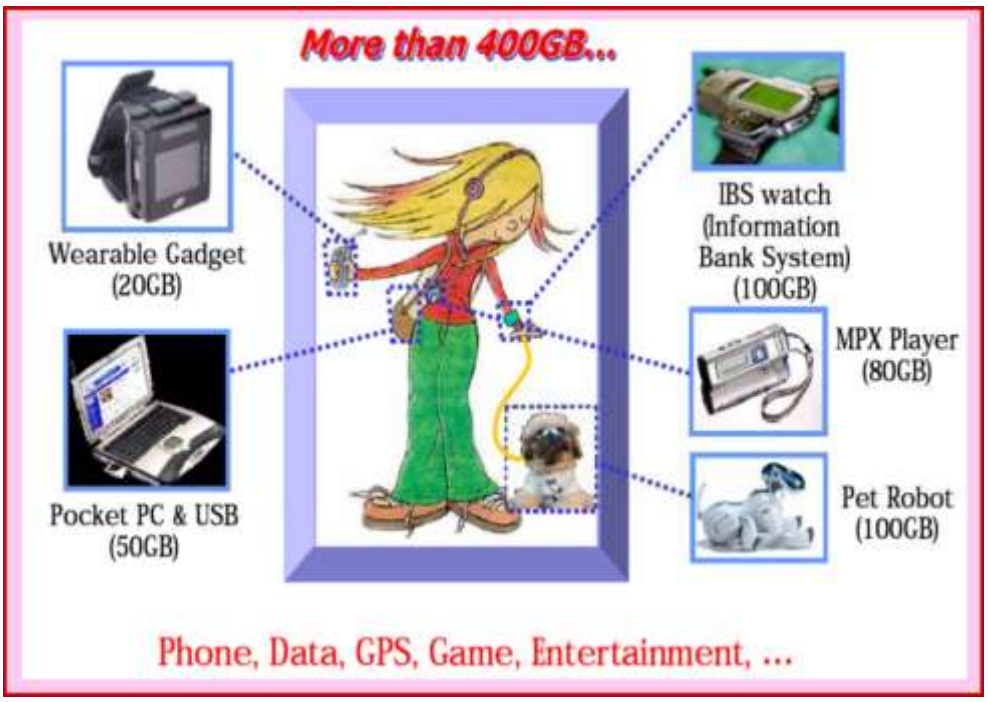

This chapter starts with a quick overview of nanotechnology and nanoscience and then classifies nanomaterials according to their dimensionality. Particular attention is devoted to 2D nanomaterials because of their attractive and appealing characteristics, which render them extremely advantageous for various applications. Further, this chapter explains how resistive random access memory works is classified based on the polarity of programming voltages and the kind of conducting pathways. An overview of the many characterization methods and memory device parameters that are utilized to explain switching phenomena is provided. Additionally, a quick description of how to modify switching parameters utilizing an organic-inorganic hybrid interface is provided.

1.1 Introduction

1.1.1 Nanotechnology and nanoscience

The potential for nanotechnology to transform the industrial and commercial markets has led to enormous growth in the fields of nanoscience and nanotechnology. The foundation of this rapidly expanding field is nanostructured materials. The properties of nanostructured materials lie between those of bulk materials and atoms, with at least one dimension of less than 100 nm[1]. Nanomaterials have differing properties from their bulk or atom counterparts due to an increase in relative surface area and the introduction of novel quantum phenomena. An increased surface-to-volume ratio improves their chemical reactivity by making more atom fractions available at the surface[2]. Figure 1.1 is a schematic depicting the increase in surface area to volume ratio as we move from a bigger size (i) to a smaller dimension (ii). Because the size is comparable to length and is in the nanoscale, the qualities of the entire material are considerably more dependent on the surface. While quantum phenomena occur as a result of spatial confinement in nanoscale dimensions.

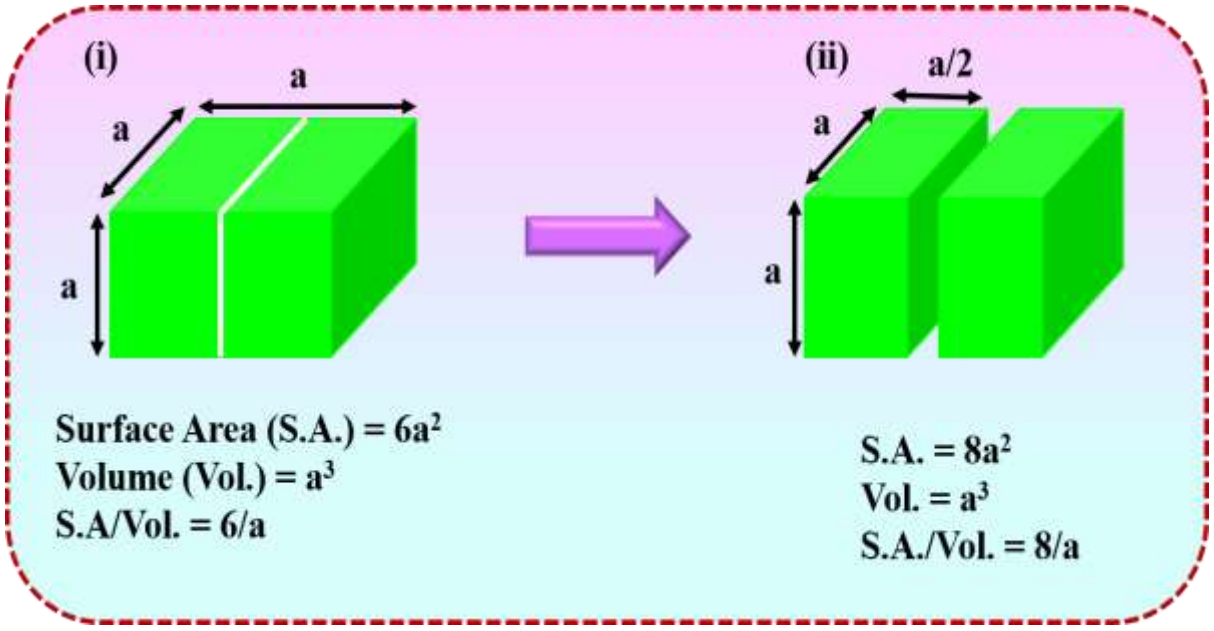

Figure 1.1: A schematic depicting the rise in surface area to volume ratio while moving from a (i) greater dimension to a (ii) smaller dimension.

1.1.2 Dimensionality-based categorization of nanostructured materials

There are four types of nanostructured materials: zero-dimensional (0D), three-dimensional (3D), two-dimensional (2D), and one-dimensional (1D). All three dimensions of 0D materials such as quantum dots and nanoparticles (NPs) are at the nanoscale, or less than 100 nm. One

of the dimensions in 1D-nanorods, nanowires, nanotubes, etc. cannot is measured at the nanoscale. Any of the two dimensions in 2D nanomaterials-nanosheets, nanoplates, etc. outside the nanoscale. Three-dimensional materials, like bulk powders, have all three dimensions outside of the nanoscale. The dimensions-based nanomaterial classification is displayed in Figure 1.2.

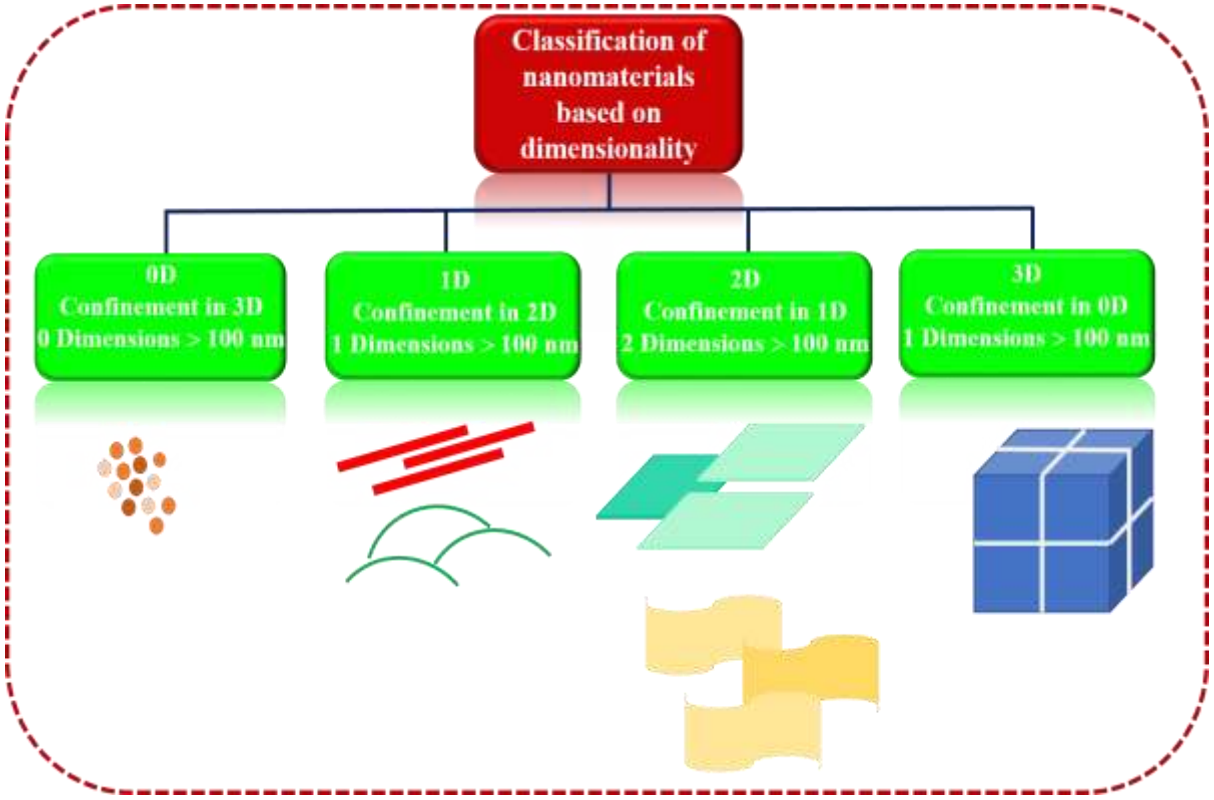

Figure 1.2 Dimensions-based categorization of nanostructured materials

Since the discovery of exceptional features in graphene in 2004 [3], research endeavours about two-dimensional nanomaterials have been particularly flourishing. The dimensionality of 2D nanomaterials determines their wide range of structural and chemical properties, allowing for several applications. The popularity of 2D nanomaterials has increased in numerous applications due to their abundance in electrical and optical properties, as well as the possibility of functionalizing these properties. Due to their surfaces abundance of exposed atoms, which makes interacting with other materials easier, 2D nanomaterials are easily functionalized [4]. 2D nanomaterials have amazing mechanical qualities, such as flexibility, lightweight, and durability, which can be very helpful for the development of wearable and portable sensors [3]. Graphene, hexagonal boron nitride (hBN), phosphorene, graphitic carbon nitride (g-C_3N_4), Mxene, and transition metal dichalcogenides (TMDs) are a few materials in this class. Graphene is the most widely used 2D nanomaterial for a variety of applications

because of its many intriguing characteristics, including its vast surface area, excellent conductivity, and single-atom thickness with zero band gaps. It is still very difficult to produce high-quality graphene at a low cost and high yield for industrial uses. Consequently, the reduction of graphene oxide (GO) yields a significant amount of graphene because it is an inexpensive and scalable process. Reduced graphene oxide (rGO) is less conductive than graphene and has a higher number of functional groups on its surface, but this makes it ideal for sensing applications that require functional groups for covalent attachment. Synthesis procedures for diverse 2D materials such as black phosphorus and MXene are still in their early stages, making it challenging to manage their yield, size, and surface features[5]. TMDs, like graphene, are a type of 2D material that is extensively explored. A chalcogenide, including tellurium (Te), sulphur (Se), or selenium (Se), is represented by the symbol X in the generic formula for transition metal deposits (TMDs), which is MX_2. Because of its many physicochemical properties, including its quick electron transfer rate, ease of functionalization, ease of synthesis, numerous synthesis routes, scalable yield, ease of dispersion in different solvents, tunable morphologies, and synergistic effect with other materials that encourage composite formation, molybdenum disulfide (MoS_2) is the TMDs that has been studied the most among the others [6]. Motivated by the variety of characteristics that MoS_2 possesses, it finds use in an extensive range of industries, such as batteries [7], super capacitors [8], hydrogen evolution reaction (HER) [9], electrical devices [10], sensors [11], and so on. MoS_2 synthesis can be performed using top-down or bottom-up methods, providing outstanding control over the material's morphology and surface functions. This makes MoS_2 an excellent choice for ReRAM applications.

A great deal of scientific interest has been focused on graphene-based nanostructures, such as carbon nanotubes, since the initial synthetization of graphene [12], a single atom-thick layer of graphite, made feasible by the fabrication of these materials. Graphene is indeed a promising material for the future of electronics and biology due to its exceptional mechanical, electrical, and thermal qualities. That is the reason for the recent interest in hexagonal boron nitride (h-BN). However, the insulating property of bulk hexagonal h-BN can still be retained. It has been demonstrated that one or a few single layers of h-BN can be folded to create nanotubes [13], which are remarkably similar to semi-metallic carbon nanotubes. The compatibility between graphene and hexagonal h-BN is much deeper because both materials have the same structure, namely a hexagonal ‘honeycomb’ lattice, and hexagonal h-BN is widely regarded as the ideal substrate for conducting graphene due to its insulating nature [14]. As a result, there has been

a need to understand both the behaviour of h-BN and graphene. Mono-layer h-BN adsorption on metals is essential both theoretically and technologically. For example, multilayer h-BN is supposed to interact weakly with a nickel substrate and stay stable at high temperatures (1000K) [15]. This could result in a two-dimensional insulator-metal interface that is ideal for the construction of nanostructured devices.

1.2 Background of RRAMs

Modern computing methods, from wearable technology to exascale supercomputers, rely heavily on memory devices, which are widely used. Microprocessors prepare information before they are executed and write it afterward, while memory is the primary site for data storage. The effectiveness of memory, which is located along the systems key path of workflow, affects overall performance. However, memory access latencies and storage density have become major factors limiting microprocessor performance improvements. While memory speed has only increased by 10% over the previous few decades, central processing unit (CPU) speed has increased dramatically at an annual pace of over 50%. As CPU and memory costs increased, computer engineering progress was hindered by what is known as the "memory wall" problem[16]. Furthermore, as Figure 1.3 illustrates, the existing memory cell size has been reduced to 10nm[17], which is very close to the limitations of science and technology. As a result, it is extremely difficult to improve memory capacity by further reducing cell size. We are encouraged to research and enhance memory device performance in recognition of this trend.

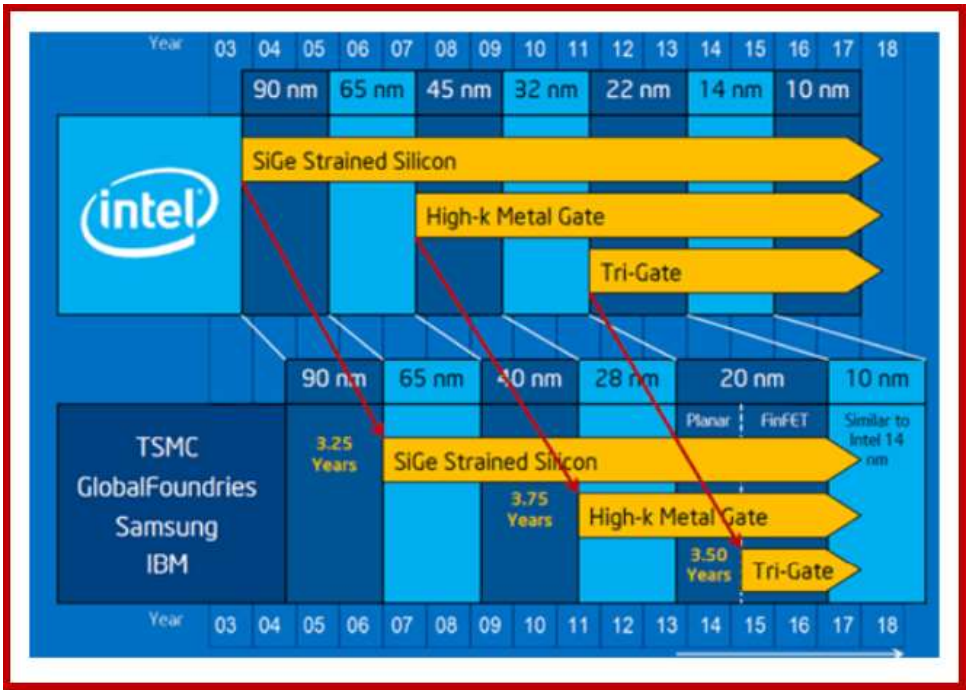

Figure 1.3 The memory size is reduced; taken from reference[18].

Modern computing systems have volatile and non-volatile memory, the most common types found in current computers are random-access memory (RAM) and flash memory. It is not enough to just increase RAMs operating speed and storage density to meet the growing need for better memory. The newest approach to overcoming the memory wall is combining non-volatile memories with RAMs, which should result in increased operation speed, storage density, and lower power consumption with an easier manufacturing process.

The next generation of non-volatile RAMs (NVRAMs) is expected to be oxide-based RAM (OxRAM), also referred to as resistive RAM (RRAM), a recently discovered contender. These oxides, on which the capacitor-like RRAM is built, exhibit reversible resistance switching behaviour among two or more stable states. Referencing Therefore, a thorough understanding of the behaviour of metal oxide resistive switching is crucial for further optimizing oxide RRAMs.

To achieve effective resistive switching for microscopic switching, lattice flaws are essential. According to reference [19], the most frequently documented flaw in RRAMs that causes successful switching is oxygen vacancy. However, oxygen vacancies are far more mobile than cationic faults, which can be challenging to manage and result in excessive current in RRAMs. In addition to limiting the potential for multi-level resistive switching, this could lead to a lower On/Off ratio as well as shorter retention and endurance. RRAMs are appropriate because multi-level resistance states allow for quadruple amounts of storage without further reducing the size of the cell, which is greatly sought. This raises the question of whether creating cationic flaws in metal oxides may effectively lead to the fabrication of multi-level resistive switching devices.

1.3 Concept of semiconducting memories

Memory technology occupies the largest market proportion of the current semiconductor industry and there is a trend that the number of memory components is becoming larger and larger than computing components on the chips[20]. For the past few decades, conventional memory in computing has been successfully sped up to reach quicker operating speed and scaled down to achieve more capacity[21]. However, as device sizes are constantly decreasing, advances in the development of new memories are greatly needed, as current materials and technologies are reaching their limits in science and technology [22].

Memories in computing can be divided into two primary categories, “volatile” and “non-volatile,” as shown in Figure 1.4. Because of its fast read/write speeds, volatile memory, such as static random-access memories (SRAM) and dynamic random-access memories (DRAM), is frequently utilized as primary storage in modern systems. Nevertheless, it needs power to preserve the data that is saved, and when the power is cut off, data is rapidly lost. Non-volatile memories (NVM) are commonly employed as secondary memory or long-term persistent storage because they can retain data even in the event of a power outage. Memory read-only memories (ROMs), such as mask ROM, EPROM, and EEPROM, are non-volatile memory that can store data without a power source; however, they often have very slow writing speeds and may not even be rewriteable. The non-volatile memory chapter is better for computing memories, but its use as primary storage to replace volatile memories has been limited because of its lower read/write performance, longer writing endurance, and greater NVM cost[23]. A classification of memory technologies is given in Figure 1.4 below.

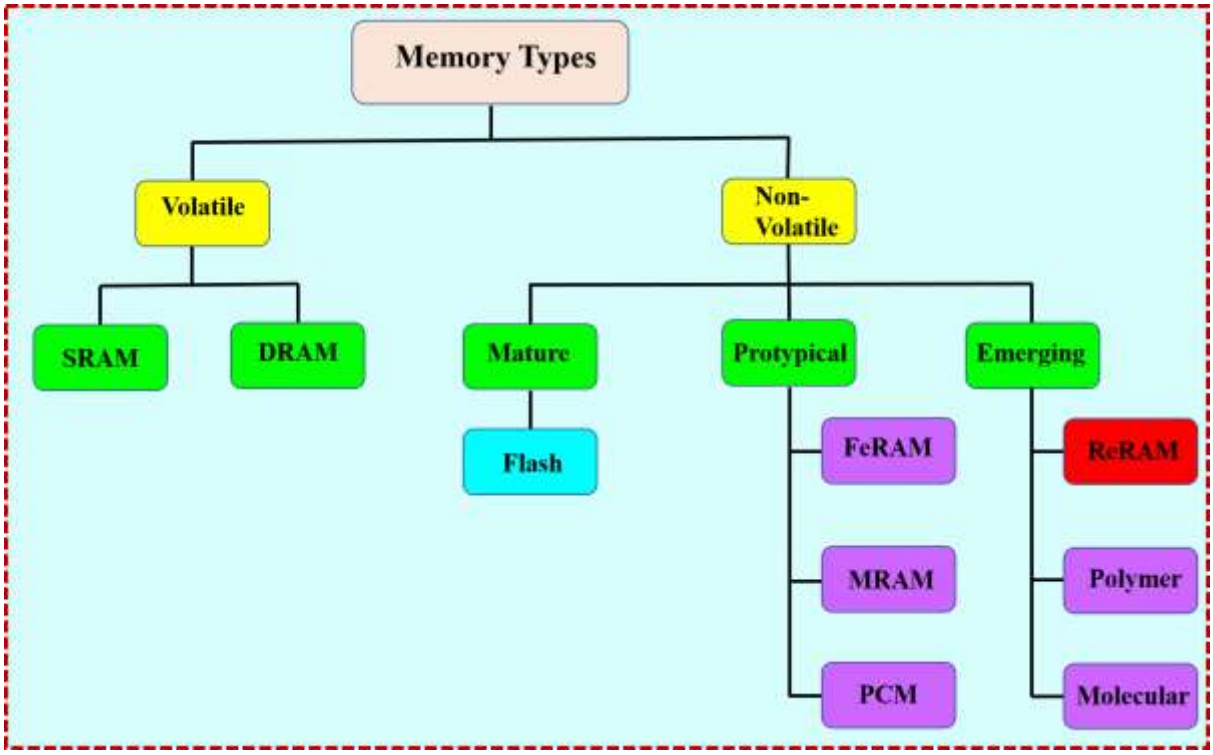

Figure 1.4 The memory taxonomy is represented by a schematic diagram.

The emergence of FLASH memory,[24] however, has influenced human life as it is both non-volatile and randomly accessible. The FLASH rewriting speed is measured in milliseconds. FLASH discs are commonly used for mobile storage, storage cards, and USB flash drives. FLASH memories are employed as data containers for a variety of consumer electronics items

these days. However, FLASH does have certain insufficiencies including, slow writing speed (microseconds to milliseconds), poor writing endurance (typically 10^5-10^6 write/erase cycles), high erasing voltage (10-20 V), etc. In addition, FLASH also faces the scaling limit, usually believed to be ~22 nm. An almost perfect non-volatile memory (NVM) is being sought for to satisfy the demands of the rapidly expanding consumer electronics sector. There have been numerous new concepts and revolutionary NVMs put forward.

1.4 Prototypical non-volatile memories

In ferroelectric random access memory (FeRAM), a ferroelectric substance is placed between the two plates of a capacitor, whose polarization state is reversed with the help of an external electric field. In FeRAM, the two polarization states of materials are used for data storage[25]. The magnetoresistive random access memory (MRAM), uses various magnetoresistance phenomena, such as anisotropic magnetoresistance (AMR), giant magnetoresistance (GMR)[26], tunneling magnetoresistance (TMR), and most importantly magnetic tunnel junction [27]. In MRAM, relative magnetization orientation shifts between parallel and antiparallel alignment can result in resistance variations of more than 100% [28, 29]. FeRAM and MRAM have similar fast switching (<20 ns) and large programming endurance (>10^{15} write/erase cycles); however, the latter device exhibits poor scalability, and switching does not scale with cell size. Additionally, programming currents in MRAM are in the milliampere range. Phase change memory (PCM) devices rely on a chalcogenide material that may transition between an amorphous and crystalline form with varying resistance values; states "0" and "1" represent high resistance state (HRS) and low resistance state (LRS), respectively. An applied current pulse's heat generation causes the phase transition to occur [30]. PCM has a substantially lower cell area than MRAM and FeRAM. Additionally, PCM has a modest cycling endurance and outstanding compatibility with current semiconductor technology. Owing to these benefits, PCM is thought to be a viable option for the high-density NVM market, particularly the constantly growing consumer electronics sector. Nevertheless, there are some drawbacks associated with PCM namely; (i) “hot” device operation that may cause heat-dissipation problems and (ii) relatively low speed in SET operation [31].

1.5 New non-volatile memory: random access memory resistance

Resistance random access memory (ReRAM) has recently gained attention as a potential advancement in NVM technology. ReRAM uses a change in resistance, just like PCM. However, ReRAM has several advantages over PCM, such as a lower amount of required

energy to switch states, superior scalability, simpler structures, and better reliability[32]. While ReRAM has good endurance for reading, it has weak endurance for writing[33].

Charge storage-based memory technologies include DRAM, SRAM, and Flash. While SRAM and DRAM depend on the charge being stored at the nodes of the cross-coupled inverters, Flash memory technology stores the charge at the floating gate of the transistor. It is currently difficult for any of these charge storage-based memory systems to scale down to a node of 10 nm or less. This is explained by the reduction of performance, reliability, and noise margin brought on by the loss of stored charge at the nanoscale. Furthermore, designing a future memory hierarchy will be extremely difficult due to the requirements for significant refresh dynamic power for DRAM and leakage power for both SRAM and DRAM. Because of this, a new class of memories known as emerging memory technologies is currently being developed and intensively investigated, mostly in the industry, to completely change the current memory hierarchy[34]. To combine the non-volatility of Flash memory, the switching speed of SRAM, and a storage density similar to that of DRAM, these new memory technologies are sure to become highly desirable options for the memory hierarchy of the future.

To classify a memory device as an ideal one, it should have the following characteristics: low operating voltage (10^{17} cycles), enhanced data retention time (>10 years), low energy consumption (fJ/bit), and superior scalability (<10 nm) [35]. Nevertheless, no one memory has been found to date that meets these ideal requirements. To fulfill some of these ideal memory attributes, numerous developing memory technologies are now being researched. Resistive random access memory (RRAM), spin-transfer torque magnetoresistive random access memory (STT-MRAM), and phase change memory (PCM) are the types of memory technologies that require a change in resistance rather than charge to store information. The switching medium in phase change memory is made of a chalcogenide substance (Ge_2-Sb_2-Te_5, GST)[36]. For effective data storage, PCM depends on the resistance differential between the crystalline and amorphous phases. The low resistance state (LRS) or ON state of the device is represented by the crystalline phase, whereas the high resistance state (HRS) or OFF state is represented by the amorphous phase. While the RESET action corresponds to HRS storing logic value “0” in the device, the SET operation corresponds to LRS often referred to as storing logic value “1”.

A tunneling dielectric is positioned between two ferromagnetic layers to create the magnetic tunneling junction (MJT) that allows spin-transfer torque magnetoresistive random access memory to store data[37]. When an external electromagnetic field is applied, the free

ferromagnetic layer's magnetic direction can be altered, while the reference layer's magnetic direction remains fixed. Referred to as being in the LRS, the MTJ occurs when the magnetization direction of the free layer and the reference layer match. Two ferromagnetic layers must have anti-parallel magnetization directions for MTJ to be in the HRS. Sitting between the two metal (M) electrodes is an insulating layer (I) that makes up RRAM[38]. RRAM depends on the conductive filaments that represent LRS and HRS, respectively, forming and breaking in the insulator that separates the two electrodes[39]. Table 1.1 displays a thorough comparison of current and upcoming memory technologies. The table clearly shows that STT-MRAM and PCM offer smaller space advantages over SRAM. On the other hand, PCM has the drawback of significant write delay, whereas STTMRAM offers quick write/read performance, extended endurance, and low programming voltage. Flash memory may eventually be replaced by RRAM since it has a lower programming voltage and a faster write/read speed than Flash. RRAM is a competitive solution for future digital memory because it has several noteworthy advantages over other emerging memory technology candidates, including easy fabrication, a simple metal-insulator-metal (MIM) structure, excellent scalability, nanosecond speed, long data retention, and compatibility with current CMOS technology[40]. The primary advantages of RRAM are displayed in Figure 1.5.

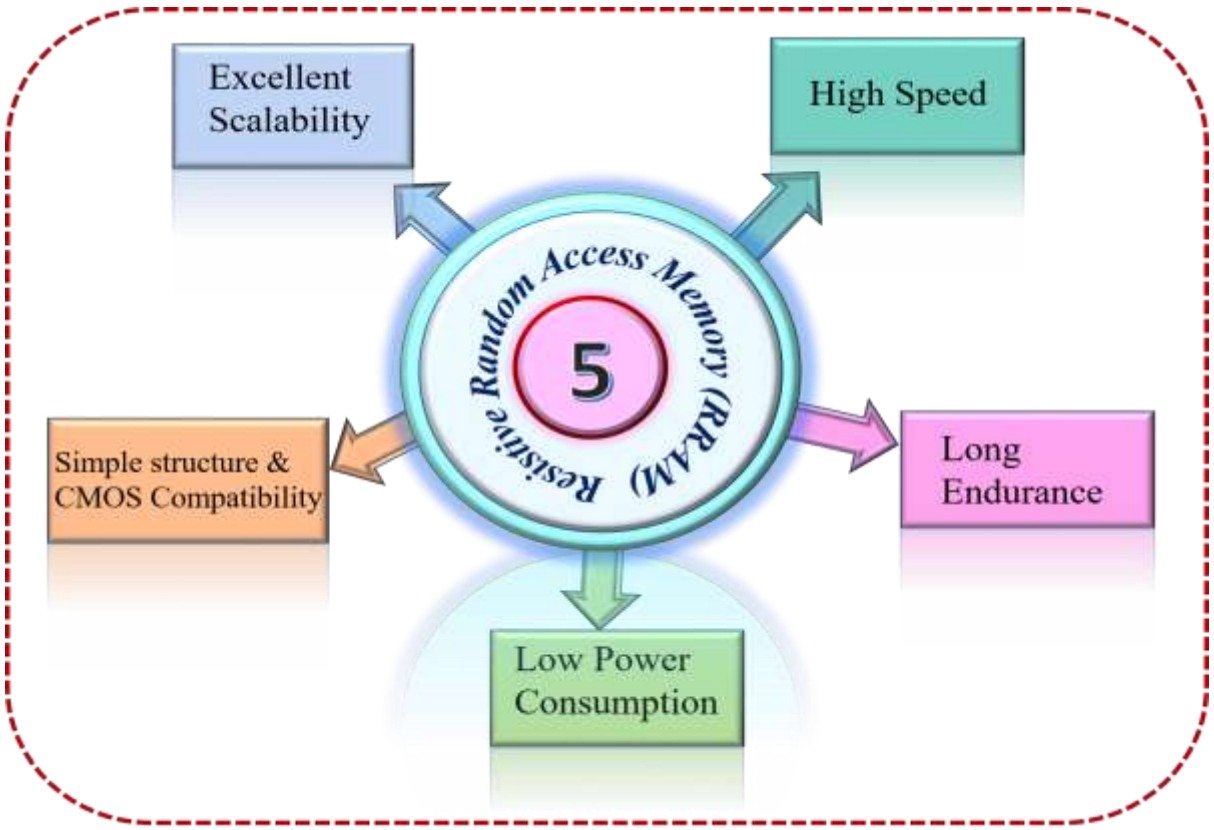

Figure 1.5 The advantages of resistive switching random access memory

A brief comparison between different types of memories based on their performance parameters is shown in Table 1.1. The chart suggests that ReRAM is a possible substitute for Flash because of its low voltage functioning and straightforward design.

Table 1.1 A comparison of recent developments in-memory technology

Memory technology	SRAM	DRAM	NAND Flash	NOR Flash	STT-MRAM	PCM	RRAM
Cell element	6T	1T1C	1T	1T	1(2)T1R	1T(D)1R	1T(D)1R
Cell area	> $100F^2$	$6F^2$	< $4F^2$(3D)	$10F^2$	6-$20F^2$	4-$20F^2$	<$4F^2$(3D)
Voltage	< 1V	< 1V	< 10 V	< 10 V	< 2 V	< 3V	< 3V
Write time	~1 ns	~10 ns	100µs-1ms	10µs-1ms	<5 ns	~50 ns	<10 ns
Read time	~1 ns	~10 ns	~10 µs	~50 µs	<10 ns	<10 ns	<10 ns
Write energy (J/bit)	~fJ	~10fJ	~10fJ	100 pJ	~0.1 pJ	~10 pJ	~0.1 pJ
Endurance	>10^{16}	>10^{16}	>10^4	>10^5	>10^{19}	>10^9	~10^6-10^{12}
Retention	N/A	~64 ms	>10 y	>10 y	>10 y	>10 y	>10 y
Scalability	Yes	Yes	Yes	Yes	Yes	Yes	Yes
Non-Volatile	No	No	Yes	Yes	Yes	Yes	Yes
Multibit	No	No	Yes	Yes	Yes	Yes	Yes
F: Feature size of lithography							

Resistive random access memory creates a metal-insulator-metal (MIM) or metal-oxide-metal (MOM) configuration by taking advantage of the resistive switching process in an insulating or semiconducting oxide layer positioned between two metal electrodes. Figures

1.6(a-b) shows the representative ReRAM-based memory cell structure in vertical sandwich and lateral planar configuration, respectively. When voltage pulses are applied, the resistive switching phenomenon causes a significant change in resistance (>1000%). By supplying the right voltage, the resistance of the cell may be adjusted to the desired values [41].

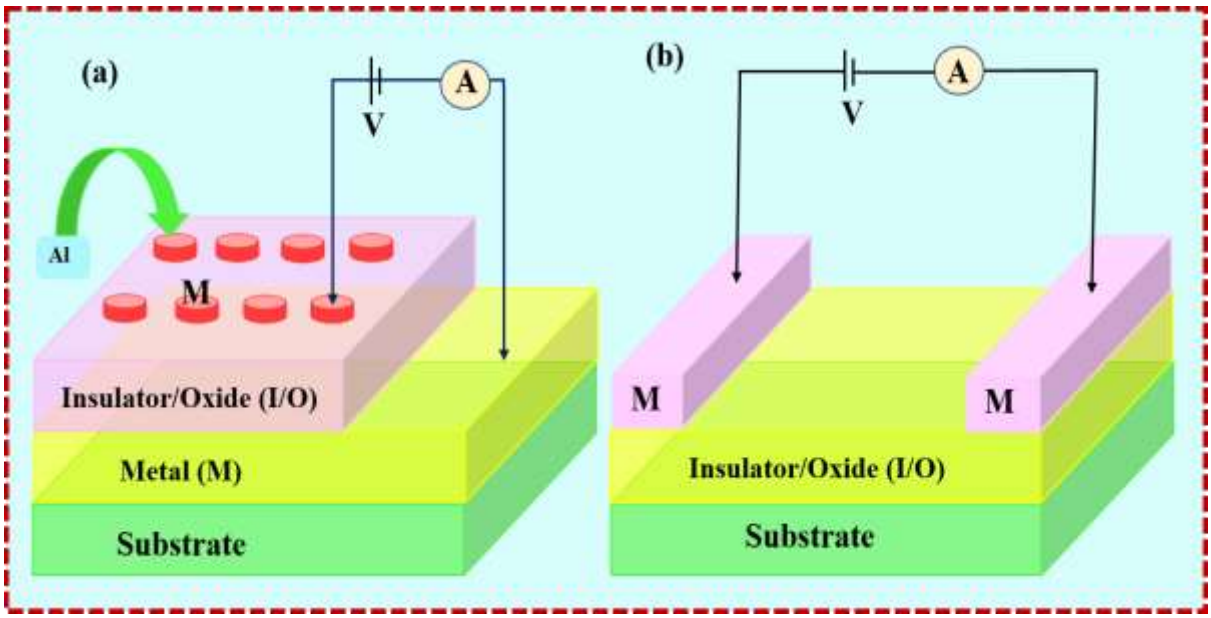

Figure 1.6. Diagram showing a ReRAM memory cell in two different configurations: (a) vertical sandwich and (b) lateral planar to create a MIM or MOM structure.

The first ReRAM-based device was reported in 2002 by researchers from Sharp Laboratories of America, Sharp Corporation, and the University of Houston[41]. In the above studies, the sample comprised of Pt/$Pr_{0.7}Ca_{0.3}MnO_3$/Pt capacitor with the PCMO films deposited by the metal-organic decomposition (MOD) technique. Later, several transition metal binary oxides were also found to exhibit reliable bistable resistance switching behaviour and were considered promising candidates for ReRAM-based memories. The resistive switching phenomena in transition metal oxides had been intensively studied during the 1960s,[42] much earlier than in PCMO. This category of materials includes NiO,[43] TiO_2,[44] Cu_xO,[45] ZnO[46] etc. Apart from binary oxides several materials, such as chalcogenides[47], organic semiconductors[48] and ferroelectric materials also exhibit resistive switching. From an industrial perspective, binary oxides are superior than perovskite materials such as PCMO because of their more straightforward structure, which consists of a single metal element (making stoichiometry easier to accomplish), which greatly streamlines the fabrication process. Furthermore, as Cu is frequently employed as connecting wire and Ti and Ni act as materials

for interconnecting silicon, oxides like NiO, Cu_xO, and TiO_2 may be able to prevent element interference in semiconductor factories.

1.6 Modes of Resistance Switching

Resistive random access memory is made up of resistive switching memory cells having a metal-insulator-metal (MIM) configuration (RRAM). The two metal electrodes (M) are positioned between an insulating layer (I) in the design. Figures 3a and 3b, respectively, depict the schematic and cross-sectional views of an RRAM cell. The device can change from a high resistance state (HRS), also known as an OFF state or logic value "0," to a low resistance state (LRS), also known as an ON state or logic value "1," and vice versa, by applying a voltage pulse across the RRAM cell. Resistive switching (RS) is thought to be the cause of resistance level fluctuations in RRAM cells. The high resistance state (HRS) is the state in which an as-prepared RRAM functions. However, introducing a high-voltage pulse causes conductive pathways to develop in the switching layer, which then converts the RRAM cell into an LRS [49]. This process of gradually disintegrating the metal-insulator-metal (MIM) arrangement is known as "electroforming," and the voltage at which it takes place is known as the "forming voltage" (V_f). Noteworthy, the oxide thickness [50] and cell area [51] are discovered to affect the formation voltage. When a high electric field is placed over an oxide film, the electroforming phenomena occur, which is essentially a soft breakdown in the film while retaining optimal current compliance to prevent film damage [21]. To facilitate this switching transition and move the RRAM cell from the LRS to the HRS, a voltage signal known as the RESET voltage (Vreset) is now applied. This operation is known as the "RESET" process [52]. When a voltage pulse is applied, the RRAMs HRS can convert to LRS. The procedure is known as the "SET" process, and the voltage at which the changeover from HRS to LRS happens is called the "SET voltage" (Vset) [53]. A low read voltage that doesn't alter the present state of the cell is necessary in order to effectively read data from an RRAM cell and determine whether it is in the logic 0 (HRS) or logic 1 (LRS) state. LRS and HRS keep the appropriate values when the provided voltage is removed, demonstrating that RRAM is a non-volatile memory. The switching modes of RRAMs can be divided into two categories based on the voltage polarity applied: (1) unipolar; (2) bipolar:

1.6.1 Unipolar switching: Applying a voltage with the same direction but variable magnitude can generate switching in unipolar switching, as demonstrated in Figure 1.7a. Hence, the polarity of the supplied voltage has no impact on the capacity of the device to switch (set and reset procedure) between various resistance states.

Numerous extremely insulating oxides, including binary metal oxides, have been shown to exhibit this kind of resistive switching behaviour [54].

1.6.2 Bipolar switching: In bipolar switching (Figure 1.7b), the RRAM cell transitions from an HRS to an LRS at one polarity (positive or negative) and then returns to the HRS at the opposite polarity. In other words, the polarity of the supplied voltage determines how the gadget transitions (sets and resets) between different resistance states. Resisted switching behaviour of this kind is typically seen in semiconducting oxides, like complex perovskite oxides [55].

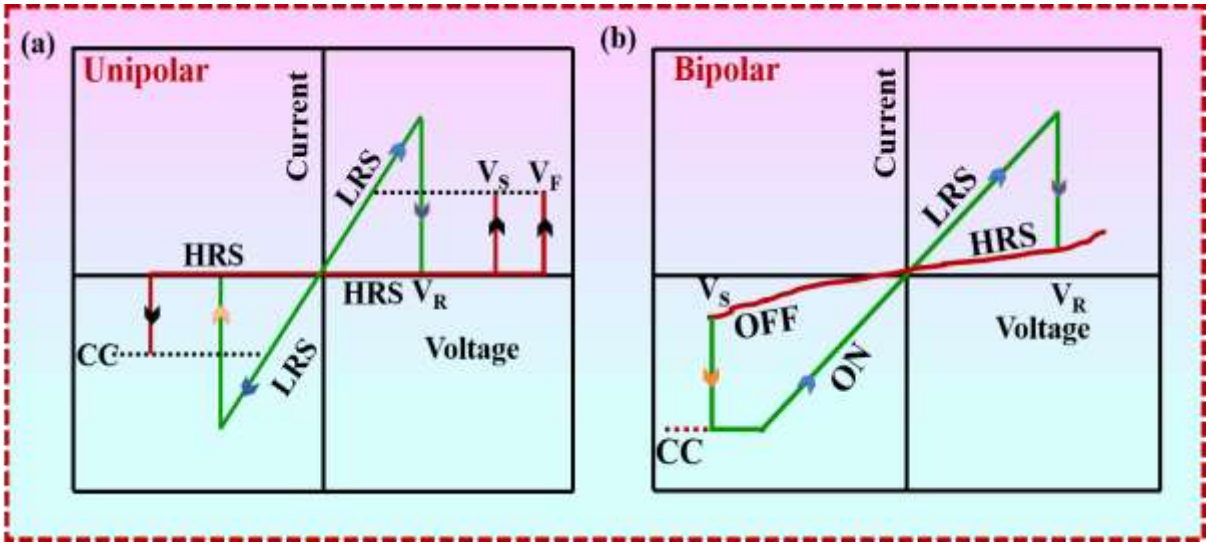

Figure 1.7. An illustration of the resistive switching behavior in (a) unipolar and (b) bipolar modes. The samples permanent breakdown is avoided by using current compliance (CC).

It is known that Joule heating is the physical process that breaks a conducting filament during the reset operation in unipolar switching. Nevertheless, Joule heating still helps to speed up the movement of charged species, which is the primary cause of conductive filament disintegration in bipolar switching. The RRAM device is subject to a compliance current (Icc) to guarantee that the dielectric switching layer does not permanently break down during the forming/set operation. During the off-chip testing, the compliance current (Icc) is often guaranteed by a semiconductor parameter analyser or a cell selection gadget (transistor, diode, resistor).

1.7 Resistance random access memory performance parameters

Different parameters which characterize the performance of the memory cells are described below:

1.7.1 Operating Voltage: An operating voltage that is too high is known to be lethal in real-world applications. The reason for this is that high power consumption is correlated with high operating voltage. Besides, a high working voltage may cause issues with reliability. To gain an advantage over Flash memory, which does suffer from high operating voltages, both the programming and erasing voltages for RRAM devices should be only a few volts [21].

1.7.3 Resistance ratio: The resistance ratio is the difference between the resistance at HRS and the resistance at LRS, and it is significant in RRAM applications since it has a direct impact on programming and erasing accuracy. In general, a resistance ratio greater than 10 is required to distinguish the two resistance states in circuit design [56]. The resistance ratio in certain RRAM devices can reach values of six or seven powers of magnitude. An enormous resistance ratio like this raises the prospect of employing multi-bit or multilevel memory to create high-density memory.

1.7.4 Endurance: A regular switch between HRS and LRS can be made on an RRAM device, although doing so can cause irreversible harm, which is usually called deterioration. The threshold for endurance, also known as electric exhaustion, is the number of set/reset cycles that must be completed before HRS and LRS become indistinguishable. To exceed Flash memory, which has a maximum write cycle count varying from 10^3 to 10^7, depending on the kind, RRAM needs to have at least the same endurance, if not more.

1.7.5 Retention time: The duration that a memory cell will stay in a particular state following programming or erasure is known as its retention time, and it represents the memory cell's inherent capacity to hold onto its information. Information retention on the majority of commercially available products is guaranteed for a minimum of ten years, regardless of power state.

1.7.6 Operating speed: The fastest programming or erasing time for a device cell is known as operating speed. A TiN/TiOx/HfOx/TiN RRAM devices bipolar resistive switching characteristics were described by Lee et al. This device has the fastest switching speed yet recorded, reaching up to 5 ns. RRAM devices currently have a maximum operating speed of 5 to 100 ns[56].

1.7.7 Number of storage levels: The capacity to store several bits at various controlled resistance levels in order to boost memory density is known as multi-level storage. The SET resistance of ReRAM can be adjusted via operating voltage or CC. Reliability and reproducibility have been achieved for the differentiation of five resistance states or memory levels using a planar graphene/SiO_2 nanogap arrangement[57].

1.7.8 Device yield: Device yield is the proportion of functional cells. The yield of the device appears to be increased by using a suitable electrode material, doped metal oxide,[58] or purposefully adding metal nanocrystals to the oxide[59].

1.8 Emerging resistive random-access memory

In order to achieve universal memory, there is a strong need to significantly enhance NVM performance. With its enormous storage capacity, quick response speed (less than 10 ns), good endurance (more than 10^7 cycles), retention (more than 10 years), low cost, and straightforward construction, the newly developed RRAM is a promising technology among NVMs[60]. RRAM cells are typically constructed using a structure resembling a capacitor, which is made up of a sandwich structure made of metal, insulator, or conductive transition metal oxide-metal (MIM), as Figure 1.8(a) illustrates. Resistive switching is the ability to switch the RRAM between high and low resistance states by applying voltage to metal electrodes. As shown in Figure 1.8(b), this straightforward construction makes it simple to achieve a high scalable cross-point structure[61].

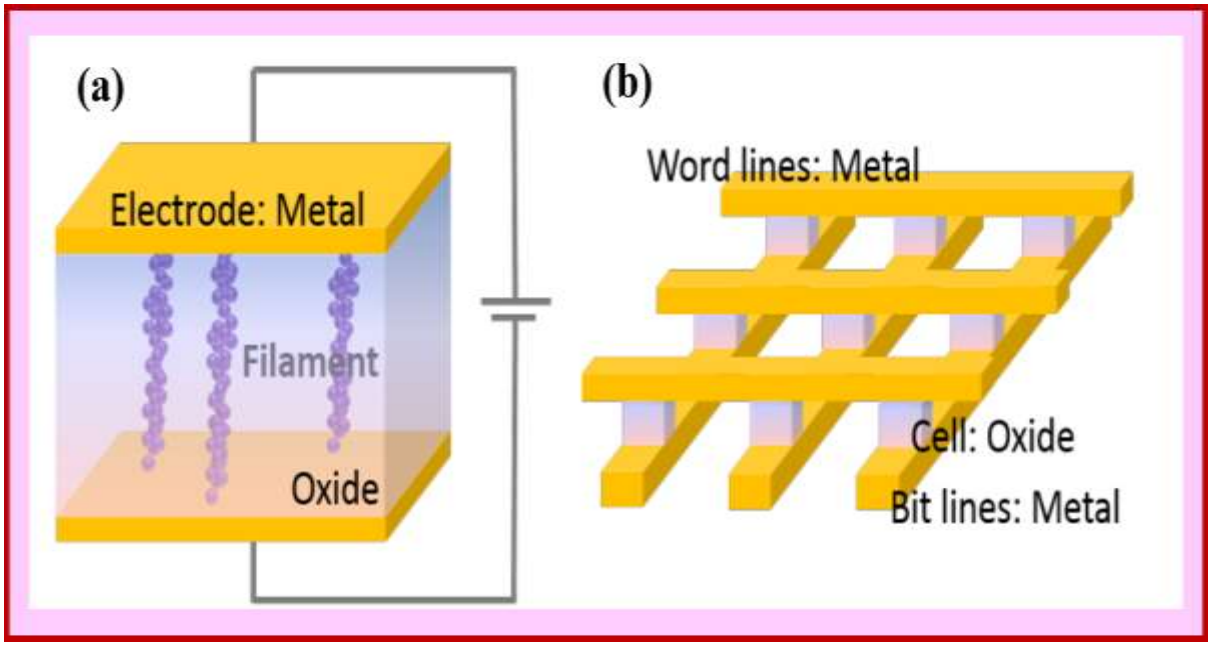

Figure 1.8 Diagrams representing (a) an RRAM cell in MIM structure and (b) a cross-point memory

Resistive switching-based memories are not a new idea; they are closely linked to mersisters. Chua initially made note of this idea in the 1970s[62], when he described the charge and flux-regulated memory. The mersister and its connection, as shown in Figure 1.9, are the basic components of a two-terminal circuit. But it wasn't until 2008 that the missing mersister was discovered. As the first mersister, researchers from HP Labs examined the current-voltage behaviour in specific titanium dioxide cross-point switches[63]. Throughout this decade, the mersister saw tremendous development, leading to improvements in durability and retention, smaller size, higher On/Off ratio, and reduced power consumption. In this chapter, we will discuss the mechanism, construction, materials, performance, and perspective of the oxide-based RRAMs in-depth, emphasizing the MIM system-based RRAMs.

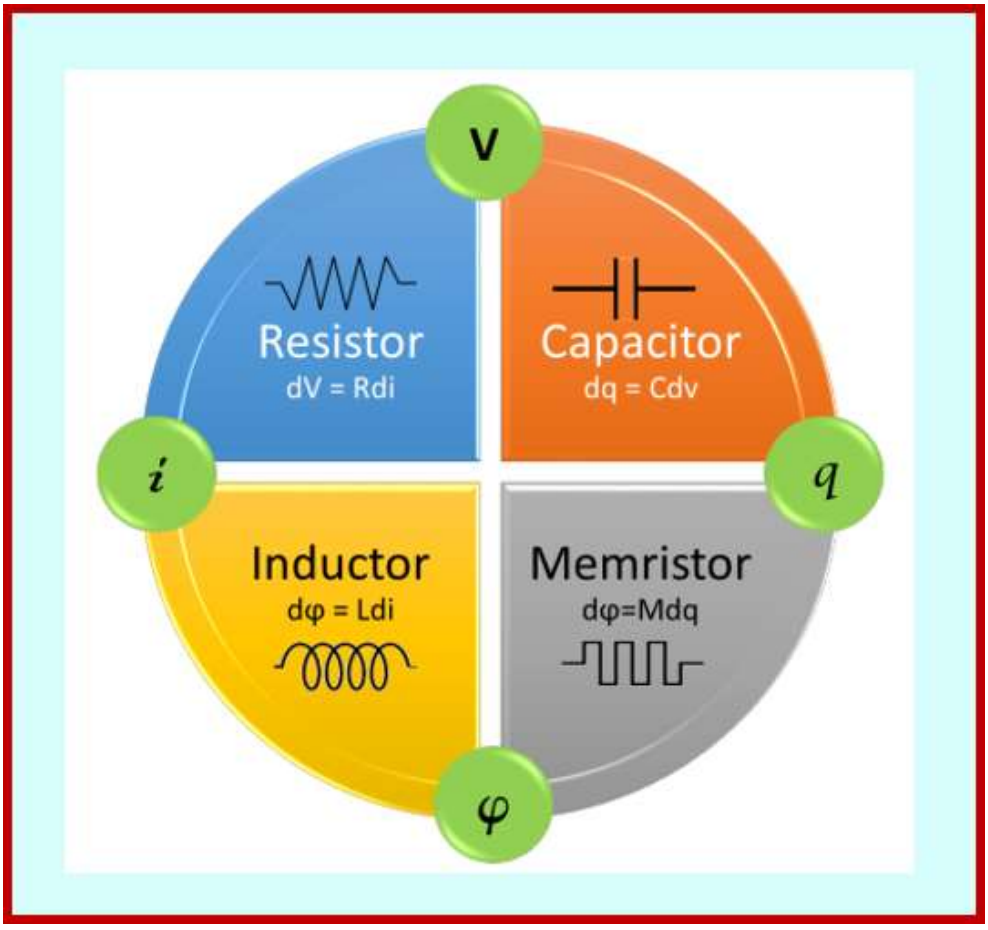

Figure 1.9 The class of basic two-terminal circuit components and their connection

1.9 Resistive switching classification; nature of conducting paths

As discussed earlier, ReRAMs have several advantages over other non-volatile memories, such as: (i) very small cell area (1R1D or 1R1T) and good scaling prospect, which makes it appropriate for high-density integration; (ii) low operation voltage (less than 1.5V) and low power consumption (especially for READ operation); (iii) fast READ/WRITE speed; (iv) excellent compatibility with current semiconductor technology; and (v) low fabrication cost. The major hindrance to the practical use of ReRAM is the difficulty in understanding its driving mechanism. Detailed experimental and theoretical studies have been carried out to understand the driving mechanism, but none of them has gained general acceptance. The mechanism seems to be very sensitive to deposition conditions and a combination of oxide and metal contact materials. In several studies, identical metal-oxide materials systems prepared by similar techniques have been observed to operate under different mechanisms [64-66].

Two types of conducting paths have been identified for the switching mechanism of ReRAM devices: (1) filamentary conducting path and (2) interface type conducting path (Schottky barrier alteration at the metal-oxide interface).

1.9.1 Filamentary type conduction: In several oxide materials, resistive switching originates from the formation and rupture of conducting filaments as a result of soft dielectric breakdown in the oxide matrix[67]. This type of switching mechanism has been used to explain both unipolar and bipolar resistive switching phenomena. Figure 1.10 (a) shows the schematic diagram depicting filamentary-type unipolar resistive switching characteristics. The as-deposited or pristine sample does not have any conducting path and hence is found to be in HRS. This situation invariably occurs in the pristine sample before electroforming. Post electroforming process, filamentary conducting paths form as a result of breakdown in the active switching layer, and hence transition to LRS occurs. During the reset process, which invariably occurs as a result of Joule heating, filaments rupture and the device switches back to HRS. Finally, the reformation of filaments takes place during the set process. Thermal redox and/or anodization near the interface between the metal electrode and the oxide may also result in the formation and rupture of the filaments[68]. Electrochemical migration of oxygen ions in the film changes the valence state of the cation, resulting in changes in electronic conductivity along filaments, which causes bipolar switching [69]. Additionally, it is proposed that the conducting filaments could be made up of flaws existing between the

electrodes and that Joule heating-induced electro thermal processes are what cause them to repeatedly burst or generate them.

1.9.2 Interface type conduction: In the interface type conduction, electrical changes responsible for resistive switching take place at the metal-oxide interface, as shown in Figure 1.10 (b). The contact resistance between metal and the active oxide layer gets modified with the application of an electric field. This type of mechanism is usually observed in the bipolar resistive switching process in perovskite oxides. Electrochemical migration of oxygen vacancies,[70] trapping of charge carriers,[71] and electric field-induced insulator to metal transition[72] are the models that have been proposed for explaining an interface-type conduction mechanism.

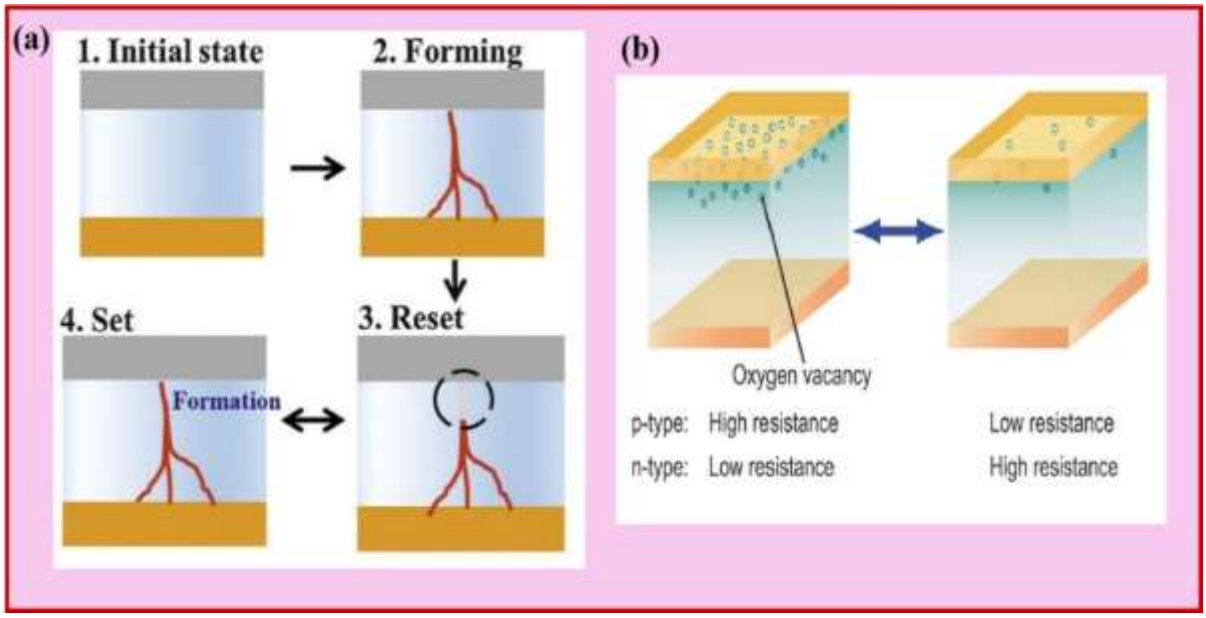

Figure 1.10 Schematic illustration of the nature of conducting path showing (a) Filamentary type induced due to soft breakdown in the oxide layer and (b) Interface type showing changes in the oxygen vacancies concentration in the vicinity of the metal-oxide interface.

1.10 Electrical fingerprint from device characteristics

Understanding the resistive switching mechanism is one of the most important requisites for improving the device performance parameters. The difference between the filamentary and interface types of resistive switching can be understood by studying the area dependence of the memory cell parameters[21]. In the filamentary type resistive switching the resistance of the memory device in LRS and HRS does not show any dependence on the device area, whereas for interface type resistive switching, device resistance scales with the device area [73]. It has

been found that the resistance of a memory cell made of semiconducting Nb-doped $SrTiO_3$ in LRS and HRS is inversely proportional to the cell area, but the resistance of an insulating NiO cell is significantly less reliant on the cell area. This indicates that in the case of Nb-doped $SrTiO_3$, resistive switching takes place over the entire area of the memory cell, whereas, for NiO transition from HRS to LRS occurs through localized filamentary conduction. Apart from providing important clues regarding the switching mechanism, area-dependent switching characteristics point towards the scaling limit of ReRAM. It was observed that as we decrease the size of the memory cell obeying filamentary mechanism, the size and current level of filaments decrease, resulting in a decrease in reset current and reset voltage, thereby, reducing the power consumption of the memory cell and hence realizing the goal of fabrication of universal memory element which combines the high-speed performance of SRAM with the non-volatility of Flash[74].

It may be mentioned here that in the case of a filamentary model, a single dominant filament or multiple filaments may control the device current. In the former case, the switching parameters, such as set voltage, reset voltage, and reset current do not scale with the device area[75]. Thus, device current or reset current does not decrease with the device dimension, and hence power consumption will increase, thereby failing the possibility of higher density memories. However, Kinoshita et. al. have proposed the idea of the existence of multiple filamentary paths being responsible for device current in LRS, whereby the switching parameters scale with the size[76].

1.11 Modification of metal-oxide interface using organic interlayer

Apart from modifying the metal-oxide interface by changing the top electrode, the ReRAM properties can also be modified by incorporating an additional layer of organic material[77-79]. This leads to the modification of structural, electrical, and optical properties of the resultant hybrid interface with improved device characteristics. Figure 1.11 shows the schematic diagram for the various types of hybrid interfaces.

Due to the structural and electronic differences between organic and inorganic materials, a study of the electrical and morphological properties of these hybrid interfaces is significant. The organic-inorganic-based hybrid devices are promising because of the advantages resulting from two types of materials. The low cost and ease of synthesis of organic materials, along with high electron mobility and great chemical and physical stability of their inorganic counterparts, resulted in devices with desired properties. By controlling the properties of organic and inorganic layers, the interfacial properties of the hybrid interfaces and the device

characteristics can be fine-tuned and controlled[80-83]. The organic-inorganic interfaces have opened up new possibilities for novel hybrid devices, such as photovoltaic devices, light-emitting diodes, and field-effect transistors. It has been observed that light emitting device based on a self-assembled monolayer (SAM) modified indium tin oxide (ITO) anode [ITO/N′-bis (3-methylphenyl)-N, N′-diphenyl-1,1′-biphenyl-4, 4′- diamine (TPD)/ tris-(8-hydroxyquinoline) aluminum (Alq3)] could endure higher current and exhibit much higher luminance in LiF devices[81]. A thin film field-effect transistor based on hybrid interfaces, involving 2D layered organic-inorganic perovskites $(C_6H_5C_2H_4NH_3)_2SnI_4$ as semiconducting channel, shows high carrier mobilities and current modulation greater than 10^4 [83]. TiO_2/P_3HT (poly(3-hexylthiophene)) hybrid interface has been found to modify energy level alignment due to dipole formation and results in the enhancement of TiO_2/P_3HT-based hybrid solar cells[80].

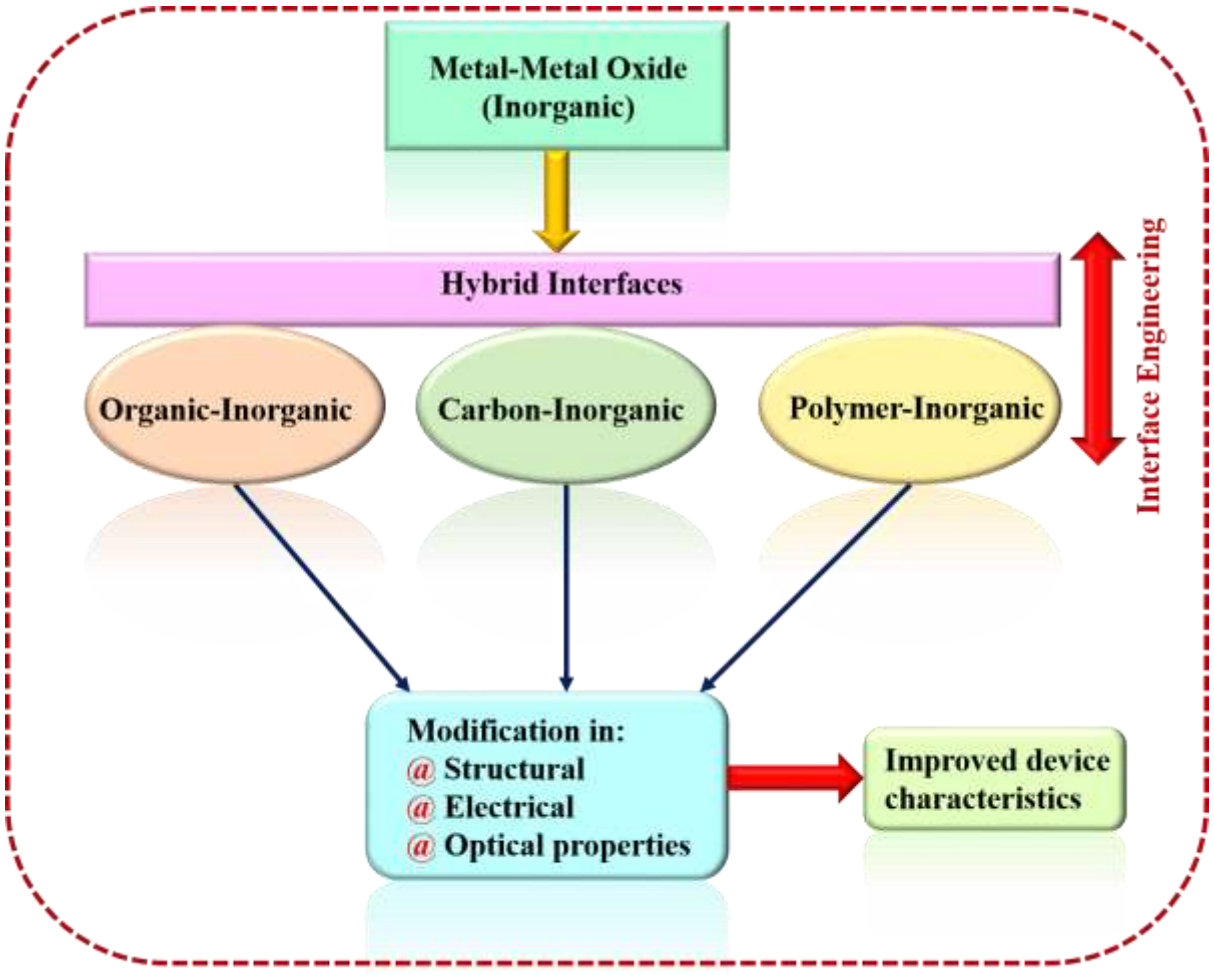

Figure 1.11 Schematic diagram illustrating the concept of interface engineering using an organic interlayer.

Non-volatile memory chips with combination interfaces have gained traction lately as viable options for use in upcoming optoelectronic and electrical devices. Because of their excellent performance, low cost, mechanical flexibility, and ease of manufacturing, hybrid organic-inorganic nanocomposites-based organic bistable devices are quickly becoming one of the most popular types of non-volatile memory devices. Many varieties of nanocomposites have been developed through research and development due to the potential uses of NVM devices fabricated from hybrid nanocomposites. Hybrid organic-inorganic nanocomposites are composed of organic layers containing metal nanoparticles,[84] semiconductor quantum dots (QDs),[85] core-shell semiconductor QDs, fullerenes, carbon nanotubes, [86] graphene molecules or graphene oxides (GOs)[87]. Figure 1.12 exhibits a flexible device based on a graphene oxide layer deposited on a flexible plastic substrate, showing bipolar resistive switching[88]. The device based on pure graphene oxide exhibited good retention time and small switching voltage, but the ON/OFF current ratio was small as compared to complementary metal-oxide-semiconductor devices. Wu et. al have improved the ON/OFF current ratio and cell-to-cell uniformity by employing a trilayer structure PI/PI:GO/PI, in which insulating polymer PI was used as the matrix for the GO sheets [89].

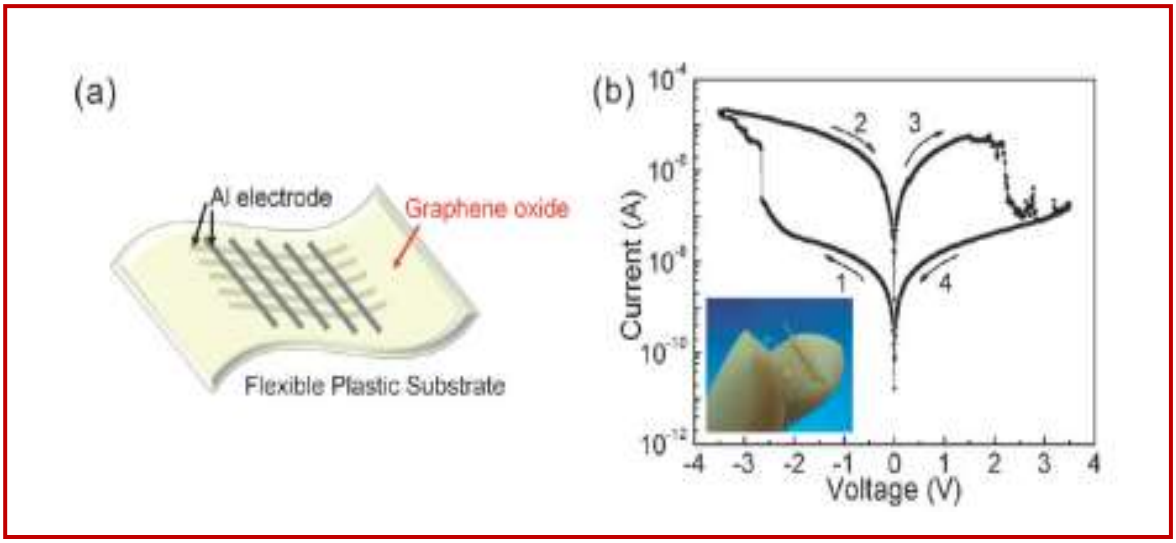

Figure 1.12. (a) Diagram of a flexible crossbar memory device based on G-O. (b) A typical I-V curve for an Al/G-O/Al/PES device is displayed on a semi-logarithmic scale. The arrows represent the voltage sweep direction. The left inset depicts a true shot of a device.

The electrical switching in PI/PI:GO/PI based structure may originate from the charge trapping and de-trapping in GO sheets. In the case of an NVM based on hybrid nanocomposites, the memory effect is strongly correlated with the presence of inorganic nanomaterials, for

example, ZnO QDs, Au nanoparticles, CdSe nanoparticles, and carbon nanotubes, embedded in a polymer matrix, because the current difference between the ON and the OFF states for the polymer-only device is negligible[90]. The importance of a hybrid interface is well demonstrated by recent results, which show improved memory effects with a wide ON/OFF ratio, high endurance, longer retention duration, and high cell-to-cell uniformity. However, some of the issues related to hybrid interface-based memory devices have hindered progress towards their commercialization. These include alignment of organic/inorganic interface, nature of structural and electronic interaction at the hybrid interfaces, etc, which require further understanding, for device optimization.

1.12 Material Selection

1.12.1 Tin oxide

SnO_2 is a metal-oxide-semiconductor with a broad bandgap that is widely utilized in many areas of oxide electronics. It has various benefits, including excellent electrical and optical properties. The inherent n-type semi-conductivity of SnO_2 and the presence of oxygen vacancies make it suitable for memristive applications. A broadband gap material with up to 97% optical transparency in the visible range is SnO_2 (3.6 eV). SnO_2 is essential for transparent conducting electrodes and gas sensors, but resistive switching (RS) memory has dedicated little attention to it. The use of transition metal oxides, such as TiO_2, SnO_2, ZrO_2, and ZnO, has grown more popular as a result of its low power requirements, quick switching, and simple structural design. Organic ReRAMs have an advantage in great mechanical strength, easy production, and low cost, but inorganic ReRAMs used as storage mediums have a notable advantage over organics in switching stability.

1.12.2 Reduced graphene oxide

Graphene, or rGO, has exceptional properties that make it suitable for use in resistive memory combinations with metal oxide. These properties include its layer-specific surface area, rapid electron transport at room temperature, and chemical stability. Various types of electronic devices, including mobile smartphones, displays, e-paper, and wearable information technology devices, have shown promise for using resistive switching memory systems. Additionally, flexible memory systems have made use of graphene oxide thin films. Since mechanical stress is reduced, graphene electrodes can enhance the electrical characteristics of memory devices. Additionally, it has been observed that while there are numerous papers available for rGO-MO based nanocomposite for photocatalytic application, energy storage, and

gas terms, there are none for rGO-SnO_2 based nanocomposite for ReRAM application, which is what motivates the current piece of work.

1.12.3 Molybdenum disulfide

In recent times, two-dimensional (2-D) materials have gained tremendous attention and growth owing to their excellent performance in applications not limited to field-effect transistors, sensors, photodetectors, non-volatile memories, and solar cells[91]. Among them, MoS_2 has been widely used as a functional material in diverse fields, such as lubrication, electronic transistors, batteries, photovoltaics, and catalysis[92]. Furthermore, MoS_2 has a unique layered structure, with each Mo layer sand-witched between two sulfur layers. Unlike graphene, a zero-gap semimetal, and bulk MoS_2, an indirect-gap semiconductor, monolayer MoS_2 has been demonstrated to have a direct bandgap. As a result, MoS_2 could be helpful in future Nanotechnologies. MoS_2 is the first of the 2-D materials. Due to their ability to endure mechanical stress, strain, and flexible circumstances, the transition metal chalcogenide that has been investigated the most strongly and its composites with polymer dielectrics have attracted considerable attention. For a memristive device to be integrated with a flexible and wearable electronic system, these are the necessary properties. There are, however, few reports of these composite thin films being used in RRAMs as a switching layer. These devices are flexible, but they also have higher working voltages and greater ON-currents, which prevent them from being a non-volatile memory device that uses less power.

1.12.4 Hexagonal boron nitride

Hexagonal boron nitride (hBN) is an intriguing ultra-wide bandgap insulating material with a crystal structure resembling graphite, [93] where boron and nitrogen atoms alternately replace the sp^2 hybridized carbon atoms. In comparison to other crystalline forms, hBN is the BN material that has been studied the most due to its graphite-like structure. Because of its graphite-like structure, hBN has great chemical and thermal stability and strong thermal conductivity, making it a viable choice for oxidation resistance and heat spreading [94]. Additionally, 2D materials provide a significant increase in the physical and chemical properties of the confinement effects, as well as a high number of active sites. From this perspective, surface-modified electrodes are crucial for improving good stability, high selectivity, and specificity in resistive switching applications compared to alternative fabrication techniques. The catalytic reaction process may be facilitated by the combination of large surface area 2D materials with metal oxide nanoparticles by increasing the kinetics of electron transport. A limited amount of research has been done on hexagonal boron nitride (hBN), despite there being a few papers on

the resistive switching effect in a variety of 2D materials, primarily graphene and molybdenum disulfide (MoS_2). Flexible resistive switching applications for hBN and its nanocomposites still have a lot of unexplored potential. These hybrid nanocomposites are expected to have a configurable bandgap, a high level of flexibility, and a combination of unusual electrical and mechanical properties; as a result, more research is required to extract more insightful conclusions [95].

1.13 Objectives of the present work

The main goal of the current objective is to investigate the structural, optical, and electrical characteristics of composites based on metal oxide-2D materials for non-volatile resistive memory devices.

The following are the key objectives of the thesis:

1. To study the structural, optical, and electrical properties of metal oxide-2D material-based composites for non-volatile resistive memory devices.
2. To study the resistive switching property of SnO_2-rGO-based composite synthesized using the hydrothermal technique. Systematic investigation of the effect of the weight percentage of 2D material in the SnO_2 matrix on switching will also be studied.

3. To explore the effect of rGO material in SnO_2 matrix on the flexible resistive switching performance will be carried out.

4. To explore the effect of MoS_2 material in SnO_2 matrix on the flexible resistive switching performance will be carried out.

5. To explore the effect of hBN material in SnO_2 matrix on the flexible resistive switching performance will be carried out.

1.14 Thesis overview

There are six chapters in the thesis. This chapter acts as the show introduction. This thesis includes a comprehensive collection of experiments and in-depth analyses that have been carefully conducted in accordance with the previously stated objectives.

The following chapters provide an overview of the results of the current thesis:

Chapter 1: **Introduction**

This chapter gives a brief introduction to various types of non-volatile memories. This chapter discusses the various materials that exhibit the phenomenon of resistive switching. An overview of different types of resistive switching is provided leading to the need for modifying resistive switching properties by incorporating hybrid interface and understanding their nature. Introduction to the concept of non-volatile memory, review of existing non-volatile memory (FeRAM, MRAM, PRAM, ReRAM), materials selection for ReRAM device physics. It also gives a brief idea about the hybrid interface and modification of device properties using the hybrid interface.

Chapter 2 Synthesis and characterization techniques for SnO_2-2D materials (rGO, MoS_2, hBN) based composites, fabrication of spin coating technique and thermal evaporation technique is used for growing top electrode.

This chapter begins with an analysis of the synthesis process and film deposition of SnO_2-2D based MIM structures for memory applications. The formation of SnO_2-2D nanostructures and its subsequent modifications are examined using various characterization techniques like X-ray diffraction (XRD), Raman spectroscopy, scanning electron microscopy (SEM), ultraviolet-visible (UV-Vis) absorption spectroscopy, transmission electron microscopy (TEM), energy dispersive X-ray analysis (EDAX), Fourier transform infrared spectroscopy (FTIR), and X-ray photoelectron spectroscopy. All these characterization techniques are described in this chapter.

Chapter 3 Improved resistive switching effect of rGO weight percentage on structural, optical, and electrical properties of rGO-SnO_2 nanocomposite based resistive memory device for non-volatile memory application.

In this chapter, we have shown how a nanocomposite made of reduced graphene oxide (rGO) and tin oxide (SnO_2) is being used as active switching layered material. Using hydrothermal method, rGO, SnO_2, and rGO-SnO_2 nanocomposite was synthesized. X-ray diffraction, SEM, and Raman spectroscopy methods were used to confirm the creation of the nanocomposite. Here, we demonstrate a spin-coated, SnO_2 and rGO-SnO_2 based bipolar resistive switching memory. The top Al electrodes were deposited by a shadow mask, while the bottom ITO electrode was covered with pure SnO_2 and rGO-SnO_2 films. It was found that devices using rGO-SnO_2 had better resistive switching than those using pure SnO_2 film. By lowering the operating voltage of the device from 4.11 V for SnO_2 to 1 V for rGO-SnO_2 composite-based

devices, the switching properties of the composite-based film are recognized to have improved. The resistance ratio in the composite-based films also significantly improved. In addition, the retention and endurance behaviour of the fabricated composite film-based device were examined for $1*10^3$ s and 100 cycles, respectively, and didn't show any signs of degradation. By fitting the current voltage characteristics in the low-resistance and high-resistance states, the memory device's working mechanism was described. The current study showed an interesting use of reduced graphene oxide to enhance the switching characteristics of tin oxide-based resistive memory systems. As it has been demonstrated that the incorporation of rGO in SnO_2 nanocomposite induced bipolar resistance switching with an improved ON/OFF ratio. After that in this chapter, the effect of the rGO content on the resistive switching capabilities of composite film was also investigated using a flexible device designed as an Al/rGO-SnO_2/ITO-PET structure. Furthermore, we have fabricated resistive switching memory devices of pure SnO_2 and rGO-SnO_2 (5, 7, and 10 wt.%) nanocomposite powder spin-coated over commercially available ITO-PET substrate. The resistive switching performance of the fabricated device was compared and observed that the device with 7 wt. % rGO in SnO_2 has a maximum ON/OFF ratio of ~ 70, in comparison to ~ 2 and ~3 for 5 and 10 wt. % sample respectively. Additionally, the Al/7%rGO-SnO_2/ITO-PET device exhibited switching characteristics with a lower switching voltage, good endurance behaviour up to 100 cycles, and another crucial factor for RRAM devices is retention time, which was measured for this device up to 2×10^3 seconds. The described devices enhanced electrical properties show potential for future RRAM memory.

Chapter 4 Effect of MoS_2 weight percentage on the resistive switching performance of the MoS_2-SnO_2 based memristive device.

In this chapter, we have used MoS_2-SnO_2 nanocomposite powder synthesized using a simple hydrothermal approach to fabricate resistive memory devices in MIM configuration. The phase purity and the structural and chemical composition of the synthesized MoS_2-SnO_2 powder were analysed using XRD, HRTEM, and XPS techniques. The XPS core level spectra for Mo 3d, S 2p, O1s, and Sn 3d peaks for the MoS_2-SnO_2 nanocomposite show stronger interfacial interaction between MoS_2 and SnO_2. Furthermore, the effect of the MoS_2 weight percentage (0, 5, 7, and 10 wt.%) in SnO_2 on the resistive switching capabilities of nanocomposite film was investigated by designing a device in MIM configuration with Al and ITO-PET as top and bottom electrodes, respectively sandwiching active MoS_2-SnO_2 memory layer. With a rise in

MoS_2 concentration, the I_{ON}/I_{OFF} ratio (3, 100, and 25) decreased, according to the observed current-voltage (I-V) characteristics over the created devices with varied MoS_2 weight percentages. Bipolar resistive switching is demonstrated by the Al/MoS_2-SnO_2/ITO-PET memory device. The fabricated Al/7%MoS_2-SnO_2/ITO-PET device showed the highest I_{ON}/I_{OFF} ratio and was 100 times greater than that of Al/SnO_2/ITO-PET device. The filament formation and rupture model due to the migration of oxygen vacancies between the electrodes, was used to explain the bipolar resistive switching mechanism. The fabricated memory device showed enhanced switching performance, endurance, and retention of about ~100, 100 switching cycles, and 2.1×10^4 seconds, respectively. Further to check the device flexibility, the fabricated memory device was subjected to100 bending cycles, and was seen that HRS and LRS exhibited no appreciable change in magnitude. The memory device created in the present study using a straightforward spin-coating technique provides a viable method for low-cost solution processing of highly dependable and programmable flexible resistive memory cells.

Chapter 5 Two-dimensional (2D) hBN-SnO_2 based flexible memory device for enhanced resistive switching application.

In this chapter, the effect of the insulating hBN content on the resistive switching capabilities of hBN-SnO_2 composite film was investigated using a flexible device designed as an Al/hBN-SnO_2/ITO-PET structure. Hydrothermal synthesis technique is also used here to successfully synthesize the 5%hBN-SnO_2, 7%hBN-SnO_2, and 10%hBN-SnO_2 nanocomposite samples, with average particle sizes of 26.1 nm, 20.8 nm, and 20.7 nm. The as-prepared nanocomposite was characterized using XRD, Raman, FT-IR, FE-SEM, TEM, and XPS analysis. The shift in B1s, N1s, C1s, O1s, and Sn 3d peaks in the hBN-SnO_2 nanocomposite in comparison to pure SnO_2 and hBN indicates an interfacial interaction. Furthermore, we have fabricated resistive switching memory devices of pure SnO_2 and hBN-SnO_2 (5, 7, and 10 wt.%) nanocomposite powder spin-coated over commercially available ITO-PET substrate. Reduction in switching parameters, and improvement in the current ratio further confirmed the modified electronic properties in the hBN-SnO_2 nanocomposite-based resistive memory device. The resistive switching performance of the fabricated device was compared and observed that the device with 7 wt. % hBN in SnO_2 has a maximum I_{ON}/I_{OFF} ratio of ~ 10^3, in comparison to ~ 96 and ~4 for 5 and 10 wt. % sample respectively. Additionally, the Al/7%hBN-SnO_2/ITO-PET device exhibited switching characteristics with a lower switching voltage, good endurance behaviour

up to 100 cycles, and another crucial factor for RRAM devices is retention time, which was measured for this device up to 1.5×10^4 seconds. The described flexible device enhanced electrical properties show potential for future RRAM memory.

Chapter 6 Conclusions and future scope of work.

This chapter summarizes the major results and conclusions of the thesis and enlightens the scope of further work in the non-volatile memory device area.

CHAPTER 2

Synthesis, Film Fabrication and Characterization Technique

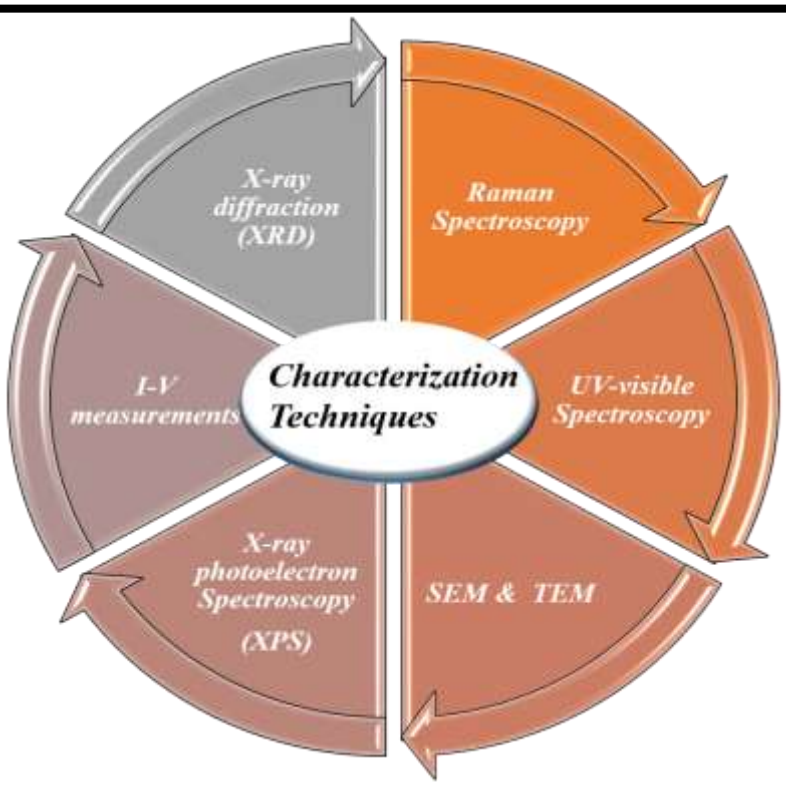

This chapter begins with an analysis of the synthesis process and film deposition of SnO_2-2D based MIM structures for memory applications. The formation of SnO_2-2D nanostructures and its subsequent modifications is examined using various characterization techniques like X-ray diffraction (XRD) is used to examine the crystal structure of the synthesized nanostructures, Raman spectroscopy, and ultraviolet-visible (UV-Vis) absorption spectroscopy. Transmission electron microscopy (TEM) and scanning electron microscopy (SEM) are used to examine the surface morphology. The examination of attachment of desired functional groups is studied using FTIR. Elemental analysis is done using EDAX and XPS. To create memory devices, metal electrodes are deposited onto the synthesized thin films via a process called thermal evaporation. The measurement of the fabricated devices voltage and current, as well as the dielectric constant, are covered in this chapter. This chapter describes each of these characterisation methods.

2.1 Synthesis of Tin Oxide based 2D (rGO, MoS_2, hBN) materials

The SnO_2-2D materials can be synthesised and modified using a variety of methods, which allows for the customisation of their structures and characteristics to fit a range of needs. These methods can be separated into two groups: 1) Top-down; 2) Bottom-up. In the top-down approach, bulk material is exfoliated into layers by employing mechanical, chemical, or ultrasonic techniques to overcome interlayer forces such Van der Waals interactions. In contrast, the Bottom-up approach makes use of individual atoms to construct nanosheets. First, precursor materials containing atoms of carbon (C), oxygen (O), tin (Sn), molybdenum (Mo), sulphur (S), boron (B), and nitrogen (N) are dissolved, and then the atoms are assembled into structures such as rGO, SnO_2, MoS_2, and hBN. It is imperative to choose a suitable synthesis route before pursuing property analysis and specific applications. To successfully achieve industrialization and commercialization, high yields of high-quality 2D nanomaterials must be synthesized[4]. Thus, we employed a straightforward and environmentally friendly hydrothermal method in our work to synthesize SnO_2-2D nanostructures.

2.2 Hydrothermal method of synthesis

The process of hydrothermal synthesis in 1845, German geologist Karl Emil von Schafhäutl released the first research paper on hydrothermal crystal formation. Since then, various scientists and researchers working around the globe have contributed to developing this technique. Hydrothermal synthesis refers to the synthesis of nanomaterials by chemical reactions occurring inside a sealed Teflon-lined stainless-steel autoclave, filled with water-dissolved reagents under certain temperature and pressure conditions. The optimum amount of aqueous reagents is filled in Teflon to create enough pressure so that nanomaterials of desired morphology and phase are obtained. Also, it must be ensured that Teflon should not overflow during the reaction process. Optimization of temperature, pressure and time for which autoclave is kept in a high-temperature oven leads to a high yield of nanomaterials of good crystallinity [96]. Figure 2.1 shows the setup of the hydrothermal autoclave used in hydrothermal synthesis.

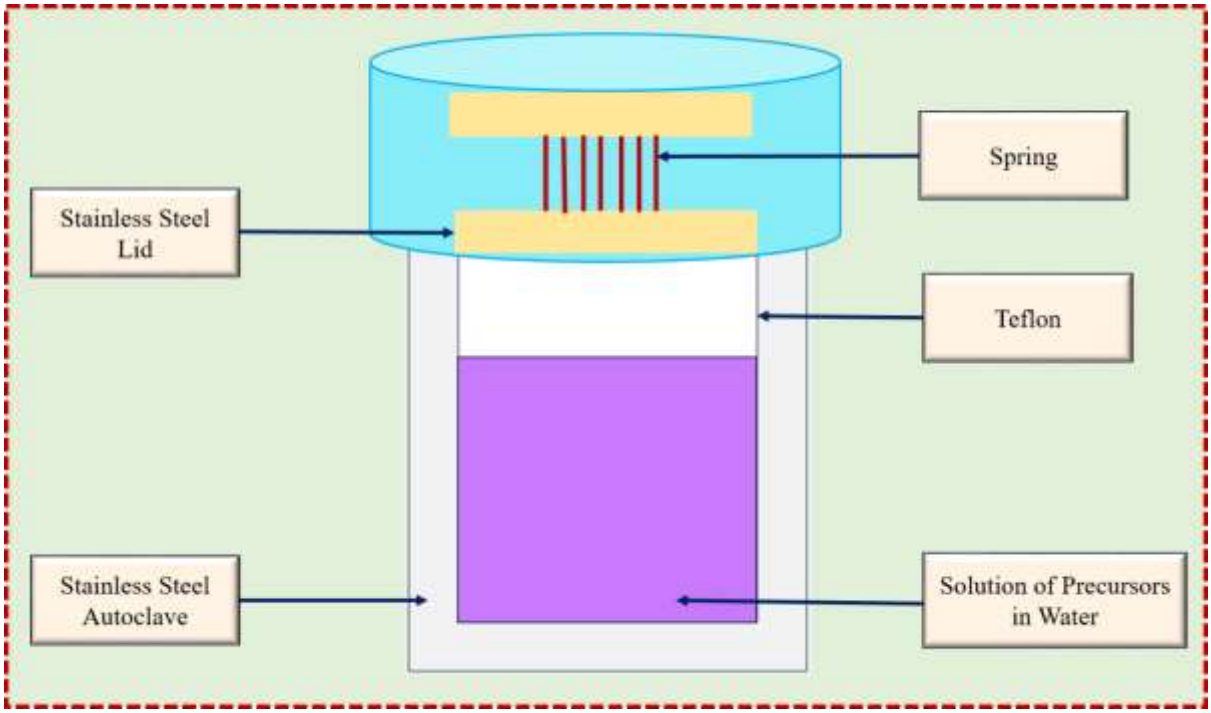

Figure 2.1: Setup of Teflon-lined stainless-steel autoclave used for hydrothermal synthesis

The components of the hydrothermal reaction are listed below:

1. Precursors: These are the reactants that react in the presence of suitable solvents to give the final product.

2. Mineralizers and other Additives: Various acids and bases are added during the reaction to attain a particular pH. These are known as mineralizers. Additives include reducing, chelating, capping, and stabilizing agents which are required to attain a certain morphology.

The advantages of the Hydrothermal method are as follows:

- Increased solubility of reactants as a result of high temperature and pressure
- Comprehensive improvements in reactant chemical activity
- Producing intermediate or metastable states is simple.
- Controlling the size, shape, and distribution of nanostructures precisely

2.2.1 Hummer's Method

The improved hummer's method is a procedure used to synthesize GO under the presence of strong oxidizing agents like potassium permanganate ($KMnO_4$), potassium chlorate ($KClO_3$), etc. The conventional hummer's method was modified by William S. Hummers and Richard

E. Offer man. The method is fast, non-hazardous, use low temperatures, as well as maintains a high C/O ratio [97].

2.2.2 Thin-film deposition techniques

The fundamental goal of this thesis is to investigate the properties of ReRAM devices made in a MIM configuration. A MIM device comprises of an active SnO_2 and SnO_2-2D layer sandwiched between two metal electrodes. For depositing these three layers, the following techniques were employed.

1. Thermal evaporation: For top electrode (TE)
2. Spin-Coating: For active SnO_2 and SnO_2-2D layer
3. Commerciale available: For bottom electrode (BE)

2.2.3 Spin coating method

The equipment comprises a turbo molecular vacuum pump that can operate at pressures of 10^{-2} torr, a rotating motor that can rotate at a maximum speed of 20000 rpm, and a substrate holding called a chuck. The user can choose the preferred rotation speed and duration using an automated setup that employs a microcontroller. Figure 2.2 (b) shows the Metrex spin coating unit located in the Department of Applied Physics Nanomaterials research laboratory at DTU in Delhi, India.

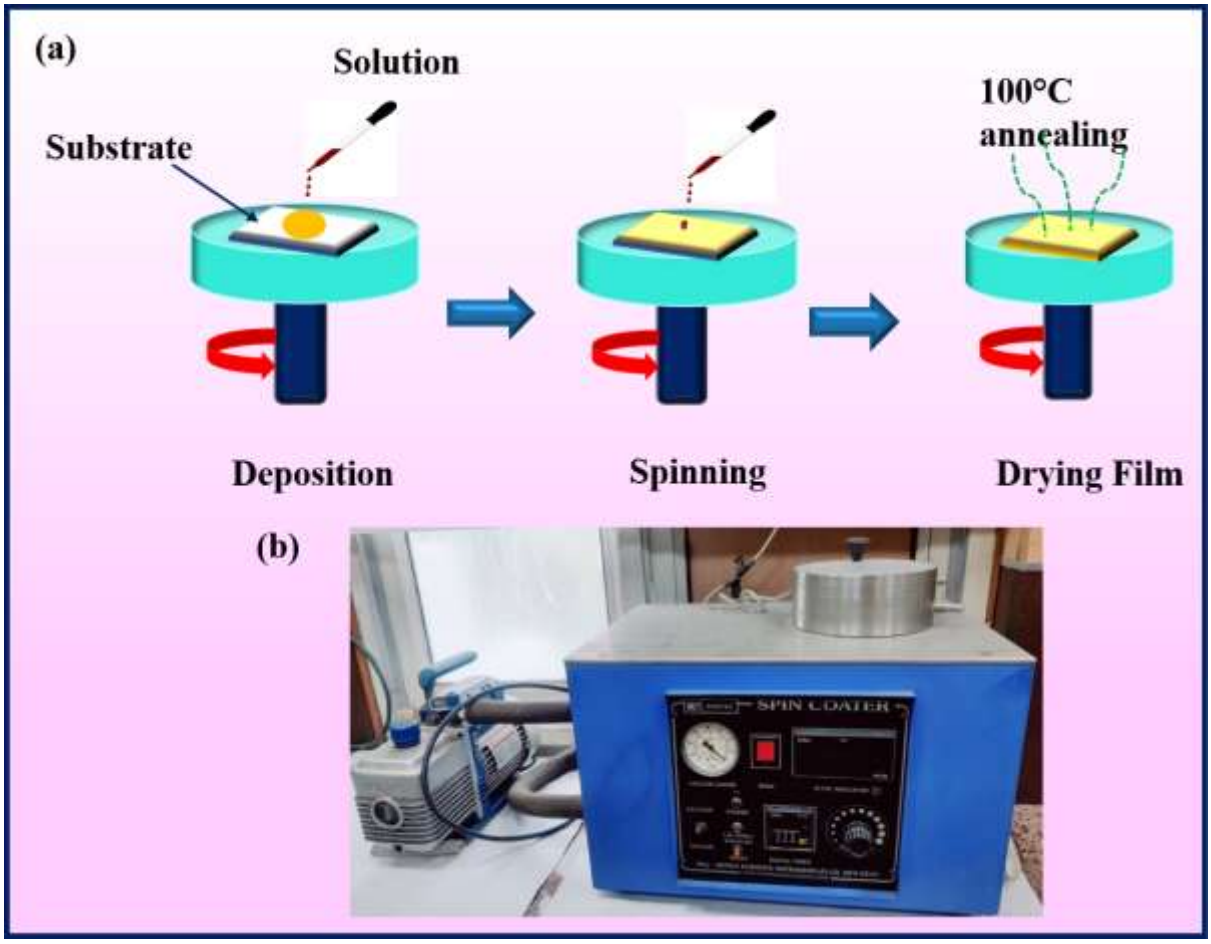

Figure 2.2: (a) Diagram of the spin coating mechanism (b) Image of the equipment

2.2.3a Working

To restrict movement, the substrate is placed on the circular disc of the chuck and vacuumed. Powder is combined with an organic or aqueous solvent to create a homogenous solution. A drop of solution is deposited on the substrate, which is then rotated at the required rpm and time [98]. The substrate is next dried to remove any remaining solvent and create the thin film layer [figure 2.2(a)].

2.2.4 Deposition of top electrode using vacuum evaporation

One of the most popular physical vapor deposition (PVD) methods for thin film deposition over an appropriate substrate is thermal evaporation. The solid material is heated inside a vacuum chamber to generate vapour pressure in the thermal evaporate technique. Even a shallow vapor pressure is enough to form a vapor cloud within a high vacuum chamber. This evaporated material has transformed into a vapour stream, which is incident on the substrate. In the present work, thin film of Al metal TEs was deposited by evaporating the respective high

purity wires (purity more than 99.999%), in a thermal evaporation system, using a tungsten boat which was resistively heated. The schematic design presented in Figure 2.3 illustrates the configuration.

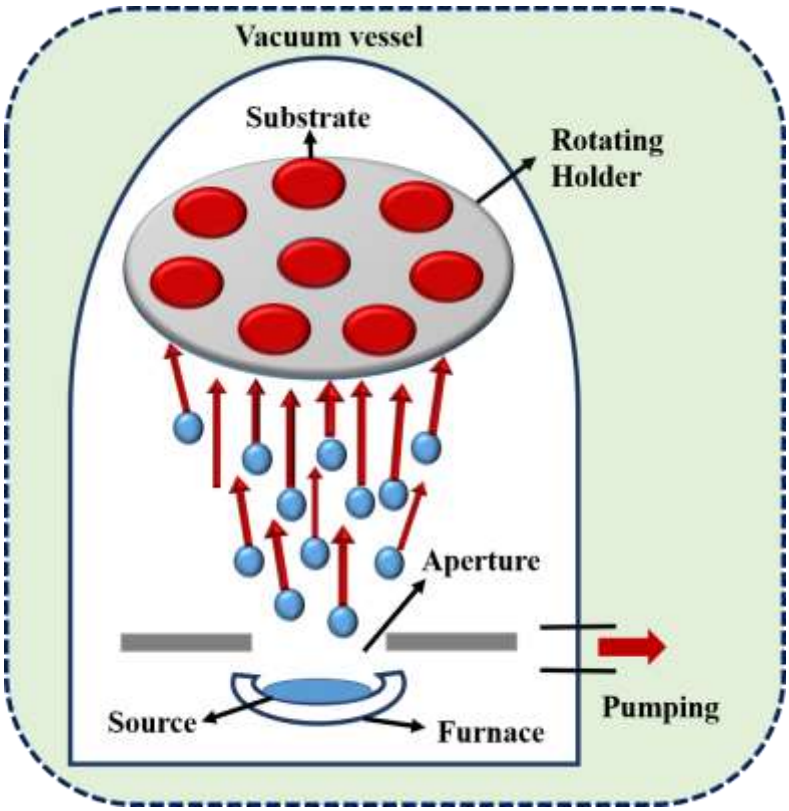

Figure 2.3: An illustration of the thermal evaporation system schematic.

The fabrication process for thermal evaporation typically involves the following steps:

1. Vacuum Chamber: The substrate and evaporation source are both contained within a vacuum chamber. A low-pressure environment is required to minimise undesired reactions and ensure controlled deposition.

2. Heating the evaporation source: The evaporation source is heated by resistive or electron beam heating, which is commonly in the form of pellets, wires, or rods. When the source reaches the evaporation temperature, it sublimates, producing vaporised particles or molecules.

3. Deposition: The substance that has evaporated moves through the vacuum chamber and makes contact with the substrate. The vapour condenses and forms a thin coating on the

substrate upon impact. The ambient temperature of the vapour source and the separation among the source and material are two examples of the elements that control the deposition rate.

4. Film Growth: The deposition time is what defines the coating's thickness. Factors like as surface pressure, temperature, and deposition rate all influence the shape, clarity, and thickness homogeneity of the resulting film.

In the present study, thermal evaporation (setup is shown in Figure 2.3) is utilized to deposit metal electrodes on SnO_2-2D based thin films in order to fabricate memory devices.

2.3 Materials characterization methods

The confirmation of the successful formation of SnO_2-2D nanostructures and subsequent modifications are examined using various characterization techniques. First of all, the structural study is done using X-ray diffraction (XRD), followed by morphological investigations using SEM, FESEM, and TEM. Then, the confirmation of layered structures is probed using Raman spectroscopy. The examination of attachment of desired functional groups is studied using FTIR. Elemental analysis is done using EDAX and XPS. The working and principles of all these characterization techniques are discussed in brief in the following section.

2.3.1 XRD

One of the maximum important and effective approaches used frequently to analyse and determine the structure of both bulk materials and nanostructures is X-ray diffractography (XRD). This method can be used to figure out the geometry, lattice constants, and phase orientation of a crystal structure, among other parameters. Additionally, the method can be used to assess a materials stress and strain [99, 100]. Moreover, the analysis using XRD does not call for any sample preparation to obtain the data. XRD is based on the principle of diffraction, therefore, when the X-ray waves having wavelength ~1Å are incident on a crystal, they get diffracted by the crystal planes since the interplanar spacing is comparable to the wavelength of x-rays. The planes of crystal act analogous to mirrors and thus can give information about the crystal structure [101]. The diffraction pattern of every crystal is unique just like the fingerprint of a human being.

The diffraction of a crystal can be described by Bragg's equation 2.1 and the schematic explaining the diffraction from a crystal is shown in Figure 2.4.

$$2d_{hkl}sin\theta_{hkl} = n\lambda \qquad (2.1)$$

where, λ stands for the wavelength of the incident light, d stands for the interplanar spacing, θ stands for the diffraction angle, h, k, and l are the miller indices for the planes of crystals, and n is the order of diffraction.

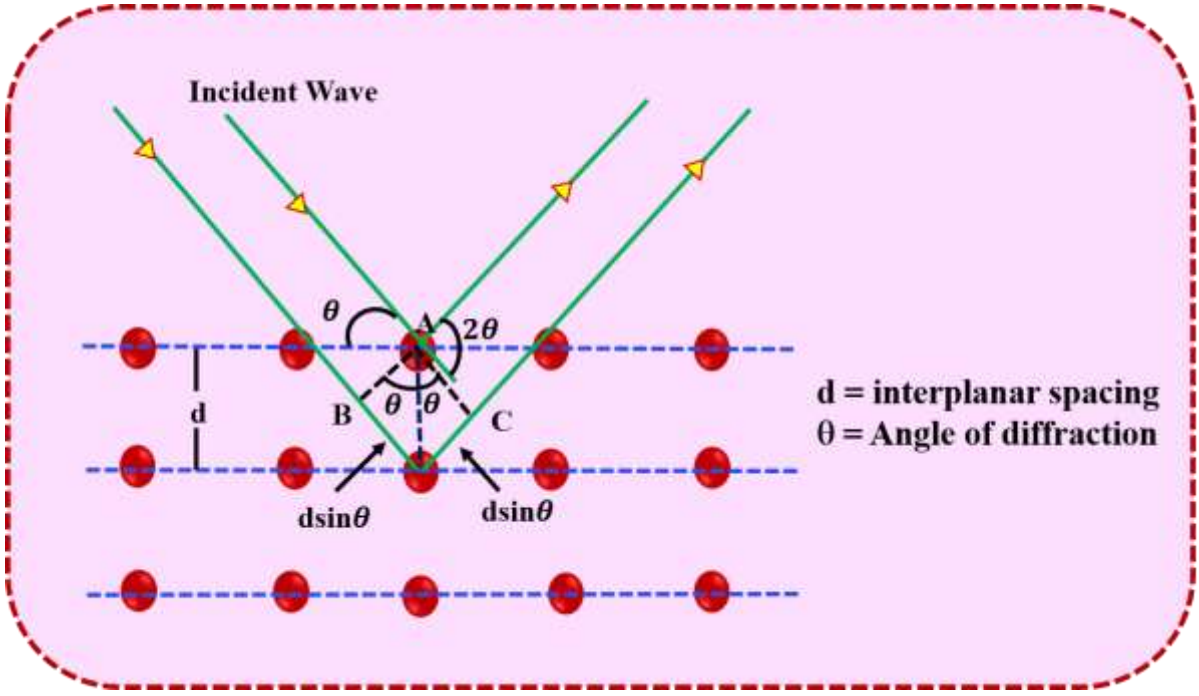

Figure 2.4: Bragg's law is illustrated by the diffraction of X-rays from parallel atomic surfaces.

Included in the XRD setup are a fixed sample holder assembly, a movable copper [Cu-(Kα)] source that emits an X-ray spectrum at a wavelength of 1.54 Å, and a high-speed energy dispersive compound silicon detector that can measure patterns with an angular range of 0.150° to 90°; the window is automatically adjustable. The source tube produces a highly collimated X-ray by hitting an anode metal target like Cu, Mo, iron (Fe), or chromium (Cr) through the high voltage electron beam in a vacuum environment. For single-crystal diffraction, Cu is the most frequently used target material. The X-ray beam falls on the sample and while the sample and detector spin, the X-ray intensity is detected. The Bragg equation is satisfied when the incident X-ray geometry impinges on the sample, causing constructive interference, and then an intensity peak appears. This radiation is captured by a detector, which also processes it. The signal is then translated to a count rate and the output is taken through a printer or computer monitor.

The crystallite size 'D' of the materials can be calculated using Scherer's formula (Equation 2.2) from the peak width [102].

$$D = k\lambda/\beta cos\theta \qquad (2.2)$$

Where β is the peak's full width at half maximum (FWHM), θ is the Bragg angle and 'k' is the constant depending upon the geometry of the material. The sample to be analysed can be in the form of powder, pellet, or even a thin film, which consists of tiny crystals called crystallites [103].

2.3.2 Raman spectroscopy

The specimen's rotational, vibrational, and other frequency modes are observed using the Raman spectroscopy method. It tells about the bonding and structure of the molecules. As a result, this method provides a fingerprint that can be used to identify molecules. This spectroscopy is based on the inelastic scattering of light (Raman Effect) [104]. Monochromatic radiation interacts with the sample differently as it incident on it and either gets scattered, reflected, or absorbed. Molecular structure information is obtained by scattered radiation. The coherent source is a general laser used for specimen analysis in Raman spectroscopy [105]. The majority of incoming radiation disperses elastically, producing Rayleigh scatter light. Only a tiny fraction, around 1 in 10^6, is in elastically scattered and primarily consists of Stokes and anti-Stokes lines, and of this small fraction, Stoke's lines are used to collect the information about the specimen. In Rayleigh Raman scattering, incident and scattered light frequency are the same. In anti-Stokes Raman scattering, the frequency of the scattered light is higher than that of the incident light, whereas in Stokes Raman scattering, the frequency of the scattered beam light is lower than that of the incident beam light [106].

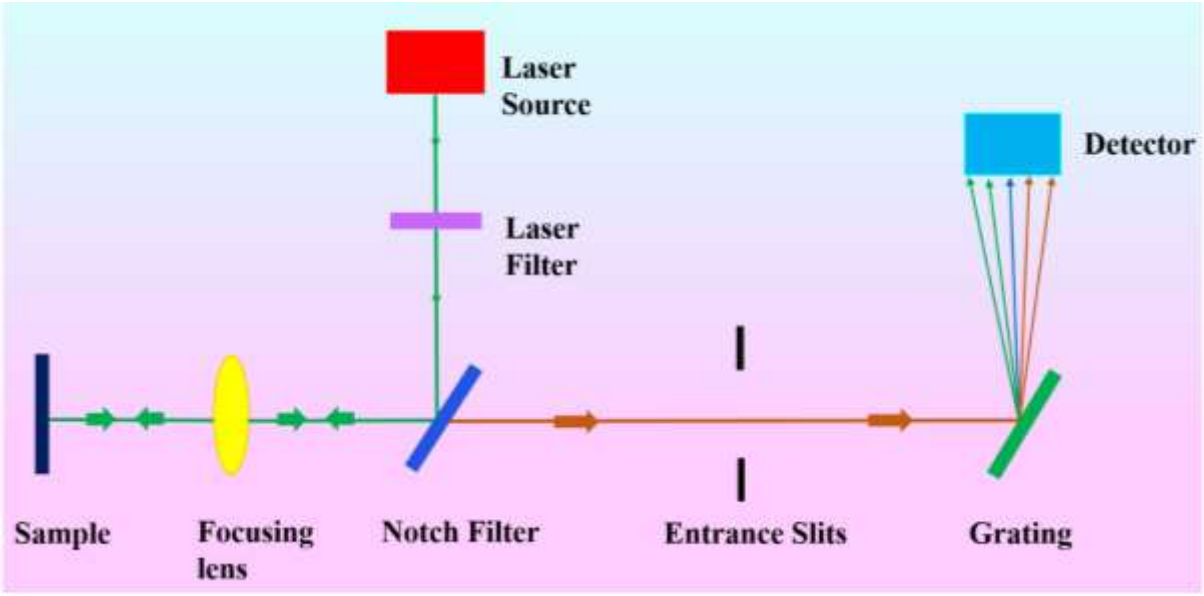

Figure 2.5: Simplified block diagram of Raman spectrometer

Raman spectrum is plotted between the intensity of scattered light and energy difference termed as Raman shift. With the photon's interaction with the molecule, a dipole moment 'P' is induced by electric field 'E' given as

$$P = \alpha E \qquad (2.3)$$

where α is the proportionality constant that tells us about the distortion of electron cloud around a molecule[107]. And these molecular bonds carrying specific energy transitions corresponding to changes in polarizability give rise to Raman active modes. Three main parts make up a modern Raman spectrometer: a laser source, a mechanism for illuminating the sample, and an appropriate spectrometer. Due to their monochromaticity and high-intensity beam, lasers are the most common sources utilized to study Raman spectra with good signal-to-noise (S/N) ratios. Raman spectrometers are either based on CCD or FTIR equipped with cooled germanium (Ge). Raman spectroscopy is frequently superior to IR spectroscopy because it may be utilized to study inorganic systems in an aqueous solution. It has been widely applied to study biological systems. Analysis using Raman spectroscopy requires a small sample quantity, further liquid and film samples can also be analysed. It can detect molecular impurities and additives. For quantitative and qualitative analysis in many settings, Raman spectroscopy has emerged as a non-corrosive technique. Figure 2.5 shows a simplified block diagram of the Raman spectrometer.

2.3.3 FTIR (Fourier Transform Infrared Spectroscopy)

Fourier-transform infrared spectroscopy (FTIR) can be used to study the vibrational characteristics of functional groups in chemical and semi-organic compounds. The chemicals are subjected to the electromagnetic field between 400 and 4000 cm^{-1} in order to perform this examination. FTIR spectroscopy is a simple yet extremely important characterization technique having numerous applications. One of the uses of this technique includes the analysis of thin films and coatings for determining the functional groups. The FTIR spectroscopy method has several advantages which include its fast-scanning speeds as compared to other dispersive methods and the ability of the method to be used for solids, liquids as well as gases.

The method is dependent on the molecular bonds of the compounds present in the sample. The nature of the molecular bonds of different molecules is dependent on the atoms present in the molecule. When these substances in a sample are illuminated with IR radiation, the molecules of the substance, upon its absorption, attain a higher energy state. When these molecules return to their original (de-excited) state, they emit radiation which has energy equal to the difference

between the energies of the de-excited and the excited state of the molecules. Each substance absorbs a unique wavelength of IR light from the many available wavelengths present in the incident light[108]. The FTIR measures these absorbed wavelengths and hence can determine the nature of the substance and its bonds. The resulting graph can include “transmittance” or “absorption” of the IR radiation plotted on the y-axis against the wavenumber on the x-axis. There can be several peaks present in the graph depending upon the nature of the molecule. These peaks are then studied and analysed against the known standard IR peaks for different materials and bonds to identify the functional groups present in the sample.

One method that is frequently used in FTIR spectroscopy is the Michelson interferometer, which is shown in Figure 2.6. Figure 2.7 shows the schematic of the several steps that are involved in FTIR spectroscopy. The light from the IR radiation source in the interferometer setup reaches the beam splitter through a collimator; the beam splitter splits the incident beam into two. Both the beams then travel to the two mirrors of the interferometer, one of which is in constant motion. This introduces a path difference between the two beams and modulates every wavelength present in the incident beam at a distinct frequency. When the beams combine after being reflected from the mirrors, they form a complex interferogram. This interferogram so obtained is then made incident on the sample, which as described earlier, will absorb light of specific wavelengths out of the several available wavelengths in the light incident on it. The detector measures the intensity of the respective wavelengths in the transmitted light. The signal obtained is then processed and converted into meaningful data using the “Fourier transform” method. The final graph obtained after using the Fourier transform method helps to identify different functional groups present in the sample of interest.

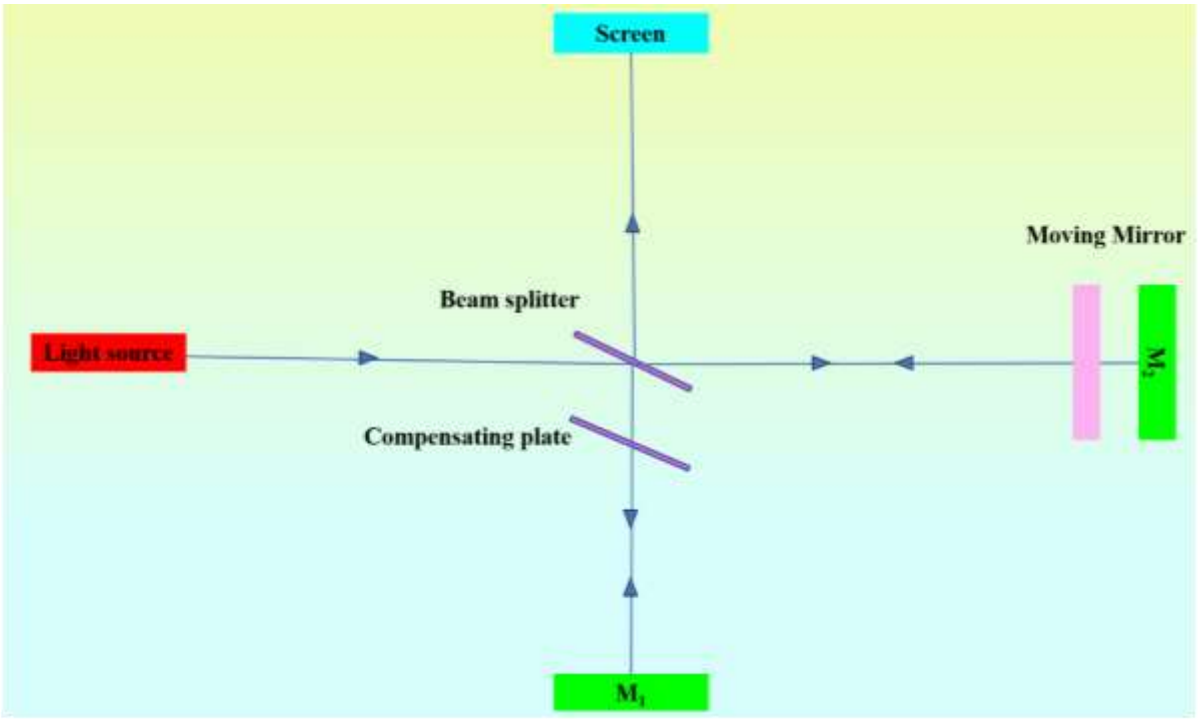

Figure 2.6: Michelson interferometer schematic.

After that, the sample is projected with the resulting interferogram. As mentioned earlier, the sample preferentially absorbs different transmitted light wavelengths from the incoming spectrum. The intensity of various transmitted light wavelengths is measured using a detector. The input signal is processed and changed into meaningful data using the "Fourier transform" method. The Fourier transform approach results in a final graph that helps to identify multiple functional groups within the sample under analysis.

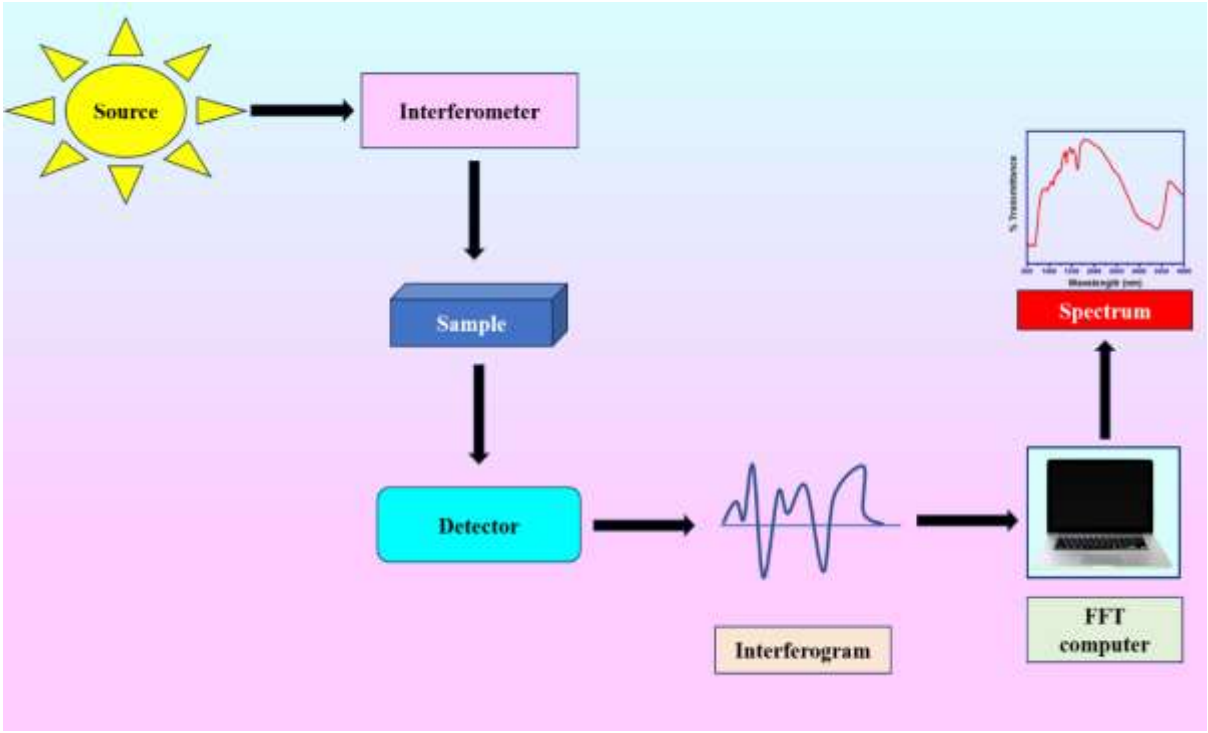

Figure 2.7: FTIR spectroscopy block diagram

2.3.4 UV-Visible spectroscopy

It is sometimes referred to as absorption spectroscopy or reflectance spectroscopy. Light in the UV range (100-1000 nm) is used in this spectroscopy, which includes the visible and neighboring spectrum regions. When electromagnetic radiation is absorbed, it causes an electronic transition in the atomic structure of nanostructured substances. In analytical chemistry, this spectroscopy is commonly used to identify transition metal ions, strongly linked chemical compounds and macromolecules in biology.

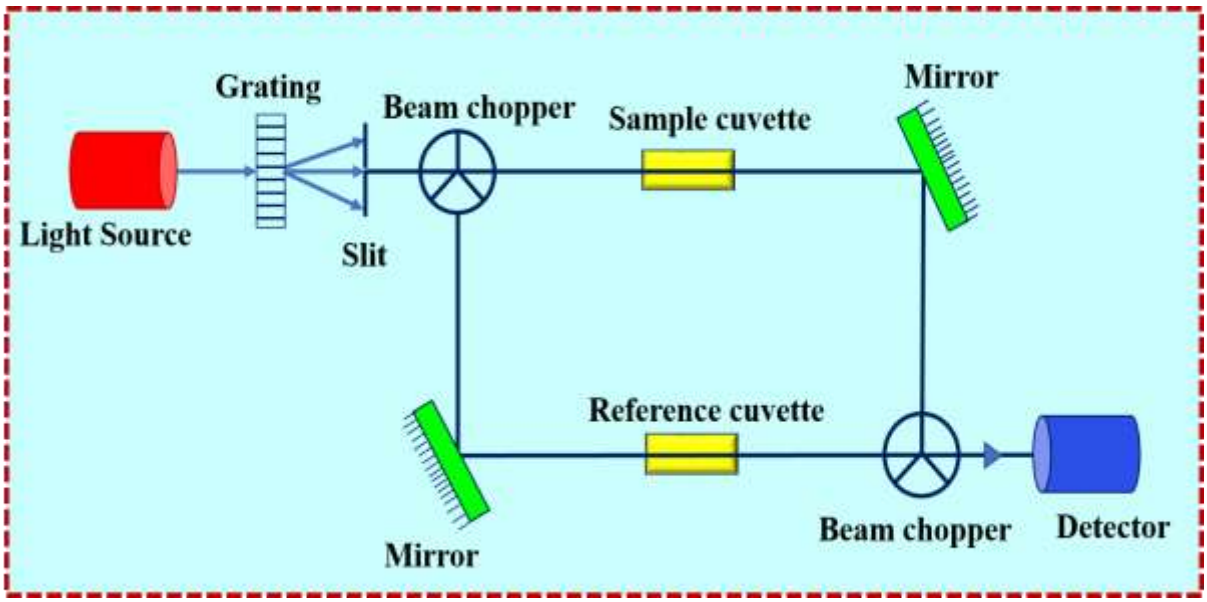

Figure 2.8: (a) UV-Vis absorption spectroscopy schematic

2.3.4.a UV-Vis spectrophotometer instrument

A Jasco V-770 UV-Vis spectrophotometer, accessible in the Materials and Atmospheric Science Research Lab, department of applied Physics, DTU, Delhi, India, was used to analyse the electronic transition of nanostructures. A double beam instrument is used, with deuterium and tungsten halogen light sources emitting UV-Vis and near-infrared (NIR) radiation, a rectangular quartz glass tube cuvette sample holder, a monochromatic diffraction grating to pass selected radiation, a chopper to split into two beams, and a photomultiplier detector to convert radiation energy into an electrical signal.

2.3.4.b Mechanism

The monochromatic grating transmits source lamp radiation with a wavelength of 200-2700 nm, enabling only UV-Vis radiation with a wavelength of 200-900 nm to pass through the chopper and split into two beams. As one beam travels through the sample, the other analyses the reference. The same solvent that was used to make the solution containing the nanostructure powder solute is first used to fill two cuvettes. To measure and document the reference beam that travels through the detector window, the cuvettes are placed inside the apparatus. Next, in order to compare the reference and sample beams, one of the cuvettes is filled again with a dispersed nanostructure solution and placed next to another solvent cuvette [figure 2.8 (a)].

According to Beer-Lambert's law, a solution absorbance is correlated with both the beam's path length and the absorbers or analyses concentration in the solution. When the length of the route is fixed, UV-Vis spectroscopy can also be used to measure the concentration of analyses in the solution. It is necessary to measure and compare the intensity of the beam (I) that is passing through the sample to the intensity of the reference beam. Absorbance (A) is the ratio I_0/I; it is generally expressed as a percentage and calculated as = log233. where I_0 indicates the intensity of the beam after it has passed through the sample and I_0 indicates the intensity of the reference beam.

2.3.4.c Optical band gap

A direct optical transition, or the transition of electrons from the ground to the excited state upon absorption of appropriate electromagnetic spectrum radiation, has been observed when exposed to radiation with higher electron concentrations in the ground state (valence band) than in the excited state (conduction band). On the other hand, indirect optical changes occur when

electrons rise to a metastable intermediate energy state before moving to the state of excited. However, the energy of incident radiation should be equivalent to or larger than the energy difference between two states, i.e. band gap energy, and there should be no change in charge carrier concentration[109]. This effect is used in optical spectroscopy, which was first shown by Jan Tauc in 1966, to study the band gap of synthesized MOX semiconductors. The tauc plot, which is derived by equation 2.4, is used to examine the optical band (i.e. Tauc gap) among semiconductors.

$$\alpha h\nu = C(h\nu - E_g)^n \qquad (2.4)$$

Where n is the transition parameter (i.e., n is a reasonable fraction for direct transitions and a non-negative integer for indirect transitions), C is the proportionality constant, h is Planck's constant, α is the absorption coefficient and E_g corresponds to the band gap. The optical band gap (E_g) for each type of transition can be found by calculating the intercept of the curve on the x-axis of the Tauc plot [$(\alpha h\nu)^{1/n}$ against hν].

2.3.5 XPS

The photoelectric effect is employed in the technique of X-ray photoelectron spectroscopy (XPS), which includes lighting the specimen with monochromatic X-rays (soft X-rays with an energy of 1000 eV). This results in electron photoemission from the host matrix's atoms. The energy of the released electrons is analyzed, and the resulting data is shown on a computer screen in terms of the number of electrons obtained as a function of energy (between 0 - source energy). Because the important signal only comes from the top 20-30, the XPS technique is highly surface sensitive. The binding energy and breadth of an electrons core level ($(n-1)^{th}$ level of a n level atom) fluctuate when the chemical environment surrounding the atom changes. Since XPS is sensitive enough to quantify these energy shifts, it is also known as electron spectroscopy for chemical analysis, or ESCA. BE varies between 0.1 to 10 eV. The specimen is exposed to known energy X-rays, hv, and electrons with binding energy EB are expelled. The kinetic energy (E_k) of the expelled electrons as measured by a spectrometer is given by (2.5).

$$E_k = h\nu - E_B - \Phi_S - \Phi_{SP} \qquad \text{----------} \quad (2.5)$$

where Φ_{sp} and Φ_s are the specimens and spectrometer work functions, respectively. As a result, the measured electron kinetic energy can be translated into the equivalent binding energy.

Figure 2.9 depicts a schematic diagram of the major components of an XPS configuration. In addition to the requisite electronics for translating the measured current into

a visible spectrum, they include an X-ray source, an electron energy analyzer, an electron detector/multiplier, and a sample/support system that are all maintained in ultra-high vacuum (UHV). This study used an X-ray photoelectron spectrometer (Perkin Elmer-1257) equipped with a 25 meV resolution hemispherical section analyzer. The apparatus consists of a dual anode X-ray source that may generate X-ray radiations of Mg Kα (1253.6 eV) or Al Kα (1486.6 eV). A manipulator can be used to modify the sample position in the x, y, z, and coordinates. A four-element lens and a hemispherical sectional analyzer are used to detect the released photoelectrons. A channeltron (preamplification/phase detection) was used to gather the data, which was then processed by a computer. The equipment has a depth resolution of 1.5 nm. Sputter cleaning of the samples and depth profiling to examine the interface were performed during XPS measurements using 4 KeV Ar^+ ions produced by a differentially pumped ion cannon.

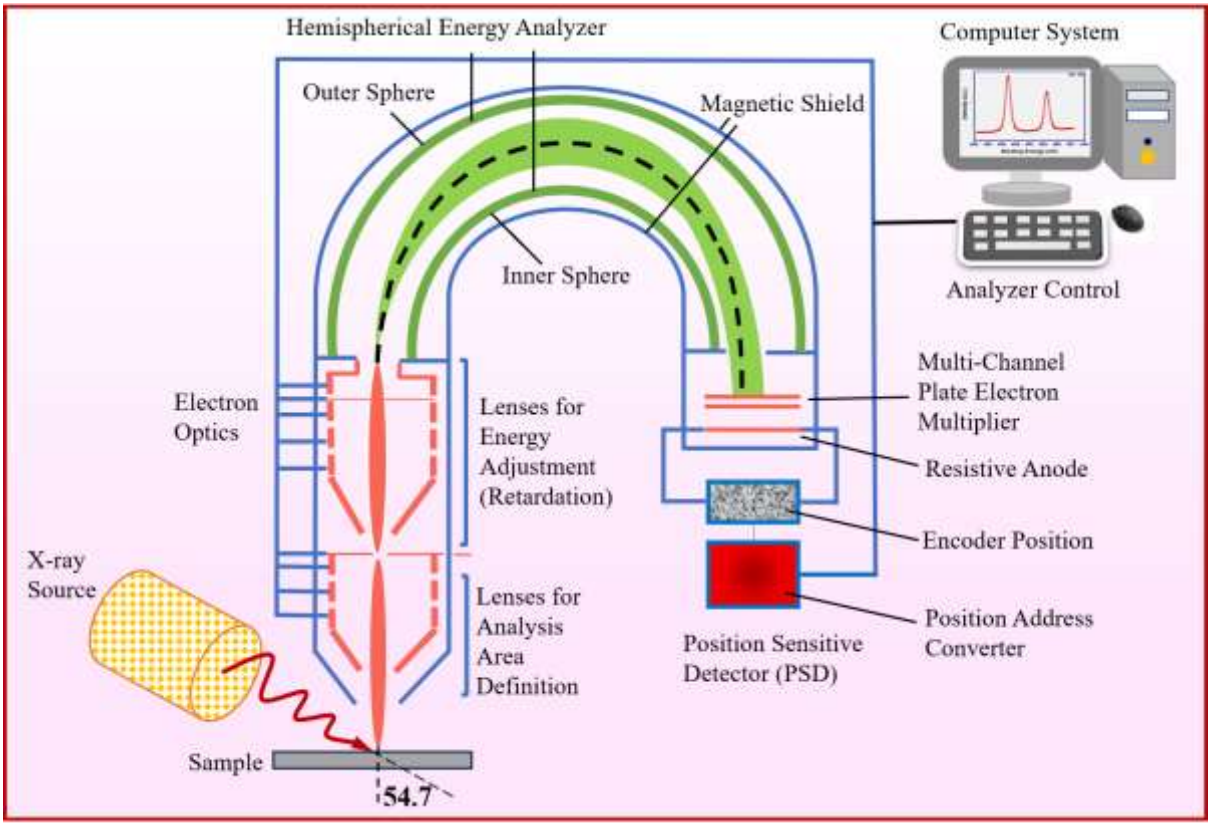

Figure 2.9 The Schematic diagram of XPS system showing various components.

2.3.6 SEM and FESEM

SEM is a sophisticated kind of microscope that studies the three-dimensional structure of solid samples using electrons rather than light. SEM technique can be utilized to accumulate a lot of information about a sample like the solid samples topography, composition, and morphology

details. On a scale varying from nano to micro scale, it can be regarded as the most efficient approach for analysing the morphology of organic and inorganic materials. With high magnification up to 30kx and even 1000kx in some contemporary models, SEM creates extremely exact pictures of a variety of materials. A scanning electron microscope uses electromagnetic "lenses" to concentrate an electron beam onto a specimen (which can be a metal, metal oxide, ceramic, or biological sample). Thus, an image is formed by documenting how the electron beam interacts with the specimen surface. When the electron beam interacts with the specimen, various types of electrons are deflected, as shown in Figure 2.10 (a).

A sample for SEM analysis is prepared by distributing powder samples or placing a thin film or a pellet over the conducting carbon tape and coating them with conducting metals like gold (Au) or platinum (Pt)[110]. The sample is coated with conducting metals to avoid the accumulation of incident electrons at a particular spot in the sample. As illustrated in Figure 2.10(b), when a passing electron ray interacts with a sample, the electrons lose energy as a result of repeated absorption and scattering within the specimen pear-shaped interaction volume 100, which reaches from less than 100 nm to about 5 nm deep into the surface. Together with the specimen density and atomic number, the beam accelerating voltage also determines the interaction volume. This interaction causes secondary electrons (<50 eV), Auger electrons, and X-rays to be emitted. Each of these signals contains particular information regarding topography, crystallography, surface qualities, specimen composition, and other attributes. In case of SEM, the detector detects the secondary electrons which escapes from the sample at a depth of around 5 to 50 nm and an image of the sample surface is constructed. In addition, SEM can be utilised for energy dispersive x-ray analysis (EDAX). EDAX measures the X-ray photon energy generated by a sample as a result of bombardment by an incident electron beam. This is useful in elemental analysis of samples since no two elements generate an X-ray photon with exactly the same energy due to variable electron binding energies.

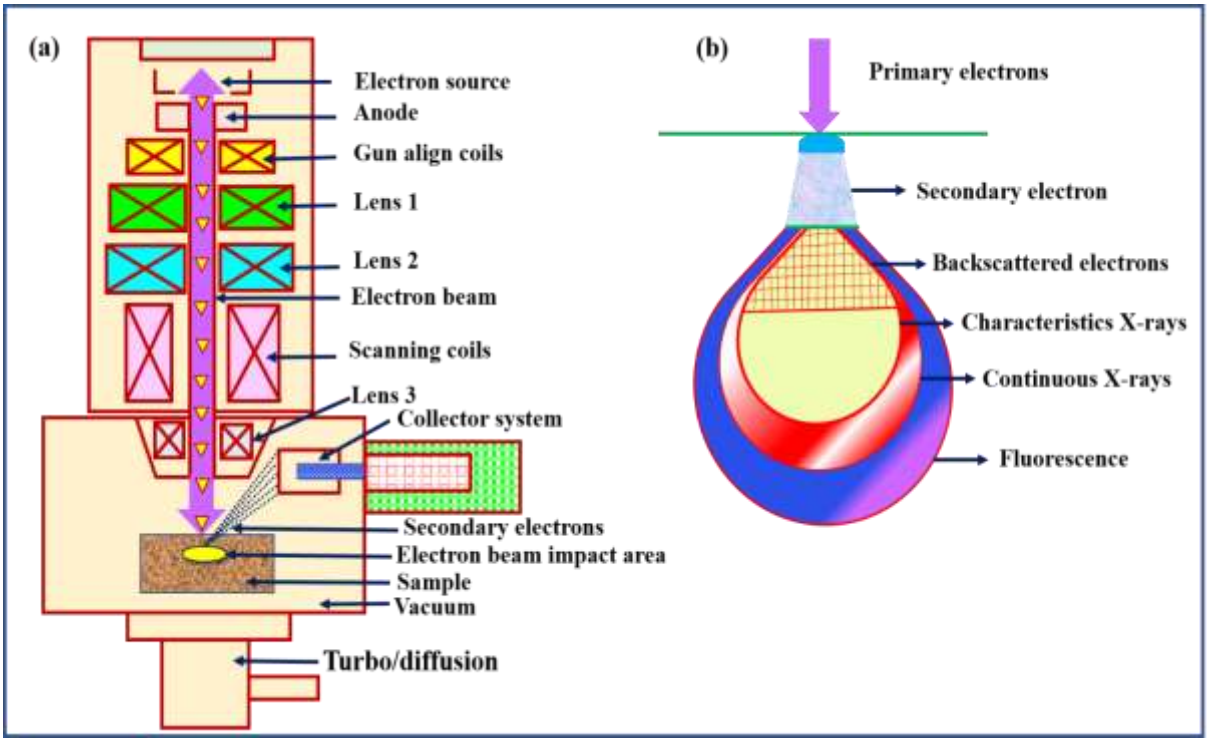

Figure 2.10 (a) SEM schematic diagram; (b) electron beam interaction with a sample.

FESEM is the microscopy technique that uses a field emission source that scans the specimen in a zig-zag pattern. The electron emitters of the field emission gun have an emission capacity up to 1000 times greater than that of a tungsten filament used in ordinary SEM [111]. Like in SEM, here also secondary electrons are collected by a scintillator detector which produces photons. In addition to this, FESEM needs higher vacuum levels and the sample is prepared by coating a very thin layer of Au or palladium (Pd). Using metal apertures and magnetic lenses, the electrons are then concentrated into a thin, monochromatic beam after leaving the electron gun. To create an image of the object, signals from detectors of each type of electron are collected. FESEM delivers information on topography and elements at very high magnifications and an almost limitless depth of field. It is three to six times more effective than ordinary SEM at producing crisper pictures with spatial resolution down to 1/2 nanometres that are less electrostatically distorted [112]. FESEM is a very popular technique amongst physicists, chemists, biologists, material scientists, and electronic engineers since structures as small as nuclei of cells to microchips can be observed.

2.3.7 Transmission electron microscopy (TEM) for morphological and crystallographic investigations

TEM is a microscopic technique that uses an electron beam that transmits through an ultrathin specimen and interacts with it to give us various information about the specimen. As it passes through it gathers the specimen morphological, and crystallographic information. In TEM an electron beam is used which is having a short wavelength, resulting in a much higher resolution of the specimen [113]. For a magnified image, imaging equipment like fluorescent screens, photographic film, or sensors like charge-coupled devices (CCD) are utilized. The system operates in two modes, namely diffraction mode and image mode. TEM setup consists of an electron gun with a high-energy electron beam that passes through a microscope vacuum tube. Next are the condenser lenses, which are used to focus the electrons. Then is a motorized specimen stage, which is used for holding conducting copper grid coated with the sample. The objective lens and the specimen chamber represent the heart of the TEM, where an electron beam gets transmitted through the thin specimen and interacts with it [114]. For the excellent TEM image, the sample thickness is usually around 100-200 nm as electrons cannot readily perforate through thickness greater than 200 nm. An objective lens and other lenses form an imaging system that helps in producing high-resolution images and diffraction patterns. The intensity distribution of electrons after transmittance is imaged with a three-stage lens system onto a fluorescent screen [115]. Lastly, there is a charged coupled device (CCD) camera to convert the electric charge into pixels of the image. The operating modes of TEM are high-resolution TEM (HR-TEM), selected area electron diffraction (SAED), or simple TEM to study particle dimensions, morphology, lattice parameters, and expansion direction of the material. Figure 2.11 shows the schematic diagram of TEM. The entire TEM equipment is placed in a high vacuum chamber and interfaced with a graphical user interface (GUI) data collecting system. Electron beams from electron guns interact with the sample, resulting in beam scattering. There are two forms of distribution that occur: elastic and inelastic. Elastic scattering arises as a result of the arrangement of atoms in nanostructure crystals. Because of coherence in electron beam scattering, it produces spot patterns. Inelastic scattering, on the other hand, causes beam absorption or emission that is unique to the compound or chemical structure of nanomaterials.

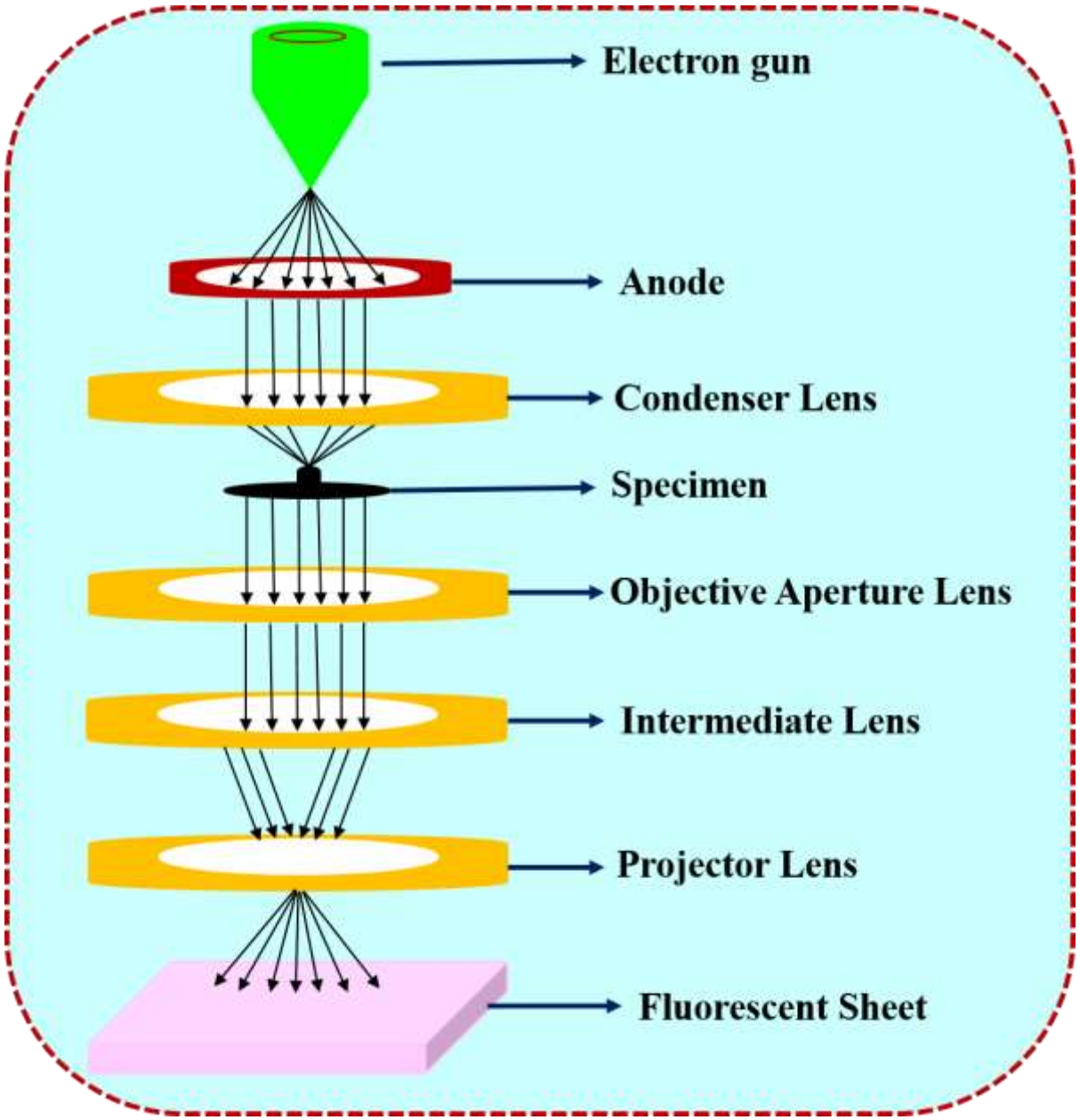

Figure 2.11 Schematic diagram of TEM

The distinction of the image depends on the bright-field image and the dark-field image mechanism. **Bright-field image:** It is formed by uniformly illuminating the entire specimen image in dark against a bright background and collecting the transmitting electrons and blocking the scattered ones.

Dark field image: Image formed on the objective lens's back focal plane by selecting the scattered electrons and blocking unscattered electrons using the objective aperture [116].

HRTEM: By increasing the accelerating voltage of the field emission gun up to 300 kV depending upon the sample compatibility, the wavelength of the electron decreases, and hence point resolution of the image can be enhanced.

The sample used in TEM must be electron transparent. The dimensions of nanostructures act as a diffraction grating for incoming electrons and electrons scattered at different angles depending on the crystal structure, satisfying Bragg's law. At the same time, transmitted electrons are allowed to pass through the sample, forming the monochromatic spots on dark backgrounds corresponding to the reciprocal lattice of crystal planes. This is called the SAED technique and is used to confirm the XRD results.

2.3.8 EDAX (energy dispersive X-ray analysis) for elemental analysis

An effective and simple method for detecting the chemical compounds and elements present in a sample is EDAX. The setup of EDAX is similar to that of SEM which primarily consists of a high electron emission source that releases high-energy electrons in an electron microscope, and then the distinctive X-rays that each element produces are detected[117]. Then, using a method known as X-ray mapping, the samples elemental composition may be seen superimposed on top of the magnified image of the sample. EDAX is particularly valuable since the number of X-ray photons released by each component inside a sample directly correlates with the concentration of that element. Because of this, it is feasible to determine the amounts of the various compounds present in a sample by converting the X-ray observations into a final X-ray spectrum. As a consequence, material science is the field that has benefited the most from EDAX. It can be used for quality control screening, verification, and certifications well as to identify and analyse products, including spotting impurities or figuring out unknown constituents. The electron beam source, detector, processor, and analyser make up the majority of an EDAX system. The charge that the incident X-ray releases within the crystal are measured by a field-effect transistor (FET) and transforms into a voltage output signal. A computer-assisted system, like the multichannel analyser (MCA), is in charge of all unattended and automatic operations [118]. The X-ray coming out from the sample hits the detector and causes a charge pulse in the detector. The energy of the observed X-ray is subsequently reflected in the amplitude of the current, which is then transformed into a voltage pulse. The last step is to convert this pulse voltage to a digital signal and increment the relevant energy channel by one more count. Due to the cumulative counts, the final measurement yields a typical X-ray spectrum which can be used to map various elements present in the specimen [119].

2.3.9 Dielectric/Impedance Analyser

William Whewell was the first person to develop the word “dielectric”. This method can be used to evaluate variations in parameters such as the loss factor (tanδ) and real and imaginary permittivity (ε′ and ε′′) with respect to frequency or temperature variations. The basic coupled electrical responses consist of electric modulus (M*), relative permittivity (ε*), admittance (Y*), and impedance (Z*).

The real and imaginary parts of dielectric permittivity correspond to the materials ability to store energy within a magnetic field and electricity absorption, respectively. Equation 2.6 is used to get the dielectric constant:

$$\varepsilon' = C_p d/\varepsilon_0 A \tag{2.6}$$

Here, d stands for the thickness of the pellet or thin film, a for the cross-sectional area of the pellet or thin film, Cp for the samples measured capacitance, and ε_0 for the permittivity of empty space, or $8.854*10^{-12}$ F/m. Equation 2.7 is used to calculate the imaginary component of dielectric (ε′′) and the loss tangent (tanδ) for the samples.

$$\varepsilon'' = \varepsilon' tan\delta \tag{2.7}$$

In this application, the "dielectric loss tangent" represents the energy wasted from the applied field into the sample, given by the tangent tanδ.

The dielectric analysis setup has a temperature range of -196°C to +300 °C and a frequency range of 1 Hz to 10^7 Hz. A variety of physical characteristics (L, C, and R) can be measured by adjusting the frequency and temperature. AC voltage is the most common voltage source. An analyser monitors current and voltage. The parameters that are measured include the resistance of the sample, inductance, impedance, and the phase angle between voltage and current. Capacitance, dissipation factor, inductance, and AC conductance can all be measured as functions of energy using an impedance analyser that is connected to a computer. With the use of different correlations, the obtained parameters from the LCR metre can be transformed into requested values. The current work formed a parallel plate capacitor using pallet-based dielectric material, and it examined the dielectric performance as a function of frequency.

2.3.10 Electrical characterization

The I-V properties of the sample are usually measured with two probes. Figure 2.12 is a schematic illustration of the experimental setup. The Two-probe measurement is the simplest

way to measure the resistance. In the present study, a Keithley 2450 source meter was used to determine the switching behaviour of ReRAM devices.

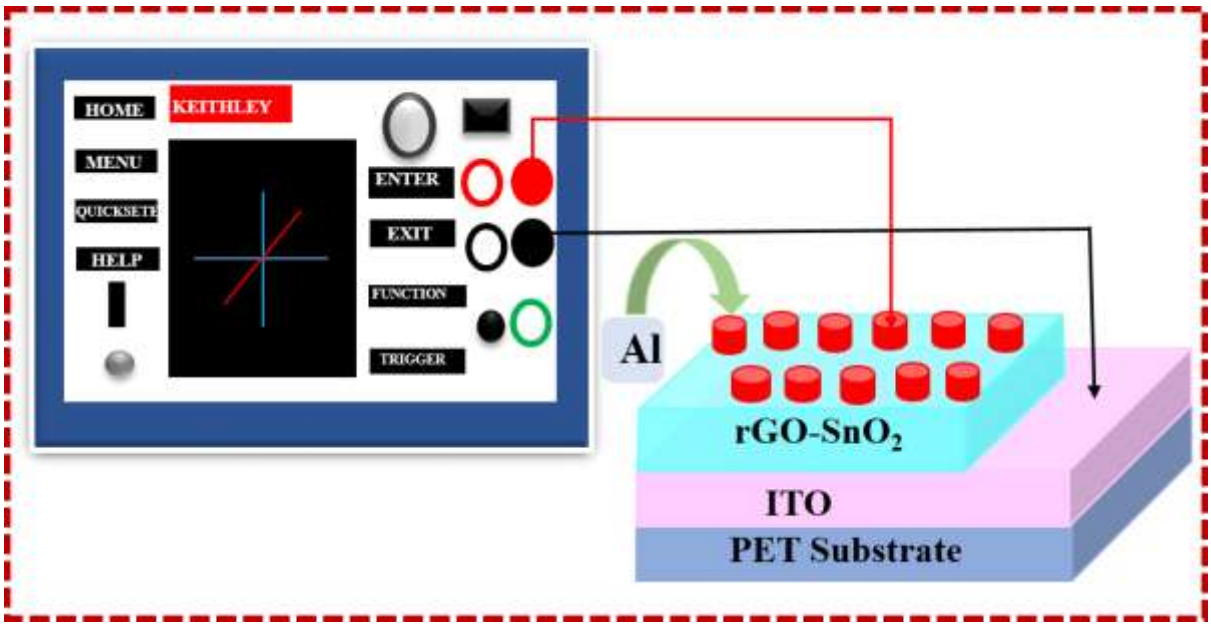

Figure 2.12 Schematics of electrical setup for top-down device geometry for measuring I-V and resistive switching characteristics.

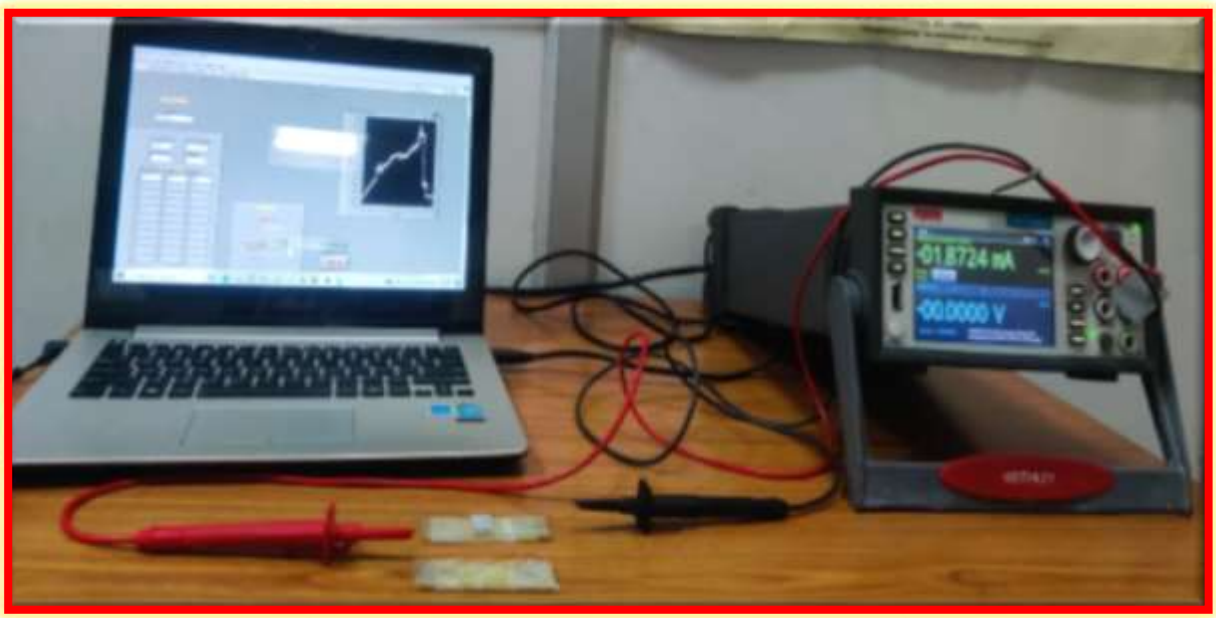

Figure 2.13 The optical image of the Source meter (2450) used for I-V measurements.

All the measurements were carried out in voltage sweep mode (Figure 2.13), in which a bias is applied by the source meter to the top electrode and bottom electrode is grounded and the corresponding current values of the devices extracted. To perform these measurements, a program was developed in LabView for automatic data acquisition using a GPIB interface. The

screen shot of the graphical user interface of the program is shown in Figure 2.14. It allows the user to enter the sample name, voltage sweep ranges, current compliance, no of cycles, wait time and average data points etc.

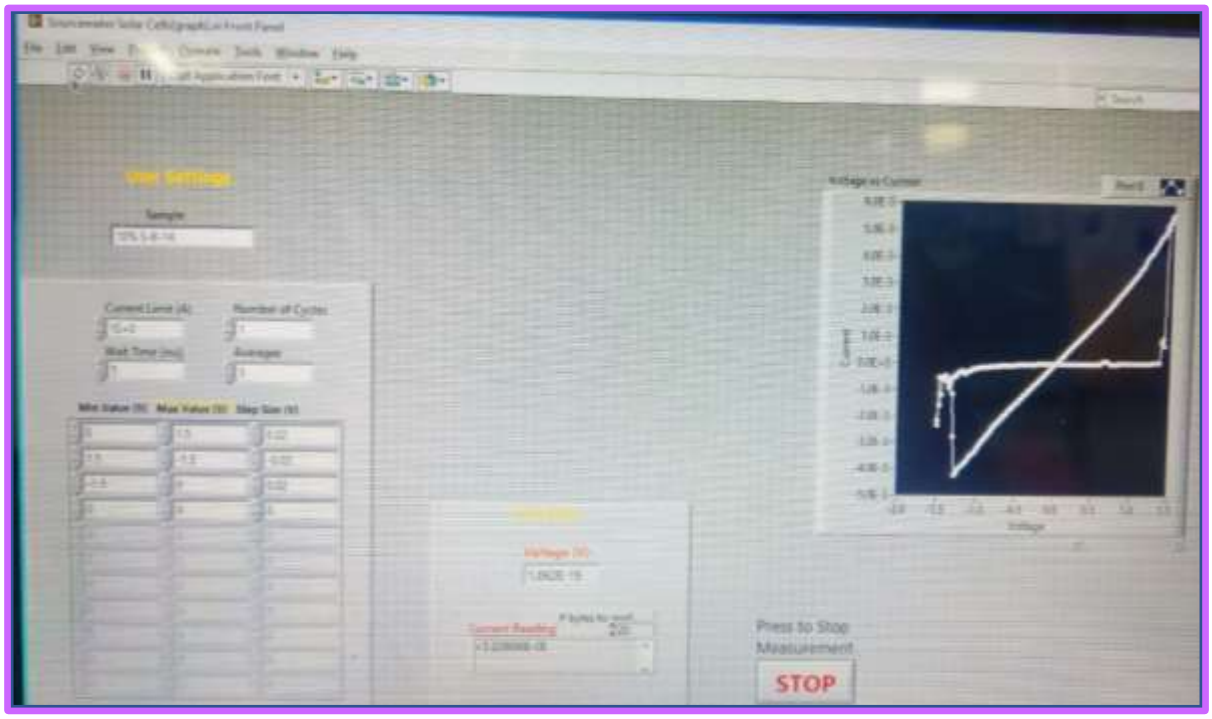

Figure 2.14 The screen shot of the graphical user interface labview program showing the bipolar resistive switching

CHAPTER 3

Effect of reduced graphene oxide incorporation on the structural, optical, and resistive switching properties of SnO_2-rGO based device.

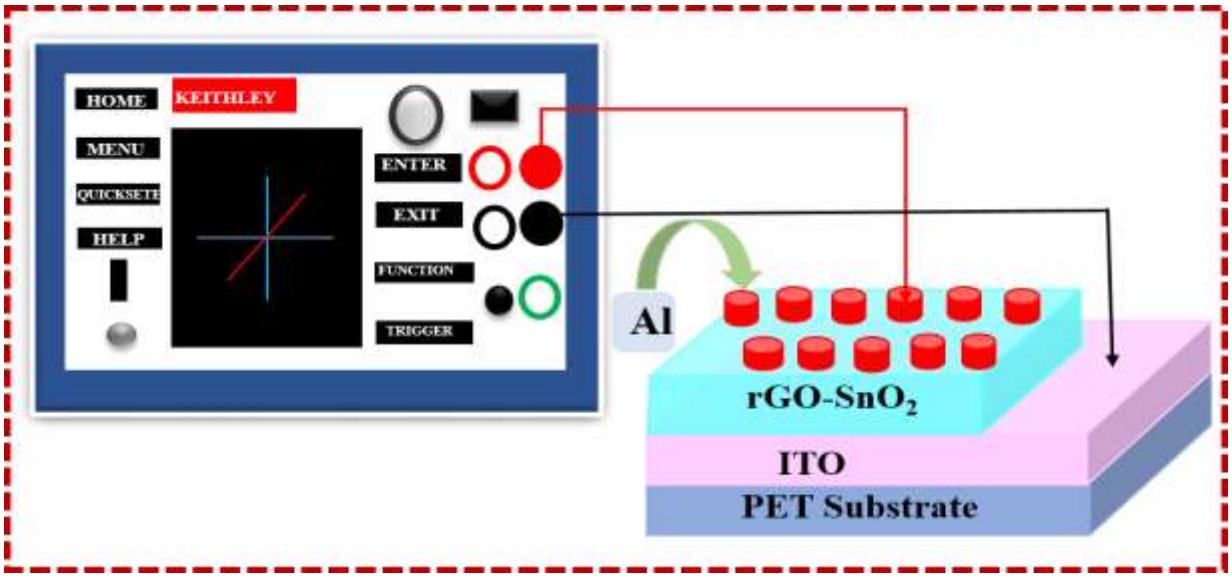

Resistive switching memory, which combines simple architectures with the ability of high density, high switching speed, and low power consumption, has sparked a lot of attention in the field of non-volatile memory devices. In this Chapter we observes the effects of pure reduced graphene oxide (rGO) inclusion on the resistive switching properties of tin oxide (SnO_2) based resistive memory device. It has been demonstrated that the incorporation of rGO in SnO_2 nanocomposite induced bipolar resistance switching with enhanced ON/OFF ratio. Here, we have fabricated flexible resistive switching memory devices of pure SnO_2 and rGO-SnO_2 (5, 7, and 10 wt.%) nanocomposite having varied concentration of rGO in SnO_2 matrix. The resistive switching performance of the fabricated devices were compared and found that the memory device with 7 wt. % of rGO in SnO_2 has a maximum ON/OFF ratio of ~ 70, in comparison to ~ 4 and ~ 3 for 5 and 10 wt. % sample respectively. The endurance and retention tests were performed on 7 wt. % rGO-SnO_2 composite film based memory device and the device shows no degradation in the memory window up to 100 cycles.

3.1 INTRODUCTION

In the recent past year, the changing market trend from low power and data-centric devices has created the opportunity for the identification of various non-volatile memory devices. The major requirement for these non-volatile memories includes the high density of integration, high speed, low cost, simple structure, low operating power, long retention time, and compatibility with the existing CMOS technology [120-122]. It has been found that several candidates are competing for the next-generation memory, including magnetic random access memory (MRAM), ferroelectric random access memory (FRAM), and phase-change memory (PCM) [123-126]. MRAM for example utilizes magnetic tunnel junctions whereas, FRAM works on the principle of reversible polarisation of ferroelectric materials, respectively, and has gained a lot of attention and has seen a lot of development in the previous few years [127]. However, both MRAM and FRAM have serious scaling issues [128, 129]. In this situation, a new possibility emerged: resistance switching random access memory (ReRAM), in which the non-volatile memory effect arises by systematic switching of the memory cell into different resistance states named as high resistance state (HRS) and low resistance state (LRS)[130]. For observing the resistive switching phenomenon, the active insulating material is sandwiched between two metal electrodes in a metal-insulator-metal (MIM) structure. It may be mentioned that initially, the device needs to be activated by applying the initial voltage called electroforming voltage (V_F) resulting in a substantial shift in resistance to LRS. After that, the memory cell switches between a high resistance state (HRS) and a low resistance state (LRS) in a repeatable manner (LRS). The 'SET' process is used to switch from the HRS to the LRS, while the 'RESET' process is used to switch back [131], which would be used in RRAM devices. Bipolar resistive switching (RS) devices require both positive and negative voltages to switch the resistance state between HRS and LRS [132]. If just one polarity of the voltage is required to switch between HRS and LRS, the RS is known as unipolar in nature (URS). Various researchers have established the ability to control RS using voltage in oxides[133], nitrides[134], and organic materials[135]. It has been found in the literature that the binary transition metal oxides such as HfO_2, TiO_2, SnO_2, ZnO, ZrO_2, and carbon-based compounds are most favoured for the ReRAM potential material as compared to ternary or quaternary oxide semiconductor films due to the ease of fabrication and compatibility with the CMOS industry [136].

Among all, SnO_2 (3.6 eV) has drawn much attention in the field of ReRAM devices due to its wide bandgap with visible optical transparency of up to 97 % and has large exciton binding energy (130 meV) [137]. Over the past few years, SnO_2 has gathered the interest of many researchers in different fields of applications, as previously reported applications of SnO_2 in perovskite devices, such as photodetectors [138], Perovskite solar cells (PSCs) [139] [140, 141], etc. Due to excellent optoelectronic properties of metal halide perovskites, such as solution-processable property, low cost, long intrinsic carrier diffusion length, small exciton binding energy, tunable bandgap, high molar absorption coefficient, and so on, perovskite solar cells (PSCs) have received a lot of attention in recent years[141]. Zhuang et al. have established a bulk and interface defect passivation technique using the synergistic impact of anion and cation at the SnO_2/perovskite interface, using multifunctional K_2SO_4. K^+ ions in K_2SO_4 diffuse into the perovskite layer and suppress the production of bulk defects in perovskite films, while SO_4^{2-} ions are anchored at the interface by strong chemical interactions with the SnO_2 and perovskite layers, respectively[140]. SnO_2-based planar PSCs have a validated PCE of 25.5 percent [142], demonstrating that they are highly promising. In its bulk form, SnO_2 has a tetragonal rutile structure [143]. Its crystal structure and stoichiometry are easy to control than multinary compounds in the application of the ReRAM devices. Owing to its interesting electrical and optical properties, it has been widely studied for ReRAM devices. The several nanostructures of SnO_2 are nanocrystals, nanowires, nanobelts, and nanotubes. Among these structures, nanocrystals are technologically essential for ReRAM devices owing to their size-dependent features [144]. However, the resistive switching mechanism has not been fully explored and needs further work in the direction to modify the switching parameters. Therefore, one of the ways for the modification is to make nanocomposite based on semiconductor metal oxide and carbon-based material such as graphene, rGO, HBC, etc.

Among the various carbon-based materials, graphene is a fast-developing substance in material science and nanotechnology, due to its large specific surface area, conductivity and remarkable mobility, optical transparency, high mechanical flexibility, and chemical stability [145, 146]. In literature, several others graphene-based photonic applications, such as imaging sensors, motion detectors, optical interconnectors, and optical modulators, have also been reported [147-149]. Zhenhua et. al presented a systematic review for solar energy conversion by using the photodetection principle in graphene and other 2D-related materials. They have discussed that for increasing the photodetection response it's very important to understand the underlying physical mechanism (photoelectric, photo-thermoelectric, and photo-bolometric regimes) in

addition to the device design and materials engineering [148]. Further, Yoo et. al has reported the graphene/P-Si based photodetector, whereby simple chemical doping of the graphene, the dark current was reduced by from orders of magnitude from 980 nA to 219 pA [147]. Several reports are available where pure reduced graphene oxide is used as active material in ReRAM and the device displays good retention time, and fast switching speed, but the current ratio is small in comparison to their metal oxide counterpart [150]. In this direction, the nanocomposites combining the properties of inorganic metal oxides and graphene-like 2D materials have been explored in literature, showing enhanced properties of the resultant device [151-153]. Along with this, it has been seen that several reports are available for metal oxide (MO) and rGO-based nanocomposite for photocatalytic application, energy storage, and gas sensing but there are few reports available for rGO-MO based nanocomposite for ReRAM application and as a result, motivates the present piece of work, where SnO_2 and rGO based nanocomposite film have been used an active material in MIM matrix. Several experimental techniques, including hydrothermal, chemical deposition, aerosol spraying, microwave synthesis, solvothermal, precipitation processes, and sol-gel auto combustion synthesis, have been intensively studied for binding of SnO_2 with rGO [154, 155]. Among all, hydrothermal synthesis is regarded as the most favourable of these procedures as it is cost-effective, uses mild synthesis conditions, and consumes little energy with basic equipment to generate homogeneous SnO_2 nanoparticles over rGO nanosheets, [156, 157]. In the current work, hydrothermal synthesis has been used to make phase pure SnO_2 and rGO-SnO_2 nanocomposites through changing weight percentages of rGO (from 5 to 10%). The resistive switching mechanism in the synthesized Al/SnO_2/ITO and Al/rGO-SnO_2/ITO nanocomposite layers (rGO ranged from 5 to 10%) has been thoroughly investigated with an aim towards their application in memory devices. To the best of my knowledge, a systematic investigation of the effect of weight % of rGO in SnO_2 for non-volatile ReRAM application has not been carried out. The effects of rGO concentration on the structural, optical, and electrical properties have been reported in detail [158, 159].

3.2 EXPERIMENTAL

3.2.1 Chemical reagents

The chemicals used in the synthesis are tin (IV) chloride pentahydrate ($SnCl_4.5H_2O$), oleic acid, oleylamine, toluene, graphite powder, concentrated sulphuric acid (H_2SO_4), hydrazine hydrate ($N_2H_4.H_2O$), hydrogen peroxide (H_2O_2), hydrogen chloride, potassium permanganate ($KMnO_4$), orthophosphoric acid (H_3PO_4) and ethanol (C_2H_5OH). Sigma Aldrich and Fisher

Scientific are the suppliers of all the chemicals. All of them are of analytical grade quality and can be used without further purification.

3.2.2 Materials Synthesis

Figure 3.1 depicts the flowchart detailing the process of material synthesis. The modified Hummers method is used to synthesize graphene oxide powder (GO) [160]. By changing the rGO weight percentage (5-10%) in SnO_2, several rGO-SnO_2 nanocomposites are synthesized by a hydrothermal process. Usually, an appropriate concentration of rGO (1mg/ml) is treated with ultrasonic energy for an hour to disperse in ethanol. In the meantime, First, 1.2 g of $SnCl_4.5H_2O$ was dissolved in a solution of 40 mL oleic acid, and 5.0 mL oleylamine is prepared separately with stirring. After that, the two solutions are combined while being constantly stirred for 3 hours. The combination was then added to a Teflon-lined autoclave composed of stainless steel, and heated for six hours at 180 °C. A rotary evaporator was used to remove the toluene from the product after the autoclave had cooled to room temperature, and the product was then centrifuged five times. To obtain the rGO-SnO_2 nanocomposite powder, the collected paste was dried in an oven for 5 hours at 60°C, followed by another 24 hours at 400°C [161].

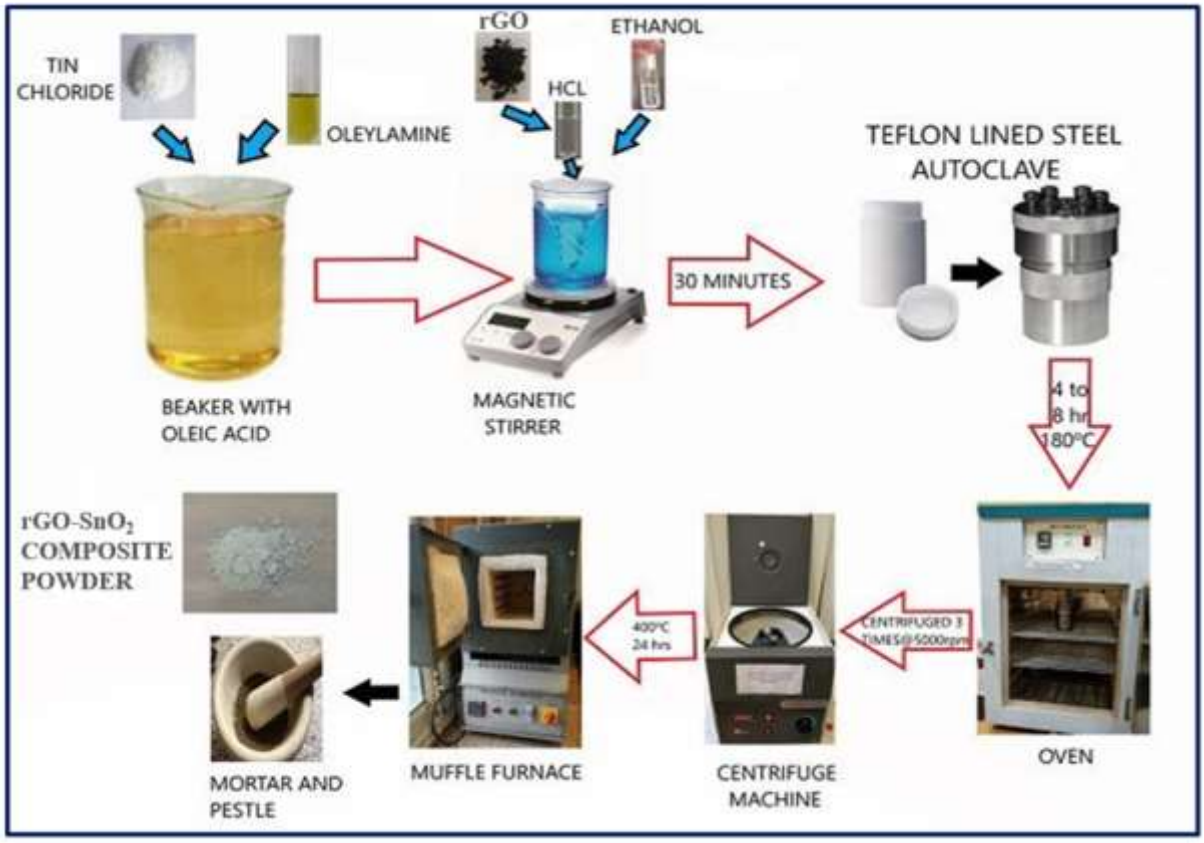

Figure 3.1 Schematic diagram illustrating the various steps used in the hydrothermal synthesis of rGO-SnO_2 (5%, 7%, and 10%) nanocomposite powder.

3.2.3 Film fabrication

The commercially available PET-coated ITO substrate was used for coating with rGO-SnO_2 (5%,7%, and 10%) nanocomposite film. The PET substrates were initially cleaned using a typical wet cleaning procedure. Following washing, on a hot plate, the substrates were dried for 15 minutes at 90°C. The spin-coater applies the spin-coating at room temperature, and the subsequent procedures are involved: (1) Following a 45-minute ultra-sonication process to dissolve 100 mg of rGO-SnO_2 in 3 ml of ethanol, The PET-glass substrate (2 cm × 1 cm) was coated with three drops of the rGO-SnO_2 solution before being rotated at 2000 rpm for 30 seconds [162]. (2) After that, the covered sample was heated for 7 minutes on a hotplate at 100°C. A film of rGO-SnO_2 (5%, 7%, and 10%) nanocomposite was then obtained after repeating this method seven times. Thermal evaporation was used to deposit the upper aluminium electrode at a pressure of 10^{-5} mbar. Figure 3.2 shows the steps necessary to make an Al/rGO-SnO_2/ITO PET-based MIM device.

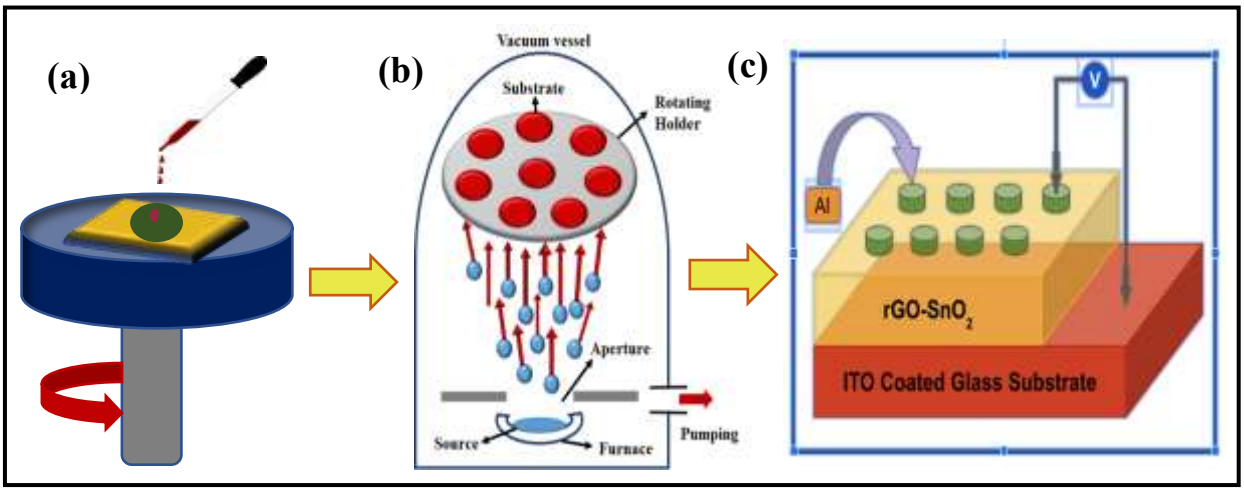

Figure 3.2 Schematic diagram showing various steps used in resistive memory device fabrication (a) spin-coating (b) thermal deposition of top Al electrode through shadow mask (c) final MIM configuration.

3.3 RESULTS AND DISCUSSION

All the prepared samples are systematically characterized using Raman Spectrometer (WiTec alpha 300RA) with a laser source of wavelength 530 nm. An X-ray diffractometer study has been used (Bruker D8 Advance) to study the crystallinity of the rGO, SnO_2, and rGO-SnO_2

(5%, 7%, and 10%) nanocomposite, with a Cu Kα radiation source (1.54 Å). The surface morphologies of the rGO, SnO_2, and rGO-SnO_2 nanocomposite were characterized by scanning electron microscopy (SEM; LYRA3 TESCAN). The bandgap of the as-prepared samples was analyzed using UV-vis absorption spectra (PerkinElmer Lambda 750 UVvis/NIR spectrophotometer) and photoluminescence spectra were carried out using a spectrofluorophotometer (RF-5301PC). Interfacial investigation of rGO, SnO_2, and rGO-SnO_2 nanocomposite structures was carried out by X-ray photoelectron spectroscopy (XPS) technique Perkin Elmer ultra-high vacuum XPS system (Model 1257 PHI) using a monochromatic Al Kα source. To fabricate the memory device, thin films were deposited by using the spin-coater, and Al electrodes of thickness ~100 nm were deposited using the thermal evaporation technique at a chamber pressure of $4x10^{-5}$ bar. Finally, the (I–V) measurements were carried out for all the prepared thin film-based memory devices (Al/SnO_2/ITO, Al/rGO-SnO_2/ITO) by using Keithley 2450 source meter.

3.3.1 X-Ray Diffraction (XRD)

Figure 3.3(a) shows an optical image showing colour variations of five powder samples including, pure samples (SnO_2 and rGO) rGO-SnO_2 (5%, 7%, and 10%) nanocomposite. The crystalline phases and crystallite size of pure rGO, pure SnO_2, and rGO-SnO_2 nanocomposite were studied using the XRD technique. XRD spectra confirm the presence of rGO and SnO_2 in the nanocomposite of rGO-SnO_2, as shown in Figure 3.3. The XRD spectra of pure SnO_2 confirm the presence of tetragonal rutile structure of SnO_2 with the occurrence of peaks at 26^o, 34^0, 52^0, and 65^o, which correspond to (110), (101), (211), and (112) planes. Similarly, the peak observed at 26^o corresponding to the (002) plane confirms the presence of rGO. Furthermore, the rGO-SnO_2 nanocomposite confirms the existence of the tetragonal rutile phase of SnO_2 with the presence of peaks at 26^0, 34^o, and 52^o attributes to (110), (101), and (211) planes. In the case of rGO-SnO_2 nanocomposite, the peaks of pure rGO are not observed owing to the low crystallinity of rGO. In the composite sample, the rGO peak observed at 26^o (002) is dominated by the diffraction peak of pure SnO_2 corresponding to the (110) plane. It may be attributed to the conversion of Sn^{4+} into SnO_2 nanoparticles in the SnO_2-rGO sample [163]. The broadening in the diffraction peaks of SnO_2 was observed with the presence of rGO. It confirms the high crystalline nature of SnO_2 particles with the presence of rGO. As crystallinity depends on crystallite size, the crystallite size was calculated by using the Scherer formula for pure rGO, pure SnO_2, and rGO-SnO_2 nanocomposite [162, 164];

$$D = k\lambda/(\beta cos\theta) \qquad (1)$$

Where λ denotes the wavelength of X-ray, β denotes the broadening of the diffraction peak measured at half maximum intensity (FWHM), θ denotes the angle corresponding to peak position, Crystallite size is D and k denotes the shape factor (k=0.94).

According to calculations, the typical crystal sizes for pure rGO, pure SnO_2, 5%rGO-SnO_2, 7%rGO-SnO_2, and 10%rGO-SnO_2 are 14.7 nm, 12.61 nm, 5.84 nm, 6.07 nm, and 6.26 nm, respectively. It has been observed that the average crystallite size of rGO- SnO_2 nanocomposite decreases owing to the growth and nucleation of SnO_2 crystals, which was hindered by rGO [165, 166].

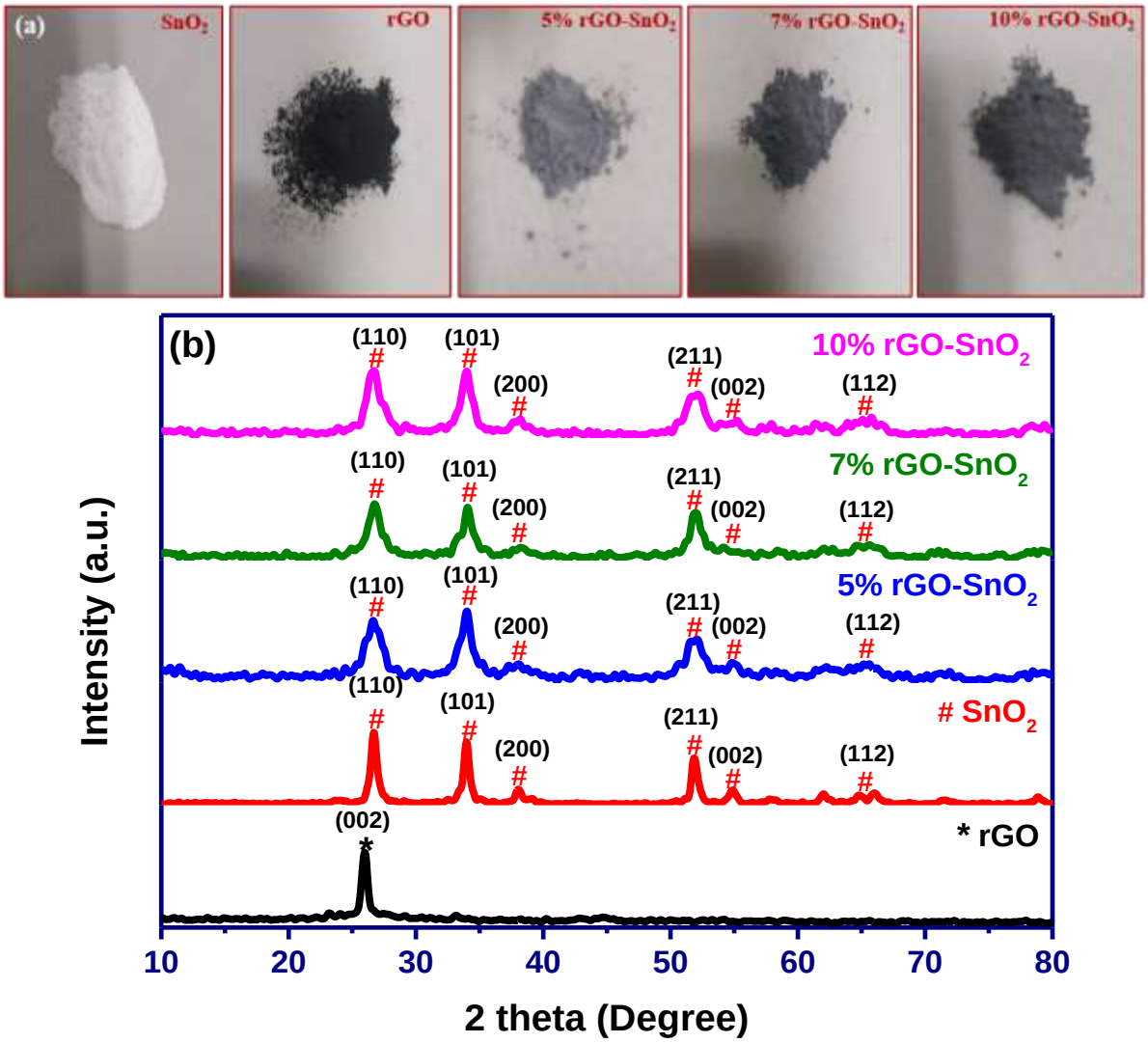

Figure 3.3 (a) Optical Images and (b) XRD spectra of synthesized samples with an indication of planes.

3.3.2 Raman Spectroscopy

The Raman scattering phenomenon is used to further confirms the formation of rGO-SnO_2 nanocomposites because it is a beneficial tool for understanding the composition of materials depending on rGO. Figure 3.4 shows Raman spectra of pure and nanocomposites with varying rGO concentrations. In the Raman spectra of pure rGO, there are two distinct peaks at 1351 cm^{-1} and 1591 cm^{-1}, which represent well-known D-band and G-band, respectively. While the structural instability at defect locations drives the D-band, the G-band is created by the vibrations of sp^2 hybridised carbon atoms. The second less powerful peak, which relates to the second order D band, was seen at 2679 cm^{-1}. In the case of SnO_2 nanoparticles three distinct Raman peaks at 475 cm^{-1}, 631 cm^{-1}, and 773 cm^{-1}, which corresponds to the E_g, $A_{1g,}$ and B_{2g} modes of SnO_2 have also been observed [167]. The Raman spectra of 5%rGO-SnO_2, 7%rGO-SnO_2, and 10%rGO-SnO_2 samples show two prominent peaks at 1351 cm^{-1}, 1603 cm^{-1}, 1351 cm^{-1}, 1600 cm^{-1}, and 1351 cm^{-1}, 1600 cm^{-1} respectively, corresponding to the D-band and G-band [159, 163]. While the D and G bands are present in all the samples, there are noticeable differences. The peak position of the nanocomposite has shifted due to interaction between rGO and SnO_2 nanoparticles during the hydrothermal synthesis process. Different rGO concentrations (5, 7, and 10%) in rGO-SnO_2 nanocomposite samples produce various heights in the Raman spectra that are connected to both rGO and SnO_2. The SnO_2 Raman scattering peaks become less prominent and those corresponding to graphene grow as the rGO absorption increases from 5% to 10%. In the rGO-SnO_2 nanocomposite samples, this suggests the development of SnO_2 and rGO phases. The improved memory phenomenon is attributed to the successful composite formation, confirmed by Raman spectroscopy, where the peak position corresponding to graphitic band (G) band shift to higher wavenumber, in comparison to pure rGO, as well as I_D/I_G ratio increased in the nanocomposite of SnO_2 and rGO. Further the nanocomposite having 7 wt. % of rGO in the SnO_2 matrix has the highest I_D/I_G ratio of 1.135, thereby indicating the presence of electronic interaction between SnO_2 and rGO in the composite. Additionally, the D and G bands intensity ratio (I_D/I_G) is 1.02 for pure rGO and increases to 1.125, 1.135, and 1.065 in the rGO-SnO_2 (5%,7%, and 10%) nanocomposite.

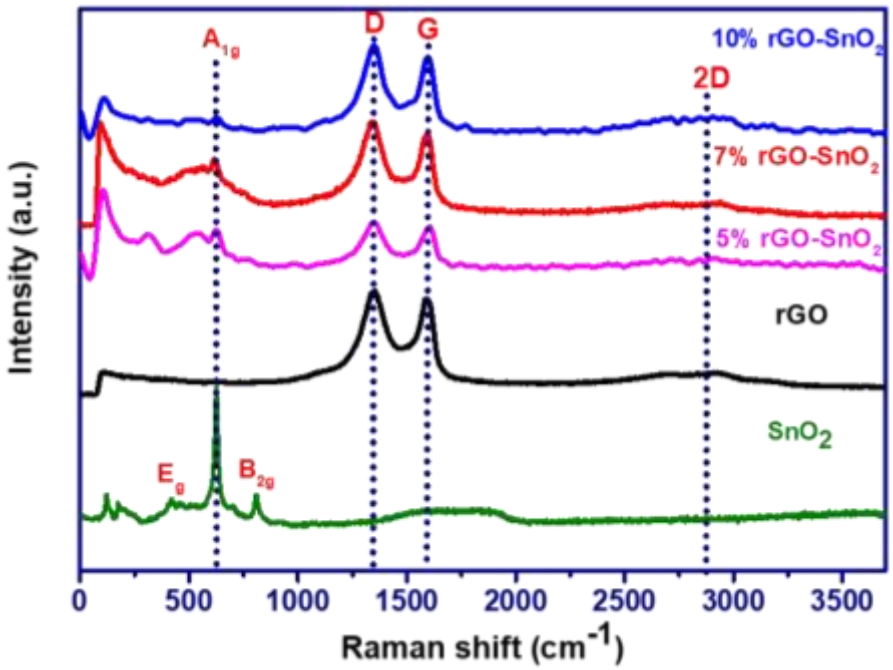

Figure 3.4 Raman spectra showing the characteristics peaks of rGO, SnO_2 nanoparticles, and rGO-SnO_2 nanocomposites with a weight percentage of 5%, 7%, and 10%.

Table 3.1. Parameters of the pure and nanocomposite samples obtained from the Raman spectroscopy.

Materials	Peak Position D-band	Peak Position G-band	I_D/I_G Ratio	Mode (A_{1g})	Mode (B_{2g})	Mode (E_g)
rGO	1351	1591	1.02	_	_	_
SnO_2	_	_	_	630	773	474
5% rGO-SnO_2	1351	1603	1.125			
7% rGO-SnO_2	1351	1600	1.135			
10% rGO-SnO_2	1351	1600	1.065			

3.3.3 UV-Visible Spectroscopy

UV-Vis spectroscopy was employed to measure the degree of oxidation for synthesized samples. Figure 3.5 shows the ultraviolet-visible absorption bands of all the pure and nanocomposite samples. The absorption peak for rGO was found at 271 nm. This absorption peak arises due to the π-π* transitions of C-C bonds present in graphitic material [160].

Furthermore, in the case of pure SnO_2, the characteristic absorption peak was found at 218 nm. Similar results were obtained for all the rGO-SnO_2 nanocomposite, which showed an immersion peak at 316, 317, and 318 nm for the 5%, 7%, and 10% rGO-SnO_2 nanocomposite, respectively. As the amount of rGO increases, reflectance levels are seen to gradually rise. Thus, it can be demonstrated that the additive content impacts the samples as-produced optoelectronic characteristics [158].

Furthermore, the bandgap of the synthesized samples was evaluated by Tauc's plot;

$$(\alpha h\nu) = A(h\text{-}E_g)^{1/2}$$

Where A is a constant, E_g is the bandgap and α is the absorption coefficient. The optical bandgap for pure SnO_2, pure rGO, 5%rGO-SnO_2, 7%rGO-SnO_2, and 10%rGO-SnO_2 nanocomposites were calculated by the plot between $(\alpha h\nu)^2$ vs. hν [168].

The linear fitting of $(\alpha h\nu)^2$ vs. hν plot gives bandgaps for rGO (1.90 eV) and SnO_2 (3.65 eV) [See Fig. 5]. Similar to this, the bandgaps were calculated to be 4.07, 4.06, and 3.78 eV for 5%, 7%, and 10% rGO-SnO_2, respectively. Accordingly, the E_g value gradually drops from 4.07 to 3.78 eV as the concentration of rGO increases this variation represents the charge is transferred from Sn to rGO. This result also indicates that the local electronic structure of the rGO structure is significantly impacted by the addition of SnO_2 [158].

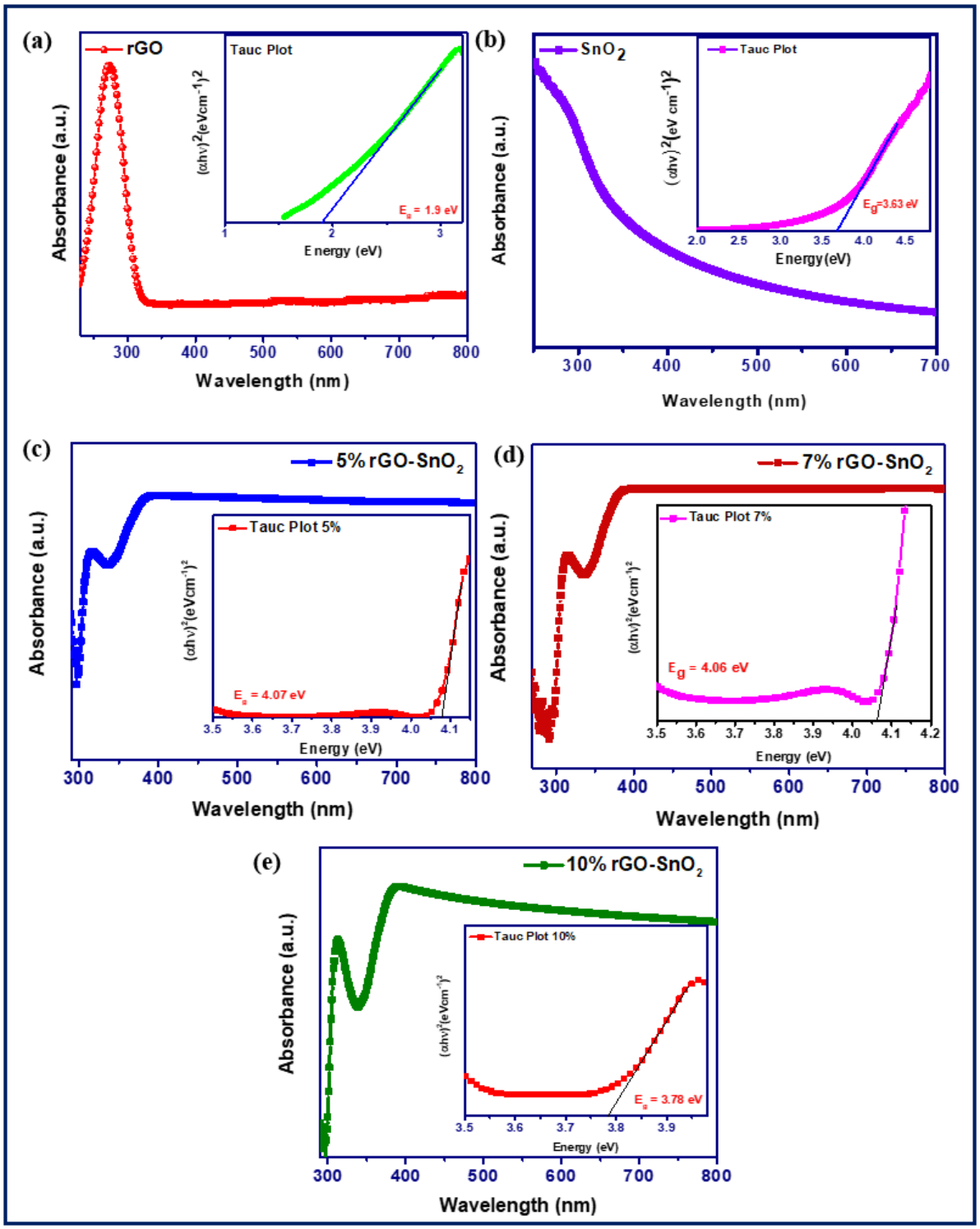

Figure 3.5 Ultraviolet-visible spectroscopy results depicting pure (a) rGO (b) SnO_2 and (c-e) rGO-SnO_2 nanocomposites with varying weight percentages of rGO (5%, 7%, and 10%), respectively, formed at 180°C for 6 hours.

3.3.4 FTIR Spectroscopy analysis

The FTIR technique can be used to comprehend more about the substance bonds and useful groups that are present in a material. Understanding the existence of specific useful groups that are adsorbed at particular frequencies during transmission mode is very helpful since it shows the structure of the material. Band locations and the number of absorption peaks are determined by morphology, chemical composition, and crystalline structure [169]. The surface is highly reactive and easily modified in nanoscale materials. An FTIR analysis was performed for all the samples between 400 and 4000 cm^{-1} at normal temperature to look at chemical groups on sample surfaces [See Figure 3.6]. The peak at 3450 cm^{-1} appears to be caused by the O-H group, while the two peaks at 1644 cm^{-1} and 1385 cm^{-1} are caused by the vibrations of skeletal rGO and cyclic hexagonal symmetry, respectively[170]. The FT-IR spectrum of SnO_2 nanoparticles shows an absorption peak located at 610 cm^{-1} related to the anti-symmetric O-Sn-O stretching of SnO_2 and an absorption peak at 458 cm^{-1} related to Sn-O vibration from the SnO_2 surface[163]. A modest peak at 2900 cm^{-1} caused by C-H bonding can be seen in the rGO-SnO_2 nanocomposites FT-IR spectra. The absorption peaks at 1067 cm^{-1} are attributed to rGO sheet C-O stretching vibrations, an absorption peak located at 610 cm^{-1} related to anti-symmetric O-Sn-O stretching of SnO_2, and a peak around 458 cm^{-1} is the characteristic peak of SnO_2 and corresponds to the Sn-O bond confirms the presence of SnO_2 in all the nanocomposites[158]. Additionally, the FT-IR spectra of rGO-SnO_2 nanocomposites show that the immersion peaks of the SnO_2 component dominate over the rGO components when the rGO concentration rises from 5% to 10%. This results in a decrease in the immersion peaks of SnO_2 at 610 cm^{-1} and 458 cm^{-1}. Therefore, this suggests that SnO_2 and rGO phase coexists in all prepared rGO-SnO_2 (5%, 7%, and 10%) which agrees well with SEM observations likewise.

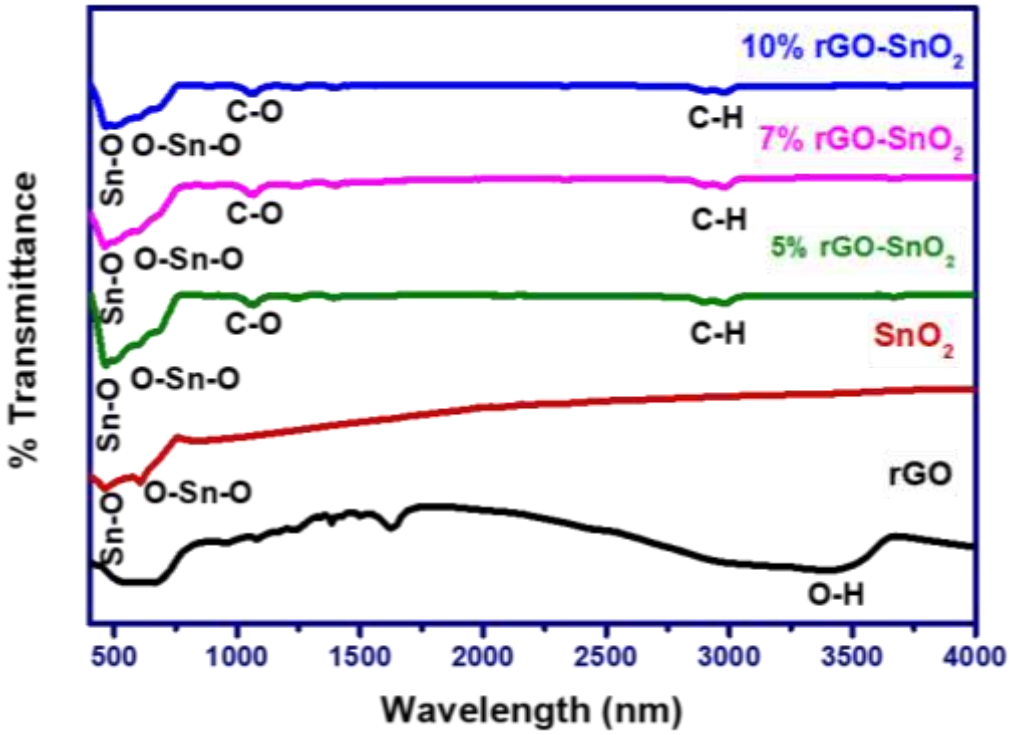

Figure 3.6 FT-IR spectra of pure rGO, pure SnO_2 nanoparticles, and rGO-SnO_2 nanocomposites with various weight percentages of rGO (5%, 7%, and 10%) concentrations.

3.3.5 Scanning Electron Microscopy (SEM)

SEM was used to examine the morphology of the pure rGO, pure SnO_2, and rGO-SnO_2 (5%, 7%, 10%) nanocomposite. The SEM image of rGO exhibits wrinkled and layered flakes on its surface as shown in Figure 3.7a. It also exhibits randomly aggregated rGO sheets. Similarly, Figure 3.7b shows the SEM image of nanocrystalline SnO_2. It shows the homogeneous and uniform distribution of SnO_2 nanocrystallites. Additionally, the SEM image of the rGO-SnO_2 (5%, 7%, 10%) nanocomposite exhibits that the rGO sheets surface is coated with SnO_2 nanoparticles [See Figures 3.7(c-e),]. It indicates that hydrothermal treatment of rGO and $SnCl_4$ solution is a successful approach for the synthesis of the rGO-SnO_2 nanocomposite [160].

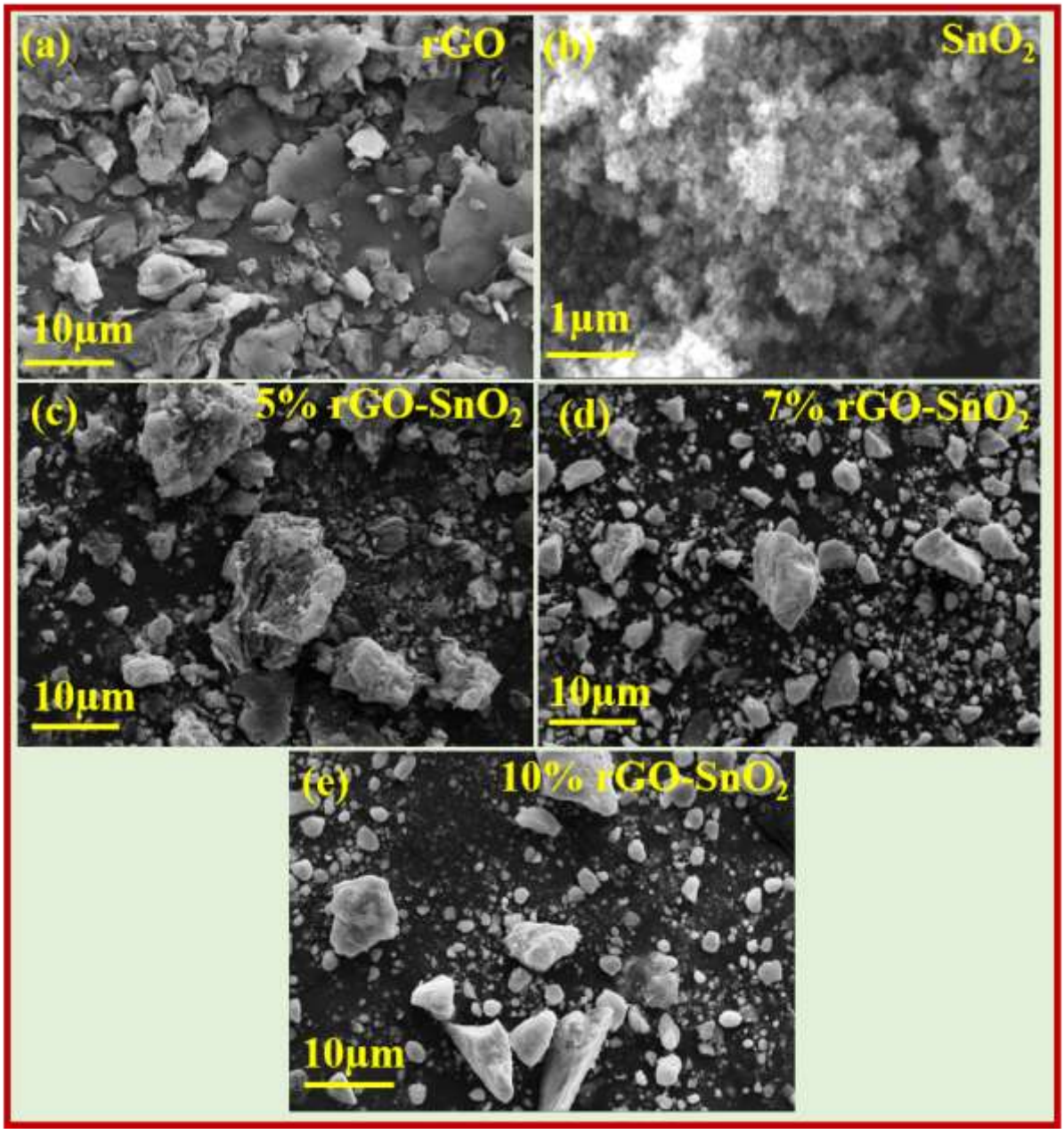

Figure 3.7 SEM micrograph of (a) rGO (b) SnO_2, and rGO-SnO_2 nanocomposite powder with different compositions of (c) 5 % (d) 7%, and (e) 10%.

3.3.6 X-ray Photoelectron spectroscopy (XPS):

The surface characterization technique used to examine the elemental and compositional information of the samples is XPS. The XPS spectra of pure rGO, pure SnO_2 and rGO-SnO_2 nanocomposite are shown in Figure 3.8a. It confirms the presence of C, Sn, and O, no other impurities could be observed.

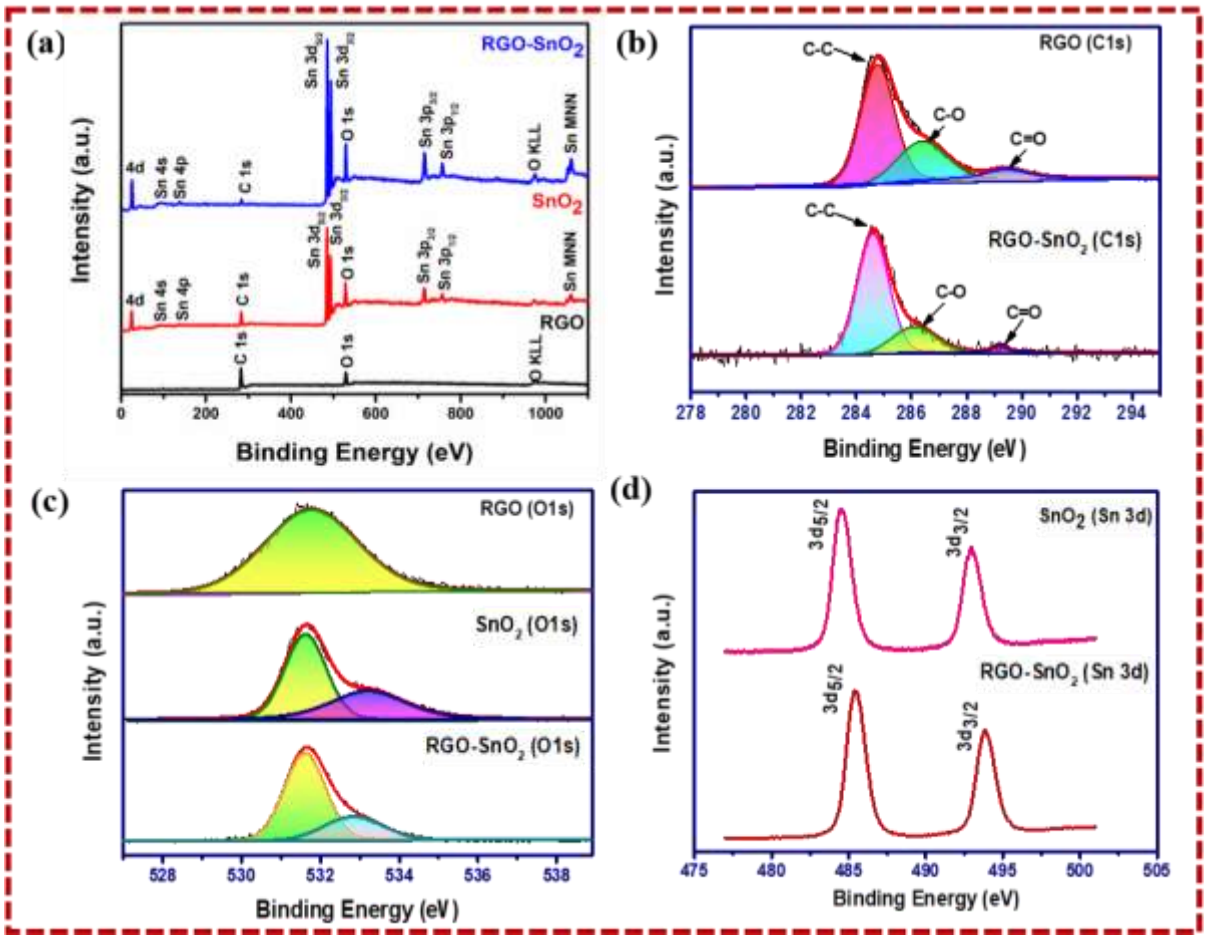

Figure 3.8 (a) XPS survey spectra and High-resolution core-level XPS spectra for pure rGO, pure SnO_2, and rGO-SnO_2 nanocomposite: (b) C1s peak; (c) O1s peak; (d) Sn 3d spectra. The larger binding energy shifts in the XPS spectra for rGO-SnO_2 in comparison to pure rGO and SnO_2 are due to interaction at the rGO-SnO_2 interface.

Carbon Spectra

Figure 3.8b shows the XPS results of the C1s present in pure rGO and rGO-SnO_2 nanocomposite. In the case of pure rGO, three characteristic peaks are observed at 284.6 eV, 286.1 eV, and 288.8 eV, corresponding to C-C, C-O, and C=O, respectively [171]. In the case of rGO-SnO_2 nanocomposites, peaks are present at 284.6, 286.1, and 289.1 eV, which correspond to the sp^2 C, C–O, and C=O groups, respectively. In the rGO-SnO_2 composite, the peak position of the C=O (289.1 eV) group shifted towards the higher binding energy side. After the hydrothermal process, carbon-oxygen bond contributions to the C1s peak are drastically reduced. The shift towards the higher binding energy side corresponds to electronic interaction at the interface of rGO and SnO_2 [172].

Oxygen Spectra

The oxygen spectrum of pure rGO, pure SnO_2, and rGO-SnO_2 nanocomposite are shown in Figure 3.8c. In the case of rGO, the peak at 531.7 eV is attributable to oxygen-containing functional groups present as a result of the hydrazine reduction phase during rGO synthesis. Similarly, two deconvoluted peaks are fitted for pure SnO_2. The peak in the O1s spectra at 531.6 eV corresponds to an extra oxygen species in the tin oxide sample. Another detected peak at 533.2 eV, suggests that the surface is significantly surrounded by hydroxide OH groups and corresponds to non-lattice oxygen [173]. Furthermore, in the case of rGO-SnO_2 nanocomposite, the O1s peak of non-lattice oxygen is shifted towards a lower binding energy side with a peak position of 532.8 eV. The shift in the peaks of O1s is shown in Table 3.2. The shift in the O1s peak shows an interfacial interaction, most likely between carbon from reduced graphene oxide and oxygen species from SnO_2 [174]. The O1s (rGO-SnO_2) spectra show narrower width of rGO which is exhibited due to the latter, i.e., at 531.6 eV, which might arise from adsorbed oxygen on the sample surface.

Tin Spectra

Figure 3.8d shows the XPS spectra of Sn 3d for pure SnO_2 and rGO-SnO_2 nanocomposite. In the case of pure SnO_2, two characteristic peaks of Sn $3d_{5/2}$ and Sn $3d_{3/2}$ are observed at 484.5 eV and 493 eV respectively, which can be seen, demonstrating that tin exists in the form of Sn^{4+} [175]. While, in the Sn 3d spectra of rGO-SnO_2 nanocomposite, the XPS peaks are observed at 485.4 eV and 493.9 eV, which shows a higher binding energy shift of 1 eV and 0.9 eV for Sn $3d_{5/2}$ and Sn $3d_{3/2}$ peaks respectively. The peak-to-peak spacing is 8.4 eV between the characteristic peaks for SnO_2 and is consistent with previous findings. The above-observed shift indicates that the SnO_2 nanoparticles are connected to the rGO nanosheets, and the same has been confirmed in a study [176]. The formation of the Sn-C-O connection between SnO_2 and rGO indicated the presence of a strong interaction between them, which was crucial in improving resistive switching performance. As a result, the Sn3d peaks from rGO-SnO_2 are moved to the higher binding energy [177]. Because SnO_2 has a smaller work function than rGO, the electrons in rGO-SnO_2 hybrids can generally flow (SnO_2 to rGO) [178]. As a result, the Sn3d peaks for rGO-SnO_2 have been moved to have greater binding energy. The electrostatic repulsive contact between O and a negative charge in the lattice allows Sn to produce more energy. The binding energy of O1s will be affected by the change in electronic orbit for Sn [179].

Table 3.2 Binding energy (eV) of pure rGO, pure SnO_2, and rGO-SnO_2 nanocomposite.

Sample Name	C 1s (eV)			O 1s (eV)		Sn 3d (eV)	
	I	II	III	I	II	I	II
RGO	284.6	286.1	288.8	531.7	-	-	-
SnO_2	-	-	-	531.6	533.2	484.5	493
RGO-SnO_2	284.6	286.1	289.1	531.6	532.8	485.4	493.9

The potential barrier at the interface plays an important role in the enhancement of memory device properties. Owing to the interfacial potential barrier, the liberated electrons will be transported between SnO_2 and rGO. This interaction leads to the modification of the interface and hence enrichment of the memory device properties. The interaction between rGO and SnO_2 is inferred by the energy band model.

3.3.7 Dielectric characteristics

Dielectric spectroscopy was used to investigate the dielectric behaviour of the prepared samples. The distribution of local electric field inside the system determine the dielectric behaviour of all bulk and nano solid materials. Therefore, the frequency-dependent dielectric constant, dielectric loss, and ac conductivity can provide significant information regarding the transport mechanism, structural changes, and defect behaviour of any synthesized solid material. These dielectric properties are significantly affected by any physical and chemical variation inside the solid, as well as their variation with frequency can give useful insight into the material relaxation mechanism. The dielectric measurements provide critical information on two important physical characteristics of the material (a) dielectric loss (b) and electrical permittivity (also known as the dielectric constant). As an alternating field is applied across the sample, charge carriers produce heat as a result of a lag in polarisation known as "dielectric loss" (D = tanδ). The combined actions of electrical conduction and dielectric relaxation result in dielectric loss inside a material [180]. The real (ε´r) and imaginary (ε´´r) components of the dielectric constant, or electric permittivity, are shown to vary with frequency in Figures 3.9a and 3.9b. Based on the Maxwell-Wagner model, it can be seen that ε'_r decreases with increasing frequency of applied field for all samples [181]. In the low frequency region, a high value of ε'_r is observed for all the samples and is attributed to ease with which the space charge polarisation induced nano dipoles orient themselves with

frequency change. Dipoles have ample time to reach the grain boundaries at low frequencies, where the accumulation of charge carriers results in significant polarization. The field direction shifts so quickly at high frequencies that the charge carriers can't keep up. As a result, carriers are unable to reach the grain boundaries, and as a result, no polarisations occur [182]. Since composites have a larger surface area due to their small size (more grains), the dielectric constant of optimally doped SnO_2 (7% rGO-SnO_2) composite is higher than in 5% rGO-SnO_2, 10% rGO-SnO_2, and pure SnO_2 [183].

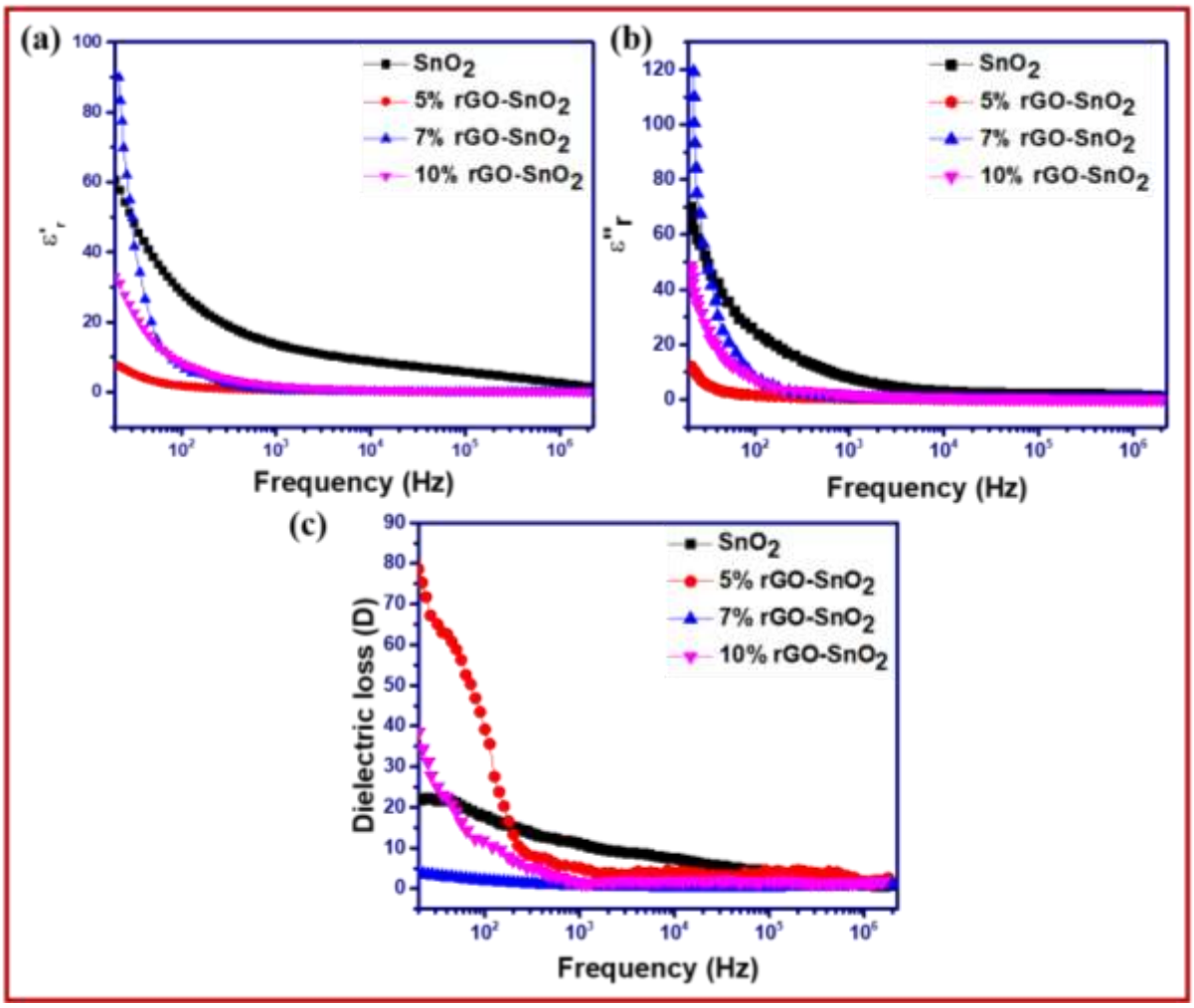

Figure 3.9 Dielectric constant variation (a) real and imaginary parts, and dielectric loss (c) for pure SnO_2, 5% rGO-SnO_2, 7% rGO-SnO_2, and 10% rGO-SnO_2 nanocomposite as a function of the frequency.

A process called dielectric loss (tanδ) signifying the dissipation of energy loss occurs in the dielectric system. Figure 3.9c displays the dielectric loss at room temperature in the frequency range 20-10^6 Hz for pure SnO_2, and rGO-SnO_2 nanocomposites (5% rGO-SnO_2, 7% rGO-SnO_2 and 10% rGO-SnO_2). In dielectric media, dielectric loss occurs when the charge carriers cannot

keep up with the electric fields fluctuations. For all samples, it is found that dielectric losses decrease with increasing applied field frequency. At higher frequencies, reduced dielectric losses are seen as a result of the forced rotational shift of magnetization due to domain wall inhibition. A possible sign of Maxwell-Wagner relaxation could be the lower values at higher frequencies. The greater dielectric loss happens at lower frequencies, as Figure 3.9c illustrates. This is caused by space charge polarisation, which can be explained by the Shockley Read mechanism [184]. In general, rGO sheets have oxygenated functional groups on their surface that are very resistive and operate as an intrinsic barrier to minimise leakage current. The minimal dielectric loss in 7%rGO-SnO_2 can readily be shown in Figure 3.9c. The quantity of energy dissipation is represented by the imaginary part of the dielectric constant (ε″), and tan δ is proportional to ε″. From Figure 3.9c, it is found that the 7% rGO-SnO_2 composite has dielectric loss tanδ that is significantly higher/ Lower than that of pure SnO_2. As the concentration of rGO is increased from 7 wt. % to 10 wt. %, the rGO-SnO_2 the dielectric loss increases as a result of a significant leakage current brought on by rGO sheets connecting directly above the percolation threshold [185, 186]. The synergistic impact between the SnO_2 nanoparticle decorations and optimum concentration of rGO nanosheets in the composite is undoubtedly responsible for the high dielectric constant and comparatively low dielectric loss in the 7 wt. % rGO-SnO_2 sample.

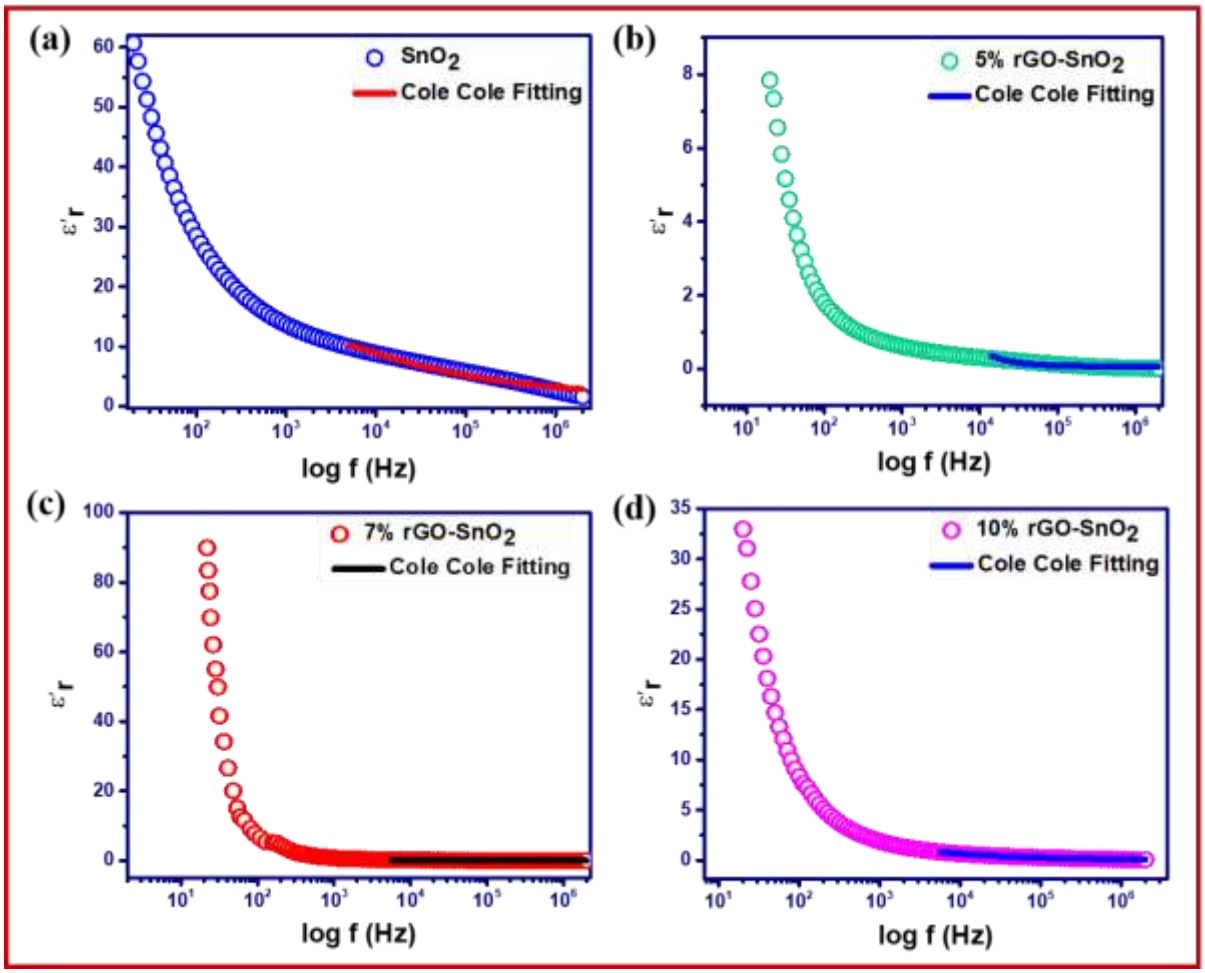

Figure 3.10 To determine the frequency dependence of the dielectric constant (real portion), (a) pure SnO_2, (b) 5%rGO-SnO_2, (c) 7%rGO-SnO_2, and (d) 10%rGO-SnO_2 nanocomposite were fitted using a Cole-Cole fitting.

In the high-frequency region, it is revealed that the fluctuation of the dielectric constant (ε'_r) with the frequency of the SnO_2, 5%rGO-SnO_2, 7%rGO-SnO_2 and 10%rGO-SnO_2 samples follows the Cole-Cole relaxation. To match the experimental ε'_r vs. f curve in the frequency range of 20 and 1.0×10^6 Hz, the following relation was applied.

$$\varepsilon'(\omega) = \varepsilon'_\infty + [\,(\varepsilon'_s - \varepsilon'_\infty)/(1+(i\omega\tau)^{1-\alpha})] \quad (3)$$

where ε' denotes the real part of the dielectric constant, ε'_s denotes the value at the lowest frequency, ε'_∞ denotes the value at the greatest frequency, ω denotes the angular frequency, τ denotes the average relaxation time, and α denotes the spread. Figure 3.10 depicts experimental data from SnO_2, 5%rGO-SnO_2, 7%rGO-SnO_2 and 10%rGO-SnO_2 samples with a Cole-Cole-

fitted curve. Table 3.3 shows the values of α and τ determined from the Cole-Cole fitting for the SnO_2, 5%rGO-SnO_2, 7%rGO-SnO_2 and 10%rGO-SnO_2 samples[186, 187].

3.3.8 Impedance spectroscopy

To examine various electrical features, such as the impact of grain and grain boundaries on the total impedance, relaxation time distribution, and kind of relaxation mechanism [180], one can analyse the complex behaviour of total impedance with frequency. Impedance spectroscopy is a powerful technique for determining the contribution of these elements to the total dielectric response and obtaining information about the resistive (real part) and reactive components (imaginary part) in the material. To represent total complex impedance, we have used the following formula:

$$Z^* = Z' + jZ'' \quad (4)$$

where Eq. 5 gives the total impedance real (Z') and imaginary (Z'') components

$$Z'' = Z\times \sin\theta \text{ and } Z' = Z\times \cos\theta \quad (5)$$

Z in this case is the measured phase angle (in radians), which is the total measured impedance. The variation in the capacitive or imaginary part and the resistive or real component (Z') with respect to the applied field frequency is seen in Figures 3.11(a-b). Lower frequency impedance values are high, and they drop as frequency increases. Impedance has decreased as frequency has increased due to the dissipation of stationary charges and greater mobility. At higher frequencies, there is a tendency for all the curves to merge due to a decrease in space charge and the cancellation of the dipole orientation effect [180]. As illustrated in Figures 3.11(c-d), Nyquist plots were used at room temperature to isolate the effects of the grains and grain boundary. Conductive grain boundaries are essential at higher frequencies in SnO_2, and 7%rGO-SnO_2 nanocomposite materials, but resistant grain boundaries are relevant at low frequencies. The semicircle reveals highly resistant grain boundaries at low frequencies. The semi-circle is produced by the conducting grains at a high frequency and a low resistance value. In our situation, all of the samples display just one semicircle, which is caused by the contribution of the grain boundaries [185], as seen in Figures 3.11(c-d). Due to their higher resistance than the grain itself, grain boundaries are thought to play a significant role in impedance [188].

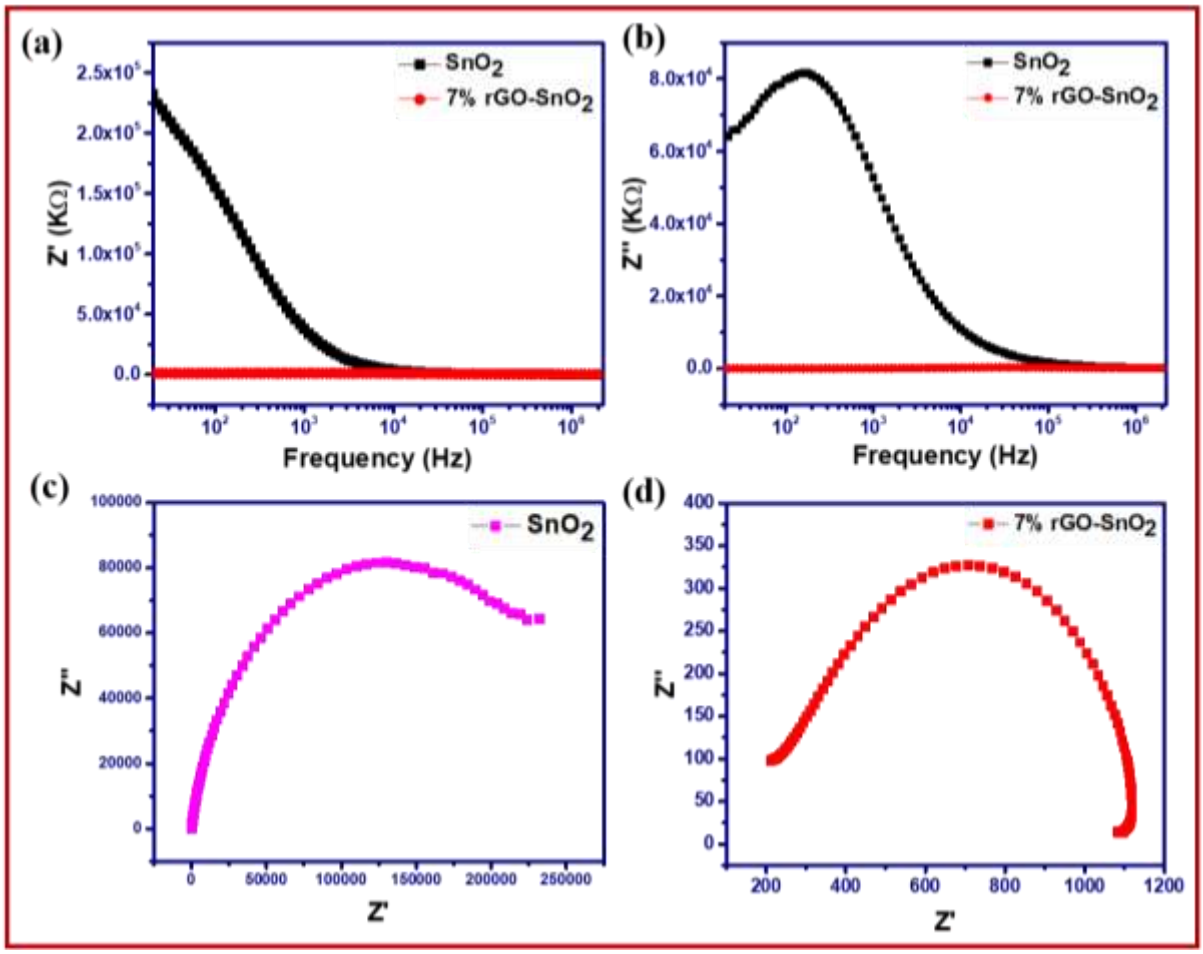

Figure 3.11 Impedance variation for the SnO_2, and 7%rGO-SnO_2 nanocomposite powder as a function of frequency (20-10^6 Hz) in both (a) real and (b) imaginary sections. (c) Nyquist plot of SnO_2, and 7%rGO-SnO_2 nanocomposite samples.

3.3.9 AC conductivity

The frequency-dependent AC conductivity of SnO_2, 5%rGO-SnO_2, 7%rGO-SnO_2, and 10%rGO-SnO_2 nanocomposite samples was investigated at room temperature in the frequency range of 20-10^6 Hz to investigate the conduction mechanism. It has been noted that when the conductivity decreases with an increase in frequency, the free charge carriers make the majority contribution, whereas when the conductivity increases with frequency, the bound charge carriers make the majority contribution [189]. The oscillating field over the sample causes carriers to jump from one faulty condition to another. Figure 3.12a shows the computed a.c. conductivity using the formula $\sigma(\omega) = \omega\varepsilon_0\varepsilon_0 \tan\delta$. It gives evidence of the presence of bound charge carriers and sheds light on the behaviour of significant frequency dependence by showing that conductivity rises with frequency. Because the carriers can hop for longer periods at lower frequencies, they can translate over longer distances and provide conductivity that is

frequency-independent. At higher frequencies, failure and successful processes conflicting processes occur because of the carrier's shorter lifetimes. The ratio of unsuccessful to successful hops is what causes the dispersed behaviour in conductivity at higher frequencies. Eqn. 6 is used to fit the frequency dependence of the a.c. conductivity data using Jonscher's power law [180].

$$\sigma_{ac}(\omega) = \sigma_{dc} + A\omega^{s} \quad (6)$$

where A is the polarization strength, s is an exponent that describes the lattice-mobile ion interaction depending on the applied field frequency, and σ_{dc} is the frequency-independent d.c. contribution. Additionally, $\sigma_{ac}(\omega)$ represents the total measured conductivity, and $A\omega^{s}$ denotes the frequency-dependent contribution. The shift between the frequency-independent and frequency-dependent regions demonstrates the transformation from long-range hopping across barriers to the short-range motion of carriers [180, 190]. When we analyse a.c. conductivity, we see a rapid rise in conductivity at higher frequencies, which raises the possibility of different conduction mechanisms and is corroborated by Jonscher's power law. Table 3.3 lists the fitting parameters that were obtained from the a.c. conductivity data, which we fitted using Jonscher's power law, as illustrated in Figures 3.12(b-e). The rise in AC conductivity that occurs when rGO is added to SnO_2 is evident from Figure 3.12a.

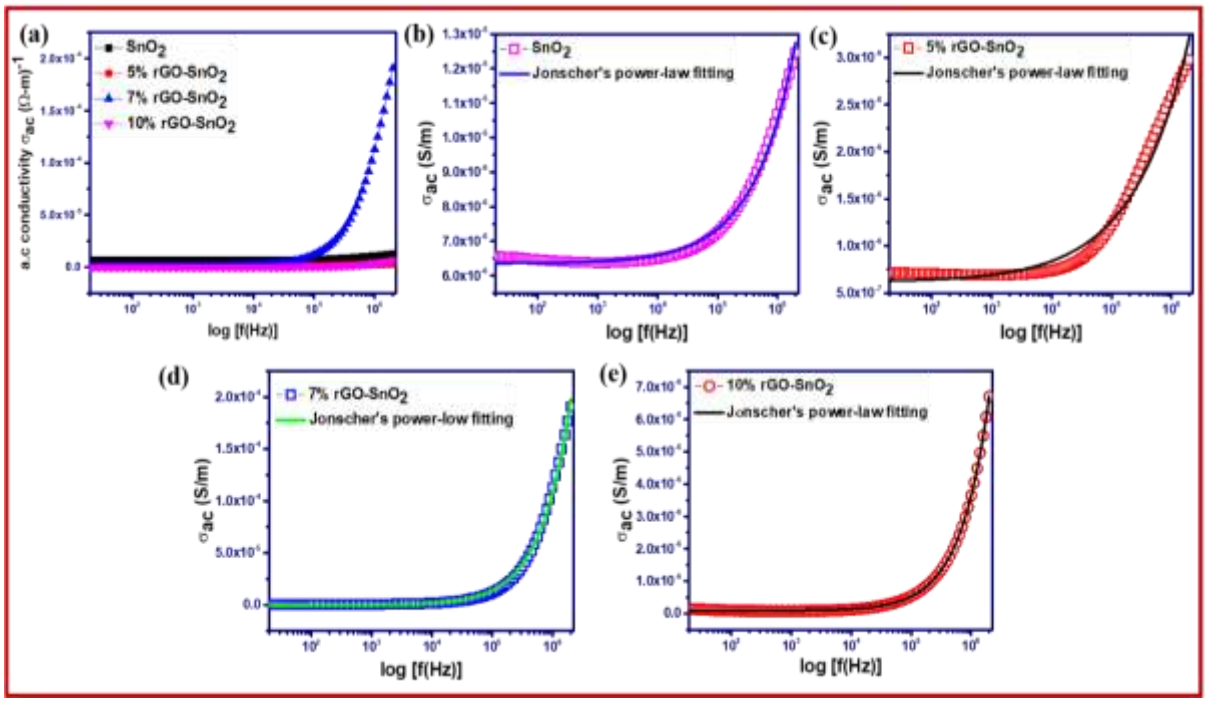

Figure 3.12 (a) The relationship between frequency and ac conductivity (σ_{ac}). (b-d) The graphs of curve fitting for SnO_2, 5% rGO-SnO_2, 7% rGO-SnO_2, and 10% rGO-SnO_2 nanocomposite were created using Jonscher's power law.

Table 3.3 Parameters are taken from the power law fitting of Jonscher's for every sample and Cole-Cole fitting for all samples.

Materials	Frequency exponents (s)	Pre exponent A	Spreading factor (α)	Relaxation time (τ)
SnO_2	0.621	7.74×10^{-10}	0.79	4.95×10^{-4}
5% rGO-SnO_2	0.465	3.06×10^{-9}	0.33	1.05×10^{-4}
7% rGO-SnO_2	0.874	6.12×10^{-10}	1.37	3.92×10^{-4}
10% rGO-SnO_2	0.901	1.39×10^{-11}	1.22	2.01×10^{-3}

Because of its two-dimensional planar form, graphene exhibits exceptional conductivity. As a result, it is possible to achieve quick charge carrier hopping. 7%rGO-SnO_2 is found to have a higher electrical conductivity than SnO_2, primarily because charge carriers hop quickly between the SnO_2 and rGO surfaces through cross-linked connections. However, this value falls in comparison to the theoretically reported conductivity of graphene [191]. This is due to the complex mechanism of electron tunnelling and charge carrier hopping in 7%rGO-SnO_2, which is distinct from graphene single layer. It is also observed that the 7%rGO-SnO_2 sample has the highest conductivity in comparison to other obtained samples due to the creation of a percolating network via the composite. Furthermore, larger rGO loading reduces composite conductivity due to significant dielectric loss generated by considerable leakage current caused by direct connection between conductive rGO sheets [185].

3.3.10 Switching characteristics of Al/SnO_2/ITO and Al/rGO-SnO_2/ITO devices

The impact of the incorporation of rGO on electrical properties [192] of SnO_2 is studied using room temperature I-V characteristics using Keithley 2450 SMU. Figure 3.13 shows the schematic illustration of the metal-insulator-metal (MIM) fabricated memory device configuration to study the I-V characteristics. The I-V characteristics for Al/SnO_2/ITO-PET and

Al/rGO-SnO_2/ITO-PET films with different rGO weight percentages in SnO_2 are shown in Figures 3.14(a-d) by varying the voltage from -1 V to +1 V.

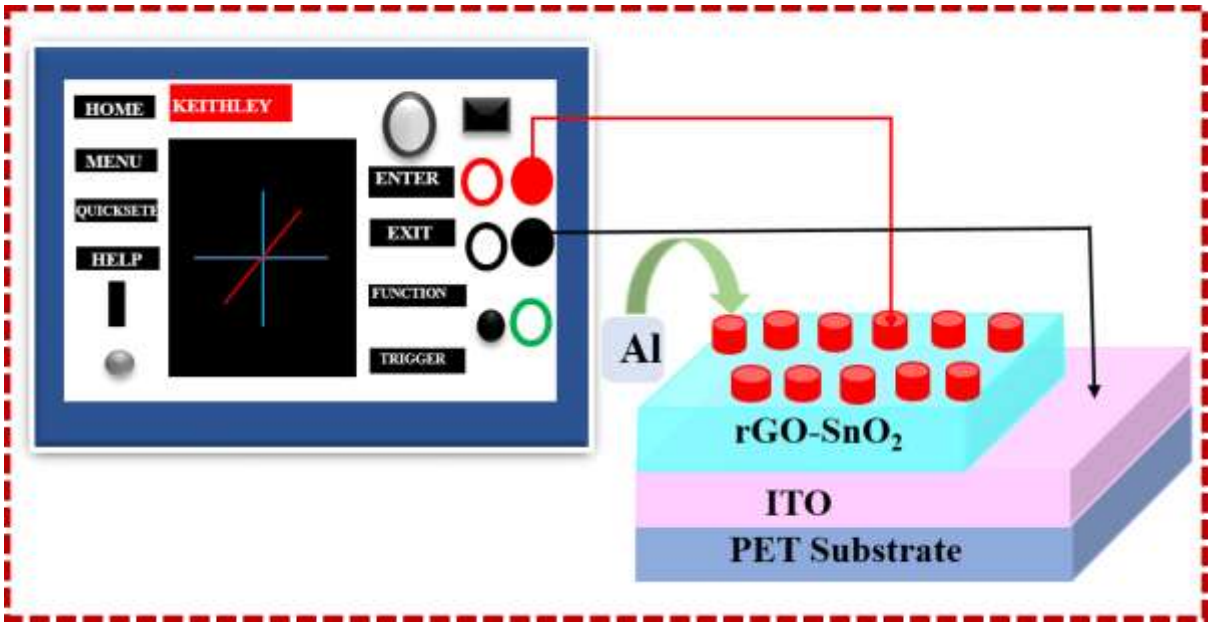

Figure 3.13 Graphical illustration of the Keithley Source meter-based two-probe experimental setup for I-V measurement of Al/SnO_2/ITO PET and Al/rGO-SnO_2/ITO PET (MIM) based devices.

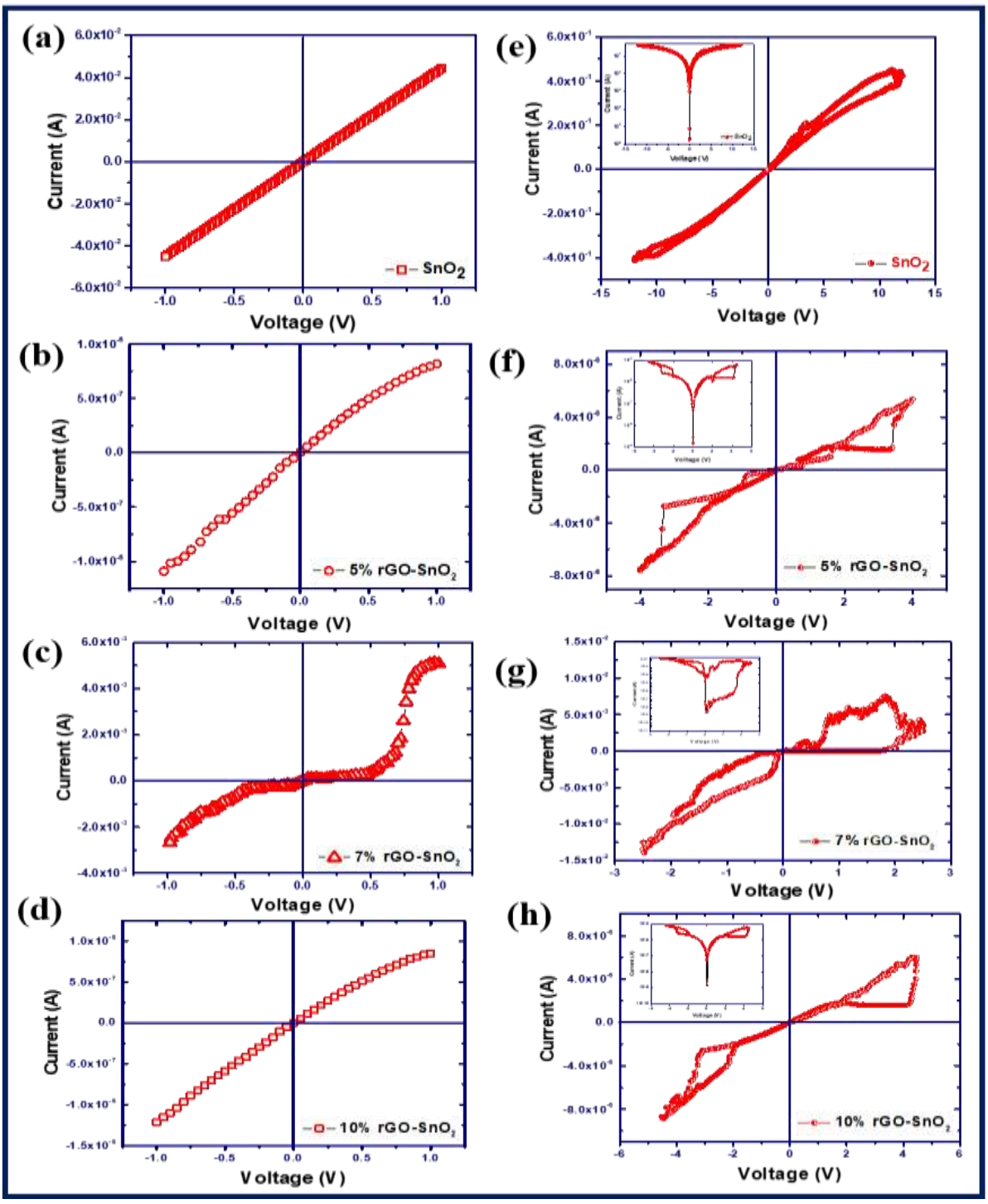

Figure 3.14 (a-d) shows the I-V characteristic and (e-h) The resistive switching properties observed for pure SnO_2, and rGO-SnO_2 nanocomposite. The Inset of resistive switching figures shows the logarithmic I-V curves.

Figures 3.14 (e-h) shows the resistive switching behaviour of all the fabricated memory device. As shown, the device with the rGO-SnO_2 based nanocomposite exhibits behaviour different from the pure SnO_2-based device, demonstrating that there is some interfacial interaction at the

rGO-SnO_2 interface. The voltage is increased further in both directions to see the memory effect. The Al/SnO_2/ITO-PET-based device is known to enter the SET state at 6.2 V. However, when the voltage is raised higher in the same direction, as shown in Figure 3.14(e), from LRS to HRS, there is no change. The reset transition has been observed to take place at -5.1 V because the voltage polarity needs to be reversed for the device to achieve the transition. The device demonstrates bipolar resistive behaviour, as evident from the polarity-dependent built-in switching. The SnO_2-based memory devices have higher switching voltages and lower hysteresis which are not useful for real-world applications. As a result, the device using rGO-SnO_2 nanocomposite as an active layer was investigated further. The various weight percentages of rGO in SnO_2-based devices have been designed and evaluated to understand the impact of 2D rGO in SnO_2 for memory device applications. As demonstrated in Figures 3.14(f-h), all of the rGO-SnO_2 nanocomposite devices exhibited bipolar resistive switching (BRS) characteristics. Additionally, the memory phenomenon with 7 weight percent rGO-SnO_2 based nanocomposite has a higher ON/OFF current ratio, as shown in Figure 3.14g. The HRS to LRS transition appear on the nanocomposite based device at a much lower voltage of 1.8 V, while the LRS to HRS transition occurs at -1.9 V, in comparison to pure SnO_2 based memory device. The device fabricated from rGO-SnO_2 exhibits better resistive switching behaviour. At a read voltage of 1V, the I_{ON}/I_{OFF} ratios for devices based on pure SnO_2, 5%, 7%, and 10% rGO-SnO_2 are 1, 4, 70, and 3, respectively. This demonstrates the hybrid 7%rGO-SnO_2 device exhibits enhanced resistive switching capabilities. The improved resistive switching ratio (I_{ON}/I_{OFF}) in the rGO-SnO_2 based memory device in comparison to pure SnO_2, may be attributed to the interfacial interaction between the rGO and SnO_2 nanoparticles. The materials ability to store charges is correlated with its dielectric constant. A greater dielectric constant in the rGO-SnO_2 nanocomposite enables more charge storage, which may help to extend the memory window. It has been reported in the literature that reduced graphene oxide and metal oxide hybridization greatly influences the oxygen vacancies concentration in the metal oxides [193]. Further, it may be mentioned that the composite formation between graphene oxide and tin oxide also greatly enhances the chemical composition, as shown in the XPS spectra, which also helps in the switching parameter enhancement[194]. Singh et. al reported the dual benefit of rGO based metal oxide nanocomposite for resistive memory application where, it not only acts as oxygen reservoir as well as the blocking layer for preventing the diffusion of oxygen from switching layers, thereby enhancing the switching ratio [174].

For understanding the switching phenomena in Al/7%rGO-SnO_2/ITO-PET, the I-V features of the positive area are displayed on a dual logarithmic scale as displayed in Figure 3.15a. The I-V graph logarithmic scale was resized using the Origin to get Figure 3.15a. At lower voltage ohmic conduction mechanism dominates in the HRS region since the fitted I-V curve for the device in the HRS has a slope of 1.2. According to the ohmic conduction process, the density of inserted charge carriers from metal electrodes is substantially lower at lower voltage areas than the density of thermally induced charge carriers in dielectric materials. The amount of induced or inserted charges from metallic electrodes is determined by the applied voltage and the electrical characteristics of the dielectric or insulator. Because of the long relaxation period, charge carriers generated by metal electrodes rarely travel through the full sample thickness. This is known as the High resistance state (HRS). As we increase the applied voltage, the number of injected charges from the metallic electrode increases. The amount of injected charge carriers becomes greater than the amount of thermally induced charge carriers. Charge carriers that are induced or injected fill all accessible trap sites, resulting in a significant increase in current. Current is proportional to the square of the voltage in this region, and ohmic conduction has been moved to follow space-charge-limited conduction (SCLC). The induced charge carriers flow through the materials once each empty trap site is completely filled. This causes a sharp increase in current through the material [187] (see Figure 3.15a). Then, all of the traps in the active layer of the 7%rGO-SnO_2 material are filled with injected electrons as a result of space-charge-limited conduction (SCLC), and the voltage squared determines the current. Therefore, based on the I-V curves, the slope rises near 2 in the high voltage region. To further confirm this, the Schottky emission model is used to fit the I-V characteristics in the high voltage region, where the log (I) vs. log (V) curve has a slope of 2. This interface-limited conduction mechanism (Schottky emission) may be attributed to the difference in the work function of electrodes and the resulting rGO-SnO_2 nanocomposites and is expressed by the following equation.

$$\text{In I} \propto \sqrt{\frac{e^3}{4\pi\varepsilon_r \varepsilon_0 d}}\ \sqrt{V}/\text{kT} \qquad (3)$$

The Inset of Figure 3.15a shows the linear plot between log (I) vs $V^{1/2}$, thereby indicating the Schottky emission as the dominant charge transport mechanism in the higher voltage region of HRS. The excellent fit of the I-V curve at a higher voltage by the Schottky model indicates that multiple charge transport mechanisms are operational in HRS [195, 196]. Further, in LRS the entire region is fitted with the slope of ohmic conduction is about 1.3. This type of mechanism

is seen in devices where the contact at the junction is ohmic in nature, allowing carriers to enter and move freely inside the insulating layer [197]. When the rate of injecting electrons into a material conduction band is higher than the rate of electron recombination, the SCLC mechanism occurs. Due to electron scattering, this high number of electrons limits the devices current flow. The vacancies in the oxygen within the rGO thin layer may be the cause of the HRS region that includes this SCLC mechanism.

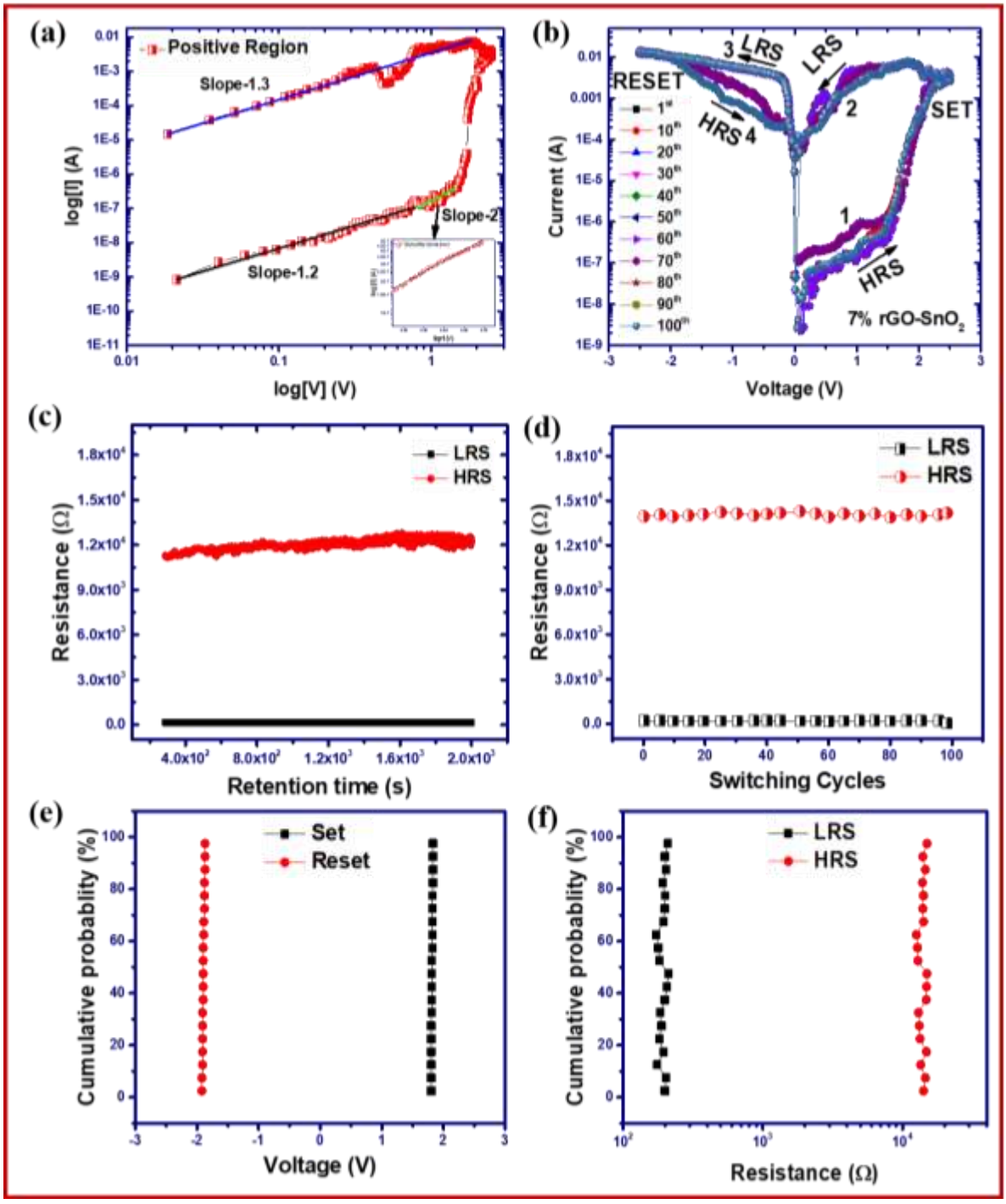

Figure 3.15 (a) Positive LRS, HRS at log-log scale. (b) Demonstrated durability over

approximately 100 switching cycles and (c) sustained resistance in HRS and LRS for roughly 2000 s stipulating robust performance. (d) Endurance performance of the rGO-SnO_2 based device for 100 resistive switching cycles. (e-f) The device-to-device of Vset-Vreset and HRS-LRS cumulative probability distribution of 7%rGO-SnO_2 RRAM devices.

A sequence of endurance tests was conducted to look at the device stability having the highest memory window(Al/7%rGO-SnO_2/ITO-PET). Figure 3.15b illustrates the fact that after 100 cycles, the device performance is still stable. Sweeping voltages of 0 to +3 V and 0 to -3 V, respectively, were applied for the functions of set and reset. The resistance between ON and OFF at ambient temperature was measured with a read voltage of 1 V. According to Figures 3.15(c-d), the memory window of the device, as determined by R_{ON}/R_{OFF}, is 70. These findings show that the Al/7%rGO-SnO_2/ITO-PET device is not degraded even after repeated cycles. These findings support the repeatability and reversibility of the transition between the OFF and ON states. Through a constant resistance ratio of LRS/HRS throughout 100 cycles both HRS and LRS are unaffected at the read voltage of 1 V. The above-mentioned results show that switching between HRS and LRS is improved for the Al/7%rGO-SnO_2/ITO-PET device, and the device performance is consistent and durable. Additionally, we have also looked at the V_{SET}-V_{RESET} and LRS, HRS cumulative probability distributions from device to device for the 7%rGO-SnO_2 RRAM devices, which are shown in Figures 3.15(e) and 3.15(f), respectively. The operation voltages of the device-to-device distribution were calculated using the average of the first 10 cycles of each of the 20 tested devices [198]. For a practical memory application, it is necessary to address the small variation in the RESET process, which can be related to the unpredictability of the filament rupture process. The SET voltage variability varies very little between devices. The fact that the device-to-device LRS and HRS vary very little should be addressed as they demonstrate the fabricated memory devices dependability [199].

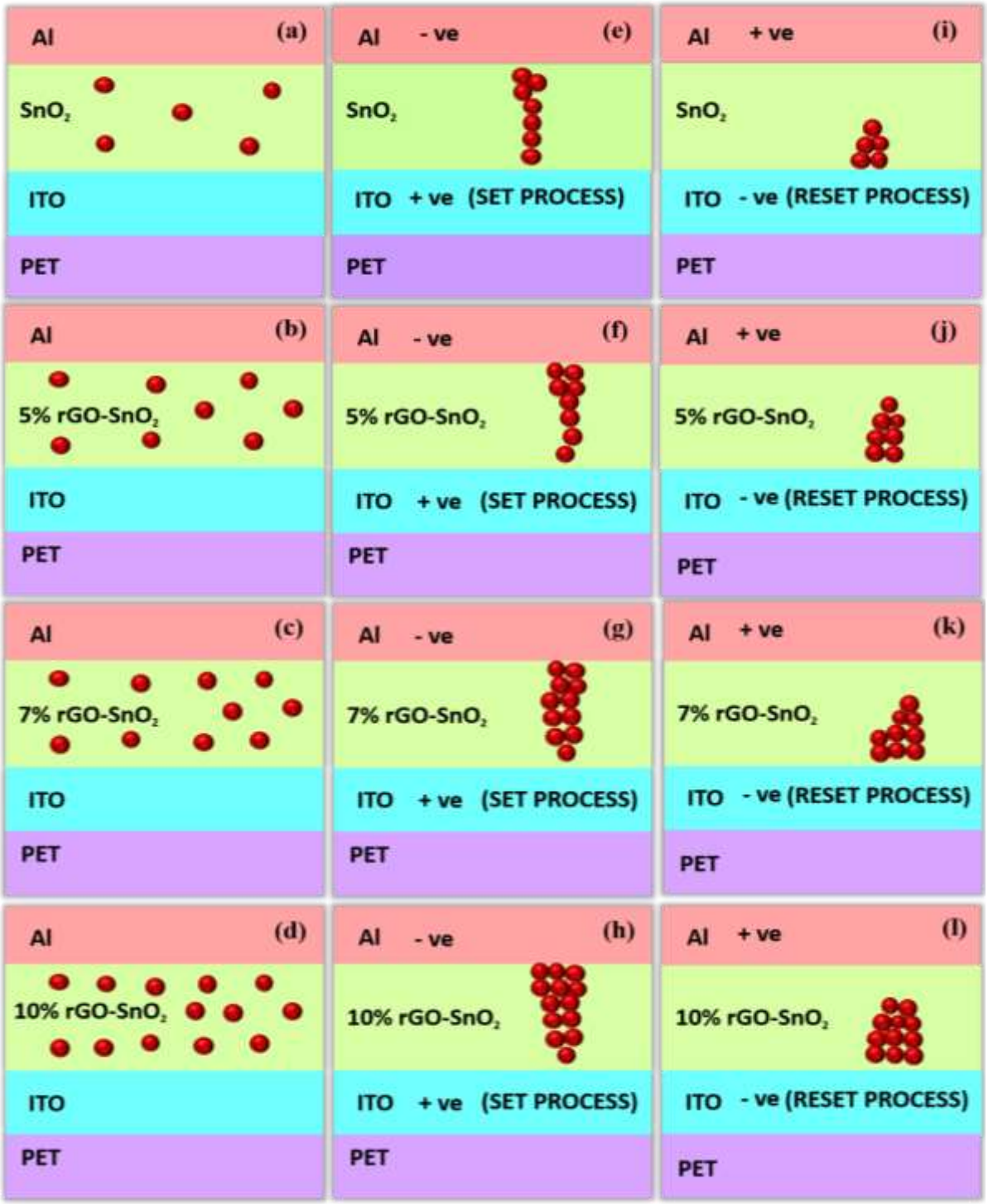

Figure 3.16 Schematic illustration of oxygen vacancy concentration in (a) pure SnO_2 and (b-d) in rGO-SnO_2 samples for different rGO concentrations. (e-h) shows the filament formation and (i-l) The mechanism behind the rupture of filaments responsible for the resistive switching process in a resistive memory device based on rGO-SnO_2.

The presence of oxygen vacancies in pure SnO_2, 5% rGO-SnO_2, 7% rGO-SnO_2, and 10% rGO-SnO_2 layers caused a conducting filament to form when the electric potential was put on the electrodes top and bottom, as illustrated in Figure 3.16. The number of oxygen vacancies in the

insulating layer affects the size and structure of conducting filaments, which is a crucial performance factor for RRAM devices. Because there are less oxygen vacancies in pure SnO_2, a filament will develop at a higher voltage, known as the SET voltage to 6.6 V or the voltage at which the device is working properly. The inclusion of oxygen vacancies is one method that might be used to reduce this operating voltage. In 5% rGO-SnO_2, the addition of rGO decreased the SET voltage to 3.3 V and increased the I_{ON}/I_{OFF} ratio. With continued additions of 7% rGO to SnO_2, the number of oxygen vacancies increased resulting in a decrease in the SET voltage to 1.8 V and an increase in the I_{ON}/I_{OFF} ratio. Furthermore, the device displayed unstable behaviour with additional increases in the concentration of 10% rGO in SnO_2, increasing operating voltage to 4.1 V and decreasing I_{ON}/I_{OFF} ratio. The different routes that electrons can take through the insulating layer to travel between the upper and lower electrodes might be because of the variation in SET voltage. Because there are many oxygen vacancies in the insulating layer, there are various routes available. Based on the creation and breaking of filaments between the electrodes, the mechanisms of LRS and HRS can be explained [200]. Figure 3.16(a) depicts a device with pure SnO_2, while Figures 3.16(b-d) depict devices with various concentrations of rGO indicating the enhancement in the concentration of oxygen vacancies as the rGO weight percentage increases. The oxygen vacancies are aligned between the electrodes and create the filaments [201, 202] as shown in Figure 3.16e under the effect of the applied electric field. As oxygen vacancies are removed from the top electrode surface when the opposite polarity is applied, the filament eventually ruptures, as depicted in Figure 3.16i. The conduction process in devices with various concentrations of rGO is shown in Figures 3.16(b-l). The filament size is determined by the number of oxygen vacancies present in the insulating layer. The filament size increases as the number of oxygen vacancies increases. The current process, which involves a systematic examination of the weight percentage of rGO in the metal oxide-based nanocomposite, has provided a unique way of modifying the switching properties of the resistive memory device, making them acceptable for actual use [203].

3.4 Conclusion

In conclusion, the impact of rGO concentration on resistive switching properties of rGO-SnO_2 based composite film has been investigated by designing the memory device in MIM configuration. Hydrothermal synthesis is used to successfully synthesize the 5%rGO-SnO_2, 7%rGO-SnO_2, and 10%rGO-SnO_2 nanocomposite powder with an average particle size of 5.84, 6.07, and 6.26 nm. The synthesis of rGO-SnO_2 nanocomposite was confirmed by SEM,

XRD, and Raman spectroscopy techniques. The shift in C1s, O1s and Sn 3d peaks in the rGO-SnO_2 nanocomposite in comparison to pure SnO_2 and rGO indicate an interfacial interaction. Dielectric characteristics provide information on the composites microstructure, which consists of a large number of grains and so has enhanced grain boundaries. A large number of grain boundaries and a high concentration of defects helped to improve dielectric characteristics. According to the dielectric measurement, the 7%rGO-SnO_2 nanocomposite had a high dielectric constant and a low loss. How impedance varies with frequency is explained by the decrease in space charge polarisation. The improvement in charge density at high frequencies is the cause of the conductivity rise. Electrical conductivity increased as a result of the charges released by flaws and conduction charge carriers, which also enhanced charge density. Finally, the effects of the rGO in SnO_2 on the resistive switching performance of nanocomposite films were studied by fabricating the device in MIM configuration with Al and ITO-PET as the upper and lower electrodes, respectively, sandwiching an active rGO-SnO_2 memory layer. Reduction in switching parameters, and improvement in the current ratio further confirmed the modified electronic properties in the rGO-SnO_2 nanocomposite-based resistive memory device. Multiple electron transport mechanism responsible for current transport also indicates that SnO_2, rGO, and SnO_2-rGO interface together determine the electrical properties of the device, especially in HRS. However, in LRS the electrical resistance is mostly governed by the oxygen vacancies induced by metallic filaments. The Al/7%rGO-SnO_2/ITO-PET device exhibited switching characteristics with a lower switching voltage and more stability. Additionally, Al/7%rGO-SnO_2/ITO-PET based memory device showed good endurance behaviour up to 100 cycles, higher I_{ON}/I_{OFF} ratio, and retention time, which was measured for this device up to 2×10^3 seconds. The present study's results are useful in comprehending the importance of rGO and its impact on the transport characteristics and structure of the rGO-SnO_2 nanocomposite. Owing to their low losses and current-voltage (I-V) hysteresis loop behaviour, rGO-SnO_2 nanocomposite shows promise in high-frequency electromagnetic devices and resistive random-access memory (ReRAM) applications. The present device with enhanced electrical properties thereby shows potential for the future non-volatile RRAM memory industry.

CHAPTER 4

Effect of MoS_2 weight percentage on the resistive switching performance of the MoS_2-SnO_2 based memristive device.

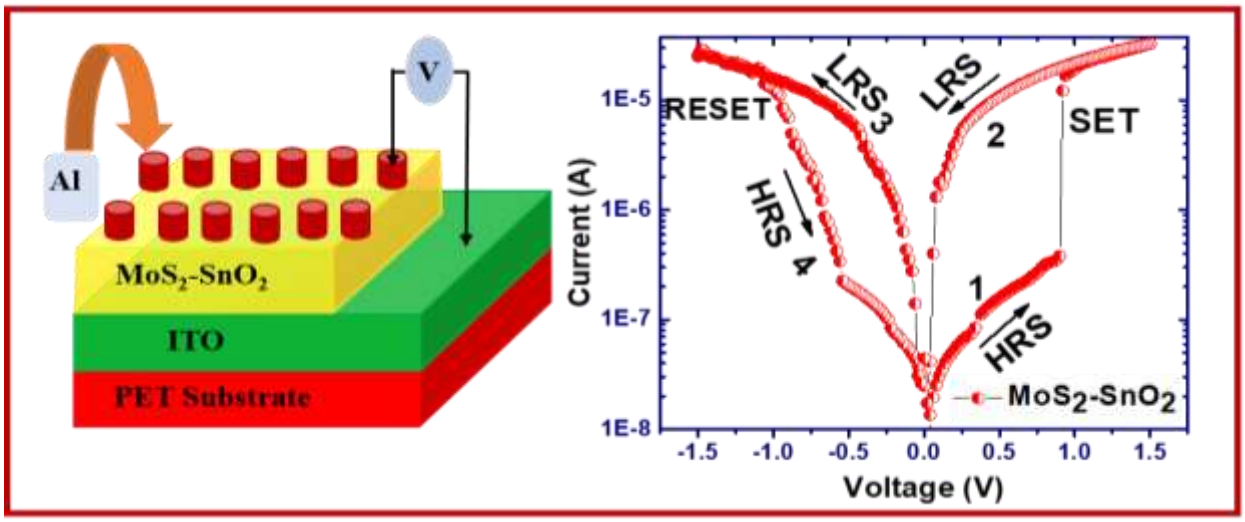

This chapter describes the effect of MoS_2 weight percentage (0, 5, 7, and 10 wt.%) in MoS_2-SnO_2 based nanocomposite in terms of the structural, optical, and electrical properties performance. Several techniques, such as transmission electron microscopy, scanning electron microscopy, UV-visible spectroscopy, and X-ray diffractometer were used to analyse the effect. Further, the effect of structural, optical and compositional changes in the MoS_2-SnO_2 nanocomposites have been utilized to fabricate resistive memory device having improved switching performance. The measured current-voltage (I-V) characteristics of the fabricated devices having different MoS_2 wt. % showed an increase in I_{On}/I_{Off} ratio (3, 100, and 25) with an increase in MoS_2 concentration. Additionally, the endurance and retention tests were conducted to verify the fabricated device cyclic performance and stability. The results showed that the 7%MoS_2-SnO_2 device demonstrated stable performance for up to 100 switching cycles without significant degradation, and that it could maintain the HRS and LRS states for up to 2×10^3 s.

4.1 INTRODUCTION

The demand for new types of memory devices has recently increased due to the popularity of flexible, wearable, foldable, lightweight, and transparent electronic devices like screens, RFID tags, sensors, mobile phones, and watches [199, 204]. The industrial and academic groups are working together to create modern non-volatile memory technology to replace the current flash memory in order to address the issues of huge information storage and memory scalability. A growing number of innovative non-volatile memory technologies are attracting interest, including FeRAM, PCRAM, MRAM, and RRAM are all types of random access memory. Among these, RRAM has undergone significant study in recent years and is now an important competitor to the next generation of non-volatile memories. It is indisputable that flexible electronic devices have also drawn a lot of interest because of their flexibility, wearability, and potential for use in wearable electronics. Flexible electronic gadgets are now more widely used than ever in numerous areas of modern life. However, the primary part of flexible, intelligent electronics is the data storage and processing systems. To address the demands of wearable technology, researchers are dedicated to fabricating flexible non-volatile resistive memory devices also known as mersisters. Flexible mersister arrays used in mersisters-based non-volatile logic-in-memory integrated circuits ensure high-performance parallel computing. To construct artificial neural networks with incredibly low energy needs for neuromorphic computing, flexible mersisters have also been used. This further suggests that the optimized flexible mersisters can be used for various applications, including wearable and aeronautical applications[205, 206]. Photoelectric mersister is going to revolutionize machine vision by integrating sensing, memory, and neuromorphic computing for the development of artificial intelligence applications. The recent decade has seen considerable advancements in mersister material optimization and its performance. Still, the search for an active switching layer that can achieve all of the performance parameters at the same time continues [207]. The basic structure of a mersister is a metal-insulator-metal (MIM) arrangement in sandwich and planar geometry, where an active semiconducting and insulating layer is enclosed between two metal electrodes, and is equivalent to two terminal structures of a synapse. Initially, the mersister is found to be in the high resistance state (HRS) and must first be turned on by using the electroforming voltage, which results in a change of resistance by switching to a low resistance state (LRS). The “low resistance state” and “high resistance state” (HRS) are then alternated by the application of suitable voltage on the mersister. In these devices, switching from the HRS to the LRS is accomplished using the ‘SET’ procedure, and returning is accomplished

using the 'RESET' process [131]. The current that flows in the device during the LRS state should be low enough to reduce the power consumption of the device and therefore require further efforts.

Human society is getting more digitalised, every aspect of our everyday existence is surrounded by data produced by media, social networks, machines, historical archives, etc. The so-called significant data era has unquestionably arrived in the World of humans. Unfortunately, using the most recent technologies to process data is not without its difficulties. Probably the most important is the hardware. A new gadget called the resistive switching (RS) device combines computing and memory functions in a single cell. The discovery of negative differential resistance in binary oxide thin films (SiOx, Al_2O_3, Ta_2O_5, ZrO_2, TiO_2) in the year 1960s led to the beginning of the RS field of study[208]. Starting in 2008, RS devices gained popularity as a research area in academia and business. RS devices have been the subject of several studies on various topics, including physical mechanisms, materials, devices, and circuits. Due to its ability to function under low operating power[209], fast switching speed[210], high scalability[121], and non-destructive readout[211], resistive random-access memory (ReRAM) is regarded as one of the prospective candidates to replace the current flash-based memories. Further, it may be mentioned that in addition to the negative differential resistance-based ReRAM device another aspirant based on the negative capacitance (NC) effect has also gained the attention of the scientific community for reducing issues related to scaling, switching speeds and power consumption of existing electronic devices [212]. It is to be noted that progress in electronics is always limited by power dissipation constraints which need to be addressed. Because they may be used with the current semiconductor production industry, ferroelectric materials based on HfO_2 and ZrO_2 show promise for negative capacitance devices. The NC effect was first reported by Sayeef Salahuddin and Supriyo Datta in 2007 and it means that a change in charge causes the net voltage across a material to change in the opposite direction so that a decrease in voltage leads to an increase in charge which is different from normal capacitor [213]. This NC effect is first reported in ferroelectric materials and is unstable, however, it could be stabilized by connecting the ferroelectric material in series with a standard dielectric capacitor. The capacitance *C* of a parallel-plate capacitor with dielectric material between the plates can be expressed as:[214]

$$C = \varepsilon\left(\frac{A}{d}\right) = \varepsilon_0 \varepsilon_r \left(\frac{A}{d}\right) = \frac{dD}{dE}\left(\frac{A}{d}\right) \quad (1)$$

where ε_0, A, d, D, and E denote vacuum permittivity, plate area, plate separation, electric displacement field, and electric field, respectively. Further for FE materials like HfO_2, the negative capacitance is due to negative permittivity and is expressed as:

$$\varepsilon_0 \varepsilon_r = \frac{dD}{dE} = \varepsilon_0 + \frac{dP}{dE} \approx \frac{dP}{dE} \quad (2)$$

By applying the electric field larger than the coercive field, the polarization state can be changed, and if the polarization occurs opposite to the applied field (dP/dE <0), a negative capacitance state is achieved. The ferroelectric material layer is anchored with a metal-oxide-semiconductor field-effect transistors gate to leverage this effect to fabricate a transistor. A negative capacitance field effects transistor (NC-FET) may potentially produce subthreshold swings below the 60 mV per year thermionic limit and on-current performance equivalent to existing devices with the right design. RAM, or read-only cache. Many semiconductor industries such as GlobalFoundaries, and Samsung have filed patents in the mentioned field [215]. Despite the progress, Negative capacitance has not seen much advancement in the development of useful devices and may be attributed to the unclear mechanism and lack of theoretical and characterization support. However, for the present study, we will only focus on ReRAM devices having more matured physics behind the resistive switching effect.

Further, it has also been observed that binary transition metal oxides, such as HfO_2 [200] are not only favoured materials for negative capacitance effect but have also been explored for ReRAM application as compared to ternary and quaternary oxide semiconductor films due to their ease of fabrication and compatibility with the CMOS industry. However, 2D transition metal dichalcogenides have superseded due to their layered structure, and distinctive physical and mechanical properties. Molybdenum disulfide (MoS_2) one of the members of the transition metal dichalcogenides (TMDs) family, is one of the most suitable materials for researchers[216]. It has been reported for use in transistors, photodetectors[217], lithium batteries[218], hydrogen evolution catalysts[219], and transistors[220], as well as these other devices. MoS_2, which has a layered structure akin to graphite and may be exfoliated to produce single or few-layer nanosheets, is made up of sandwich units made of covalently coupled hexagonal planes of Mo and S atoms linked together by the weak van der Waals attraction[221]. To improve the performance of devices based on MoS_2, researchers are focusing on combining MoS_2 with other promising nanomaterials to create nanocomposites, such as reducing graphene oxide-MoS_2/TiO_2 heterostructures for photocatalytic actives and MoS_2/CdS heterojunction for H_2 evolution under light irradiation[222].

Among the commonly used binary metal oxides, SnO_2 has attracted the interest of numerous scientific groups for various applications, which include gas sensors[223], photo catalysis[224], batteries[225], solar cells[226], etc. In addition to the mentioned applications, the SnO_2 device-based resistive memory has also gained attention due to its simple stoichiometry and crystal structure, which is quick to synthesize than the multinary oxide materials. Recent literature has shown, that SnO_2 can be synthesized in various forms such as nanocrystals, nanowires, nanobelts, etc. Because of their unique size-dependent electrical and mechanical properties, nanocrystals are technologically necessary for ReRAM devices [144]. On the other hand, the resistive switching mechanism has yet to be completely investigated, and further work in changing the switching parameters is required. Hence, one method of variation is to create nanocomposites based on two-dimensional materials such as MoS_2 combined with SnO_2 nanoparticles to improve charge transmission[227]. MoS_2 nanosheets are produced using top-down techniques, including liquid phase exfoliation, mechanical exfoliation, and ball milling, or bottom-up processes, like hydrothermal and chemical vapour deposition (CVD) [228]. The most efficient and straightforward approach for creating MoS_2 nanosheets is liquid-phase exfoliation. The bulk MoS_2 particles are exfoliated into nanosheets using reagents such as N-Methyl-2-pyrrolidone dimethylformamide (DMF), and ethanol. As a result, this thought that using MoS_2 nanosheets alongside SnO_2 nanoparticles will improve the switching performance of SnO_2 has been quite significant and has motivated the present study.

Particularly, MoS_2 is the first and most actively researched transition metal dichalcogenides among the 2-D materials. Its composites have attracted considerable attention due to their strength to withstand mechanical stress, strain, and stretchable conditions, which are essential for a memristive device to be integrated with a flexible and wearable electronic system[229]. The outstanding properties of MoS_2, such as layer-specific surface area, fast electron transport at room temperature, and chemical functionalities, ensure that it can be combined with metal oxide for the fabrication of resistive memory[230]. Additionally, it has been observed that numerous papers are accessible for MoS_2-MO-based nanocomposite for photocatalysis, gas sensors, electrochemical energy storage, etc. Here, we use MoS_2 and SnO_2 to create MoS_2-SnO_2 nanocomposite with various MoS_2 concentrations using an easy one-step hydrothermal approach. MoS_2 nanosheets can firmly attach to the SnO_2 nanoparticle surface in the produced nanocomposite sample. The growth of SnO_2 nanoparticles is somewhat affected by the amount of MoS_2 present. As compared to pure SnO_2, the results demonstrate that the composite samples have better resistive switching performance. The best resistive

switching performance of them all is achieved by 7%MoS_2-SnO_2 nanocomposite-based devices demonstrated in terms of the I-V hysteresis loop, endurance, and retention test. Further, a thorough investigation of the charge transport mechanism to support the resistive switching behaviour was obtained by plotting the I-V characteristics on a log-log scale. The flexibility of the fabricated ReRAM device was manifested by showing that the stable resistive switching results were obtained after bending 100 times repeatedly down to a 10 mm radius. Further, it may be mentioned that up to the best of our knowledge, there is no report available for MoS_2-SnO_2-based nanocomposite for the ReRAM application.

4.2 Experimental

4.2.1 Chemical reagents

The precursors utilized during the synthesis are Ammonium molybdate (99.98%), thiourea (>99.0%), sodium hydroxide (NaOH, 98%), tin (IV) chloride pentahydrate ($SnCl_4.5H_2O$, 98%), and ethanol (C_2H_5OH, 99.9%). Fisher Scientific and Sigma Aldrich supply all the chemicals. There is no need for additional purification because every chemical employed in the synthesis processor is analytically grade pure.

4.2.2 Materials Synthesis

Ammonium molybdate (2.48 g) and thiourea (1.2 g) were first mixed into 72 mL of deionized (DI) water and then stirred for 30 minutes at room temperature to create MoS_2 using a simple hydrothermal method [231]. After properly mixing, the mixture was put into a 100 mL Teflon-lined stainless steel autoclave, which was placed inside the oven to react at 200°C for 24 hours before cooling at ambient temperature. To collect the black precipitates, the product was centrifuged after being rinsed with Di-water and two times ethanol. The MoS_2 powder was then obtained by drying the collected paste for 12 hours at 60°C in a vacuum oven [232].

4.2.3 Synthesis of 5%MoS_2-SnO_2, 7%MoS_2-SnO_2 and 10%MoS_2-SnO_2 nanocomposites:

To synthesize 5%MoS_2-SnO_2, 7%MoS_2-SnO_2, and 10%MoS_2-SnO_2 nanocomposite, synthesized MoS_2 (200 mg, 280 mg, 400mg) with 4 ml DI water ultra-sonicated for 1 hour. $SnCl_4 \cdot 5H_2O$ (2.10 g) and NaOH (1.68g) were added into 80 ml DI-water and magnetically stirred for 2 hours to get a homogenous solution[232]. Then finally, after 2 hours of stirring,

the SnO_2 solution is added to the MoS_2 solution and stirred for 60 minutes. This prepared suspension was put into a 100 ml Teflon-lined autoclave made of stainless steel, shut up, and heated at 180 °C for 18 hours. The product underwent three centrifugal washes with ethanol and three centrifugal washes with di-water. The residue was dried in a vacuum oven at 70°C for 6 hours[233]. Figure 4.1 depicts the two-step mentioned hydrothermal method of MoS_2-SnO_2 nanocomposite.

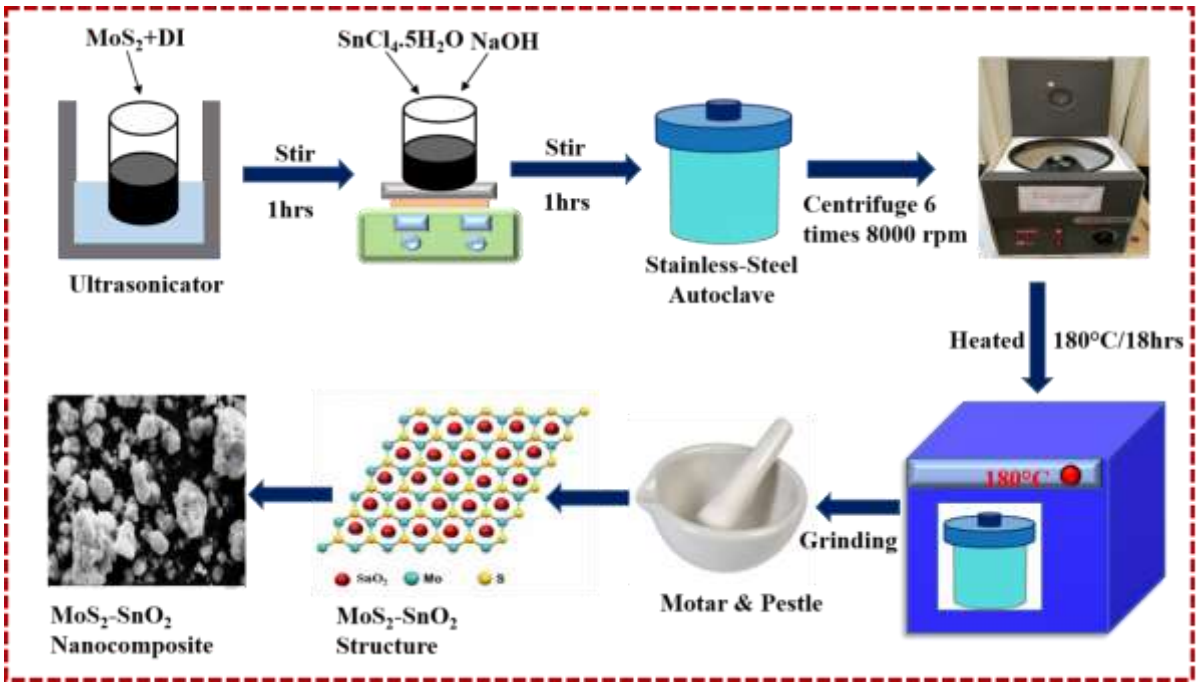

Figure 4.1 A schematic depicts the two-step hydrothermal technique used to prepare the MoS_2-SnO_2 nanocomposite.

4.2.4 Film fabrication

The spin coating method has been used to deposit film, which includes the following steps: (1) ITO-PET substrates were cleaned before ultrasonic use by acetone, ethanol, and deionized water. (2) Using an ultrasonic bath to dissolve 50 mg of MoS_2-SnO_2 in 1.5 ml of ethanol for 30 minutes, four drops of the resulting solution were then deposited onto a piece of ITO-PET glass, which was then spun at 2000 rpm for 60 seconds. (2) For 10 minutes, a hot plate set to 90°C was used to heat the coated sample. We then obtained a film of MoS_2-SnO_2 eight times by repeating this method. Through the use of the thermal evaporation technique and a pressure of 10^{-5} bar, the top aluminum electrode of a thickness of 100 nm was deposited. The schematic illustration for fabrication of different weight percentages of MoS_2, Al/5%MoS_2-SnO_2/PET,

Al/7%MoS_2-SnO_2/PET, and Al/10%MoS_2-SnO_2/PET-based MIM device is shown in Figure 4.2.

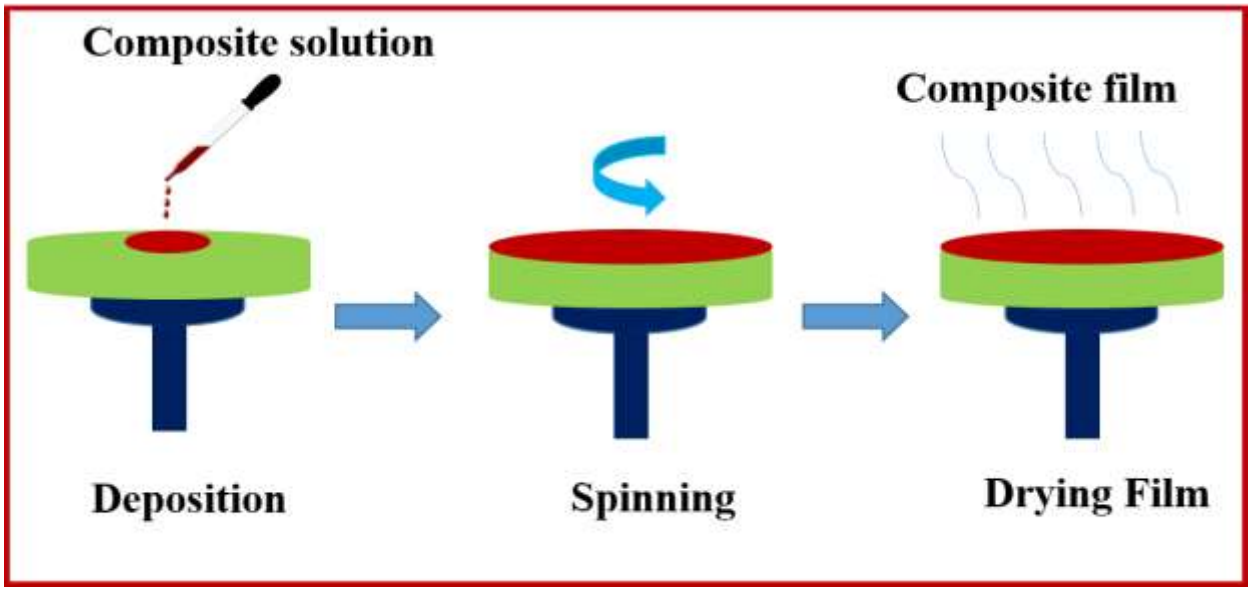

Figure 4.2 A schematic illustration depicts the spin coating procedures used in the fabrication of resistive memory devices.

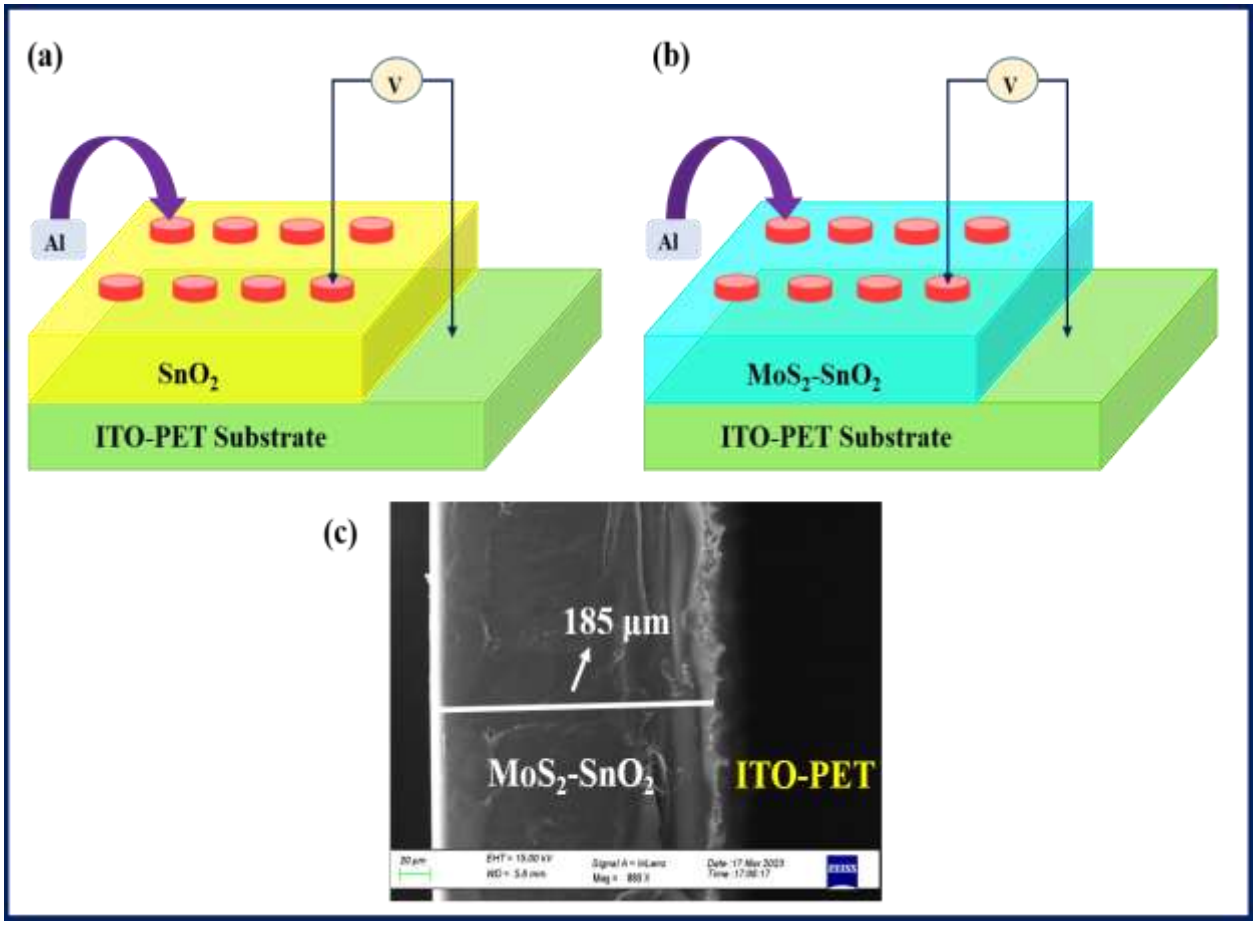

Figure 4.3 A schematic of the (a) AI/SnO_2/ITO PET and (b) AI/MoS_2-SnO_2/ITO PET subtract-based MIM devices is shown. **(c)** Image captured using a cross-sectional FESEM of a MoS_2-SnO_2 nanocomposite layer on a PET substrate covered with ITO.

4.3 Results and discussion

Firstly, the crystal structure of the synthesized samples, MoS_2, SnO_2, and MoS_2-SnO_2 (5%, 7%, 10%) nanocomposites were investigated using an X-ray diffractometer (Bruker D8 Advance) with Cu Kα radiation source (1.54Å). The WiTec alpha 300RA Raman Spectrometer with a laser source of wavelength 530 nm was used to carry out the structural investigations. Additionally, the surface morphologies of the materials synthesised MoS_2, SnO_2, 5%MoS_2-SnO_2, 7%MoS_2-SnO_2, and 10%MoS_2-SnO_2 were observed using a SEM. A Keithley 2450 source meter was used to conduct (I-V) measurements on all fabricated thin film-based memory devices (Al/SnO_2/ITO, Al/MoS_2-SnO_2/ITO).

4.3.1 XRD

The crystal structure, phase purity, and crystallite size of pure MoS_2, pure SnO_2, and MoS_2-SnO_2 (5%, 7%, 10%) nanocomposite are determined using the XRD technique. In Figure 4.4, the XRD spectra of pure MoS_2, SnO_2, and various nanocomposites of MoS_2-SnO_2 (5, 7, and 10 wt. %) confirm the existence of MoS_2 and SnO_2 phases. The XRD results for the SnO_2 sample show diffraction peaks of SnO_2 observed at 2θ diffraction angles of 26.36°, 33.82°, 52.62°, and 65.21°, corresponding to (110), (101), (211), and (301) characteristic planes, respectively, indicating the tetragonal structure of SnO_2[234]. The prominent and sharp diffraction peaks show the remarkable crystallinity of the SnO_2 nanoparticles. Similar to this, the primary MoS_2 diffraction peaks can be seen at 9.2°, 18.3°, 32.5°, 35.18°, 43.4°, and 57.32° which correspond to the (0 0 2), (004), (1 0 0), (101), (103) and (110) crystal planes of MoS_2, respectively[235-237]. The hexagonal MoS_2 phase is responsible for these peaks. Furthermore, the appearance of peaks at 26°, 34°, and 52° that correspond to the (110), (101), and (211) planes in the MoS_2-SnO_2 nanocomposite supports the existence of the tetragonal rutile phase of SnO_2. Because of the poor crystallinity of Mo, the peaks of pure MoS_2 cannot be seen in the case of the MoS_2-SnO_2 nanocomposite, which might be due to the low amount of molybdenum disulfide in the MoS_2-SnO_2 composites as well as the intense peaks of SnO_2. As crystallinity depends on crystallite size, the crystallite size was calculated by using eqn.-3 called the Scherrer's equation [238] for pure MoS_2, pure SnO_2, 5% MoS_2-SnO_2, 7% MoS_2-SnO_2, and 10% MoS_2-SnO_2 nanocomposite [162, 164];

$$D = K\lambda/(\beta\cos\theta) \quad (3)$$

Where λ denotes the wavelength of X-ray, β denotes the broadening of the diffraction peak measured at full-width half maximum intensity (FWHM), θ denotes the angle corresponding to peak position, Crystallite size is D, and k denotes the shape factor (k=0.94). The calculated average crystal size for pure MoS_2, pure SnO_2, 5% MoS_2-SnO_2, 7% MoS_2-SnO_2, and 10% MoS_2-SnO_2 are found to be 6.52 nm, 12.68 nm, 13.4 nm, 12.26 nm, and 10.25 nm respectively. As the concentration of MoS_2 in SnO_2 is very small, therefore to complement the XRD results of nanocomposite formation a highly sensitive Raman technique will be used.

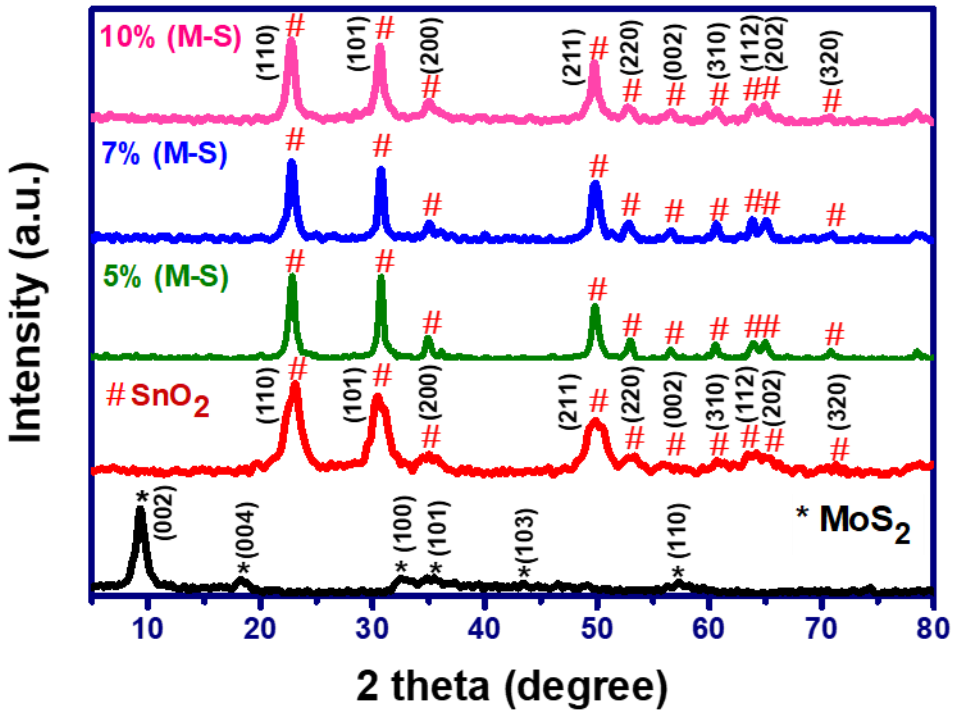

Figure 4.4 XRD graph of pure MoS_2, pure SnO_2, and MoS_2-SnO_2 nanocomposite with a different weight percentage of 5% MoS_2-SnO_2, 7% MoS_2-SnO_2, and 10% MoS_2-SnO_2. The planes corresponding to MoS_2 and SnO_2 have been marked by (*) and (#), respectively.

Table 4.1 XRD analysis of MoS_2, SnO_2, 5%MoS_2-SnO_2, 7%MoS_2-$SnO_2$and 10%MoS_2-SnO_2 nanocomposite.

Sample	Peak Position (2θ)	Planes (*hkl*)	FWHM	Crystal size (nm)	Average crystal size (nm)
SnO_2	26.36	(110)	0.01035	13.76	12.68
	33.82	(101)	0.00887	16.34	
	52.62	(211)	0.00972	15.86	
	65.21	(301)	0.03455	4.77	
MoS_2	9.2	(002)	1.22142	6.52	6.52
5%MoS_2-SnO_2	26.57	(110)	0.68038	11.99	13.40
	34.02	(101)	0.52873	15.71	
	51.84	(211)	0.70678	12.49	
7%MoS_2-SnO_2	26.62	(110)	0.76659	10.64	12.26
	34.03	(101)	0.54595	15.21	
	51.86	(211)	0.80827	10.92	
10%MoS_2-SnO_2	26.56	(110)	0.80695	10.11	10.25
	33.93	(101)	0.81696	10.16	
	51.77	(211)	0.84346	10.46	

4.3.2 Raman Spectroscopy

Since Raman scattering is an effective technique for analysing the composition of MoS_2-based materials, it was used to investigate the formation of MoS_2-SnO_2 nanocomposites in greater detail. Figure 4.5 shows the Raman spectrum of SnO_2 nanoparticles and MoS_2-SnO_2 nanocomposite at different concentrations of MoS_2.The peak of SnO_2 nanoparticles has Raman peaks at 628 cm^{-1} corresponding to the A_{1g} vibration mode[234]. The usual peaks of MoS_2 are principally observed at 380 cm^{-1} and 406 cm^{-1}, which are connected with the E_{2g} phase (opposite vibration of two S atoms about Mo atoms) and the A_{1g} mode, respectively. This is also consistent with the previously reported Raman spectroscopy of MoS_2[239]. Raman spectra of MoS_2-SnO_2 nanocomposite materials exhibit distinctive peaks caused by both MoS_2 and SnO_2 at different MoS_2 concentrations (5, 7, and 10%). For the 5% MoS_2-SnO_2 composite sample, the Raman spectrum is a simple superposition of the single vibration modes of MoS_2 and SnO_2, which is consistent with the literature[240]. The peak positions do not change, however, the peak intensities of the MoS_2 vibration modes E_{2g} and A_{1g} are dramatically reduced, With the increase of MoS_2 content, the peak intensity for the A_{1g} mode of SnO_2 decreases, indicating the successful fabrication of the nanocomposite substance with variable MoS_2 content.

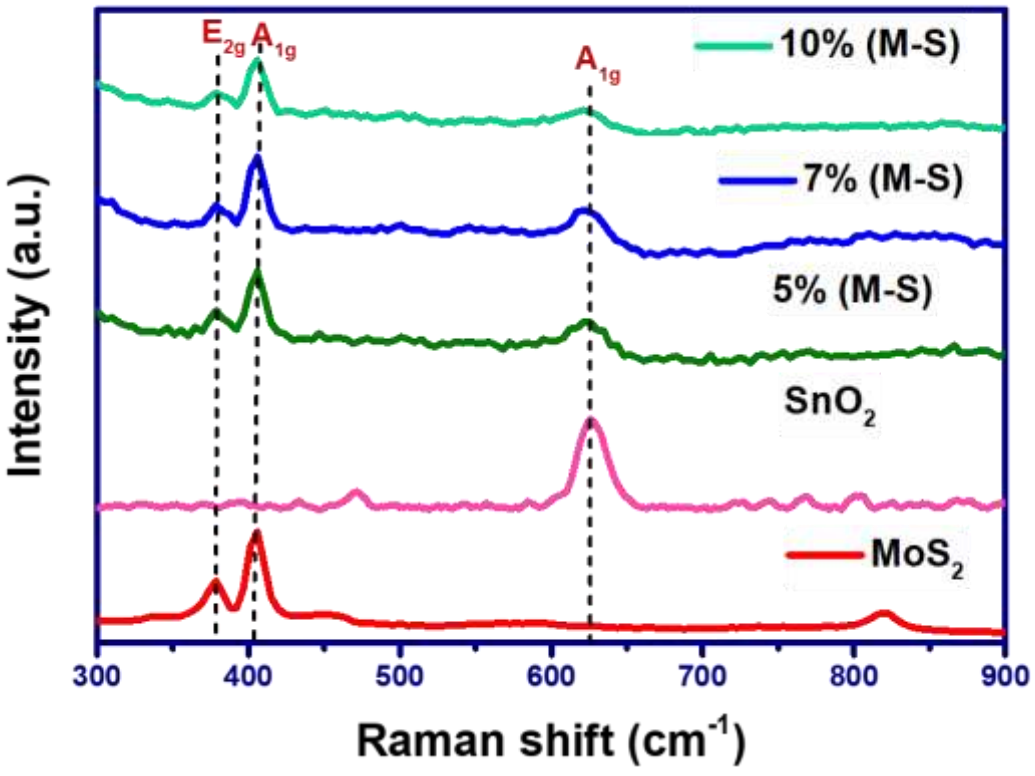

Figure 4.5 Raman spectra of pure MoS_2, pure SnO_2 nanoparticles, 5%MoS_2-SnO_2, 7%MoS_2-SnO_2, and 10%MoS_2-SnO_2 nanocomposites.

4.3.3 UV-visible Spectroscopy

The optical characteristics of the MoS_2, SnO_2, 5%MoS_2-SnO_2, 7%MoS_2-SnO_2, and 10%MoS_2-SnO_2 nanocomposites are examined using the diffuse UV-vis reflection spectrum, as shown in Figure 4.6. SnO_2 mostly absorbs ultraviolet light and has a relatively modest absorption in the visible spectrum (420-700 nm). MoS_2 that has been synthesised is black and does not show any visible absorption edges across the whole spectrum. Consequently, MoS_2 shows considerable absorption intensity over the complete spectrum. The optical characteristics of MoS_2 have carried over to the 5%MoS_2-SnO_2, 7%MoS_2-SnO_2, and 10%MoS_2-SnO_2 composites, which have a substantially higher visible absorption capability. The increase in the optical band gap as the MoS_2 weight percentage is increased from 5 to 10 % may be attributed to overall crystallite size reduction due to the quantum confinement feature of MoS_2 nanoparticles in the synthesized nanocomposites [241]. The results are also supported by XRD-based crystallite size calculation in Table 4.1.

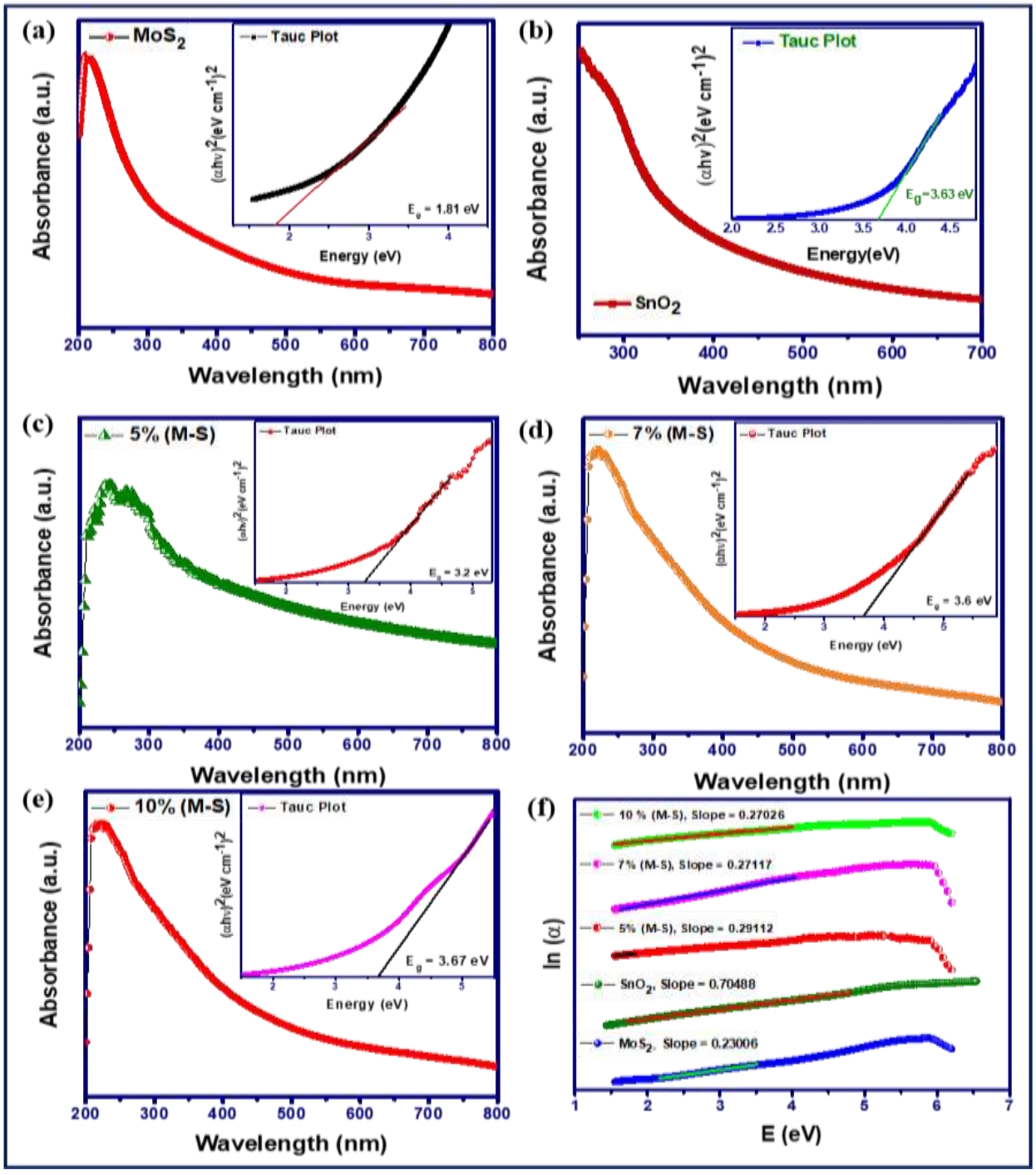

Figure 4.6 UV–vis spectra with optical band energy (E_g) of (a) MoS_2 flakes, (b) SnO_2 nanoparticle, (c) 5%MoS_2-SnO_2, (d) 7%MoS_2-SnO_2 and (e) 10%MoS_2-SnO_2 nanocomposites. (f) Illustration of (lnα) vs photon energy (eV) for MoS_2, SnO_2, 5%MoS_2-SnO_2, 7%MoS_2-SnO_2, and 10%MoS_2-SnO_2 nanocomposites to determine Urbach energy.

The formula below has been used to determine the energy bandgap (Eg) and is given by equation -4[200].

$$(\alpha h\nu) = A(h\text{-}Eg)^{1/2} \quad (4)$$

Where A is a constant, Eg is the bandgap, and α is the absorption coefficient. The optical bandgap for pure SnO_2, pure MoS_2, 5%MoS_2-SnO_2, 7%MoS_2-SnO_2, and 10%MoS_2-SnO_2 nanocomposites were calculated by the plot between $(\alpha h\nu)^2$ vs $h\nu$. According to Table 4.2, the estimated bandgap energies for pure SnO_2, MoS_2, 5%MoS_2-SnO_2, 7%MoS_2-SnO_2, and 10%MoS_2-SnO_2 were 3.63 eV, 1.81 eV, 3.2 eV, 3.6 eV, and 3.67 eV, respectively. Following the addition of MoS_2 to the SnO_2 nanoparticles, the bandgap value rises and the absorption spectra hump continuously shifts to lower wavelengths in the MoS_2-SnO_2 nanocomposites. To further understand the effect of MoS_2 weight percentage in the SnO_2, Urbach energy calculations have been carried which correlate the amount of disorder on the absorption properties shown in Figure 5.6(f). An activated electron from the valence band enters the conduction band bottom when a molecule absorbs a photon and passes through the energy gap. The density of electronic states, tails through the energy difference in the valence and conduction bands, if any disorder in the molecule exists throughout this transition process. [242]. The term "Urbach tail" describes the tail of the density of electronic states that penetrates the energy bandgap [243]. It is frequently interpreted as the width of the band tail caused by localized states linked to material disorder[244]. Equation 5 represents the exponential relationship, referred to as the Urbach rule, between photon energy and absorption coefficient.

$$\alpha = \alpha_0 \times \exp[E/E_u] \quad (5)$$

Here $E = h\nu$ is the energy of the incident photons, and E_u is the Urbach energy in this instance. The calculated value of Urbach energy is given in Table 4.2 and indicates that as we increase the MoS_2 weight percentage from 5 % to 10 % in SnO_2, the Urbach energy shows the enhancement from 3.43 to 3.70 respectively. This small improvement could be explained by the increase in defects caused by oxygen vacancies as an outcome of adding MoS_2. It is possible to assume that the distortion advances with increasing MoS_2 content in the materials since this raises the Urbach energy in the material. The increase in distortion may be brought on by two factors: either the presence of MoS_2 in the system produces oxygen vacancies that raise levels near the conduction band or the presence of MoS_2 in the system distorts the lattice structure [245].

Table 4.2: Calculated optical bandgap and Urbach energy values.

Sample	Bandgap (eV)	Urbach Energy (eV)
SnO_2	3.63 eV	1.41
5% MoS_2-SnO_2	3.2 eV	3.43

7% MoS_2-SnO_2	3.6 eV	3.68
10% MoS_2-SnO_2	3.67 eV	3.70
MoS_2	1.81 eV	4.34

4.3.4 SEM

The morphology of the pure MoS_2, pure SnO_2, 5% MoS_2-SnO_2 (M-S), 7% MoS_2-SnO_2, and 10% MoS_2-SnO_2 nanocomposite was examined using the SEM technique. As seen in Figure 4.7a, layered flakes can be seen on the surface of MoS_2 in the SEM image. Additionally, aggregated MoS_2 sheets are shown randomly. The SEM image of the nanocrystalline SnO_2 is also depicted in Figure 4.7b. It demonstrates the homogeneous and uniform dispersion of SnO_2 nanocrystallites. Additionally, the SEM image of the MoS_2-SnO_2 (5%, 7%, 10%) nanocomposite, as seen in Figures 4.7(c-e), demonstrates that SnO_2 nanoparticles are uniformly adhered to the surface of MoS_2 sheets. It indicates that hydrothermal treatment of MoS_2 and $SnCl_4$ solution is a successful approach for the synthesis of the MoS_2-SnO_2 nanocomposite [160]. Further to check the purity of synthesized nanocomposite powder, the Energy Dispersive X-ray Spectroscopy (EDAX) technique has been used. Figures 4.7(f-j) shows the elemental mapping pictures of Mo, Sn, S, and O elements, respectively of 10 % MoS_2-SnO_2 powder. EDAX spectra shown in Figure 4.7(k) revealed no additional elements, thereby further demonstrating the purity of the produced nanocomposite samples. Figure 4.7(l) shows the corresponding weight percentage and atomic percentage of the different elements in the synthesised powder, which are also tabulated.

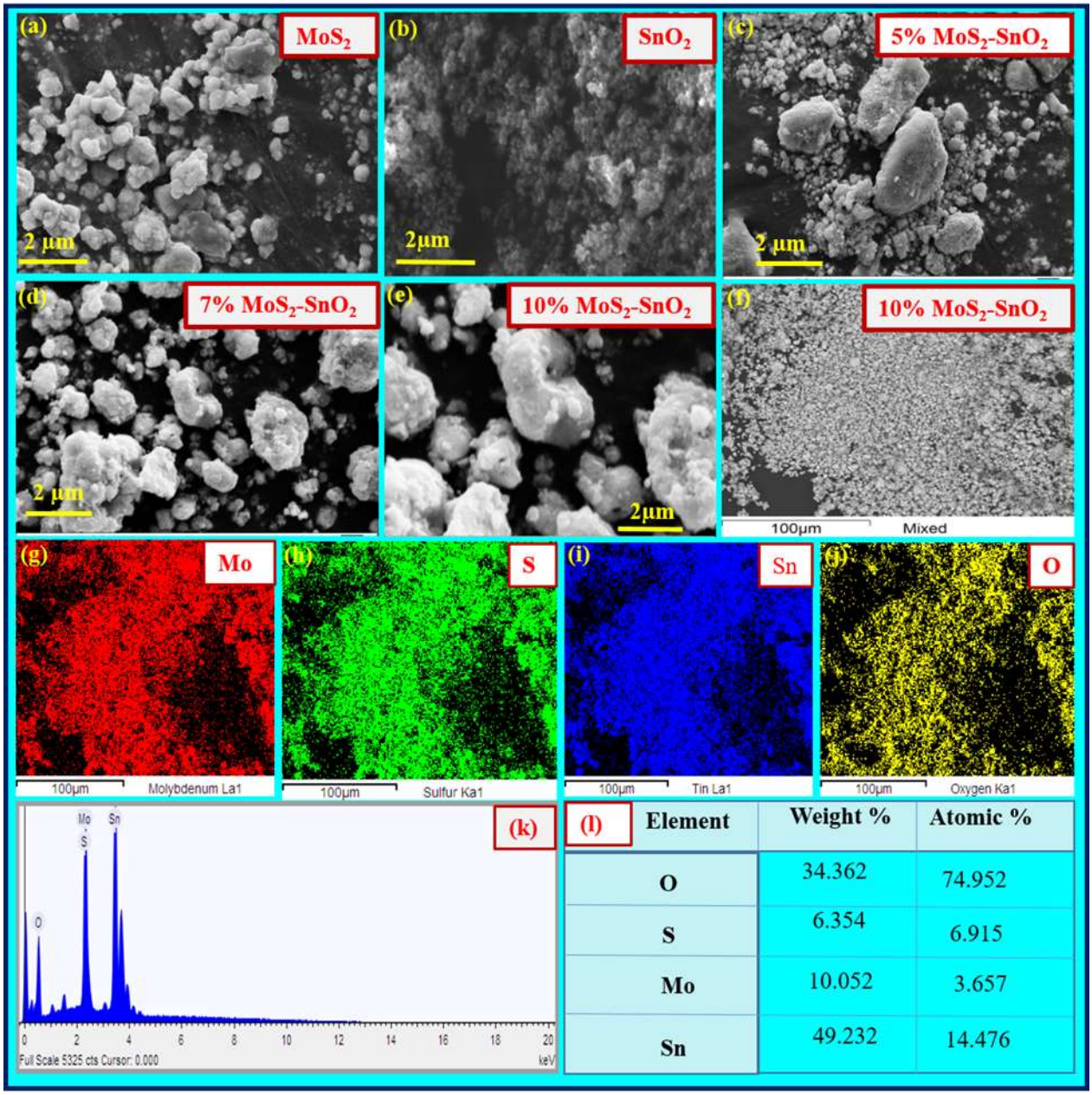

Figure 4.7 SEM micrograph of MoS_2, SnO_2, and MoS_2-SnO_2 nanocomposites: (a) MoS_2, (b) SnO_2, (c) 5% MoS_2-SnO_2, (d) 7% MoS_2-SnO_2 (e) 10% MoS_2-SnO_2 (f-j) elemental mapping and (k-l) EDX spectra of the synthesized 10% MoS_2-SnO_2 nanocomposite showing the purity of the synthesized powder.

4.3.5 TEM

TEM and HRTEM were used to describe the morphology of the synthesised nanocomposite powders and determine lattice spacing, respectively. Figure 4.8a shows the TEM image of synthesized MoS_2 flakes with a calculated lattice spacing of 0.68 nm by the HRTEM image of Figure 4.8b. Furthermore, the planes of the hexagonal MoS_2 structure can be indexed to the

SAED pattern shown in Figure 4.8c. The morphology of SnO_2 nanoparticles is depicted in Figure 4.8d, which makes the nanoparticles spherical shape abundantly obvious. The fact that SnO_2 nanoparticles can be seen, yet the identified particles from Figure 4.8d are agglomerated and incoherently clustered. Figure 4.8e predicts the lattice spacing of 0.36 nm in size corresponding to the (110) plane of the tetragonal SnO_2 phase[246]. The two prominent diffraction peaks of standard SnO_2 identified in the XRD investigation correlate to two crystal faces identified in the HRTEM images as (110) and (101), respectively. The SAED rings in Figure 4.8f have been indexed with respect to the planes of the tetragonal rutile SnO_2 structure[247]. As shown in Figure 4.8g, the morphological image of the MoS_2-SnO_2 nanocomposite contains both SnO_2 nanoparticles and MoS_2 nanosheets, with SnO_2 nanoparticles appearing to have uniformly stuck to MoS_2 surfaces. The fact that these observations and the SEM images are in strong agreement should be noted. In Figure 4.8h, HRTEM images of MoS_2-SnO_2 lattice fringes can be observed in all their detail. According to Figure 4.8i, the fringe spacing for the SnO_2 (1 1 0) crystal plane and MoS_2 (0 0 2) crystal plane, respectively, is 0.33 nm and 0.62 nm. It demonstrates how MoS_2 and SnO_2 are joined to form nanocomposite powder with improved properties [233, 248, 249].

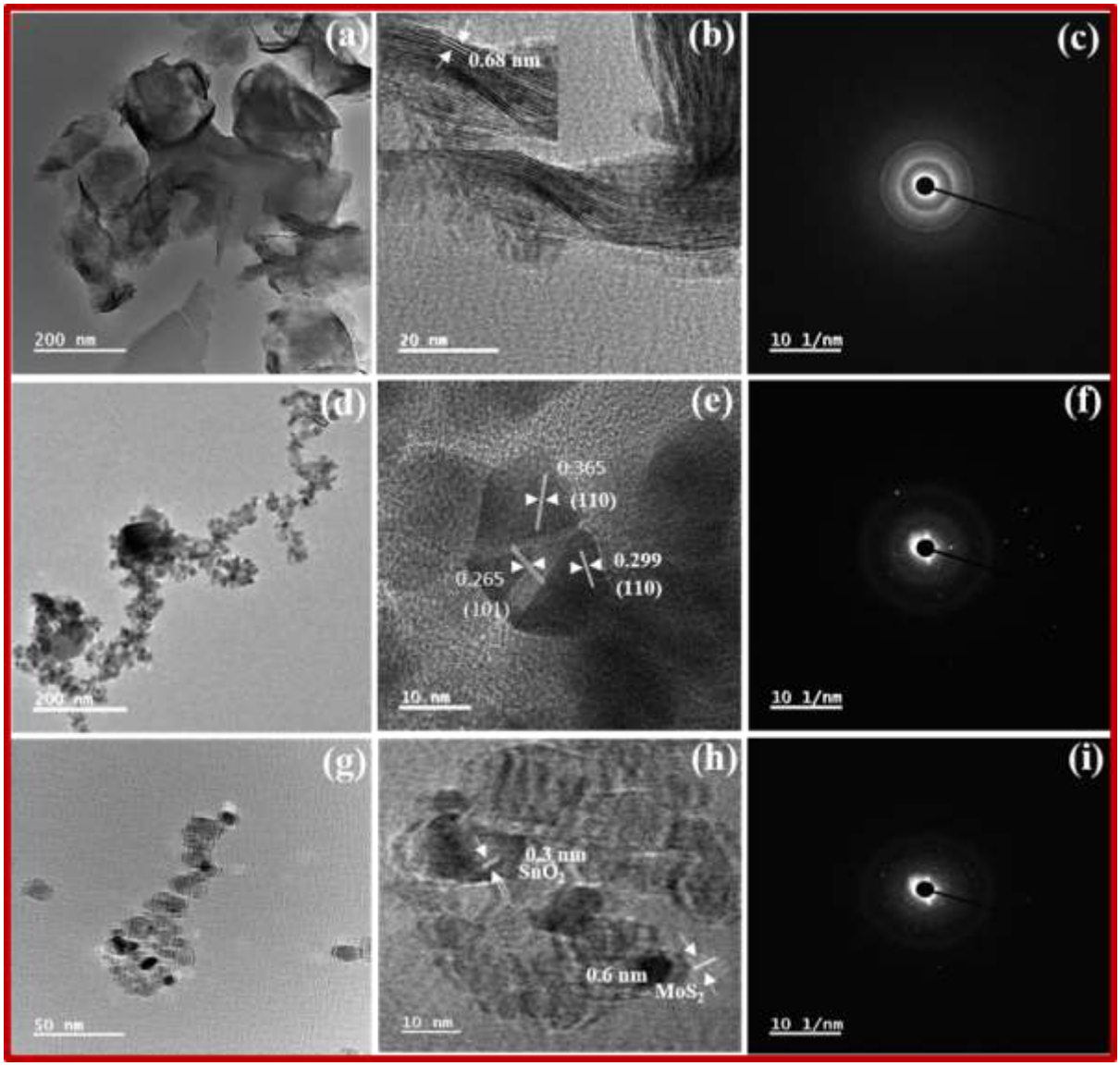

Figure 4.8 Displays TEM images of (a) Flakes of MoS_2 nanosheets, (b) the distance between two layers in MoS_2 nanosheets, (c) the SAED pattern of MoS_2 nanosheets, (d, e) as-synthesized SnO_2 nanosheets, (f) the SAED pattern of SnO_2 nanoparticles, and (g) hybrid MoS_2-SnO_2. HRTEM images of (h) MoS_2-SnO_2 and (i) the SAED pattern of the MoS_2-SnO_2 nanocomposite.

4.3.6 XPS

Figure 4.9 shows, hydrothermally synthesized MoS_2, SnO_2, and MoS_2-SnO_2 nanocomposites were examined using XPS to ascertain their composition, purity, and oxidation states. The survey spectra shown in Figure 4.10 validate the presence of Mo, S, Sn, and O without any additional impurities. Further, the high-resolution spectrum of Mo 3d, S 2p, Sn 3d, and O1s are shown in Figure 4.10.

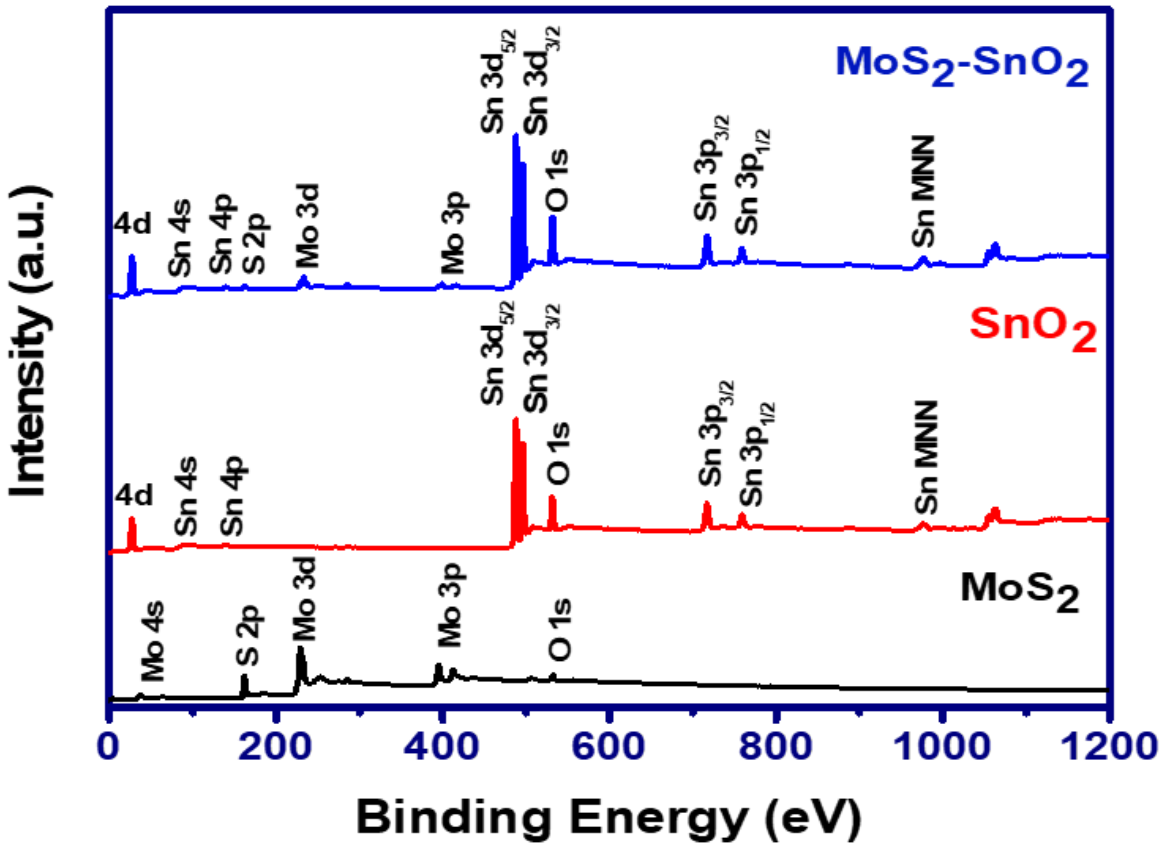

Figure. 4.9 XPS survey spectra with prominent peaks of Mo, S, Sn, O1s, and Sn3d for Pure MoS_2, SnO_2, and MoS_2-SnO_2 nanocomposite powder.

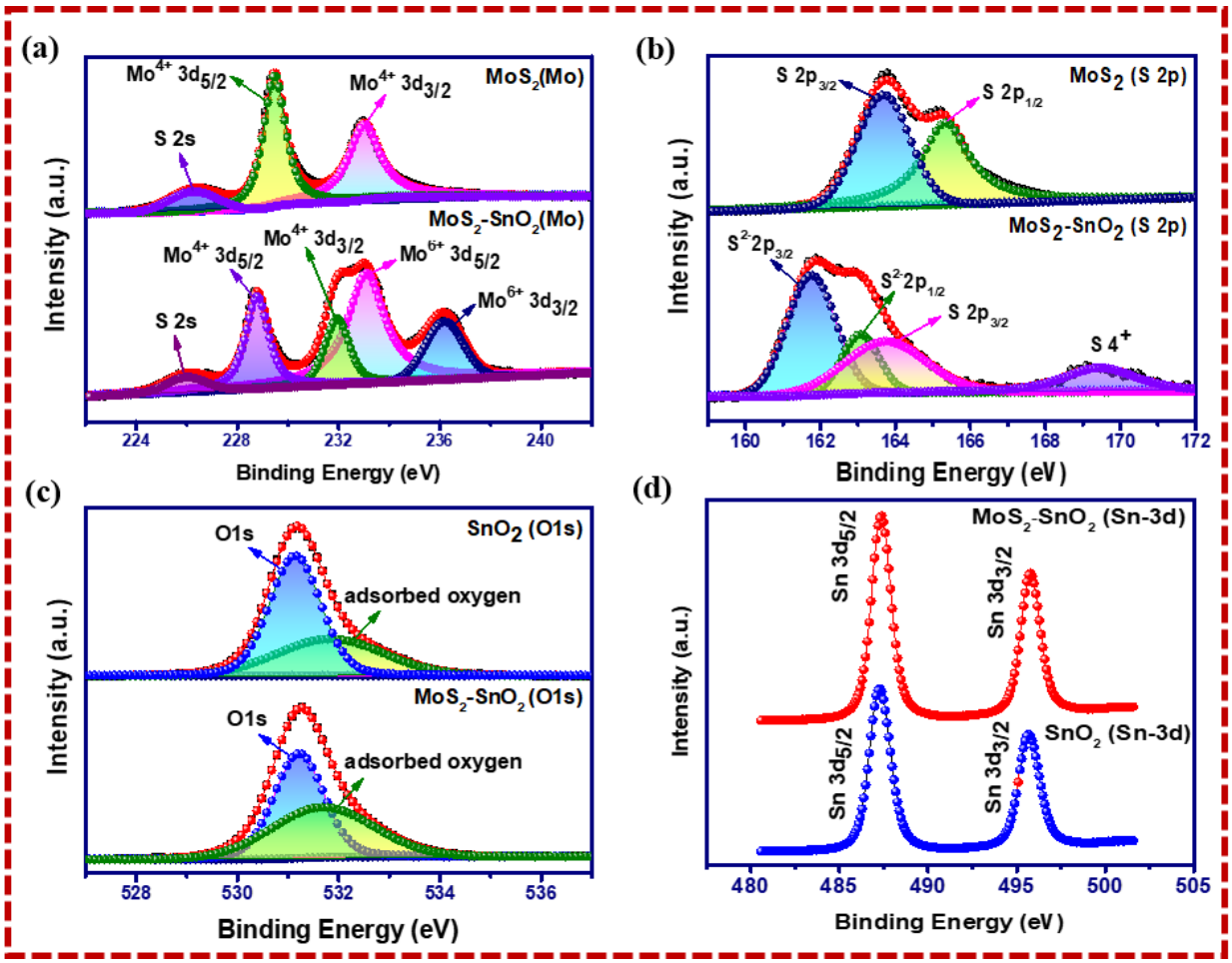

Figure. 4.10 High-resolution core-level XPS spectra: (a) Mo3d; (b) S 2p; (c) O1s (d) Sn 3d

Mo Spectra

Figure 4.10a shows the Mo 3d core level spectra for pure MoS_2 and MoS_2-SnO_2 nanocomposite, where Mo (3d) peaks were de-convoluted into different spin-orbit doublet sets. Peaks at 228.6 eV and 231.8 eV correspond to $Mo^{4+}(3d_{5/2})$ and $Mo^{4+}(3d_{3/2})$ binding energies, respectively, and are consistent with previously published values [231, 250] and indicate the formation of Mo-S bonds[251, 252]. There is also a modest absorption shoulder at 225.8 eV, which corresponds to the S (2 s) electrons binding energy[231, 253, 254]. In the case of MoS_2-SnO_2 nanocomposite powder, the majority of the Mo signal comes from the peaks at around 229.2 and 232.2 eV, which correspond to Mo^{4+} $3d_{5/2}$ and Mo^{4+} $3d_{3/2}$ of 2H-MoS_2, respectively[233]. Mo^{6+} is responsible for the peaks at 233.2 and 235.8 eV, which may be attributed to the partial oxidation of MoS_2 in the air to generate MoO_3 or MoO_4, or MoS_2-SnO_2 interfacial interaction [255, 256].

S (2p) Spectra

The S2p core level spectra for MoS_2 and MoS_2-SnO_2 nanocomposite are shown in Figure 4.10b. The core level spectra revealed two spin-orbit doublets in the sulphur. When divalent sulphide ions are present in MoS_2 nanosheets, they create characteristic peaks at 161.5 eV and 162.9 eV, which correspond to the binding energies of S $2p_{3/2}$ and S $2p_{1/2}$, respectively[131]. The deconvolution of S 2p (MoS_2-SnO_2) spectra yielded four primary peaks at 161.7, 163.08, 163.8, and 169.4 eV (Figure 4.10b). The first two have been assigned to $S^{2-}2p_{3/2}$ and $S^{2-}2p_{1/2}$ of 2H-MoS_2, respectively[248]. The latter two, which have more considerable binding energies, validate the Mo +6 oxidation state.

Oxygen Spectra

As displayed in Figure 4.10c, the O1s core level spectra were de-convoluted into two peaks. For pure SnO_2 the peak at the binding energy position of 531.18eV is attributed to tetravalent Sn ions in the O vault, given the information of lattice O. Another peak at 532.08 eV indicates that the surface is surrounded by hydroxide OH groups and is nonlattice[173]. Furthermore, the case of MoS_2-SnO_2 shows two peaks at 531.18 and 531.78 eV in the O 1s spectra that are shifted towards a lower binding energy side. It is likely that Mo from MoS_2 and the oxygen species from SnO_2 interacted at the interface, as evidenced by the opposite direction shift in binding energy position for the O1s and Mo 3d peak [257].

Tin Spectra

The results of the Sn 3d states of the SnO_2 and MoS_2-SnO_2 composite samples are given in Figure 4.10d. In the case of pure SnO_2, two characteristic peaks of $Sn3d_{5/2}$ and $Sn3d_{3/2}$ are observed at 484.5 and 493 eV, respectively, which correspond to the typical oxidized form of Sn^{4+} [175, 258]. While the XPS peaks in the MoS_2-SnO_2 nanocomposite Sn 3d spectra are found at 487.2 eV, and 495.6 eV, respectively, they exhibit a more significant Sn $3d_{5/2}$ and Sn $3d_{3/2}$ peaks had binding energy shifts of 2.7 eV and 2.6 eV, respectively. From peak to peak separation between the SnO_2 characteristic peaks is 8.4 eV, consistent with earlier observations. The above-observed shift indicates that the SnO_2 nanoparticles are connected to the MoS_2 nanosheets, and have also been confirmed in the literature[176]. It was essential for enhancing resistive switching performance to have a strong interaction between SnO_2 and MoS_2, as evidenced by the creation of the Sn-O connection between the two materials. The MoS_2-SnO_2, Sn 3d peaks are consequently shifted to the region of increased binding energy. Because SnO_2 has a smaller work function than MoS_2, the electrons in MoS_2-SnO_2 hybrids can generally flow (SnO_2 to MoS_2)[178, 200]. Due to this, the MoS_2-SnO_2 Sn3d peaks have been shifted to take

higher binding energies. The shift in the Sn electronic orbit will have an impact on the binding energy of O1s [179]. Interestingly, the corresponding peaks of S 2p, Mo 3d, and Sn 3d change positively when the synthesized MoS_2-SnO_2 nanocomposite while the peaks of O1s move negatively, showing a substantial interaction between SnO_2 and MoS_2. The XPS outcome also demonstrates the close agglomeration of ultrafine MoS_2 flakes on the SnO_2 surfaces.

4.3.7 Dielectric properties

The real (ε'_r) and imaginary (ε''_r) components of the dielectric constant, or electric permittivity, are shown to vary with frequency in Figures 4.11(a) and (b). The real (ε'_r) and imaginary (ε''_r) components of the dielectric constant, or electric permittivity, are shown to vary with frequency in Figures 4.11(a) and (b). On the basis of the Maxwell-Wagner model, it can be seen that ε'_r decreases with increasing frequency of applied field for all samples [181]. A large value of ε'_r is observed in the low-frequency zone as a result of oscillating nano-dipoles being easily oriented in the direction of the applied electric field due to space charge polarisation. At low frequencies, dipoles take a while to reach the grain boundaries, where the buildup of charge carriers causes a noticeable polarisation. The charge carriers can't align with the rapid changes in field direction at high frequencies. As a result, carriers are unable to reach the grain boundaries, and as a result, no polarisations occur [182]. Due to the fact that composites have a larger surface area due to their small size (more grains), the dielectric constant in composites is higher than in pure SnO_2 and MoS_2[183].

Energy is lost in the dielectric system through a process known as dielectric loss ($\tan\delta$). The dielectric loss for MoS_2, SnO_2, and 10%MoS_2-SnO_2 nanocomposite at room temperature is shown in Figure 4.11c as a function of the frequency range of 10-10^6 Hz. Dielectric loss happens if the charge carriers in a dielectric media are unable to keep up with changes in the electric field. It is discovered that when the applied field frequency rises, dielectric losses for all samples decrease. Inhibition of domain walls causes magnetization to be forced to shift rotation, and lower dielectric losses are observed at higher frequencies. The lower values at higher frequencies may also be an indication of Maxwell-Wagner relaxation. Figure 4.11c shows that the larger dielectric loss occurs at lower frequencies. This is caused by space charge polarisation, which can be explained by the Shockley-Read mechanism [184]. The dielectric loss $\tan\delta$ of pure MoS_2 and SnO_2 is discovered to be considerably lower than that of the MoS_2-SnO_2 composite [259]. The increase in dielectric loss in the case of the MoS_2-SnO_2

nanocomposite may result from a significant leakage current caused by the direct connection of MoS_2 sheets above the percolation threshold [185].

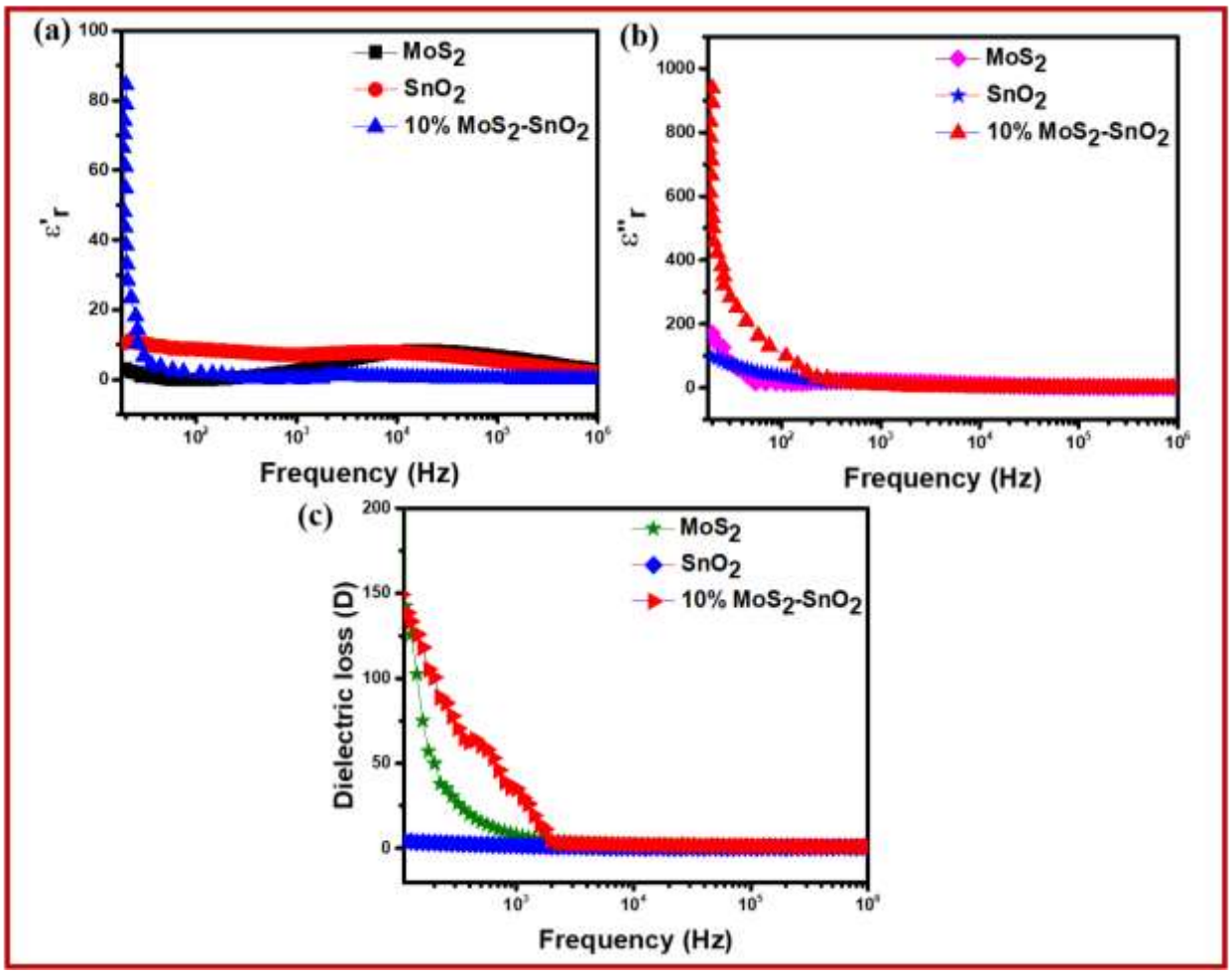

Figure 4.11 Variation of dielectric constant (a) real and (b) imaginary part and Fig (c) dielectric loss for the pure MoS_2, SnO_2, and 10%MoS_2-SnO_2 nanocomposite as a function of the frequency

In the high-frequency region, it is discovered that the variation of the dielectric constant (ε'_r) with the frequency of the MoS_2, SnO_2, and 10%MoS_2-SnO_2 samples follows the Cole-Cole relaxation. The following relation was used to fit the experimental ε'_r vs. f curve in the frequency range between 20 and 1.0×10^6 Hz.

$$\varepsilon'(\omega) = \varepsilon'_\infty + [(\varepsilon'_s - \varepsilon'_\infty)/(1+(i\omega\tau)^{1-\alpha})] \quad (6)$$

where ω indicates the angular frequency, τ the mean relaxation time, α the spread, and ε' specifies the real component of the dielectric constant. ε'_∞ means the value at the largest

frequency, ε'_s the value at the smallest frequency. Figure 4.12 shows experimental data with a Cole-Cole-fitted curve of MoS_2, SnO_2, and 10%MoS_2-SnO_2 samples. Table 4.3 demonstrates the values of α and τ for the MoS_2, SnO_2, and 10%MoS_2-SnO_2 samples derived from the Cole-Cole fitting [186, 187].

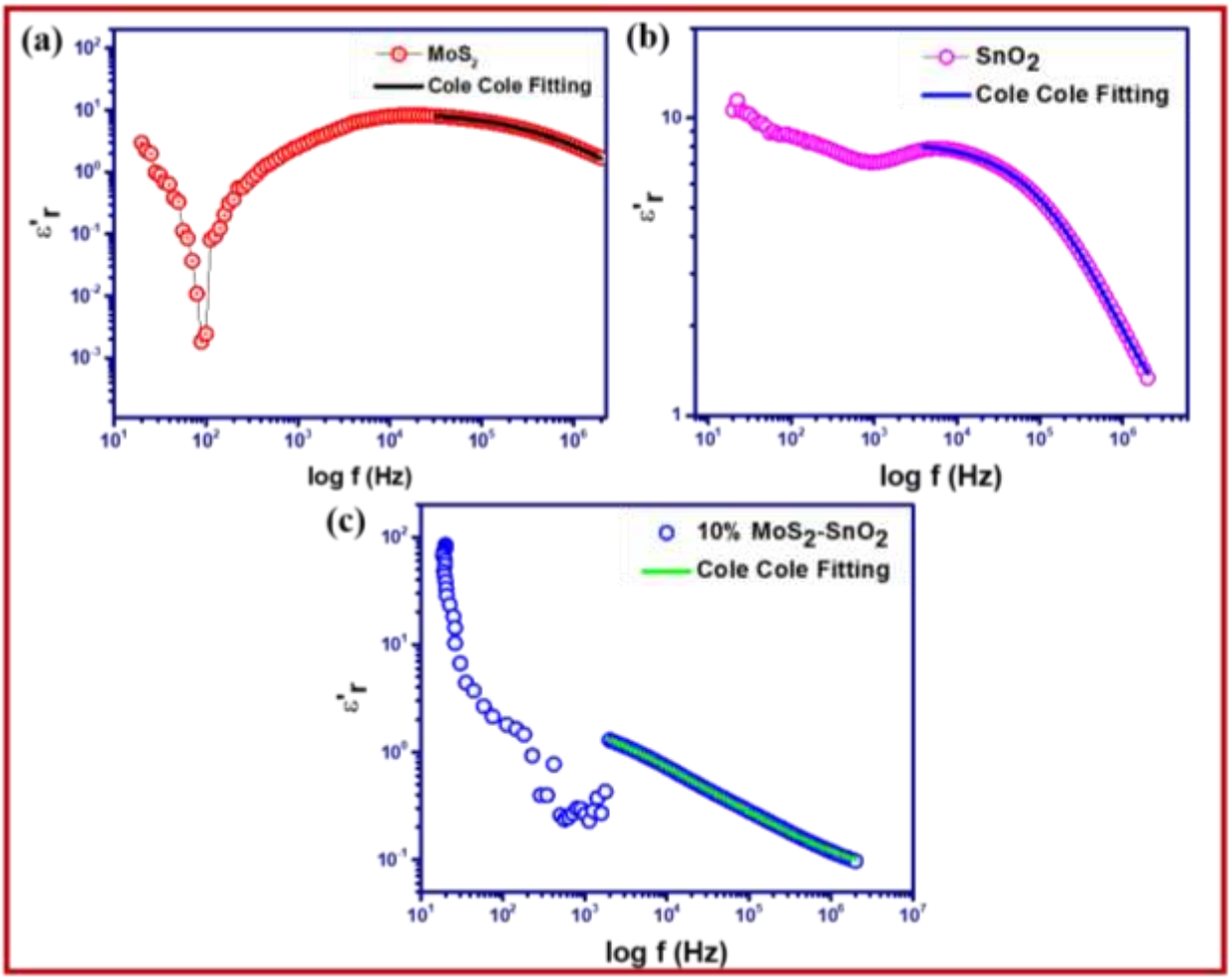

Figure 4.12 (a) MoS_2, (b) SnO_2, and (c) 10%MoS_2-SnO_2 nanocomposite were fitted using a Cole-Cole fit to measure the frequency dependence of the dielectric constant (real part).

4.3.8 Impedance spectroscopy

To examine various electrical features, such as the impact of grain and grain boundaries on the total impedance, relaxation time distribution, and kind of relaxation mechanism[180], one can analyse the complex behaviour of total impedance with frequency. The following formula can be used to represent the total complex impedance:

$$Z^* = Z' + jZ'' \tag{7}$$

Where the total impedance real (Z') and imaginary (Z'') components are given by equation -8

$$Z' = Z\times\cos\theta \text{ and } Z'' = Z\times\sin\theta \quad (8)$$

In this case, Z represents a total measured impedance for θ, which is the measured phase angle (in radians). Figures 4.13(a-b) illustrate how the frequency of the supplied field affects both the resistive, or real component (Z'), and its capacitive, or imaginary part. At lower frequencies, the impedance values are high, and they decrease as the frequency increases. Impedance has lowered due to the dissipation of stationary charges and the enhanced mobility with increasing frequency. At higher frequencies, there is a tendency for all the curves to merge due to a decrease in space charge and the cancellation of the dipole orientation effect [180]. At room temperature, Nyquist plots were utilised to separate the effects of the grains and grain boundary, as shown in Figure 4.13(c). Conducting grain boundaries is important at higher frequencies in MoS_2, SnO_2, and 10%MoS_2-SnO_2 nanocomposite materials, while resistive grain boundaries dominate at low frequencies. At low frequencies, the semicircle indicates highly resistant grain boundaries. The conducting grains produce the semi-circle at high frequency and low resistance value. In our situation, all of the samples display just one semicircle, which is caused by the contribution of the grain boundaries [185], as seen in Figure 4.13c. Due to their higher resistance than the grain itself, grain boundaries are thought to play a significant role in impedance [188]. Due to the high conductivity of MoS_2, it is evident that the MoS_2-SnO_2 nanocomposite has lower resistance than SnO_2.

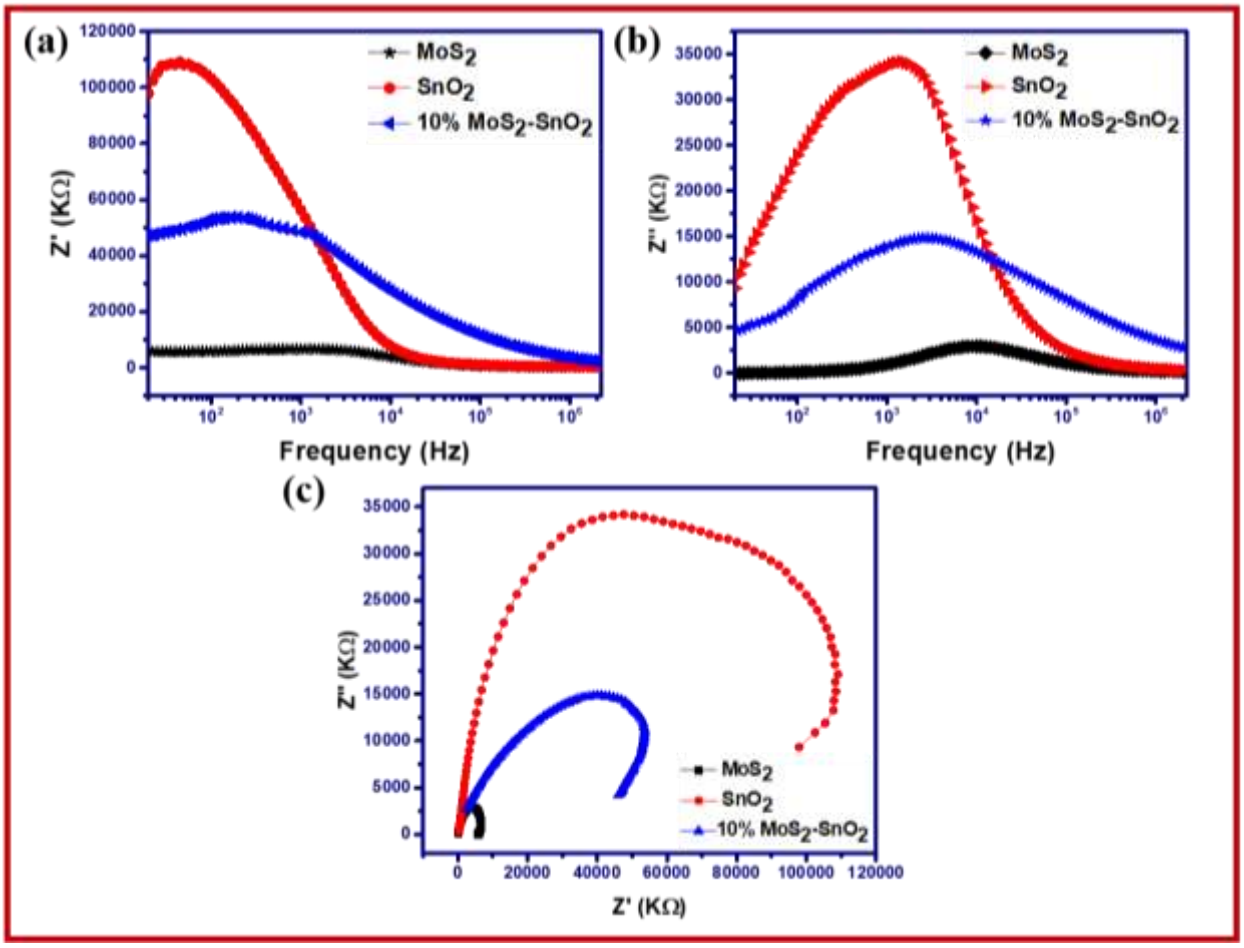

Figure 4.13 Variation of impedance (a) real and (b) imaginary parts of impedance as a function of frequency (10-10^6 Hz) for the MoS_2, SnO_2, and 10%MoS_2-SnO_2 nanocomposite powder. (c) Nyquist plot of MoS_2, SnO_2, and 10%MoS_2-SnO_2 nanocomposite samples.

4.3.9 AC conductivity

In order to examine the conduction process in synthesised MoS_2, SnO_2, and 10%MoS_2-SnO_2 nanocomposite samples, room-temperature frequency-dependent AC conductivity within the 10-10^6 Hz frequency range has been studied. The a.c. conductivity determined by applying the formula $\sigma(\omega) = \omega\varepsilon_0\varepsilon_r\tan\delta$ is shown in Figure 4.14(a). It demonstrates that conductivity increases with frequency, supporting the involvement of bound charge carriers and illuminating the behaviour of substantial frequency dependence. The carriers are able to hop for longer periods of time at lower frequencies, which leads to long-range translational motion and frequency-independent conductivity. Due to the carrier's shorter durations, failed and successful hopping, two competing processes, happen at higher frequencies. The scattered behaviour in conductivity at higher frequencies is caused by the ratio of failed to successful

hops. Jonscher's power law is used to fit the frequency dependence of a.c. conductivity data using Eq. 9[180].

$$\sigma_{ac}(\omega) = \sigma_{dc} + A\,\omega^{s} \quad (9)$$

In this case, $\sigma_{ac}(\omega)$ represents total measured conductivity, σ_{dc} represents frequency-independent d.c. contribution and $A\omega^{s}$ represent frequency-dependent contribution, A and s denote the amount or strength of polarisation and the relationship, based on the amplitude of the supplied field, among the lattice and moving ions. The shift between the frequency-independent and frequency-dependent regions demonstrates the transformation from long-range hopping across barriers to the short-range motion of carriers[180, 190]. In the investigation of A.C. conductivity, we observe a dramatic rise in conductivity at higher frequencies, which suggests the potential of alternate conduction pathways, which is corroborated by Jonscher's power law. As shown in Figures 4.14(b-d), Jonscher's power law was used to fit the a.c. conductivity data. Table 4.3 lists the fitting parameters that were obtained. Figure 4.14a makes it evident that the AC conductivity rises when MoS_2 is added to SnO_2.

Table 4.3 Parameters extracted from Jonscher's power law and Cole-Cole fitting for all samples.

Materials	Frequency exponents (s)	Pre exponent A	Spreading factor (α)	Relaxation time (τ)
MoS_2	0.805	2.92×10^{-10}	0.60	2.66×10^{-6}
SnO_2	0.698	4.46×10^{-12}	0.56	5.69×10^{-6}
MoS_2-SnO_2	0.467	2.00×10^{-9}	0.72	1.06×10^{-3}

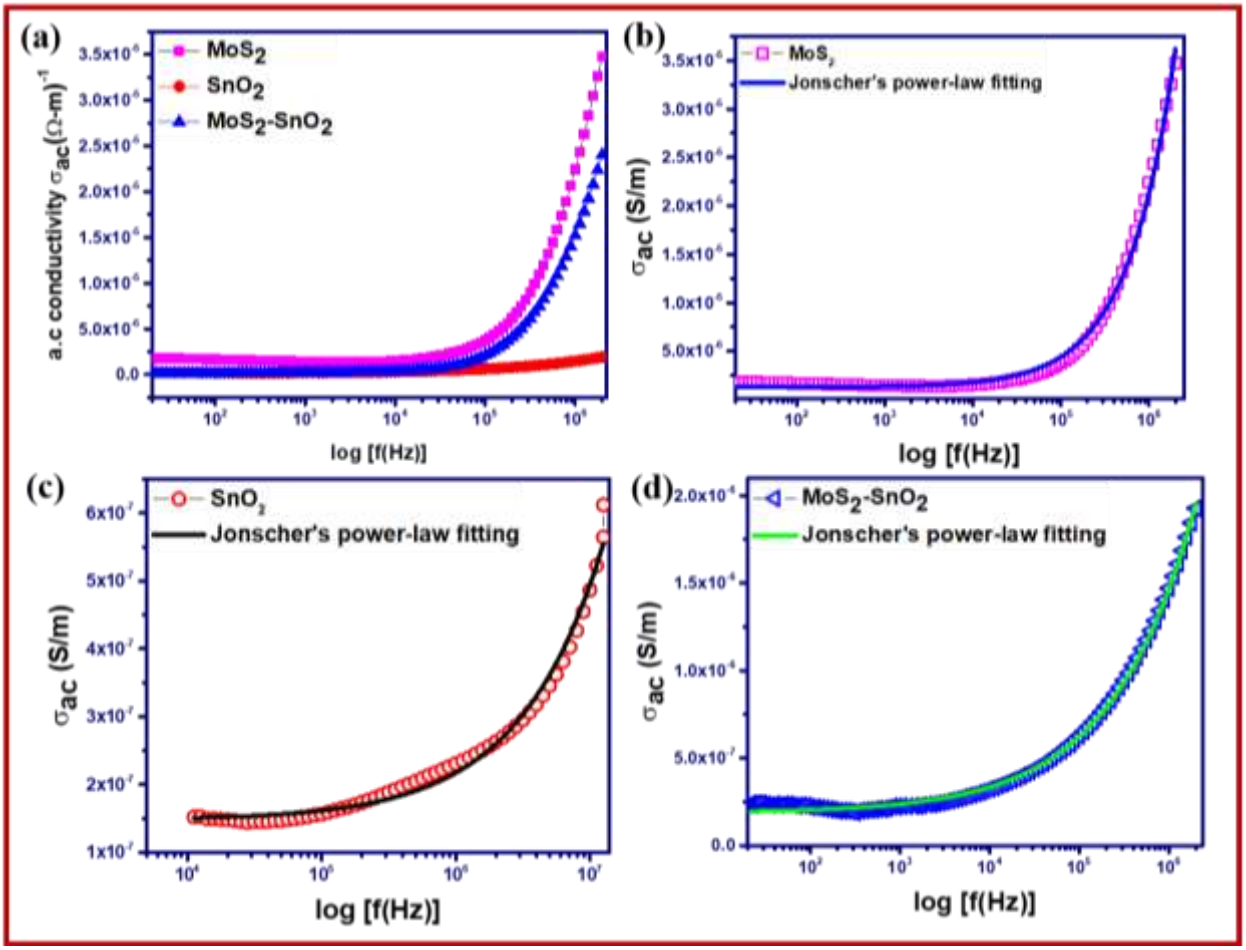

Figure 4.14 (a) Ac conductivity (σ_{ac}) as a function of frequency. (b-d) The graphs of curve fitting by using Jonscher's power law for MoS_2, SnO_2, and 10% MoS_2-SnO_2 nanocomposite.

4.3.10 Switching characteristic of Al/SnO_2/ITO-PET, Al/5%MoS_2-SnO_2/ITO-PET, AI/7%MoS_2-SnO_2/ITO-PET, and AI/10%MoS_2-SnO_2/ITO-PET devices.

The schematic diagram for the Al/SnO_2/ITO-PET, Al/MoS_2-SnO_2/ITO-PET based memristive devices is shown in Figures 4.3(a, b), and Figure 4.3c shows a cross-sectional FESEM picture of Al/MoS_2-SnO_2/ITO-PET. The MoS_2-SnO_2 active layer has a homogeneous thickness of 185 µm and is deposited on the ITO-PET. The cross-sectional FESEM image demonstrates that 7%MoS_2-SnO_2 is uniformly deposited as the active layer. The fabricated metal-insulator-metal (MIM) structure is subjected to various voltages through a LabVIEW program interfaced Keithley 2450 Source meter with top Al and bottom ITO coated PET substrate as shown in Figure 4.15a, respectively. Figure 4.15b depicts the optical image of the real device constructed on a flexible substrate.

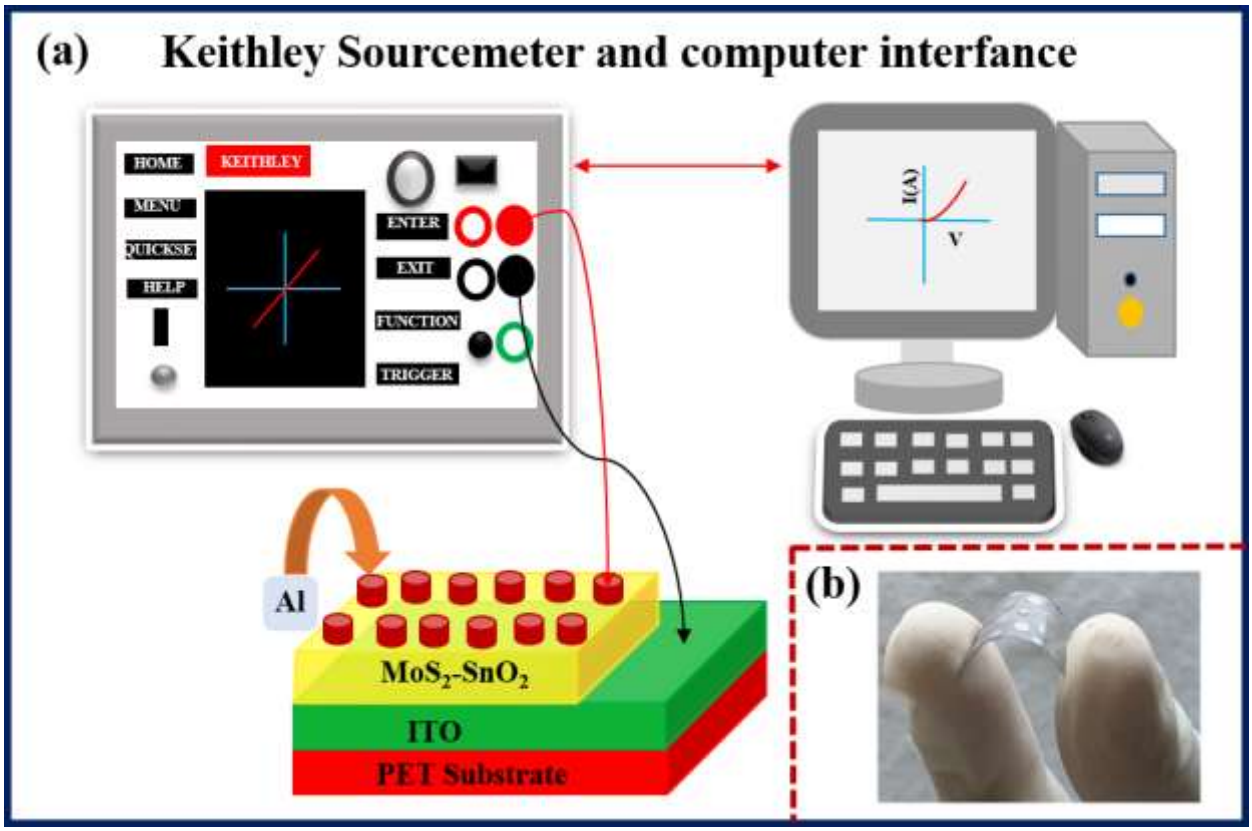

Figure 4.15 (a) Schematic showing the measurement method where LabVIEW controlled program was used for I-V measurement using Keithley 2450 Source meter. (b) Optical image of the real memory device.

Figure 4.16 shows the current-voltage characteristics of the created memory gadget in a metal-insulator-metal (MIM) structure, which has been carried out to understand the resistive switching behaviour. Figures 4.16(a-d) illustrates the current-voltage characteristics of the Al/SnO_2/ITO-PET and Al/MoS_2-SnO_2/ITO-PET (5%, 7%, 10%) based devices, respectively, within -1 V to +1V using a Keithley Source meter. It can be seen that the device with MoS_2-SnO_2 based nanocomposite has non-linear behaviour in comparison to the pure SnO_2 based

device. In order to observe the memory effect, the voltage is further raised in both directions. It has been noted that the Al/SnO_2/ITO-PET based device enters the SET state at 5.01 V, where the device switches from the high resistance state (HRS) to the low resistance state (LRS). However, as demonstrated in Figure 4.16(e), there is no transition from LRS to HRS when the voltage is increased further in the same direction. Since the voltage polarity must be reversed for the device to make the reset transition, it has been discovered that the reset transition occurs at -5.1 V. The device exhibits bipolar resistive behaviour, as demonstrated by the polarity-dependent switching of the constructed structure. The lower hysteresis and higher switching voltages of the SnO_2-based memory device are not useful for practical application. Therefore, the device with MoS_2-SnO_2 nanocomposite as an active layer was studied further. To understand the effect of 2D MoS_2 in SnO_2 for memory device application, the different weight percentages of MoS_2 in SnO_2-based devices were fabricated and tested. All of the MoS_2-SnO_2 nanocomposite devices displayed bipolar resistive switching (BRS) characteristics, as shown in Figures 4.16(f-h) (arrows indicate the voltage sweep direction). In addition, as shown in Figure 4.16g, the memory phenomenon with 7 wt.% MoS_2-SnO_2 based nanocomposite has the largest ON/OFF current ratio. The nanocomposite-based device displays the HRS to LRS transition at a reduced voltage of 0.89 V and the LRS to HRS transition at -0.85 V as shown in Figure 4.16g, which are greatly decreased in comparison to pure SnO_2, 5%MoS_2-SnO_2, and 10%MoS_2-SnO_2 based devices. The 7%MoS_2-SnO_2 based device demonstrates an improved resistive switching behaviour. The I_{ON}/I_{OFF} ratios for pure SnO_2, 5%MoS_2-SnO_2, 7%MoS_2-SnO_2, and 10%MoS_2-SnO_2 based devices are 1, 3, 100, and 25, respectively. This demonstrates the improved resistive switching properties of the hybrid 7%MoS_2-SnO_2 device.

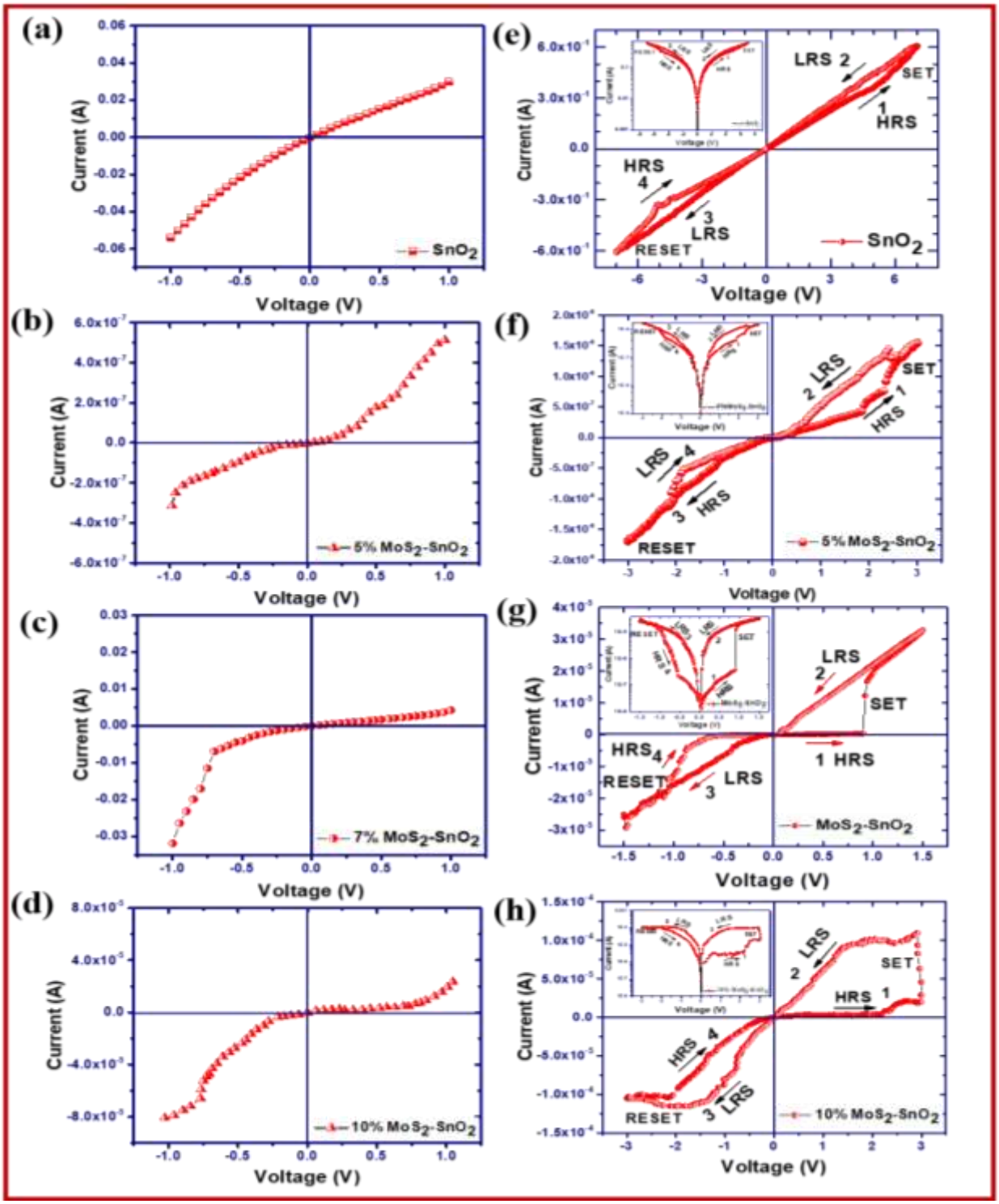

Figure 4.16 I-V characteristic of (a) SnO_2 (b) 5%MoS_2-SnO_2, (c) 7%MoS_2-SnO_2 (d) 10%MoS_2-SnO_2 and resistive switching characteristic of (e) SnO_2 (f) 5%MoS_2-SnO_2, (g) 7%MoS_2-SnO_2(h) 10%MoS_2-SnO_2 nanocomposite.

Figure 4.17a shows the double logarithmic plot of the I-V curve of the fabricated MoS_2-SnO_2 nanocomposite-based memory device in a positive voltage region. Furthermore, several models for conduction were employed to match the I-V plot in order to comprehend the mechanism of

resistive switching in Al/MoS_2-SnO_2/ITO-PET. The log (I) vs. log (V) for MoS_2-SnO_2 nanocomposite based device is depicted in Figure 4.17a. The log (I) vs. log (V) curve in the LRS state of the positive regions shows ohmic conduction with a slope value of 1.3, whereas a log (I) vs. log (V) curve in the HRS state in the positive region shows linear behaviour at lower voltage with a slope of 1.0 and a slope of 2 at higher voltage-thereby suggesting that other charge transport mechanism may be responsible[201]. This is further supported by fitting the I-V properties in the high voltage area (where the slope of the log (I) vs. log (V) curve is 2) with the Schottky emission model. This interface-limited conduction mechanism (Schottky emission) may be attributed to the difference in the work function of electrodes and the resulting MoS_2-SnO_2 nanocomposites and is expressed by the following equation.

$$\text{In I} \propto \sqrt{\frac{e^3}{4\pi\varepsilon_r\,\varepsilon_0\,d}}\ \sqrt{V}/\text{kT} \tag{10}$$

The Inset of Figure 4.17a shows the linear plot between log (I) vs $V^{1/2}$, thereby indicating the Schottky emission as the dominant charge transport mechanism in the higher voltage region of HRS. The excellent fit of the I-V curve at higher voltage by the Schottky model indicates that multiple charge transport mechanisms are operational in HRS [195, 196].

Further, the literature has also noted that reduced graphene oxide and metal oxide hybridization have a significant impact on the concentration of oxygen vacancies in the metal oxides[179]. According to Singh et al., metal oxide-rGO based nanocomposite has two advantages for resistive switching memory applications, firstly it serves as both an oxygen reservoir and secondly, acts as a blocking layer to keep oxygen from diffusing into the switching layers for improving the switching performance[174]. It has been reported in the literature that the concentration of oxygen vacancies changes in the nanocomposite powder sample and tailors the electron confinement which results in the conductivity modulation of the filamentary path [201]. These findings suggest that, in comparison to pure SnO_2, the electric field is enhanced by the creation of oxygen vacancies along the MoS_2-SnO_2 interface, which improves our memory device performance. Thus the bipolar resistive switching observed in the present case may be attributed to oxygen ion and vacancy migration with the help of an electric field at the MoS_2-SnO_2 interface.

Further, to check the stability of the device subjected to various switching cycles, an endurance test was carried out over the Al/MoS_2-SnO_2/ITO-PET based device for 100 cycles. Figure 4.17b shows the stable hysteresis loops for 100 switching cycles. A sweeping voltage of 0 to +1.5 V

was used for the SET and 0 to -1.5 V was used for the RESET. At room temperature, the ON and OFF resistances were measured using a read voltage of 0.5 V voltage. Even after a repetitive cycle, the Al/MoS_2-SnO_2/ITO-PET device shows no signs of degradation, as evidenced by resistance values of HRS and LRS in Figure 4.17c These findings show that the switching from OFF to ON is reversible and reproducible. Further, the retention characteristics shown in Figure 4.17d show that the MoS_2-SnO_2 based device can retain HRS and LRS without any serious degradation for longer than 2×10^3 seconds. We have also examined the device-to-device V_{SET}-V_{RESET} and LRS, HRS cumulative probability distributions of MoS_2-SnO_2 RRAM devices in Figures 4.17(e) and 4.17(f), respectively. The average of the first 10 cycles of each of the 20 tested devices was used to determine the operation voltages of the device-to-device distribution[198]. The device-to-device variability is very low in the SET voltage, however RESET process has slight variation, which may be attributed to the randomness in the filament rupture process and need to be addressed for the practical memory application. It may be highlighted that the device-to-device LRS and HRS have very little variation and signify the reliability of the fabricated memory devices [199]. The Inset of Figure 4.17e shows the optical image of the fabricated device with ~3 mm^2 as the device area.

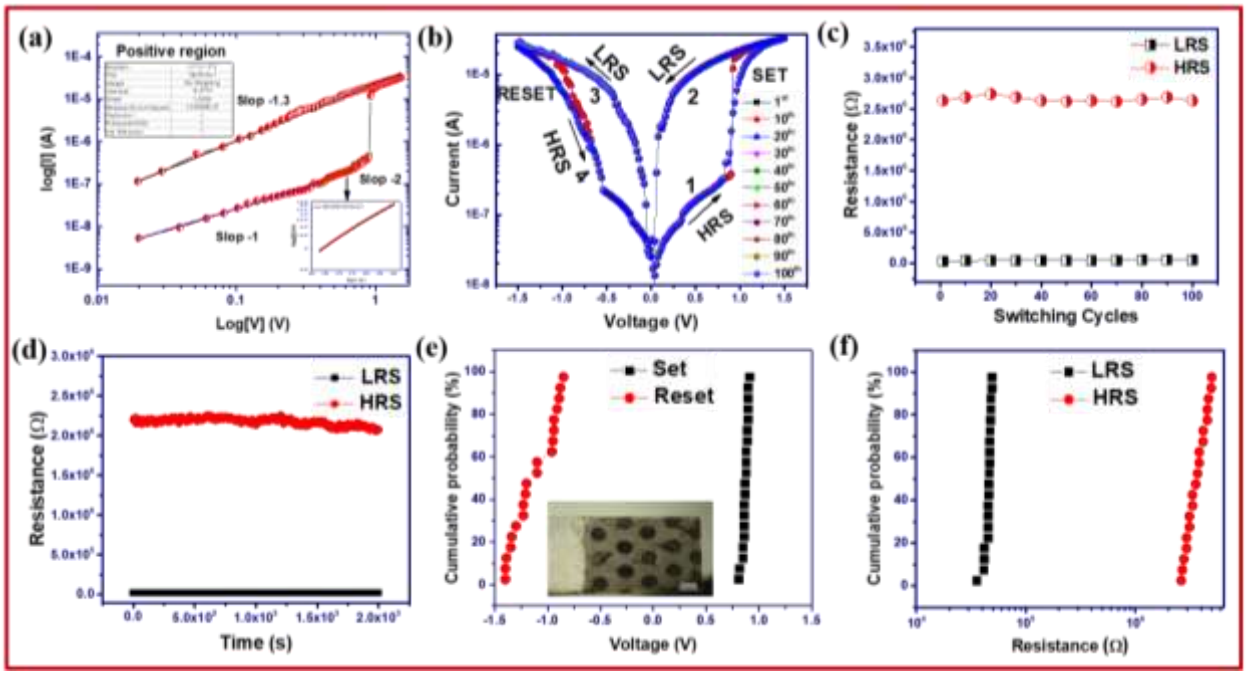

Figure. 4.17 (a) Double-logarithmic plot of the I-V characteristics of MoS_2-SnO_2 based device having a slope of roughly 1.3 in the LRS, thus indicating the ohmic conduction, whereas, for HRS, the device exhibits linearity with a slope of around 1 for lower voltages, however the deviation from linearity at higher voltages indicates the multiple charge transport mechanism.

(b-c) Endurance performance of the MoS_2-SnO_2 based device for 100 resistive switching cycles and (d) retention behaviour of HRS and LRS for a time period of 2×10^3 seconds at a reading voltage of 0.5 V. (e-f) The device-to-device cumulative probability distributions of Vset-Vreset and HRS-LRS of 7%MoS_2-SnO_2 RRAM devices.

Thereafter, to check the feasibility of the fabricated device for flexible electronic application, the mechanical stability test was carried out by subjecting numerous bending cycles. The resistive switching characteristics of the devices with a fixed 10 mm radius under compressive bending force are displayed in Figure 4.18a. The I-V properties of the bent device are plotted in double logarithmic form in Figure 4.18b. As illustrated in Figure 4.18c, after 100 cycles, the device performance remains stable. The set procedure, which used a sweeping voltage of 0 to +6 V for the HRS to LRS transition at 3.57 V, and 0 to -6 V for the LRS to HRS transition at -2.61 V, is referred to as the reset process. At room temperature, the ON and OFF resistances were measured with a read voltage of 0.5 V. R_{OFF}/R_{ON} was used to compute the device memory window, which was observed to be ~100 given in Figure 4.18e. Even after many cycles, the Al/MoS_2-SnO_2/ITO PET device shows no signs of degradation and the switching from OFF to ON is reversible and reproducible. The resistive switching behaviour, endurance, and retention characteristics of the Al/MoS_2-SnO_2/ITO-PET based device in the flat and bend geometry have been compared in Figures 4.18(d, e, f), respectively. Furthermore, table 4.4 shows the comparison between the obtained results in our study and other reported work.

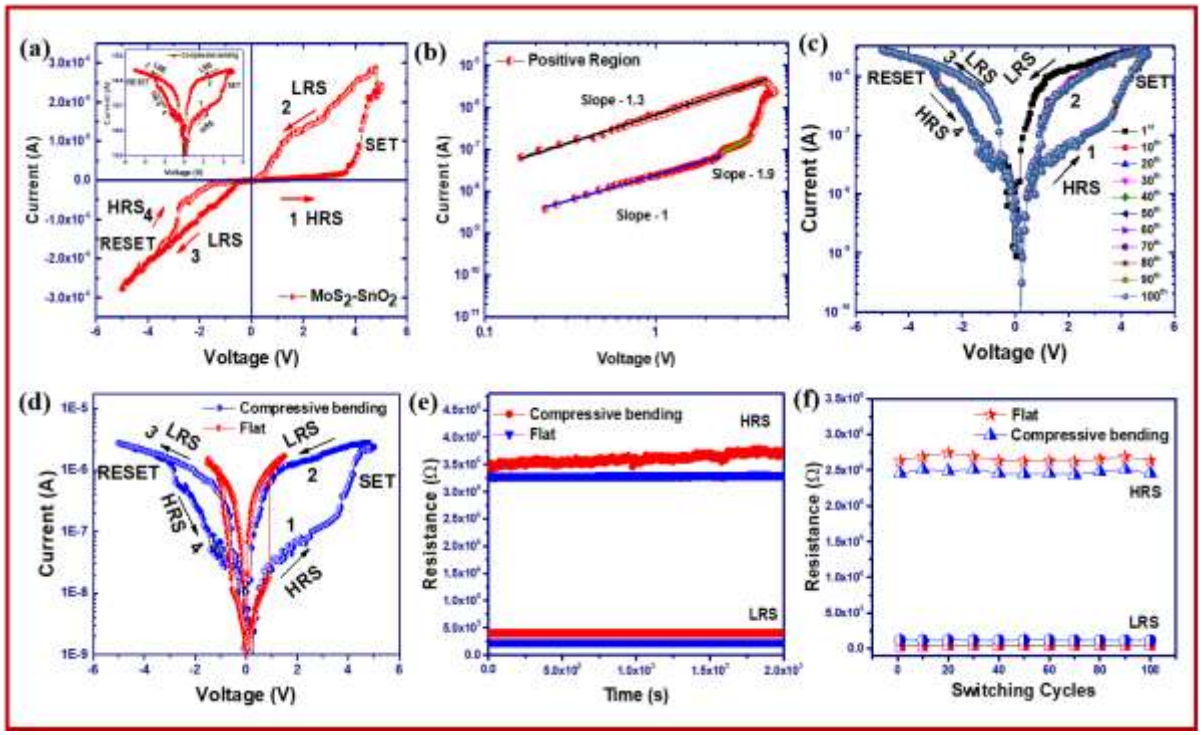

Figure 4.18 (a) Resistive switching performance of a flexible non-volatile memory device based on MoS_2-SnO_2 nanocomposite powder, and (b) Double-logarithmic plot of the I-V curves in the positive bias region. Fig. (c, f) show the endurance characteristics of a flexible non-volatile memory device based on a low-resistance state (LRS) and a high-resistance state (HRS) at a reading voltage of 0.5 V. (e) Good performance is shown by the retention of resistances in high resistance state (HRS) and low resistance state (LRS) for approximately 2×10^3 seconds.

Table 4.4- Comparison of the output performance of our devices with the other RRAM devices.

Device	V_{set} (V)	V_{reset} (V)	Operation mode	I_{ON}/I_{OFF} ratio	Endurance	Retention	Reference
Ag/SnO_2/FTO	-15.7	+17	Bipolar	NS	10 cycle	NS	[260]
Al/Sb:SnO_2/TiO_2 /Al	-3.0	+1.5	Bipolar	9 x 10^1	40 cycle	NS	[261]
Al/RGO-SnO_2/ITO	+4.93	-3.21	Bipolar	4.11	100 cycle	$1*10^3$s	[200]
SnO_2	+20	-20	Bipolar	NS	NS	NS	[262]
Ag/MoS_2-SnO_2/Quartz substrate	+5	-5	Linear behaviour	NS	NS	NS	[255]
Ag/SnO_2:Fe/Ag	+2	-2	Bipolar	18	NS	NS	[263]
Al/MoS_2-SnO_2/ITO-PET	+1.96	-1.52	Bipolar	25	NS	NS	[264]
Al/MoS_2-SnO_2/ITO-PET	+0.89	-0.85	Bipolar	100	100	2×10^3 s	**This work**

The above phenomenon of enhanced bipolar resistive switching in MoS_2-SnO_2 based memory devices may be attributed to the increase in the oxygen vacancies in the nanocomposite-based structure which is supported by XPS results[265]. The hybrid MoS_2-SnO_2 device has higher oxygen vacancy content which is aligned when voltage is applied to the structure, creating a filament inside the oxide-based matrix that connects the top and bottom electrodes and causes the device to enter into LRS. One possible reason for the SET transition, where the device switches from HRS to LRS, can be that on the application of +Ve voltage to the top electrode,

the positive bias electrode pulls the oxygen ions and leaves oxygen vacancies behind in the MoS_2-SnO_2 composite layer, as shown in Figure 4.19a. The oxygen-deficient layer makes the conductive filament that connects the top and bottom electrodes. Further on reversing the -Ve voltage, the migrated oxygen ions move back to the MoS_2-SnO_2 layer, thereby oxidizing the formed conducting filament and making the RESET transition, as shown in Figure 4.19b. The memory phenomenon is caused by repeatedly applying voltage with the opposite polarity to the device, resulting in the migration of oxygen ions and vacancies, as well as the oxidization of the electrochemically active Al layer to form the AlOx layer at the interface [266]. It may be highlighted that the reduction in the switching voltages for the Al/MoS_2-SnO_2/ITO-PET device (V_R = -0.85 V, V_S = 0.89 V) in comparison to Al/SnO_2/ITO-PET (V_R=-5.1 V, V_S = 5.01 V) device is due to lowering of band gap from pure SnO_2 to MoS_2-SnO_2 as shown in Figure 4.6. Therefore, the present study opens the possibility of flexible resistive memory devices with enhanced switching properties.

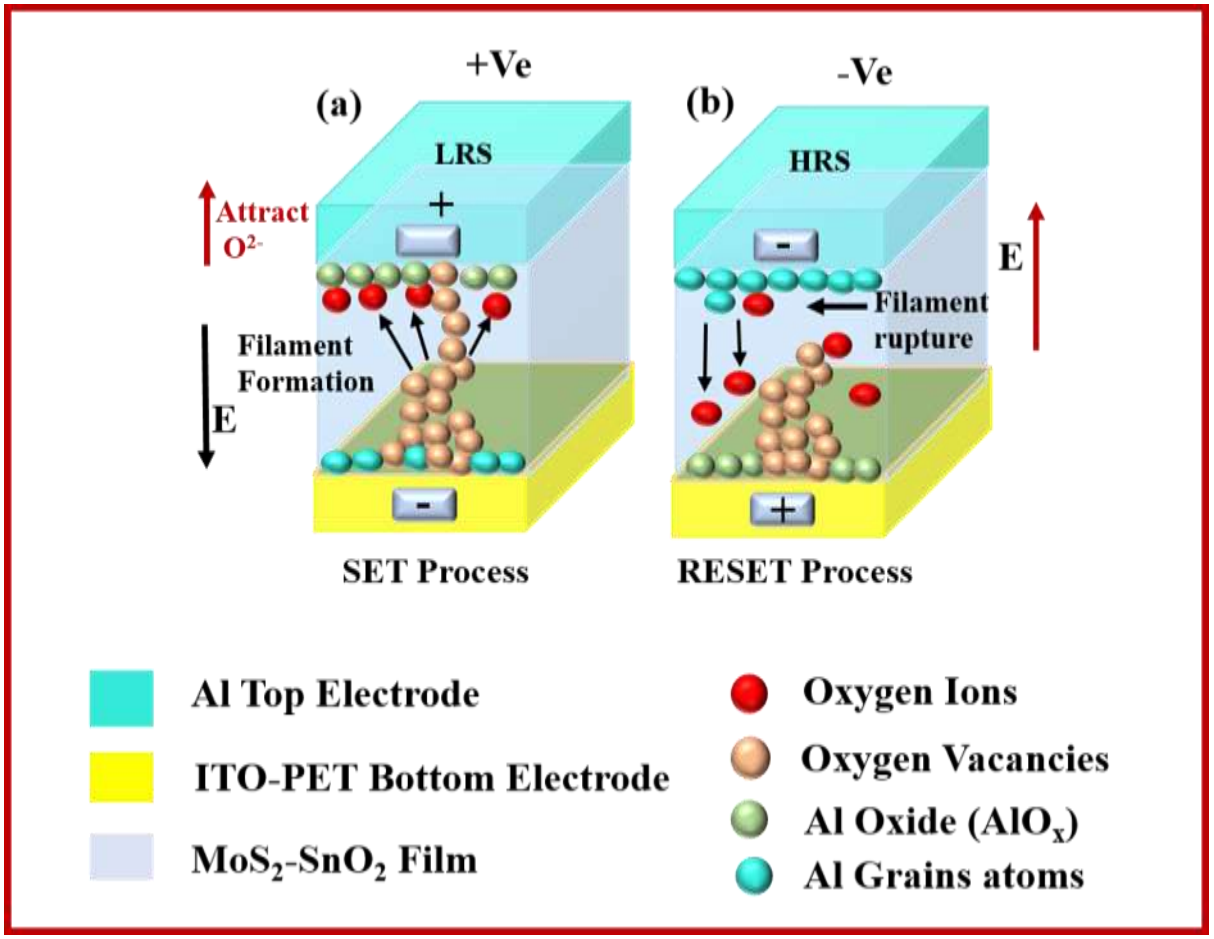

Figure 4.19 Schematic illustrations showing the filament formation and rupture mechanism in MoS_2-SnO_2 based memory device.

4.4 Conclusion

In summary, the effect of the MoS_2 content on the resistive switching performance of MoS_2-SnO_2 composite film was investigated using a device designed as an Al/MoS_2-SnO_2/ITO-PET structure. Hydrothermal synthesis is used to successfully synthesize the 5%MoS_2-SnO_2, 7%MoS_2-SnO_2, and 10%MoS_2-SnO_2 nanocomposite samples, with average particle sizes of 13.40 nm, 12.26 nm, and 10.25 nm. The phase purity and the structural and chemical composition of the synthesized MoS_2-SnO_2 powder were analysed using XRD, HRTEM, and XPS techniques. The XPS core level spectra for Mo 3d, S 2p, O1s, and Sn 3d peaks for the MoS_2-SnO_2 nanocomposite show stronger interfacial interaction between MoS_2 and SnO_2. The dielectric measurement indicates that, as compared to pure SnO_2 and MoS_2 material, the 10%MoS_2-SnO_2 nanocomposite had a high dielectric constant and dielectric loss. The reduction in space charge polarisation accounts for how impedance changes with frequency. The Nyquist plots have just one semicircle, which can be attributed to a result of the contribution of the grain boundary to the conduction process. The a.c. conductivity data confirms the involvement of bound charge carriers and is fitted with Jonscher's power law. Furthermore, the impacts of the MoS_2 in SnO_2 on the resistive switching capabilities of nanocomposite film were investigated by designing a device in MIM configuration with Al and ITO-PET as top and bottom electrodes, respectively sandwiching active MoS_2-SnO_2 memory layer. The Al/MoS_2-SnO_2/ITO-PET memory device displays the bipolar resistive switching phenomenon. The I_{On}/I_{Off} ratio for the fabricated Al/7%MoS_2-SnO_2/ITO-PET device was 100 times greater than that of Al/SnO_2/ITO-PET device. The fabricated memory device showed enhanced switching performance, with resistance ratio, endurance, and retention of about ~100, 100 switching cycles, and 2.1×10^3 seconds, respectively. After 100 bending cycles, HRS and LRS exhibited no appreciable change in magnitude, making it perfect for a flexible electronic device. The memory device fabricated in the present study using a straightforward spin-coating technique provides a viable method for low-cost solution processing of highly dependable and programmable flexible resistive memory cells.

CHAPTER 5

A flexible memory device made of SnO_2-hBN nanocomposite exhibits stable resistive switching application

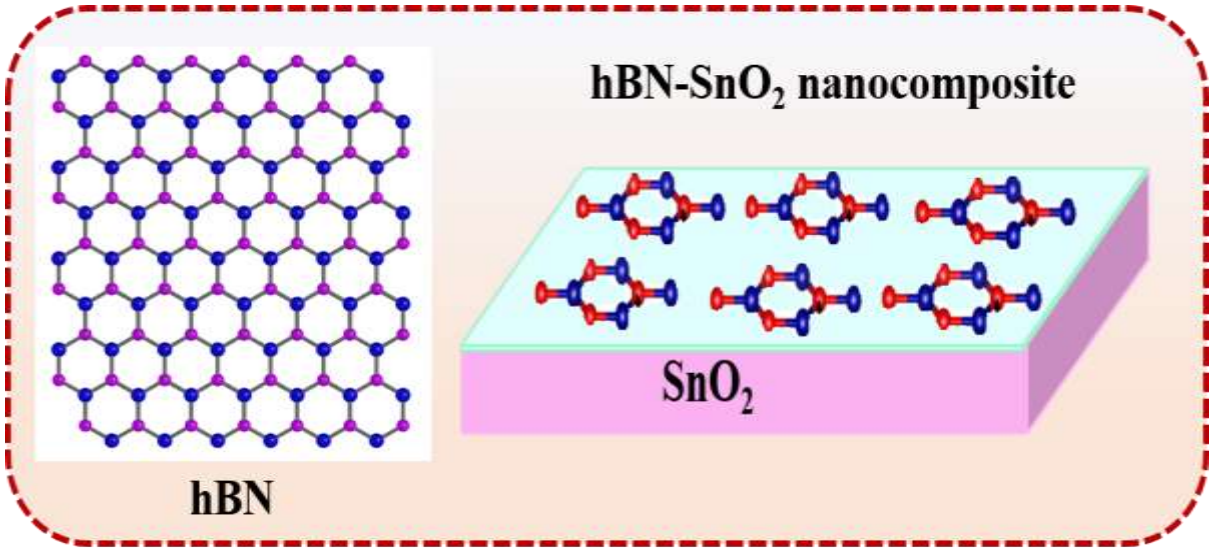

This chapter discuss the bipolar resistive switching mechanism based on insulating hexagonal boron nitride (hBN) and tin oxide (SnO_2)-based memory device. The synthesised nanocomposite powder was characterised by X-ray diffraction and Raman spectroscopic methods. A pure SnO_2 and hBN-SnO_2 nanocomposite film was spin-coated on an ITO-PET flexible substrate to create the memory device. The resistive switching performance of the fabricated devices were compared and observed that the memory device with 7 wt. % of hBN in SnO_2 has a maximum ON/OFF ratio of ~ 1000, in comparison to ~ 96 and ~10 for 5 and 10 wt. % sample respectively. The endurance and retention tests were performed on 7 wt. % hBN-SnO_2 composite film based memory device and the device shows no degradation in the memory window up to 100 cycles. The current hBN-SnO_2 based hybrid nanocomposite for resistive switching applications is found to be the best materials due to its reduced charge leakage property and high band gap, that is favourable for non-volatile memory technology.

5.1 Introduction

To address the issue of huge information storage and memory scalability, both the industrial and academic groups are working to develop innovative non-volatile memory technologies to replace the current flash memory [195]. The fact that flexible electronics can be bent, stretched, and used in wearable electronics has undoubtedly drawn a lot of interest in these gadgets [267]. Recently, there has been a growth in the requirement for flexible, wearable, foldable, lightweight, transparent electronic devices in many aspects of modern life. Examples of these devices include mobile phones, radio frequency identification tags, sensors, displays, and watches. The essential component of intelligent flexible electronics is the data processing and storage systems. In order to address the demands of wearable gadgets, researchers are dedicated to creating flexible mersisters [268]. Some new non-volatile memory devices with promising prospects are attracting increasing attention, such as magnetoresistive random access memory (MRAM), phase-change random access memory (PCRAM), ferroelectric random access memory (FeRAM), and resistive random access memory (RRAM)[269]. Among them, RRAM has been extensively studied in the past decades and has become a strong competitor of the next-generation non-volatile memories[270]. The ongoing desire for greater computer performance requires the development of new computing technologies that are scalable and flexible. Among the many competitors for non-volatile memory, resistive switching memories, which can be scaled down to less than 10 nm and offer high write/ erase speed, high endurance, and low power consumption, have attracted great interest and have high potential to replace charge-based memory devices [271]. Therefore, a wide variety of materials exhibiting resistive switching behaviours such as metal oxides, organic polymers, proteins, chalcogenides, and 2D nanomaterials, have been studied as potential candidates [272]. Based on resistive switching (RS) behaviour, a common RRAM device is a metal-insulator-metal (MIM) capacitor structure. It is possible to change a devices resistance state switching from one of high resistance (HRS) to low resistance (LRS) by applying electrical stress. This RS behaviour occurs through the formation and annihilation of conductive filaments (CFs) in the dielectric, which is generated by the assembly of metal ions migrating from an active metal electrode or donor-type point defects [273]. To achieve a high-performance RRAM device, the RS phenomena have been studied in various class of materials among which metal oxides such as HfOx , TiOx , AlOx , TaOx , and ZnO; polymer dielectrics such as poly(4-vinylphenol) (PVP), polyvinyl carbazole, polymethyl methacrylate, and polyvinyl alcohol; and low-dimensional materials such as graphene oxide (GO), molybdenum disulfide (MoS_2), reduced GO, tungsten disulfide, and

hexagonal boron nitride are the key contributors [274]. In recent times, hybrid RRAMs have gained significant attention, mainly due to their reliable and low-power switching operations [275]. The term hybrid RRAM is attributed to the nonconventional multilayer structure of the device with either organic polymer composites or metal oxide or both, where the metal oxide layer enhances the memory window, and the polymer composite contributes toward improved reliability [276]. However, these devices high ON-current remains an important problem that needs to be fixed in order to increase their power efficiency.

In recent times, two-dimensional (2-D) materials have gained tremendous attention and growth owing to their excellent performance in applications not limited to field effect transistors, sensors, photodetectors, non-volatile memories, and solar cells [277]. Hexagonal boron nitride (hBN) is an intriguing ultra-wide bandgap insulating material with a crystal structure resembling graphite, [93] where boron and nitrogen atoms alternately replace the sp^2 hybridized carbon atoms. Because of its graphite-like structure, hBN has great chemical and thermal stability and strong thermal conductivity, making it a viable choice for oxidation resistance and heat spreading [94]. Additionally, hBN provides a notable improvement in the confinement effects chemical and physical characteristics, as well as a high number of active sites. Very few studies have been reported on hexagonal boron nitride (hBN), despite most of the studies on the resistive switching effect in 2D materials primarily focuses on graphene and molybdenum disulfide (MoS_2). Flexible resistive switching applications for hBN and its nanocomposites still have a lot of unexplored potential. These hybrid nanocomposites are expected to have a configurable bandgap, a high level of flexibility, and a combination of unusual electrical and mechanical properties as a result more research is required to extract more insightful conclusions [95].

SnO_2 was chosen as a switching material because it is an n-type semiconductor that is conducted by oxygen vacancies and was reported to have high thermal stability [278]. In the literature, SnO_2-based sensors have demonstrated good endurance. Because the Frenkel defect energy (7 eV) is substantially greater than the band gap (3.6 eV), SnO_2 is resistant to displacement damage. Because of these features, SnO_2 is an excellent contender for resistive memory applications in radiation-hard situations. However, further research is required to completely understand the MIM devices filament and current mechanisms and to increase its reliability. For this reason, SnO_2 has received limited attention even though it has shown

promising properties for resistive switching [279]. SnO_2 is an n-type broadband semiconductor in its purest form, and the electrical conductivity of this material is caused by structural flaws or, more specifically, departures from stoichiometry in the lattice. It has been demonstrated that oxygen vacancies in the SnO_2 lattice are the predominant structural flaws in pure SnO_2 thin films, suggesting that tin atoms across the lattice may exist on a microscopic level as well. The electrically conductive properties of transparent SnO_2 semiconductors thin films can be increased by adding donor impurities. In thin layers of SnO_2, the amount of free electrons is decreased upon the addition of impurities with a valence of less than four, such as zinc (Zn), which lowers the thin films electrical conductivity. However, the converse happens when impurities like Sb, which have a valence of more than four, are added; as a result, thin films conduct electricity more readily. Antimony (Sb) and fluorine (F) are common contaminants for SnO_2 thin films. The thin coating electrical conductivity becomes more thermally stable when Sb is added to SnO_2. Also, the electrical conductivity of transparent SnO_2 semiconductor thin films can be increased by adding hexagonal boron nitride (hBN) addition [280].

In the current study, pure SnO_2 and hBN-SnO_2 with the different wt. % of hBN nanocomposite powder was made using the simple hydrothermal process [255] and was used further for spin coating the active memory layer in MIM configuration. The resistive switching properties of devices based on Al/SnO_2/ITO-PET and Al/hBN-SnO_2/ITO-PET were proven regarding the I-V hysteresis loop, durability, and retention tests. The log-log scale graphing of the I-V characteristics allowed for a comprehensive analysis of the electrical charge transport mechanism responsible for the resistive switching behaviour. The ability to get constant resistive switching outcomes even after bending down 100 times was used to illustrate the flexibility of the ReRAM devices that were created.

5.2 EXPERIMENTAL

5.2.1 Substances

The components utilized in the production of tin (IV) chloride pentahydrate ($SnCl_4.5H_2O$) include Boron nitride powder (BN, 98%) is procured from Sigma Aldrich. Sodium hydroxide (NaOH, 98%), ethanol (C_2H_5OH, 99.9%), isopropanol (C_3H_7OH, IPA), and hydrazine hydrate ($N_2H_4H_2O$, >99%) are purchased from Fisher Scientific. Since the compounds were in analytic purity, no more purification was necessary.

5.2.2 Synthesis of hBN Flakes:

A simple in situ hydrothermal process has been used to produce hexagonal Boron Nitride Nanosheets. The dispersion is typically made by mixing 50 ml of isopropyl alcohol (C_3H_7OH) and 10 ml of hydrazine hydrate ($N_2H_4.H_2O$) with 0.75 g of bulk h-BN powder. Add 50 ml of deionized (DI) water to this dispersion and mix for two hours. The final step is to pour the resulting dispersion into a 100 ml Teflon-lined stainless steel autoclave vessel and seal it. An oven with a high temperature is used to keep the autoclave at 220°C for 20 hours. The bulk BN powder nanosheets were exfoliated in a stainless steel autoclave. Ultimately, the finished product was dried for 12 hours at 90°C after being repeatedly cleaned with DI water. The white powder in Eppendorf is gathered and kept until it is required at room temperature (RT-25 °C).

5.2.3 hBN-SnO_2 nanocomposite synthesis:

To synthesize 5%hBN-SnO_2, 7%hBN-SnO_2, and 10%hBN-SnO_2 nanocomposites, firstly, synthesized hBN (200 mg, 280 mg, and 400 mg) was dissolved in 4 millilitres of DI water, then ultrasonically sonicated for 30 minutes. Furthermore, $SnCl_4 \cdot 5H_2O$ (1.76 g) and NaOH (2 g) were dissolved in a mixture of ethylene glycol (12 ml) added into 88 ml DI-water and magnetically stirred for 1 hour to get a homogenous solution[232]. The SnO_2 solution was then added to the hBN solution after 1 hour of stirring and stirred for 30 minutes. After the suspension was prepared, it was put inside a 100 mL Teflon-lined stainless steel autoclave and heated to 180°C for eighteen hours. Both ethanol and DI water were used for three centrifugations of the material. The leftovers were dried for five hours at 50°C in a vacuum oven [233]. The two-step hydrothermal process for making hBN-SnO_2 nanocomposite is depicted in Figure 5.1.

5.2.4 Fabrication of films

A thin coating of hBN-SnO_2 nanocomposite was applied on top of four-sided ITO-PET substrates. To begin, the ITO-PET substrates were cleaned using a standard wet cleaning procedure. After washing, the materials were dried by heating them to 100°C for 20 minutes. The solution was created by ultrasonically mixing 100 mg of hBN-SnO_2 powder with 3 ml of ethanol solution for 45 minutes, then applying the mixture to the ITO-PET substrate (2 cm x 1 cm) and spinning it for sixty seconds at 2000 rpm. The sample covered in coatings was placed on a heated plate for 10 minutes at 100°C. After seven cycles of spin coating, a homogenous layer of hBN-SnO_2 was formed. Finally, the top aluminum electrode was deposited through the

shadow mask using the thermal evaporation process under vacuum conditions of 10^{-5} bar [200]. The fabrication of the Al/hBN-SnO_2/ITO-PET based MIM device is schematically shown in Figure 5.1 [281].

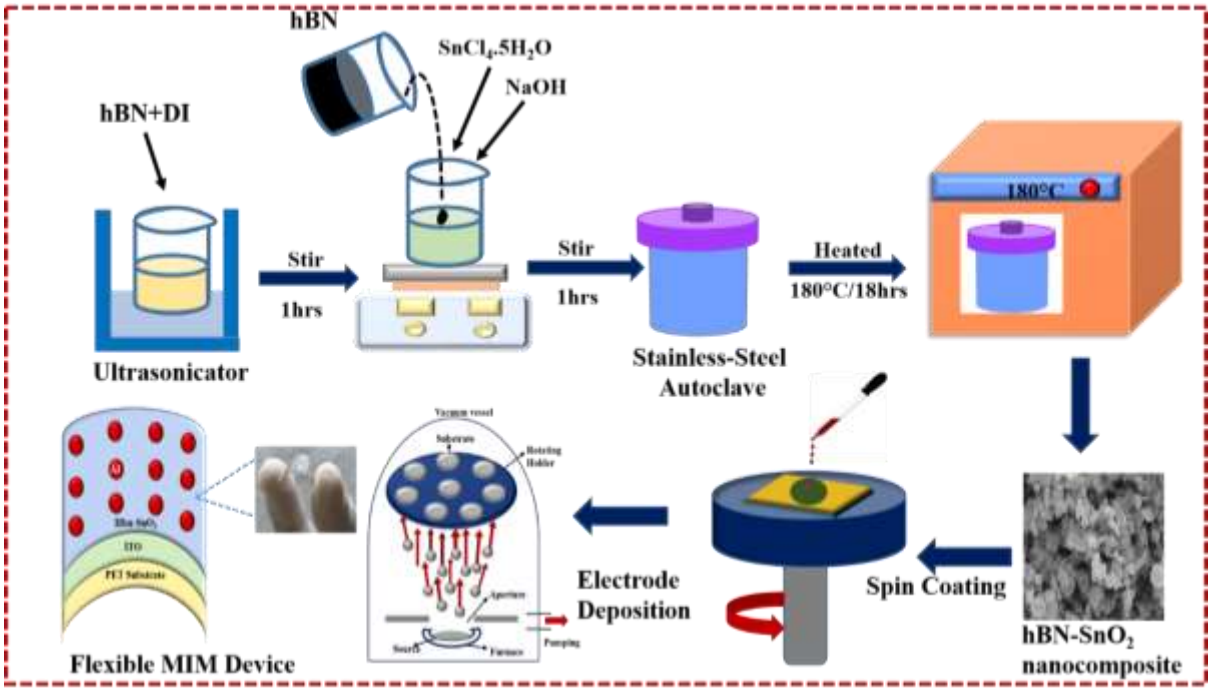

Figure 5.1 A visual representation showing the synthesis of hBN-SnO_2 (5%, 7%, and 10%) nanocomposite powder using the hydrothermal method and the pictorial presentation of steps involved in the fabrication of resistive memory devices.

5.2.5 Materials Characterization Techniques

Firstly, synthesized samples are investigated using the Raman Spectrometer (WiTec alpha 300RA), which has a 530 nm laser source wavelength. Using a Cu Kα source (λ = 1.54 Å) and an X-ray diffractometer (Bruker D8 Advance), the structural phase of the materials hBN, SnO_2, and hBN-SnO_2 (5%, 7%, and 10%) was investigated. The hBN, SnO_2, and hBN-SnO_2 nanocomposite materials surface morphologies were investigated using electron microscopy (FE-SEM; ZEISS). Using a monochromatic Al Kα source and a Perkin Elmer ultra-high vacuum XPS machine (Model 1257 PHI), the interfacial analysis of hBN, SnO_2, and hBN-SnO_2 nanocomposite structures was achieved. The method of spin coating is employed to deposit the thin layer of synthesized hBN-SnO_2 nanocomposite film. Memory devices were fabricated by employing the thermal evaporation method to create aluminium electrodes with a thickness below 100 nm. The fabricated thin-film memory cells (Al/SnO_2/ITO, Al/hBN-SnO_2/ITO) were then subjected to (I-V) measurements utilizing a Keithley source meter 2450.

First, we used the capacitance method to test the dielectric using a sample that had been covered with silver paste on each side and heated to 260°C for two hours. The frequency (20-10^6 Hz) and loss tangent (D = tanδ) measurements were examined with each other using an Agilent LCR meter (Model E4980A).

5.3 Results and discussion

5.3.1 X-ray diffractometer

The XRD method was used to examine the crystalline states and sizes of pure hBN, pure SnO_2, 5%hBN-SnO_2, 7%hBN-SnO_2, and 10%hBN-SnO_2 nanocomposites. As illustrated in Figure 5.2a, XRD spectra verify that hBN and SnO_2 are present in the hBN-SnO_2 nanocomposite. The existence of tetragonal rutile structure in pure SnO_2 is confirmed by its XRD spectra, which show peaks at 26°, 34°, 52°, and 65°, corresponding to the (110), (101), (211), and (202) planes. Similar to this, the as-synthesized h-BN samples peaks are roughly indexed at 26.86°, 41.8°, 44.01°, 50.5°, 55.34°, and 76.1°, which correspond to the hexagonal Boron Nitride (002), (100), (101), (102), (004), and (110) distinctive hkl planes. The XRD data showed the development of a pure hexagonal phase of BN with good crystallinity, with no extra impurity peaks detected. In comparison to the diffraction planes (100), (101), (102), (004), and (110), the intensity of the peak connected to the (002) diffraction plane seen in Figure 5.2a is significantly higher. This suggests that the h-BN (002) crystal plane is more exposed. The tetragonal rutile phase of SnO_2 is further confirmed by the hBN-SnO_2 nanocomposite, which displays peaks at 26°, 34°, 52°, and 65° that are related to the (110), (101), (211), and (202) planes. Because hBN has a low crystallinity, the peaks of pristine hBN are not visible in the hBN-SnO_2 nanocomposite. The pristine SnO_2 diffraction peak, which corresponds to the (110) plane, dominates the hBN peak in the composite sample, which is visible at 26° (002). It could be explained by the SnO_2-hBN samples transformation of Sn^{4+} into SnO_2 nanoparticles [163]. The addition of hBN was found to cause the SnO_2 diffraction peaks to expand. High crystalline quality SnO_2 particle is confirmed by hBN presence. As crystallinity depends on crystallite size, the crystallite size was calculated by using the Scherer formula for pure hBN, pure SnO_2, and hBN-SnO_2 nanocomposite [162, 164];

$$D = k\lambda/(\beta cos\theta) \qquad (1)$$

Where λ denotes the wavelength of X-ray, β denotes the broadening of the diffraction peak measured at half maximum intensity (FWHM), θ denotes the angle corresponding to peak position, Crystallite size is D and k denotes the shape factor (k=0.94).

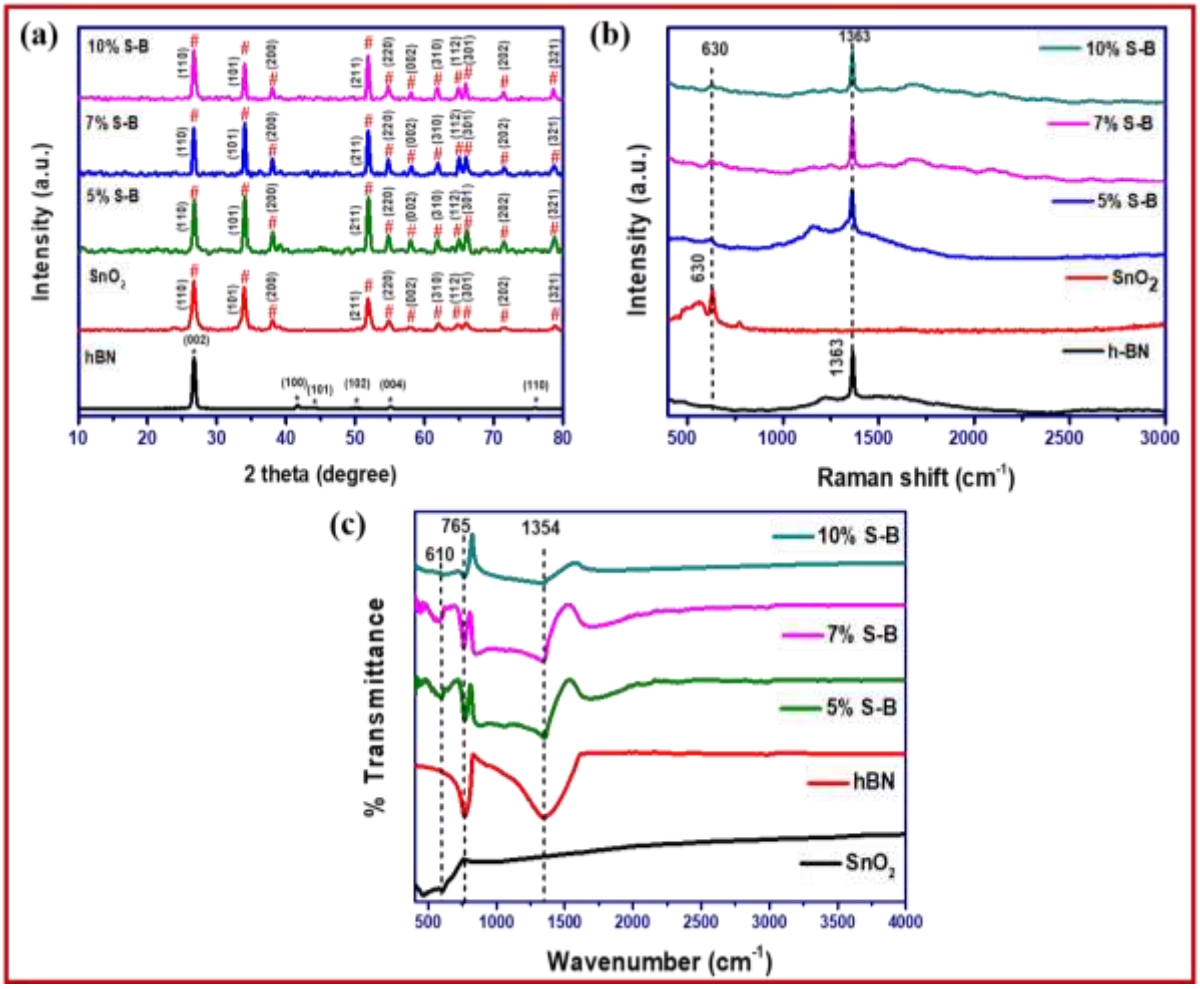

Figure 5.2 (a) XRD diffract gram (b) Raman spectroscopy and (c) FT-IR analysis of hBN, SnO_2, and hBN-SnO_2 nanocomposite with the different weight percentages of hBN powder.

The average crystal size determined for pure SnO_2, pure hBN, 5%hBN-SnO_2, 7%hBN-SnO_2, and 10%hBN-SnO_2 nanocomposites are discovered to be 13.2 nm, 19.5 nm, 26.1 nm, 20.8 nm, and 20.7 nm, respectively. It has been observed that the average crystallite size of hBN-SnO_2 nanocomposite decreases owing to the growth and nucleation of SnO_2 crystals, which was hindered by hBN [165, 166].

5.3.2 Raman analysis

As Raman scattering is an effective process for examining the structure of hBN-based substances, it was used to investigate the hBN-SnO_2 nanocomposite structure in more detail. The Raman spectra of SnO_2 nanoparticles and hBN-SnO_2 nanocomposites at various hBN concentrations are displayed in Figure 5.2b. The peak of SnO_2 nanoparticles has Raman peaks at 630 cm^{-1} corresponding to the A_{1g} vibration mode [167]. Raman spectroscopy was utilised

to study bulk hBN 2D flakes. The Raman spectra of in-plane vibrational mode (E_{2g}) for the samples Bulk h-BN have an intense peak at 1363 cm^{-1} respectively [93, 95]. Raman spectra of substances containing hBN-SnO_2 nanocomposite reveal distinct peaks at different hBN concentrations (5, 7, and 10%). For the 5%hBN-SnO_2 composite sample, the Raman spectrum is a simple superposition of the single vibration modes of hBN and SnO_2, which is consistent with the literature [282]. Peak positions remain unchanged, but the hBN vibration modes E_{2g} and A_{1g} have significantly lower peak intensities. As the hBN content increases, the peak intensity of the SnO_2 A_{1g} mode decreases, signifying the successful creation of the nanocomposite material with a variable hBN content.

5.3.3 FTIR spectra

The FTIR technique can be used to comprehend more about the substance bonds and useful groups that are present in a material. Understanding the existence of specific useful groups that are adsorbed at particular frequencies during transmission mode is very helpful since it shows the structure of the material. Band locations and the number of absorption peaks are determined by morphology, chemical composition, and crystalline structure [169]. The surface of nanoscale materials is extremely sensitive and easily altered. An FTIR study at room temperature was performed to examine the chemical structures on the outer layer of the materials over a wave number between 400-4000 cm^{-1}. Figure 5.2c displays the FTIR spectra of pure hBN, pure SnO_2, 5%hBN-SnO_2, 7%hBN-SnO_2, and 10%hBN-SnO_2 nanocomposites. Pure hBN exhibits two strong peaks in its FT-IR at 790 and 1378 cm^{-1}, respectively. The broad B-N stretching was observed, including in-plane stretching vibration (B-N, 1378 cm^{-1}) and the out-of-plane bending mode (B-N, 809 cm^{-1}), as shown in Figure 5.2c [283]. The band exhibited in the low wavenumber region 610 cm^{-1} is attributed to the Sn-O stretching vibration [169, 284]. Characteristic peaks of hBN-SnO_2 occurred at 1378 cm^{-1}, 709 cm^{-1} (B-N stretching vibration), and 610 cm^{-1} (Sn-O vibration), furthermore, the peak positions do not change, however, the peak intensities of the hBN vibration modes B-N are dramatically reduced and also the peaks are broadened, With the increase of hBN content, the peak intensity for the Sn-O mode of SnO_2 decreases, indicating the successful fabrication of the nanocomposite substance with variable hBN content [285].

5.3.4 Ultraviolet-visible spectroscopy

In Figure 5.3, Using the diffused UV-vis reflection spectrum, the optical characteristics of the hBN, SnO_2, 5%hBN-SnO_2, 7%hBN-SnO_2, and 10%hBN-SnO_2 nanocomposites. With the

exception of a little amount of absorption in the visible range (200-800 nm), SnO_2 mostly absorbs ultraviolet light. UV-visible spectra have been used to quantify a shift in the bandgap energy of materials evenly dispersed in ethanol-water. Boron Nitride is a material having a high direct bandgap (n=2) and the capacity to transition. Bulk h-BN has the lowest value of Eg whereas h-BNNS holds the highest value of E_g [286]. A wider bandgap emphasizes quantum confinement in the substance and results in smaller crystallite sizes. The synthesised samples bandgap was also analysed using Tauc's figure;

$$(\alpha h\nu) = A(h\text{-}Eg)^{1/2} \qquad (2)$$

In this equation, Eg is the bandgap, α is the absorption coefficient, A is a constant, and E is the photon energy obtained from E = hν, where h is Planck's constant and ν is the UV visible spectrum frequency. Plotting $(\alpha h\nu)^2$ against hν allowed for the calculation of the optical bandgap for pure hBN, pure SnO_2, 5%hBN-SnO_2, 7%hBN-SnO_2, and 10%hBN-SnO_2 nanocomposites. The calculated bandgap energies for pure SnO_2, hBN, 5%hBN-SnO_2, 7%hBN-SnO_2, and 10%hBN-SnO_2 were found to be 4.8 eV, 3.65 eV, 2.82 eV, 2.72 eV, and 2.69 eV. Once hBN is added to the SnO_2 nanoparticles, the bandgap value in the hBN-SnO_2 nanocomposites drops, and the hump in the absorption spectrum keeps moving downward in wavelength.

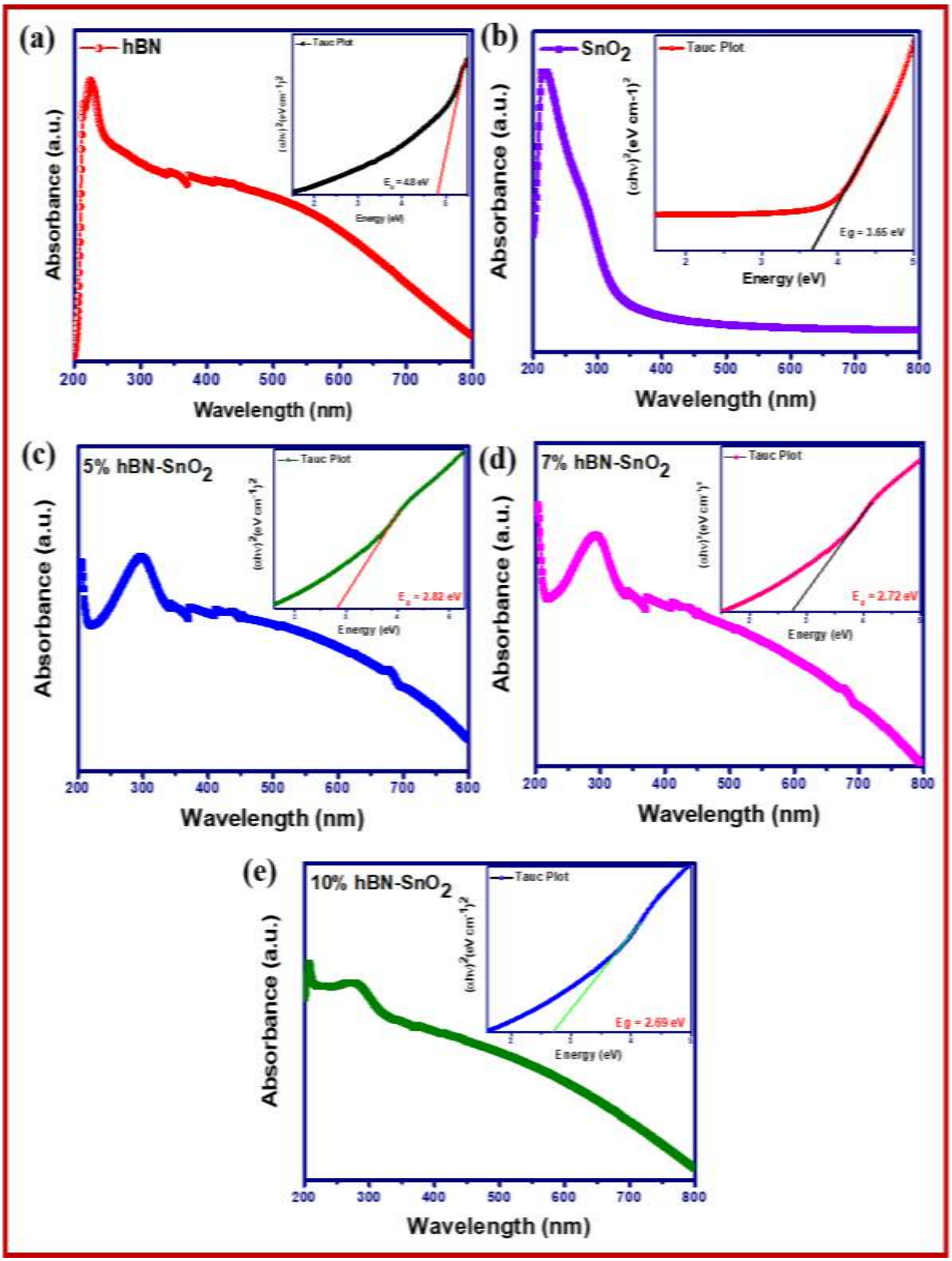

Figure 5.3 UV-visible spectra of a, hBN flakes, b SnO_2 nanoparticle, c 5%hBN-SnO_2, d 7%hBN-SnO_2, and e 10%hBN-SnO_2 nanocomposites with optical band energy (Eg).

5.3.5 FESEM

Figure 5.4 depicts the morphology of pure hBN, pure SnO_2, 5%hBN-SnO_2, 7%hBN-SnO_2, and 10%hBN-SnO_2 nanocomposite. It is feasible to verify that the morphology of the nanoflakes produced during the hydrothermal exfoliation of hBN was successfully synthesized using field emission scanning electron microscopy (FESEM). Figure 5.4(a) displaying Fe-SEM image of hBN which is synthesized at reaction temperature 220°C for 18 h displays large lateral size nanoflakes[287, 288]. Furthermore, aggregated hBN sheets are displayed at random. The FESEM picture of nanocrystalline SnO_2 is shown in Figure 5.4(b). It demonstrates the homogeneous and uniform dispersion of SnO_2 nanocrystallites [289]. Moreover, the FESEM image of the hBN-SnO_2 (5%, 7%, and 10%) nanocomposite, as displayed in Figure 5.4(c-e), specifies that SnO_2 nanoparticles adhere consistently to the surface of hBN sheets. It indicates that hydrothermal treatment of hBN and $SnCl_4$ solution is a successful approach for the synthesis of the hBN-SnO_2 nanocomposite [282]. The combination of SnO_2 with hBN nanocomposite demonstrates irregular shape particles combined with lateral-size nanoflakes could be favourable for electron transfer properties [287]. Energy-dispersive X-ray spectra, or EDX, are among the best methods available for determining sample purity. The hBN-SnO_2 (5, 7, and 10%) nanocomposite is depicted in Figure 5.5 and contains elements such as tin (Sn), oxygen (O), boron (B), and nitrogen (N), verified.

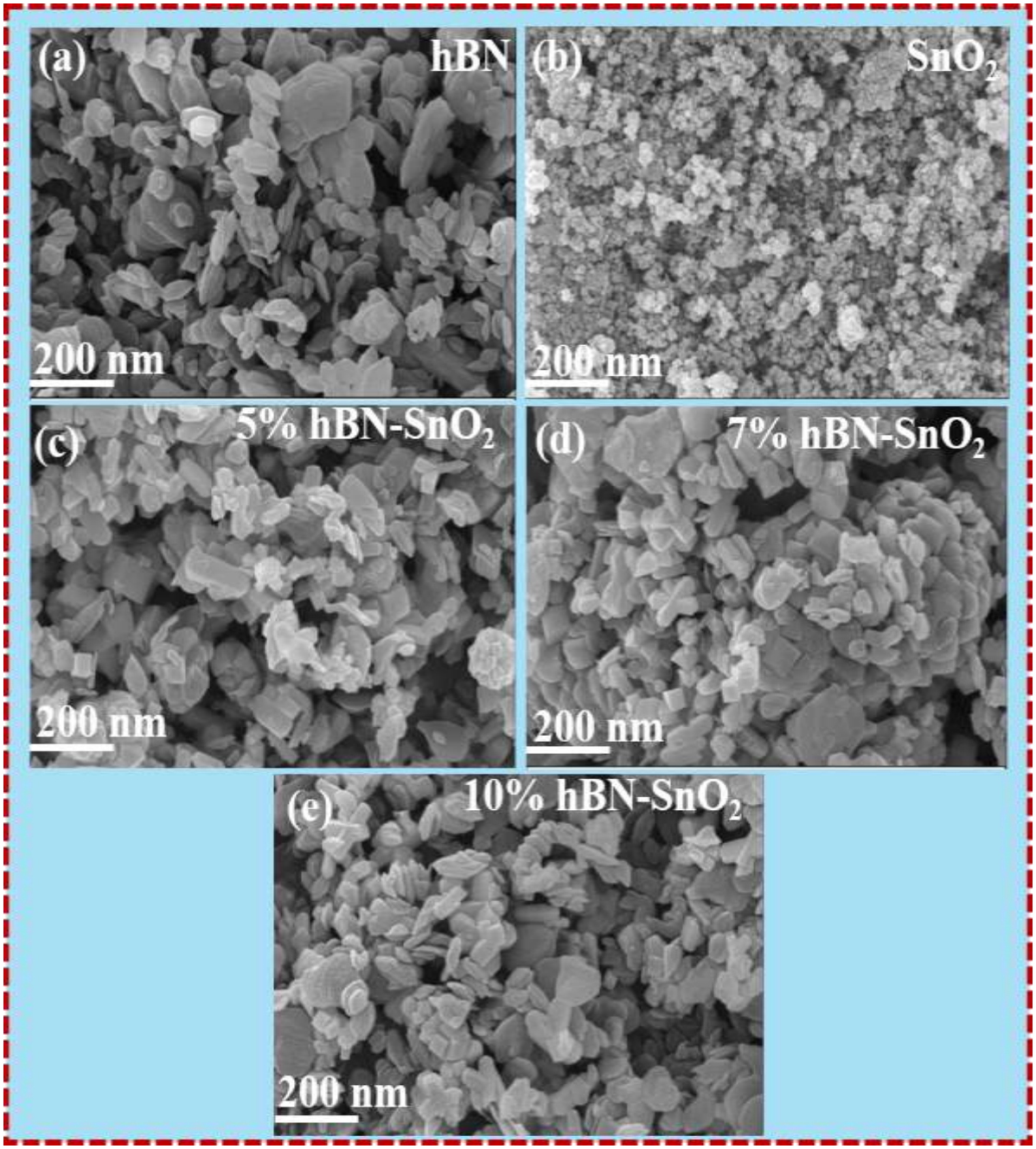

Figure 5.4 FE-SEM images of hBN, SnO_2, and hBN-SnO_2 nanocomposites with the different weight percentages of hBN: (a) hBN, (b) SnO_2, (c) 5%hBN-SnO_2, (d) 7%hBN-SnO_2 (e) 10%hBN-SnO_2

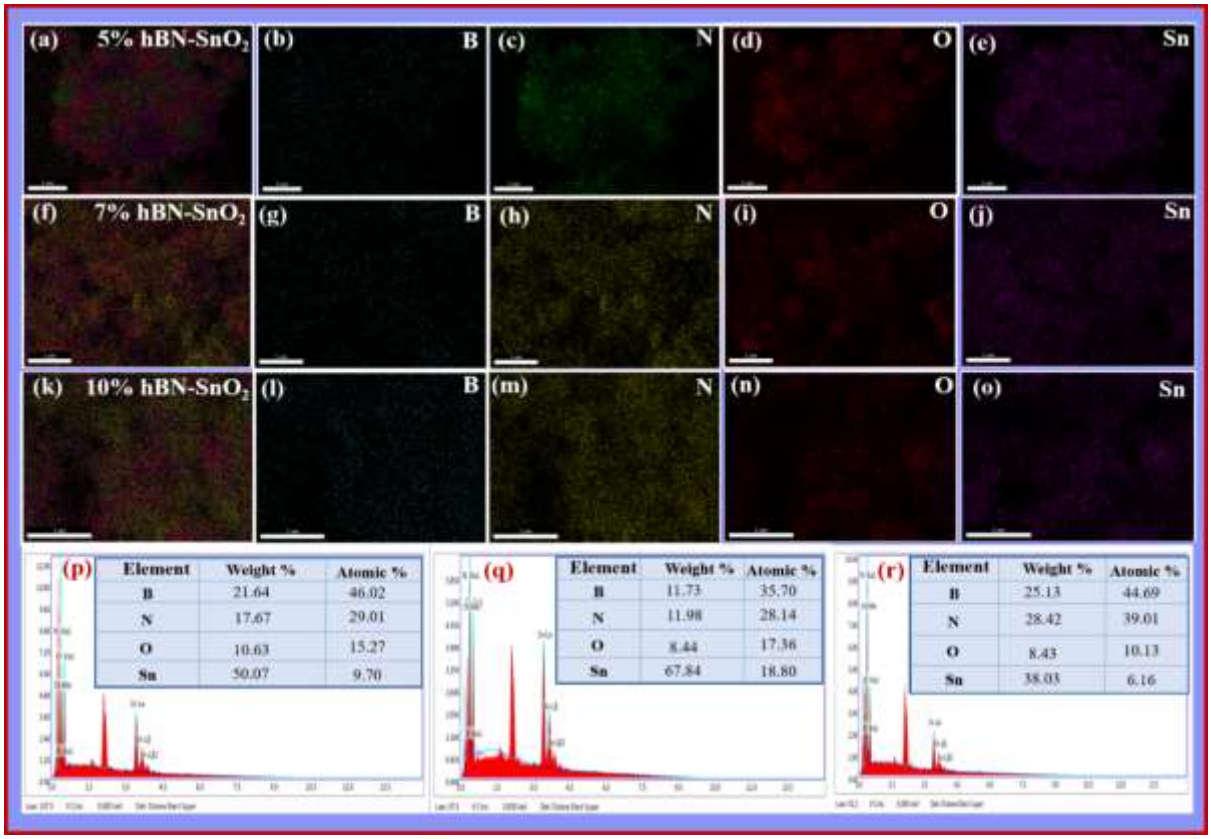

Figure 5.5 (a-o) Elemental mapping, (p-r) The synthesised EDX spectra of 5% hBN-SnO_2, 7% hBN-SnO_2, and 10% hBN-SnO_2 nanocomposites showing the purity of the synthesized powder.

5.3.6 XPS

Further, X-ray Photoelectron Spectroscopy (XPS) is used to analyze the chemical composition of synthesized, hBN, SnO2, and hBN-SnO2 nanocomposite powder. In the absence of any other impurity, the survey spectra in Figure 5.6(a) support the existence of B, N, C, Sn, and O. The high-resolution core level spectra of Sn 3d, B1s, N1s, C1s, and O1s are given in Figure 5.6(b-e).

B Spectra

Figure 5.6(b) shows the B1s core level spectra for pure hBN and hBN-SnO_2 nanocomposite, where**,** high-resolution B1s spectrum with the main peak located at 190.2 eV which corresponds to BN bonds and a smaller peak at 190.6 eV assigned to BO bonds [287]. In the case of hBN-SnO_2 nanocomposite powder, the majority of the B signal comes from the peaks at around 190 and 190.3 eV, which correspond to BN and BO, respectively [290]. The shift towards the lower binding energy side corresponds to electronic interaction at the interface of hBN and SnO_2 [291].

N Spectra

Figure 5.6(c) shows the N1s core level spectra of the hBN and hBN-SnO_2 nanocomposite. It is also possible to fit the broad peak surrounding the nitrogen 1s lines with two distinct peaks at 397.9 and 398.2 eV, which are in good agreement with the B-N and N-C bonds. These results show good agreement with previous studies, suggesting that hBN nanosheets fabricated by the hydrothermal method display functional groups on their surface [292]. The deconvolution of N1s (hBN-SnO_2) spectra yielded two primary peaks at a binding energy of 397.6 and 397.8 eV (Fig. 6c). The peak located at 397.6 eV corresponds to the B-N bond of hBN whereas the peak located at lower energy (397.8 eV) can be attributed to the N-C bond, respectively [293].

Tin Spectra

The Sn 3d states of the SnO_2 and hBN-SnO_2 composite samples are displayed in Figure 5.6(d). In the case of pure SnO_2, two characteristic peaks of $Sn3d_{5/2}$ and $Sn3d_{3/2}$ are observed at 485.4 and 493.8 eV, respectively, which correspond to the typical oxidized form of Sn^{4+} [175, 258]. XPS peaks in the Sn 3d spectrum of the hBN-SnO_2 nanocomposite show more substantial Sn $3d_{5/2}$ and Sn $3d_{3/2}$ peaks with binding energy changes of 1.3 eV, etc. These peaks are observed at 486.7 eV and 495.1 eV, respectively. The characteristic SnO_2 peaks are separated from one another by 8.4 eV, which is in line with previous findings. The above-observed shift indicates that the SnO_2 nanoparticles are connected to the hBN nanosheets, and have also been confirmed in the literature [176]. A significant interfacial interaction between SnO_2 and hBN was required to improve resistive switching performance, as indicated by the formation of the Sn-O link between the two materials. As a result, the hBN-SnO_2, Sn 3d peaks have been moved to a higher binding energy position. Because SnO_2 has a smaller work function than hBN, the electrons in hBN-SnO_2 hybrids can generally flow (SnO_2 to hBN) [178, 200]. Therefore, the hBN-SnO_2 Sn3d peaks have been shifted to have a higher binding energy. Sn can produce more energy due to the electrostatic repulsive interaction between O and a negative charge in the lattice. The shift in the Sn electronic orbit will impact the binding energy of O1s [179]. Remarkably, when the hBN-SnO_2 nanocomposite is synthesized, the associated peaks of B1s, N1s, and Sn 3d change positively, whilst the peaks of O1s move positively, indicating a significant interaction between SnO_2 and hBN. The XPS results also show that ultrafine hBN flakes are agglomerated on the SnO_2 surfaces.

Oxygen Spectra

The deconvoluted O1s core level spectra were found to consist of two peaks, as illustrated in Figure 5.6(e). Considering the information of lattice O, tetravalent Sn ions in the O vault are responsible for the peak for pure SnO_2 at the binding energy location of 530.3 eV. Another peak at 530.9 eV indicates that the surface is surrounded by hydroxide OH groups and corresponds to nonlattice oxygen [173]. Additionally, two peaks at 530.2 eV and 531.1 eV in the O1s spectra, corresponding to B-O and C-O bonds, are visible in the case of hBN-SnO_2, and they are displaced towards the lower binding energy side. BN from hBN and the oxygen species from SnO_2 likely interacted at the interface, as evidenced by the opposite direction shift in binding energy position for the O1s and BN peak [257].

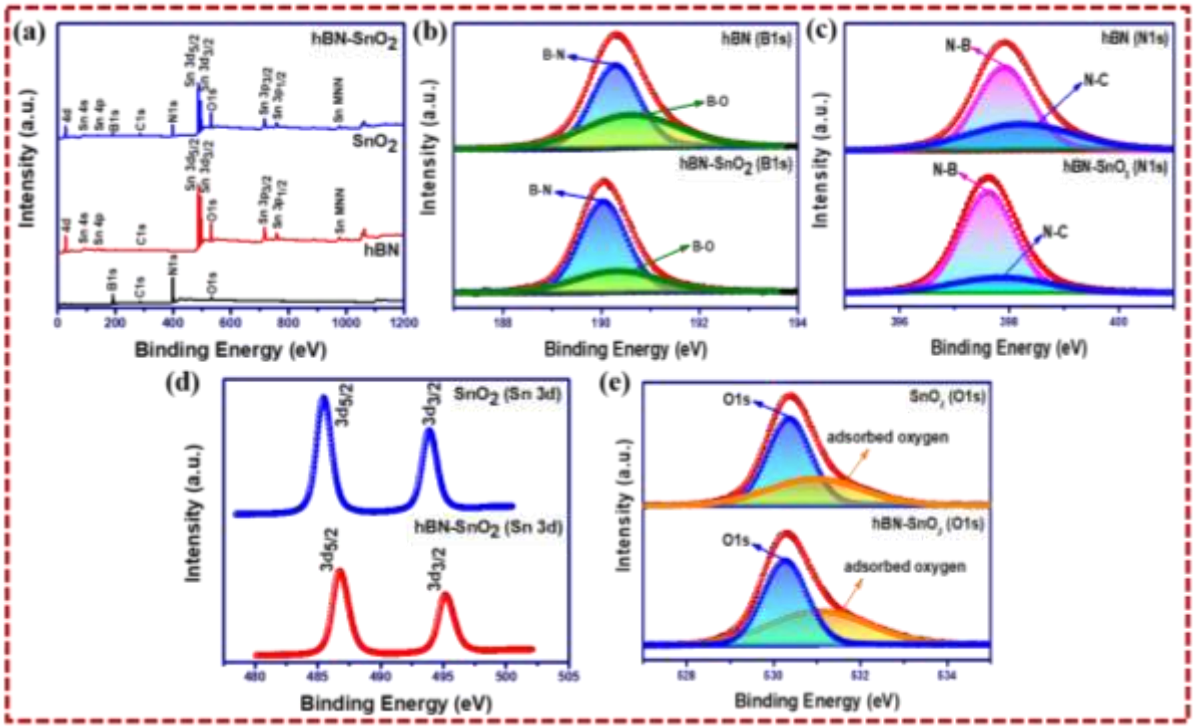

Figure 5.6 (a) An XPS survey scan of hBN-SnO_2 reveals the existence of elements such as B, N, Sn, and O, as well as increased resolution spectrums of (b) B1s, (c) N1s, (d) Sn 3d and (e) O1s.

5.3.7 Dielectric characteristics

Figures 5.7(a-b) illustrate how the dielectric constant, also known as electric permittivity, varies with frequency in terms of its real (ε´r) and imaginary (ε´´r) components. Based on the Maxwell-Wagner model, it can be seen that ε'_r decreases with increasing frequency of applied field for all samples [181]. Space charge polarisation enables nano-dipoles that oscillate to facilitate easy orientation in the direction of the supplied electrical field; therefore, a high value

of ε'_r is observed in the low-frequency zone. Since composites have a larger surface area due to their small size (more grains), the dielectric constant in 7% hBN-SnO_2 composite is higher than in 5% hBN-SnO_2, 10% hBN-SnO_2, pure SnO_2, and pure hBN[183]. A process called dielectric loss (tanδ) occurs in the dielectric system when energy is lost. Based on a frequency range of 20-10^6 Hz, Figure 5.7c displays the dielectric loss for the room temperature nanocomposite of hBN, SnO_2, 5% hBN-SnO_2, 7% hBN-SnO_2 and 10% hBN-SnO_2. In dielectric media, dielectric loss occurs when the charge carriers cannot keep up with the electric fields fluctuations. For all samples, it is found that dielectric losses decrease with increasing applied field frequency. At higher frequencies, reduced dielectric losses are seen as a result of the forced rotational shift of magnetization due to domain wall inhibition. A possible sign of Maxwell-Wagner relaxation could be the lower values at higher frequencies. The greater dielectric loss happens at lower frequencies, as Figure 5.7c illustrates. This is caused by space charge polarisation, which can be explained by the Shockley Read mechanism [184]. From Figure 5.7c, it is observed that the dielectric loss tangent of hBN-SnO_2 (5-10%) samples decreases from pure SnO_2, and pure hBN; thus, composites sample will be better in case of dielectric application [185, 186].

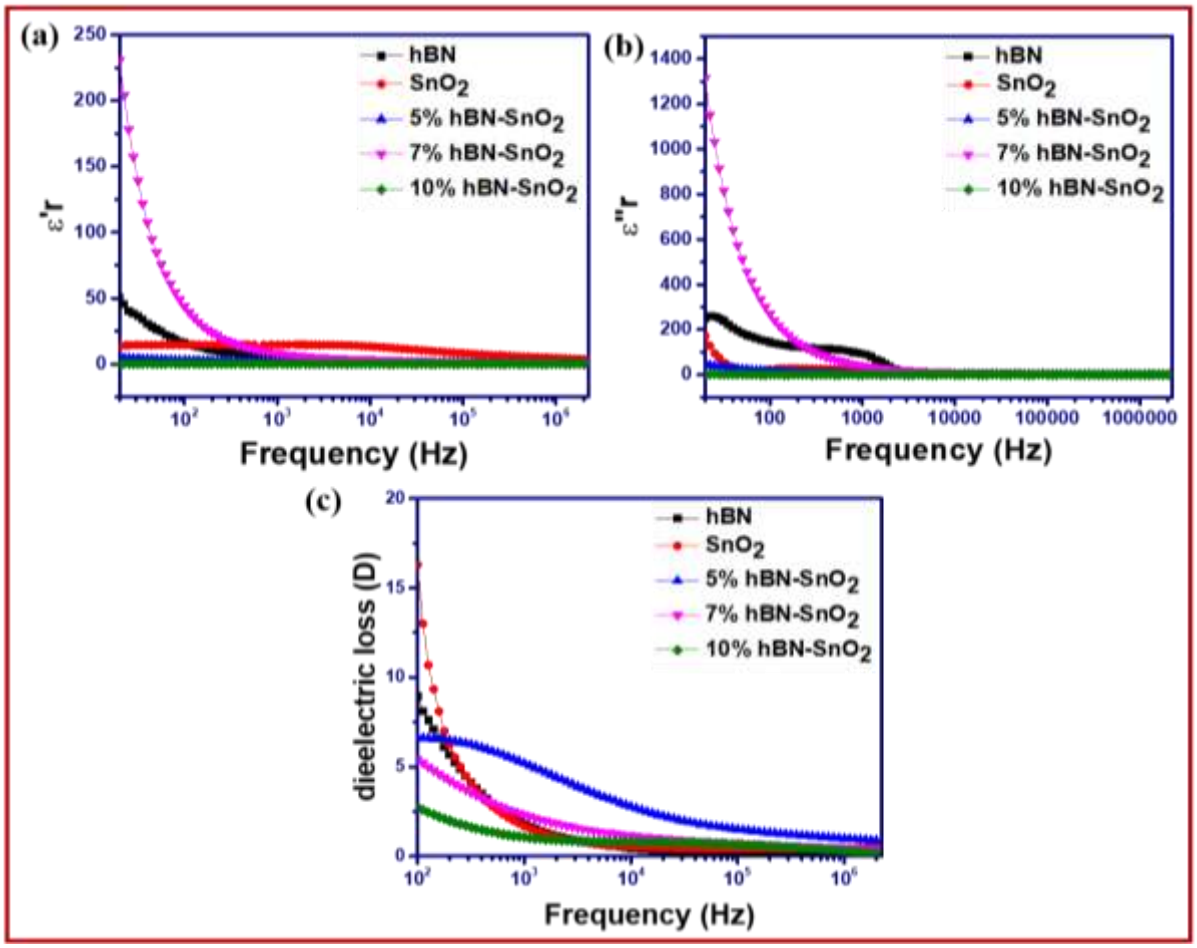

Figure 5.7 Dielectric constant variation (a) real and imaginary parts, and dielectric loss (c) for pure hBN, SnO_2, 5% hBN-SnO_2, 7% hBN-SnO_2, and 10% hBN-SnO_2 nanocomposite as a function of the frequency.

5.3.8 Impedance spectroscopy

To examine various electrical features, such as the impact of grain and grain boundaries on the total impedance, relaxation time distribution, and kind of relaxation mechanism [180], one can analyse the complex behaviour of total impedance with frequency. To represent total complex impedance, use the following formula:

$$Z^* = Z' + jZ'' \quad (3)$$

where Eq. 4 provides the total impedance real (Z') and imaginary (Z") components.

$$Z'' = Z\times \sin\theta \text{ and } Z' = Z\times \cos\theta \quad (4)$$

Z in this case is the phase angle that is measured (in radians), which is the total measured impedance. The variation in the capacitive or imaginary part and the resistive or real component (Z') with respect to the applied field frequency is seen in Figures 5.8(a, b). Lower frequency impedance levels are high, but they decrease as frequency increases. Impedance has decreased as frequency has increased due to the dissipation of stationary charges and greater mobility. At higher frequencies, there is a tendency for all the curves to merge due to a decrease in space charge and the cancellation of the dipole orientation effect [180]. As illustrated in Figure 5.8c, Nyquist plots were used at room temperature to isolate the impacts of grains and grain boundaries. Conductive grain boundaries are essential at higher frequencies in hBN, SnO_2, 5%hBN-SnO_2, 7%hBN-SnO_2, and 10%hBN-SnO_2 nanocomposite materials, but resistant grain boundaries are relevant at low frequencies. As can be shown in Figure 5.8c, in our case, all the samples show only one semicircle, which is due to the contribution of the grain boundaries [185]. Grain boundaries are believed to be a major factor in impedance because of their higher resistance than the grain itself [188]. Due to hBN significant conductivity, the hBN-SnO2 nanocomposite is less resistant than SnO_2.

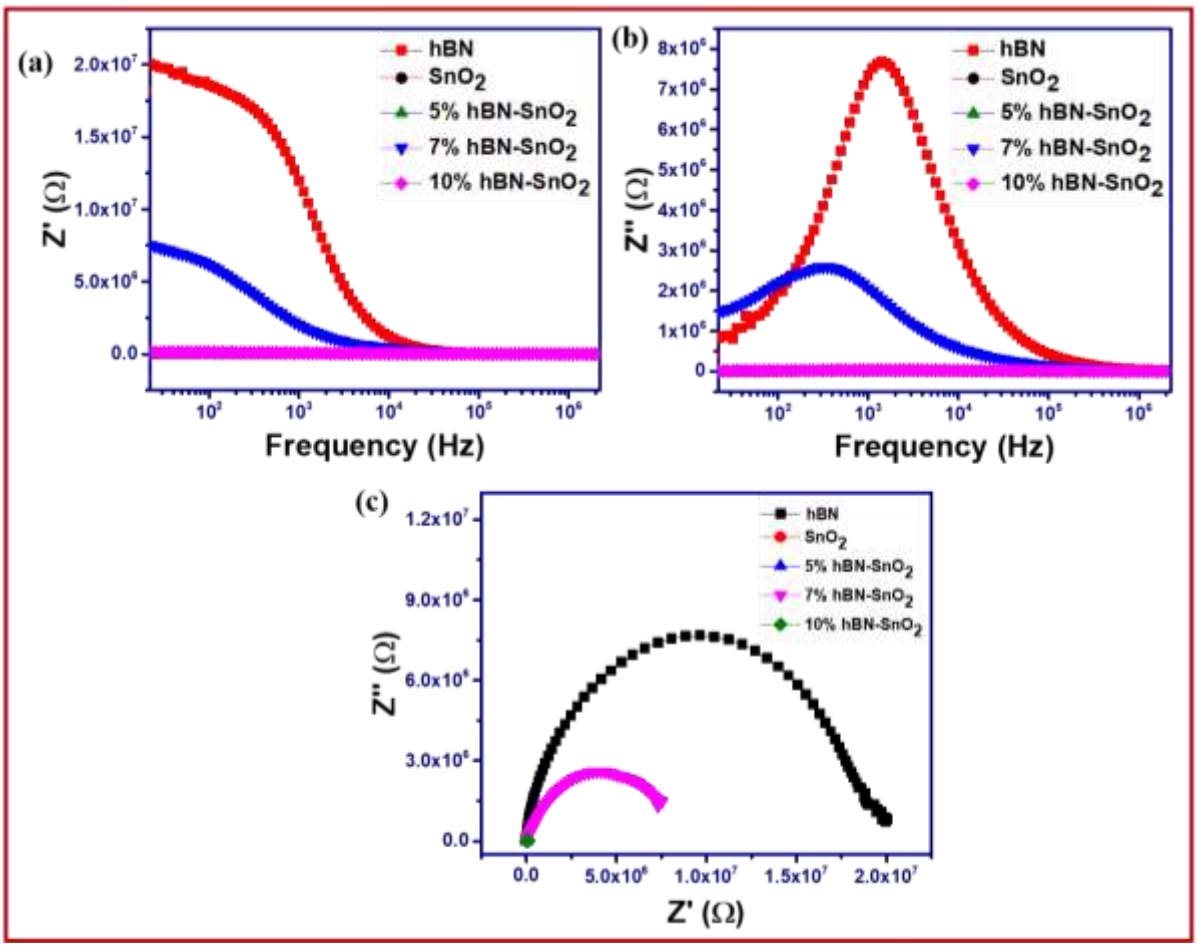

Fig. 5.8 Impedance variation for the hBN, SnO_2, 5%hBN-SnO_2, 7%hBN-SnO_2, and 10%hBN-SnO_2 nanocomposite powder as a function of frequency (20-10^6 Hz) in both (a) real and (b) imaginary sections. (c) Nyquist plot of hBN, SnO_2, 5% hBN-SnO_2, 7% hBN-SnO_2, and 10% hBN-SnO_2 nanocomposite samples.

5.3.9 AC conductivity

To better understand the conduction process, the frequencies-dependent AC electrical conductivity of hBN, SnO_2, 5%hBN-SnO_2, 7%hBN-SnO_2, and 10%hBN-SnO_2 composites specimens were examined at room temperature in the frequency range of 20-10^6 Hz. Figure 5.9a shows the computed a.c. conductivity using the formula $\sigma(\omega) = \omega\varepsilon_0\varepsilon_0\tan\delta$. It provides proof of the presence of bonded charge carriers and offers light on the behaviour of considerable frequency dependency by demonstrating that conductivity increases as frequency. Because the carriers can hop for longer periods at lower frequencies, they can translate over longer distances and provide conductivity that is frequency-independent. At higher frequencies, failure and successful processes conflicting processes occur because of the carrier's shorter lifetimes. The ratio of unsuccessful to successful hops is what causes the dispersed behaviour

in conductivity at higher frequencies. Eqn. 5 is used to fit the frequency dependence of the a.c. conductivity data using Jonscher's power law [180].

$$\sigma_{ac}(\omega) = \sigma_{dc} + A\omega^{s} \quad (5)$$

where A is the polarization strength, s is an exponent that describes the lattice-mobile ion interaction depending on the applied field frequency, and σ_{dc} is the frequency-independent d.c. contribution. Additionally, $\sigma_{ac}(\omega)$ represents the total measured conductivity, and $A\omega^{s}$ denotes the frequency-dependent contribution. The shift between the frequency-independent and frequency-dependent regions demonstrates the transformation from long-range hopping across barriers to the short-range motion of carriers [180, 190]. An examination of a.c. conductivity reveals a sharp increase at higher frequencies, supporting Jonscher's power law and suggesting the potential of other conduction pathways. Table 5.1 lists the fitting parameters that were obtained from the a.c. conductivity data, which we fitted using Jonscher's power law, as illustrated in Figure 5.9(b-f). The rise in AC conductivity that occurs when hBN is added to SnO_2 is evident from Figure 5.9a.

Table 5.1 Parameters are taken from the power law fitting of Jonscher's for every sample.

Materials	**Frequency exponents (s)**	**Pre exponent A**
hBN	0.558	1.56×10^{-7}
SnO_2	0.543	9.22×10^{-10}
5% hBN-SnO_2	0.467	1.33×10^{-8}
7% hBN-SnO_2	0.870	1.17×10^{-10}
10% hBN-SnO_2	0.391	3.40×10^{-10}

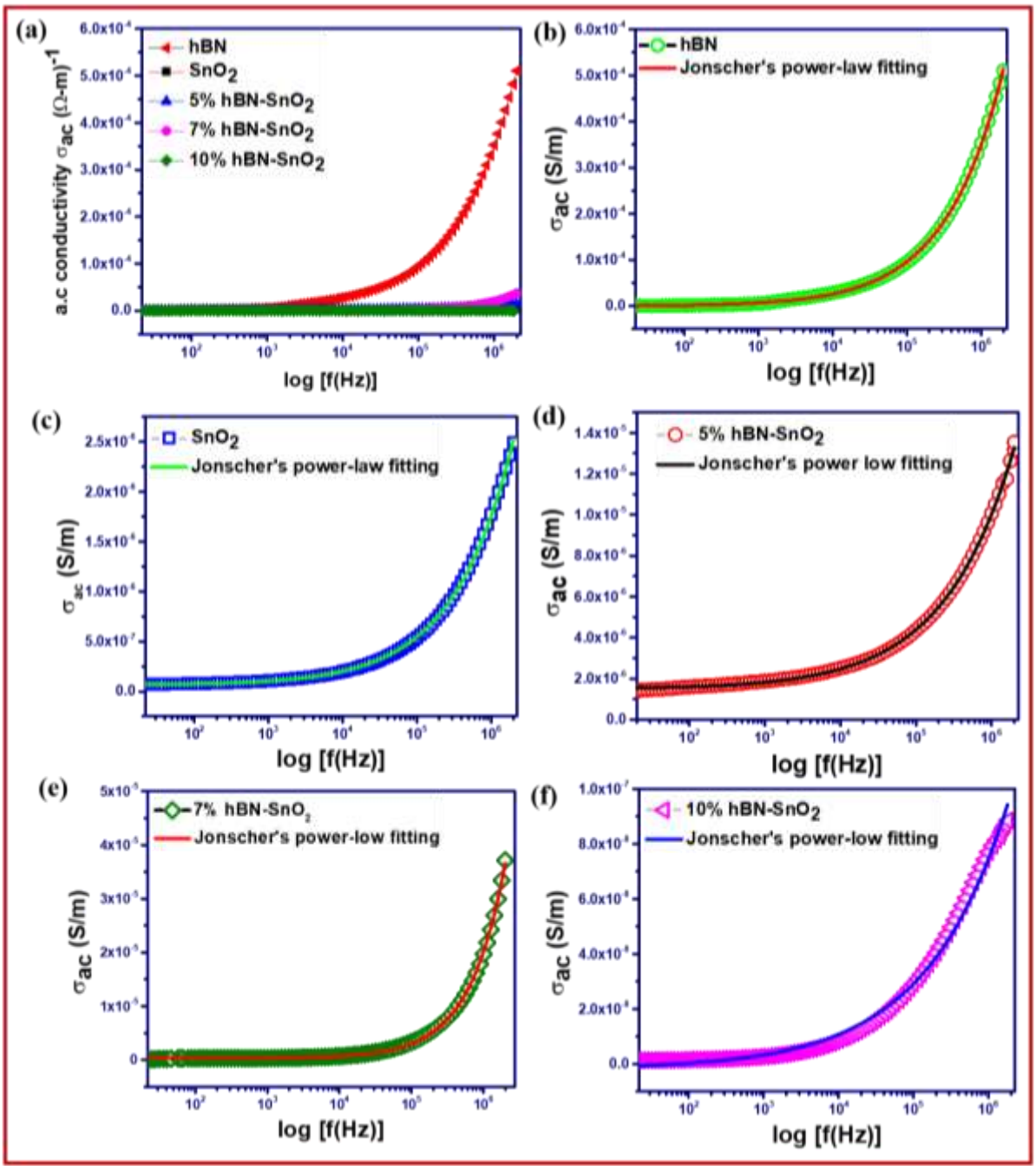

Figure 5.9 (a) The relationship between frequency and ac conductivity (σ_{ac}). (b-d) The graphs of curve fitting for hBN, SnO_2, 5% hBN-SnO_2, 7% hBN-SnO_2, and 10% hBN-SnO_2 nanocomposite were created using Jonscher's power law.

5.3.10 Electrical characterization

The impact of hBN incorporation on SnO_2 electrical qualities is examined by ambient temperature I-V characteristics obtained using a Keithley 2450 SMU. The schematic representation of the metal-insulator-metal (MIM) created memory device configuration to explore the I-V characteristics are depicted in Figure 5.10.

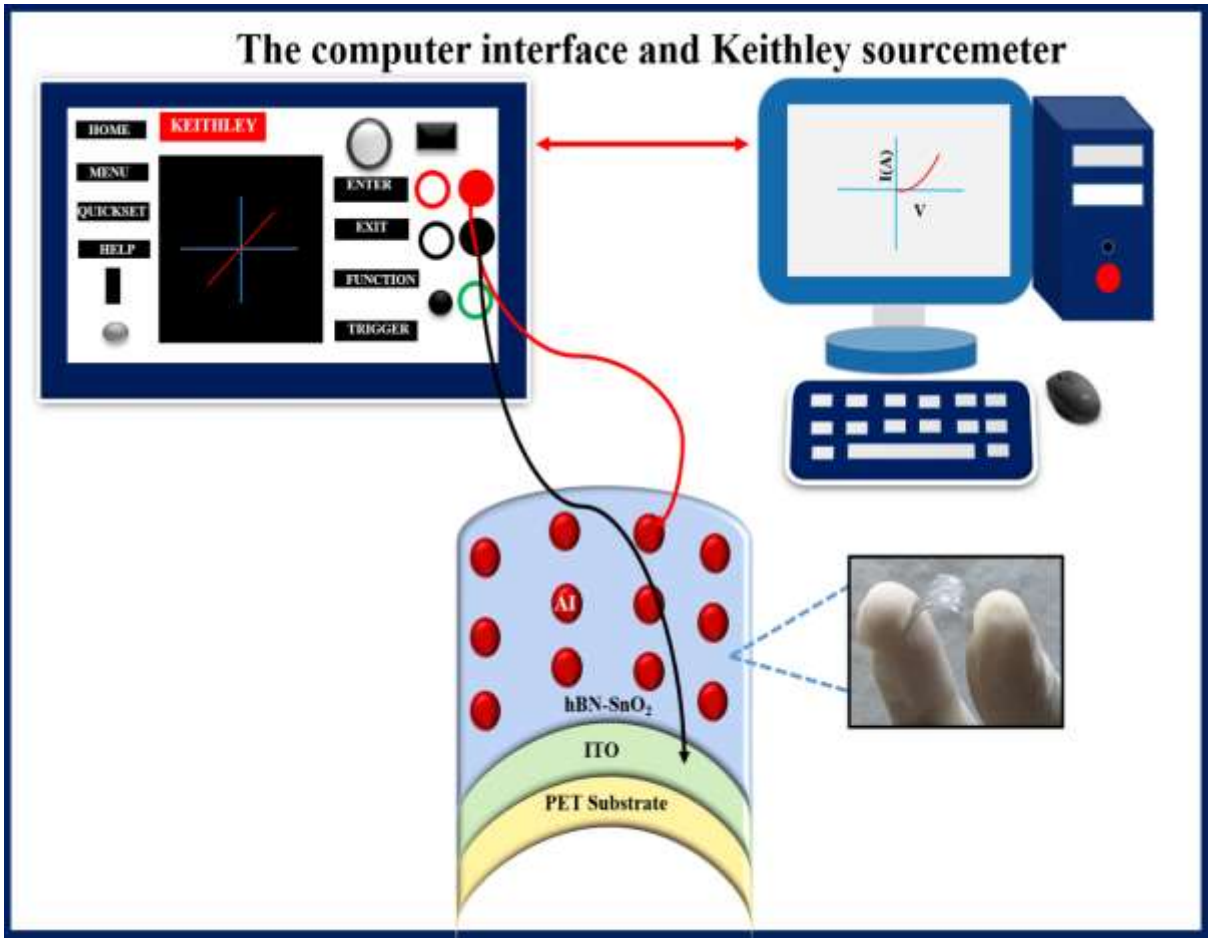

Figure 5.10 Schematic depicting the measuring procedure used an optical image of the actual memory device and a Keithley 2450 source meter with a LabVIEW-controlled program for I-V measurement.

Figures 5.11(a-d) displays the I-V properties for Al/SnO_2/ITO-PET and Al/hBN-SnO_2/ITO-PET films with various hBN weight percentages in SnO_2 by increasing the voltage from -1 V to +1 V. Figures 5.11(e-h) depicts the resistive switching behaviour of all produced memory devices. As shown, the device with the hBN-SnO_2 based nanocomposite exhibits behaviour different from the pure SnO_2-based device, demonstrating that there is some interfacial interaction at the hBN-SnO_2 interface. To investigate the memory phenomenon further, the voltage is raised. It is found that the device enters the SET state (6.5 V) for pure SnO_2-based devices (Al/SnO_2/ITO-PET), transitioning from the early HRS to the LRS. However, while the voltage continues to rise in the same direction, as shown in Figure 5.11e, there is no transition from LRS to HRS. For the device to complete the reset transition, the voltage polarity needs to be reversed. The bipolar resistive switching behaviour is demonstrated by the gadget, which has been found to operate at -5.5 V. The direction of the voltage sweep is shown by the arrow. The SnO_2 based memory devices have higher switching voltages and lower hysteresis

which are not useful for real-world applications. As a result, the device using hBN-SnO_2 nanocomposite as an active layer was investigated further. The various weight percentages of hBN in SnO_2 based devices have been designed and evaluated to understand the impact of 2D hBN in SnO_2 for memory device applications. As demonstrated in Figures 5.11(f-h), all of the hBN-SnO_2 nanocomposite devices exhibited bipolar resistive switching (BRS) characteristics. Additionally, the memory phenomenon with 7 weight percent hBN-SnO_2 based nanocomposite has a higher ON/OFF current ratio, as shown in Figure 5.11g. The HRS to LRS transition appears on the nanocomposite-based device at a much lower voltage of 0.5 V, while the LRS to HRS transition occurs at -0.7 V, in comparison to pure SnO_2 based memory device. The device fabricated from hBN-SnO_2 exhibits better resistive switching behaviour. At a read voltage of 0.5V, the I_{ON}/I_{OFF} ratios for devices based on pure SnO_2, 5%, 7%, and 10% hBN-SnO_2 are 2, 96, 1000, and 10, respectively. This demonstrates the hybrid 7%hBN-SnO_2 device exhibits enhanced resistive switching capabilities. When compared to pure SnO_2, a higher resistive switching ratio (I_{ON}/I_{OFF}) may be caused by the interfacial contact between hBN and SnO_2 nanoparticles. Additionally, it should be noted that, as seen in the XPS spectra, the composite formed from SnO_2 and hBN also significantly improves the switching parameter. According to Singh et al., resistive memory-based metal oxide nanocomposite applications have two advantages: they not only serve as an oxygen reservoir but also as a blocking layer to stop oxygen from diffusing into the switching layers, improving the switching ratio [203].

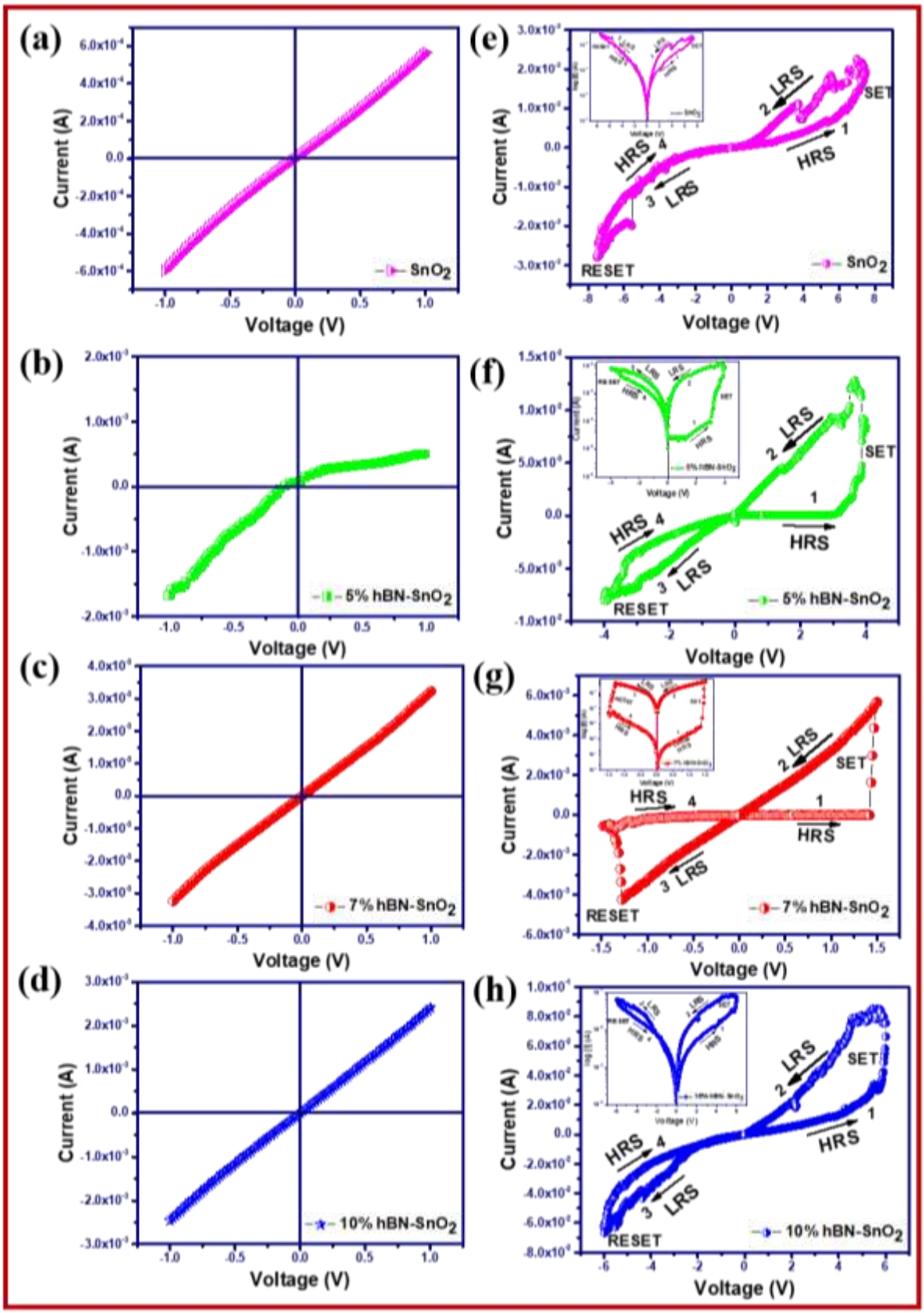
(a)
Current (A)
Voltage (V)
SnO2
(e)
Current (A)
Voltage (V)
SET
LRS
HRS
RESET
SnO2
(b)
Current (A)
Voltage (V)
5% hBN-SnO2
(f)
Current (A)
Voltage (V)
SET
LRS
HRS
RESET
5% hBN-SnO2
(c)
Current (A)
Voltage (V)
7% hBN-SnO2
(g)
Current (A)
Voltage (V)
SET
LRS
HRS
RESET
7% hBN-SnO2
(d)
Current (A)
Voltage (V)
10% hBN-SnO2
(h)
Current (A)
Voltage (V)
SET
LRS
HRS
RESET
10% hBN-SnO2

Fig. 5.11 (a-d) shows the I-V properties and (e-h) The resistive switching properties observed for pure SnO_2, and hBN-SnO_2 nanocomposite with the different weight percentages of hBN powder. The Inset of resistive switching figures shows the logarithmic I-V curves.

For understanding the switching phenomena in Al/7%hBN-SnO_2/ITO-PET, the I-V features of the positive area are displayed on a dual logarithmic scale as displayed in Figure 5.12a. At lower voltage ohmic conduction mechanism dominates in the HRS region since the device fitted I-V curve in the HRS has a slope of 1, as illustrated in Figure 5.12a. Due to electron trapping in the HRS, a good conductive filament most likely exists because the applied voltage changes approximately proportionally to the change in current. Then, every trap within the active layer of the 7%hBN-SnO_2 material are filled with injected electrons as resulting from space-charge-limited conduction (SCLC), and the voltage squared determines the current. Therefore, based on the I-V curves, the slope rises near 2.5 in the high voltage region. This is further supported by fitting the I-V characteristics in the high voltage area (slope of 2.5 on the log (I) vs. log (V) curve) with the Schottky emission model. The work function of the electrode and the resultant hBN-SnO_2 nanocomposites vary, which is responsible for this interface-limited conduction process, as shown by the equation below.

$$\text{In I} \propto \sqrt{\frac{e^3}{4\pi\varepsilon_r\,\varepsilon_0\,d}}\ \sqrt{V}/\text{kT} \qquad (6)$$

In the higher voltage area of HRS, Schottky emission is the predominant charge transport method, as indicated by the linear plot between log (I) vs $V^{1/2}$ displayed in the Inset of Figure 5.12a. The excellent fit of the I-V curve at a higher voltage by the Schottky model indicates that multiple charge transport mechanisms are operational in HRS [195, 196]. Further, in LRS the entire region is fitted with the slope of ohmic conduction is about 1.2. This type of mechanism is seen in devices where the contact at the junction is ohmic, allowing carriers to enter and move freely inside the insulating layer [197]. When the rate of injecting electrons into a material conduction band is higher than the rate of electron recombination, the SCLC mechanism occurs. Due to electron scattering, this high number of electrons limits the devices current flow. The vacancies in the oxygen within the hBN thin layer may be the cause of the HRS region that includes this SCLC mechanism.

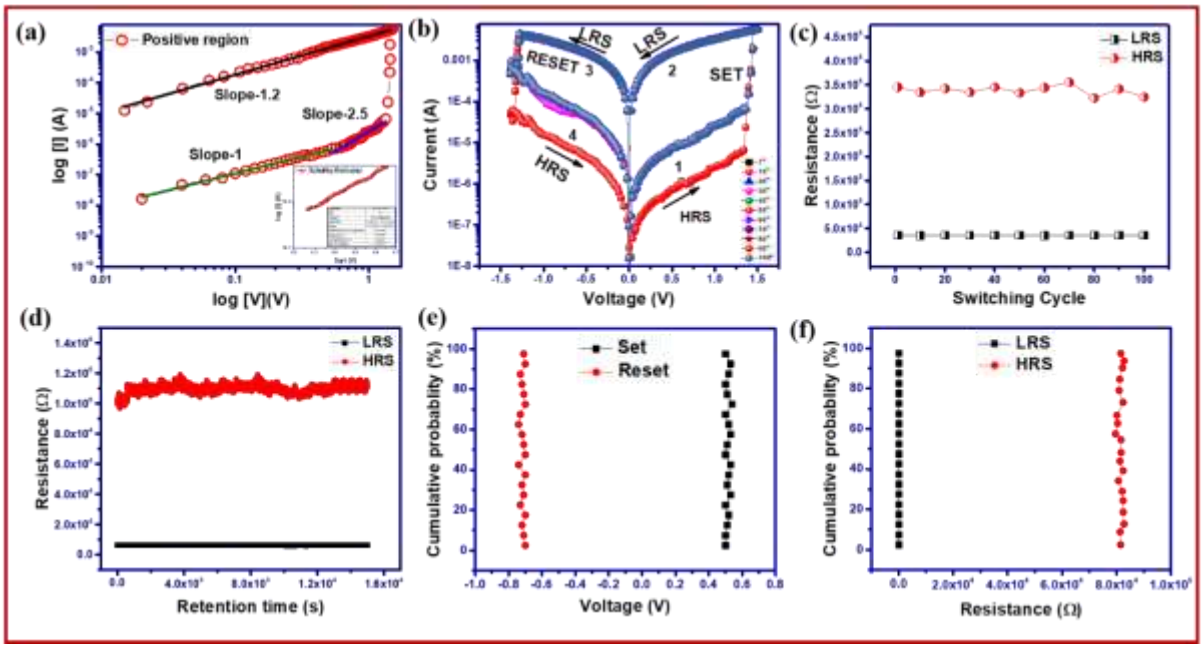

Fig. 5.12 (a) Positive LRS, HRS at log-log scale. (b-c) The hBN-SnO_2 based device endurance performance over 100 resistive switching cycles. (d) Sustained resistance in HRS and LRS for roughly 1.6×10^4 s stipulating robust performance. (e-f) The device-to-device cumulative probability distributions of Vset-Vreset and HRS-LRS of 7%hBN-SnO_2 RRAM devices.

A sequence of endurance tests was conducted to look at the device stability having the highest memory window(Al/7%hBN-SnO_2/ITO-PET). Figure 5.12b illustrates the fact that after 100 cycles, the device performance is still stable. Sweeping voltages of 0 to +1.5 V and 0 to -1.5 V, respectively, were applied for the functions of set and reset. The resistance between ON and OFF at ambient temperature was determined using a 0.5 V read voltage. The retention parameters displayed in Figure 5.12d demonstrate that HRS and LRS may be retained by the 7%hBN-SnO_2 based device for more than 1.6×10^4 seconds without suffering any significant degradation. According to Figure 5.12c, the devices memory window, as determined by R_{ON}/R_{OFF}, is 1000. These findings show that the Al/7%hBN-SnO_2/ITO-PET device is not degraded even after repeated cycles. These findings support the repeatability and reversibility of the transition between the OFF and ON states. Through a constant resistance ratio of LRS/HRS throughout 100 cycles both HRS and LRS are unaffected at the read voltage of 0.5 V. The above-mentioned results show that switching between HRS and LRS is improved for the Al/7%hBN-SnO_2/ITO-PET device, and the device performance is consistent and durable. Additionally, we looked at the V_{SET}-V_{RESET}, LRS, HRS continuous probability distributions from device to device for the 7%hBN-SnO_2 RRAM devices, which are shown in Figures 5.12(e) and 5.12(f), respectively. The operation voltages of the device-to-device distribution

were calculated using the average of the first 10 cycles of each of the 20 tested devices [198]. For a practical memory application, it is necessary to address the small variation in the RESET process, which can be related to the unpredictability of the filament rupture process. The SET voltage variability varies very little between devices. The fact that the device-to-device LRS and HRS vary very little should be addressed as they demonstrate the fabricated memory devices dependability [199].

5.4 Summary

In conclusion, a memory device based on Al/hBN-SnO_2/ITO-PET structure has been fabricated to explore the impact of hBN concentration on the resistive switching performance. The 5%hBN-SnO_2, 7%hBN-SnO_2, and 10%hBN-SnO_2 nanocomposite samples, with average particle sizes of 26.1 nm, 20.8 nm, and 20.7 nm, are successfully synthesized via hydrothermal synthesis. FTIR, FESEM, TEM, XRD, Raman, and XPS analysis were used to characterize the nanocomposite as it was formed. The hBN-SnO_2 nanocomposite in comparison to pure SnO_2 and hBN, shows the shift in the core level peaks, corresponding to B1s, N1s, C1s, O1s, and Sn 3d peaks, thereby indicating an interfacial interaction. The dielectric constant, dielectric loss factor, and AC conductivity were found to change with hBN quantity and frequency. In comparison to SnO_2, 5%hBN-SnO_2, and 10%hBN-SnO_2 nanocomposites, the 7%hBN-SnO_2 nanocomposite had a higher dielectric constant, lower loss, and increased ac conductivity. The percolation theory of conductive filler may explain dramatic variations in dielectric characteristics of hBN-SnO_2. The Nyquist plots only show one semicircle due to the grain boundary's contribution to the conduction process. AC conductivity was shown to be substantially dependent on frequency, with conductivity increasing at higher frequencies. AC conductivity follows the universal Jonscher's power law. Later, the fabricated devices made up of pure SnO_2 and hBN-SnO_2 (5, 7, and 10 wt.%) nanocomposite powder were tested for resistive switching applications. The resistive memory device based on hBN-SnO_2 nanocomposite further demonstrated its altered electrical properties with a decrease in switching parameters and an increase in the current ratio. The resistive switching performance of the fabricated device was compared and observed that the device with 7 wt. % hBN in SnO_2 has a maximum I_{ON}/I_{OFF} ratio of ~1000, in comparison to ~ 96 and ~10 for 5 and 10 wt. % sample respectively. Additionally, the Al/7%hBN-SnO_2/ITO-PET device exhibited switching characteristics with a lower switching voltage, good endurance behaviour up to 100 cycles, and another crucial factor for RRAM devices is retention time, which was measured for this device

up to 1.5×10^4 seconds. The described flexible device enhanced electrical properties show potential for future RRAM memory.

CHAPTER 6

Conclusions and scope for future work

This chapter summarizes the major conclusions of the present thesis and lists further studies that can be carried out to augment the present research work.

6.1 Summary and conclusions

This present thesis focuses on the synthesis of SnO_2-2D nanocomposite films and their use in resistive switching memory devices. We have demonstrated the significance of different 2D (rGO, MoS_2, hBN) materials in improving the performance of SnO_2 based memory device throughout this work. We have shown that, the adding of these nanostructures to SnO_2 increases its applicability for memory device properties. In this study, we have successfully fabricated hybrid SnO_2-2D nanocomposites for resistive memory device application. When compared to individual impacts, the hybrid systems perform much better. The main results gained from this investigation will be expanded on in the following parts.

1. The simple hydrothermal technique has been used for the synthesis of pure SnO_2 and SnO_2-2D materials (rGO, MoS_2, hBN) based nanocomposite.
2. Detailed structural, chemical composition, morphological studies have been investigated using XRD, Raman, FTIR, XPS, SEM, TEM and FESEM techniques. The shift in XPS peaks and variation of bang gap for the synthesized nanocomposite samples indicates the interfacial interactions. The resistive memory devices were fabricated in sandwich structure, by using spin-coating technique for depositing thin films of pure SnO_2 and SnO_2-2D materials over flexible ITO coated PET substrate with top Al electrodes.
3. Initially, the resistive switching effect of pure SnO_2 based memory device was studied, where it was observed that pure tin oxide-based memory device does not exhibit resistive switching property. Hence to induce the resistive switching effect which is commonly attributed to filament formation and rupture process occurring due to defect and oxygen ion/vacancies migration, the nanocomposite based on pure reduced graphene oxide and tin oxide was synthesized and tested for resistive memory device performance. The fabricated hybrid device (Al/ rGO-SnO_2/ITO-PET) showed the bipolar resistive switching behaviour with improved switching parameters and memory window. To further quantify the output performance,

different weight percentage of rGO (5%, 7%, and 10 wt.%) was incorporated into the SnO_2 matrix. The shift in the Sn 3d, C1s and O1s spectra for the SnO_2-rGO samples confirmed the interfacial interaction and are attributed to reduction in switching parameters, and improvement in the current ratio (I_{ON}/I_{OFF}) of 70 for nanocomposite sample having 7 wt % rGO in comparison to pure SnO_2 based resistive memory device. The Al/7%rGO-SnO_2/ITO-PET device exhibited best switching characteristics with a lower switching voltage and more stability. Additionally, Al/7%rGO-SnO_2/ITO-PET based memory device showed good endurance behaviour up to 100 cycles, higher I_{ON}/I_{OFF} ratio, and retention time, which was measured for this device up to 2×10^3 seconds.

4. To further improve the performance of SnO_2 based memory device, semiconducting 2D materials MoS_2 in SnO_2 matrix was used with varying concentration. The XPS core level spectra for Mo 3d, S 2p, O1s, and Sn 3d peaks for the MoS_2-SnO_2 nanocomposite show stronger interfacial interaction between MoS_2 and SnO_2. The dielectric measurement shows that the 10%MoS_2-SnO_2 nanocomposite exhibited highest dielectric constant, and dielectric loss in comparison to pure SnO_2 and MoS_2 material. The reduction in space charge polarisation accounts for how impedance changes with frequency. The Nyquist plots have just one semicircle, which can be attributed to a result of the contribution of the grain boundary to the conduction process. The a.c. conductivity data confirms the involvement of bound charge carriers and is fitted with Jonscher's power law. Furthermore, the impacts of the MoS_2 in SnO_2 on the resistive switching capabilities of nanocomposite film were investigated by designing a device in MIM configuration with Al and ITO-PET as top and bottom electrodes, respectively sandwiching active MoS_2-SnO_2 (5%, 7%, and 10 wt.%) memory layers. The Al/MoS_2-SnO_2/ITO-PET memory device displays the bipolar resistive switching phenomenon. The I_{On}/I_{Off} ratio for the fabricated Al/7%MoS_2-SnO_2/ITO-PET device was 100 times greater than that of Al/SnO_2/ITO-PET device. The fabricated memory device showed enhanced switching performance, with resistance ratio, endurance, and retention of about ~100, 100 switching cycles, and 2.1×10^3 seconds, respectively. To check the potential of fabricated device for flexible electronic applications, the device was exhibited 100 bending cycles, without any serious degradation in high and low resistance states.
5. To further enhance the memory window, the insulating and high band gap two dimensional layered materials hexagonal boron nitride (hBN) with SnO_2 was used as an active switching layer in sandwich configuration. The fabricated devices were Al/hBN-SnO_2/ITO-PET with varying hBN (5%, 7%, and 10 wt.%) content in composite films. When comparing the hBN-SnO_2 nanocomposite to pure SnO_2 and hBN, the shift in the B1s, N1s, C1s, O1s, and Sn 3d

peaks indicates an interfacial interaction. The effect of this interaction was also observed in the calculated optical band gap, dielectric constant, morphological structure also. The electrical performance of hBN-SnO_2 nanocomposite films further demonstrated modified properties with a decrease in switching parameters and an increase in the current ratio with varying hBN content. The resistive switching performance of the fabricated device was compared and observed that the device with 7 wt. % hBN in SnO_2 has a maximum I_{ON}/I_{OFF} ratio of ~1000, in comparison to ~96 and ~10 for 5 and 10 wt. % sample respectively. Additionally, the Al/7%hBN-SnO_2/ITO-PET device exhibited switching characteristics with a lower switching voltage, good endurance behaviour up to 100 cycles, and another crucial factor for RRAM devices is retention time, which was measured for this device up to 1.5×10^4 seconds. The observed bipolar resistive switching is attributed to the polarity induced migration of enhanced oxygen defects created inside the SnO_2-2D based nanocomposite layers.

6.2 Scope for future studies

1. There is a large scope for research work on the effect of 2D layered-inorganic metal oxide materials nature, the nature of alignment, bonding between the 2D layer to the binary metal oxides and metal, electronic states of the interface and chemical composition, needs be investigated. However, additional research into the switching process is required to clarify the transport mechanism in RRAMs. This research should focus on electrode materials, electrode sizes, temperature-dependent measurement, etc., and greater spectroscopic examination, such as advanced microscopies like AFM, Raman spectroscopy, and in-depth XPS. Cross sectioned HRTEM imaging, Auger electron spectroscopy, and EDAX analysis can be carried out to further study the nature of hybrid interface.
2. The major hindrance for the practical application of the ReRAM device is the large dispersion of the switching parameters (reset voltage, set voltage, memory window). It has been reported that nanoparticles embedded in the oxide matrix leads to the enhancement of electric field in their vicinity. This can be used for reducing the forming voltage and also the metal nanoparticle can work as nanoscale intermediate electrodes leading to the control of filament position in the oxide matrix. For this, size selected nanoparticles can be either incorporated in the oxide or can also work as bottom electrodes and control the filament size (reset current) and position, thereby, eliminating the dispersion in the memory device parameters.
3. Swift heavy ion irradiation is a powerful technique to systematically create the defect states (metal vacancies and/or interstitial oxygen in the oxides). As the resistive switching is due to the formation and rupture of conducting filaments which may be composed of either metallic

ion or oxygen vacancies/ions. Ion irradiation experiments can be carried out to create intentional defects and control oxygen vacancies in the active SnO_2-2D layer.

4. The crossbar memory structure based on various binary oxides in 1T1R (1 transistor - 1 resistor) and 1D1R (1 diode - 1 resistor) configuration can be designed and fabricated for improving the device density.
5. To control the switching parameters, underlying mechanism should be clear, and therefore atomic-scale first-principles simulations using density functional theory (DFT) will be carried out for understanding the interfacial interaction between metal oxide and 2D material during formation and rupture of filaments.

References:

[1] A.S. Edelstein, R. Cammaratra, Nanomaterials: synthesis, properties and applications, CRC press, 1998.
[2] B.D. Malhotra, M.A. Ali, Nanomaterials in biosensors: Fundamentals and applications, Nanomaterials for biosensors, (2018) 1.
[3] C. Anichini, W. Czepa, D. Pakulski, A. Aliprandi, A. Ciesielski, P. Samorì, Chemical sensing with 2D materials, Chemical Society Reviews, 47 (2018) 4860-4908.
[4] H. Zhang, H.-M. Cheng, P. Ye, 2D nanomaterials: beyond graphene and transition metal dichalcogenides, Chemical Society Reviews, 47 (2018) 6009-6012.
[5] Y. Zhu, S. Murali, W. Cai, X. Li, J.W. Suk, J.R. Potts, R.S. Ruoff, Graphene and graphene oxide: synthesis, properties, and applications, Advanced materials, 22 (2010) 3906-3924.
[6] A. Sinha, B. Tan, Y. Huang, H. Zhao, X. Dang, J. Chen, R. Jain, MoS2 nanostructures for electrochemical sensing of multidisciplinary targets: A review, TrAC Trends in Analytical Chemistry, 102 (2018) 75-90.
[7] Y. Zhao, L. Kuai, Y. Liu, P. Wang, H. Arandiyan, S. Cao, J. Zhang, F. Li, Q. Wang, B. Geng, Well-constructed single-layer molybdenum disulfide nanorose cross-linked by three dimensional-reduced graphene oxide network for superior water splitting and lithium storage property, Scientific Reports, 5 (2015) 8722.
[8] L. Wang, Y. Ma, M. Yang, Y. Qi, Hierarchical hollow MoS2 nanospheres with enhanced electrochemical properties used as an electrode in supercapacitor, Electrochimica Acta, 186 (2015) 391-396.
[9] Z. Li, J. Ma, Y. Zhou, Z. Yin, Y. Tang, Y. Ma, D. Wang, Synthesis of sulfur-rich MoS2 nanoflowers for enhanced hydrogen evolution reaction performance, Electrochimica Acta, 283 (2018) 306-312.
[10] A. Di Bartolomeo, A. Grillo, F. Urban, L. Iemmo, F. Giubileo, G. Luongo, G. Amato, L. Croin, L. Sun, S.J. Liang, Asymmetric Schottky contacts in bilayer MoS2 field effect transistors, Advanced Functional Materials, 28 (2018) 1800657.
[11] T. Wang, H. Zhu, J. Zhuo, Z. Zhu, P. Papakonstantinou, G. Lubarsky, J. Lin, M. Li, Biosensor based on ultrasmall MoS2 nanoparticles for electrochemical detection of H2O2 released by cells at the nanomolar level, Analytical chemistry, 85 (2013) 10289-10295.
[12] K.S. Novoselov, A.K. Geim, S.V. Morozov, D.-e. Jiang, Y. Zhang, S.V. Dubonos, I.V. Grigorieva, A.A. Firsov, Electric field effect in atomically thin carbon films, science, 306 (2004) 666-669.
[13] N.G. Chopra, R. Luyken, K. Cherrey, V.H. Crespi, M.L. Cohen, S.G. Louie, A. Zettl, Boron nitride nanotubes, science, 269 (1995) 966-967.
[14] C.R. Dean, A.F. Young, I. Meric, C. Lee, L. Wang, S. Sorgenfrei, K. Watanabe, T. Taniguchi, P. Kim, K.L. Shepard, Boron nitride substrates for high-quality graphene electronics, Nature nanotechnology, 5 (2010) 722-726.
[15] G. Grad, P. Blaha, K. Schwarz, W. Auwärter, T. Greber, Density functional theory investigation of the geometric and spintronic structure of h-BN/Ni (111) in view of photoemission and STM experiments, Physical Review B, 68 (2003) 085404.
[16] W.A. Wulf, S.A. McKee, Hitting the memory wall: Implications of the obvious, ACM SIGARCH computer architecture news, 23 (1995) 20-24.
[17] P. Kotasthane, A. Manchi, When the Chips Are Down: A Deep Dive into a Global Crisis, Bloomsbury Publishing, 2023.
[18] Z. Xu, Defects and Interface Engineering of SnO2 Based Nanomaterials for High Performance Memory Applications, in, UNSW Sydney, 2018.
[19] S.-Y. Wang, D.-Y. Lee, T.-Y. Huang, J.-W. Wu, T.-Y. Tseng, Controllable oxygen vacancies to enhance resistive switching performance in a ZrO2-based RRAM with embedded Mo layer, Nanotechnology, 21 (2010) 495201.
[20] K. Kim, D.J. Jung, A VISION OF FRAM AS A FUSION MEMORY, Integrated Ferroelectrics, 96 (2008) 100-111.

[21] A. Sawa, Resistive switching in transition metal oxides, Materials today, 11 (2008) 28-36.
[22] J.J. Yang, M.D. Pickett, X. Li, D.A. Ohlberg, D.R. Stewart, R.S. Williams, Memristive switching mechanism for metal/oxide/metal nanodevices, Nature nanotechnology, 3 (2008) 429-433.
[23] M.H. Lankhorst, B.W. Ketelaars, R.A. Wolters, Low-cost and nanoscale non-volatile memory concept for future silicon chips, Nature materials, 4 (2005) 347-352.
[24] R. Bez, E. Camerlenghi, A. Modelli, A. Visconti, Introduction to flash memory, Proceedings of the IEEE, 91 (2003) 489-502.
[25] J.F. Scott, C.A. Paz de Araujo, Ferroelectric memories, Science, 246 (1989) 1400-1405.
[26] M.N. Baibich, J.M. Broto, A. Fert, F.N. Van Dau, F. Petroff, P. Etienne, G. Creuzet, A. Friederich, J. Chazelas, Giant Magnetoresistance of (001)Fe/(001)Cr Magnetic Superlattices, Phys. Rev. Lett., 61 (1988) 2472-2475.
[27] Y. Suezawa, Y. Gondō, Spin-polarized electrons and magnetoresistance in ferromagnetic tunnel junctions and multilayers, Journal of Magnetism and Magnetic Materials, 126 (1993) 524-526.
[28] E.T. Wertz, Q. Li, Magnetoresistance after initial demagnetization in La[sub 0.67]Sr[sub 0.33]MnO[sub 3]/SrTiO[sub 3]/La[sub 0.67]Sr[sub 0.33]MnO[sub 3] magnetic tunnel junctions, Appl. Phys. Lett., 90 (2007) 142506-142503.
[29] Y. Ogimoto, M. Izumi, A. Sawa, T. Manako, H. Sato, H. Akoh, M. Kawasaki, Y. Tokura, Tunneling Magnetoresistance above Room Temperature in La$_{0.7}$Sr$_{0.3}$MnO$_{3}$/SrTiO$_{3}$/La$_{0.7}$Sr$_{0.3}$MnO$_{3}$ Junctions, Jpn. J. Appl. Phys., 42 L369.
[30] A.V. Kolobov, P. Fons, A.I. Frenkel, A.L. Ankudinov, J. Tominaga, T. Uruga, Understanding the phase-change mechanism of rewritable optical media, Nat Mater, 3 (2004) 703-708.
[31] M. Wuttig, N. Yamada, Phase-change materials for rewriteable data storage, Nat Mater, 6 (2007) 824-832.
[32] K. Seonghyun, K.P. Biju, J. Minseok, J. Seungjae, P. Jubong, L. Joonmyoung, L. Wootae, S. Jungho, P. Sangsu, H. Hyunsang, Effect of Scaling <formula formulatype="inline"> <img src="/images/tex/19696.gif" alt="\hbox {WO}_{x}"> </formula>-Based RRAMs on Their Resistive Switching Characteristics, Electron Device Letters, IEEE, 32 (2011) 671-673.
[33] C.-Y. Lin, C.-Y. Wu, C.-Y. Wu, L. Tzyh-Cheang, Y. Fu-Liang, H. Chenming, T.-Y. Tseng, Effect of Top Electrode Material on Resistive Switching Properties of <formula formulatype="inline"> <img src="/images/tex/592.gif" alt="\hbox {ZrO}_{2}"> </formula> Film Memory Devices, Electron Device Letters, IEEE, 28 (2007) 366-368.
[34] H.-S.P. Wong, S. Salahuddin, Memory leads the way to better computing, Nature nanotechnology, 10 (2015) 191-194.
[35] S. Yu, Resistive random access memory (RRAM), Morgan & Claypool Publishers, 2016.
[36] H.-S.P. Wong, S. Raoux, S. Kim, J. Liang, J.P. Reifenberg, B. Rajendran, M. Asheghi, K.E. Goodson, Phase change memory, Proceedings of the IEEE, 98 (2010) 2201-2227.
[37] D. Apalkov, B. Dieny, J.M. Slaughter, Magnetoresistive random access memory, Proceedings of the IEEE, 104 (2016) 1796-1830.
[38] V. Gupta, S. Kapur, S. Saurabh, A. Grover, Resistive random access memory: a review of device challenges, IETE Technical Review, 37 (2020) 377-390.
[39] D. Ielmini, Resistive switching memories based on metal oxides: mechanisms, reliability and scaling, Semiconductor Science and Technology, 31 (2016) 063002.
[40] X. Yang, Demonstration of ultra-fast switching in nanometallic resistive switching memory devices, Journal of Nanoscience, 2016 (2016).
[41] W.W. Zhuang, W. Pan, B.D. Ulrich, J.J. Lee, L. Stecker, A. Burmaster, D.R. Evans, S.T. Hsu, M. Tajiri, A. Shimaoka, K. Inoue, T. Naka, N. Awaya, A. Sakiyama, Y. Wang, S.Q. Liu, N.J. Wu, A. Ignatiev, Novel colossal magnetoresistive thin film nonvolatile resistance random access memory (RRAM), in: Electron Devices Meeting, 2002. IEDM '02. International, 2002, pp. 193-196.
[42] T. Hickmott, Low-frequency negative resistance in thin anodic oxide films, Journal of Applied Physics, 33 (1962) 2669-2682.

[43] I.G. Baek, M.S. Lee, S. Seo, M.J. Lee, D.H. Seo, D.S. Suh, J.C. Park, S.O. Park, T.I. Kim, I.K. Yoo, U.i. Chung, J.T. Moon, Highly scalable nonvolatile resistive memory using simple binary oxide driven by asymmetric unipolar voltage pulses, in: Electron Devices Meeting, 2004. IEDM Technical Digest. IEEE International, 2004, pp. 587-590.
[44] B.J. Choi, D.S. Jeong, S.K. Kim, C. Rohde, S. Choi, J.H. Oh, H.J. Kim, C.S. Hwang, K. Szot, R. Waser, B. Reichenberg, S. Tiedke, Resistive switching mechanism of TiO[sub 2] thin films grown by atomic-layer deposition, J. Appl. Phys., 98 (2005) 033715-033710.
[45] C. An, S. Haddad, W. Yi-Ching, F. Tzu-Ning, L. Zhida, S. Avanzino, S. Pangrle, M. Buynoski, M. Rathor, C. Wei, N. Tripsas, C. Bill, M. VanBuskirk, M. Taguchi, Non-volatile resistive switching for advanced memory applications, in: Electron Devices Meeting, 2005. IEDM Technical Digest. IEEE International, 2005, pp. 746-749.
[46] W.-Y. Chang, Y.-C. Lai, T.-B. Wu, S.-F. Wang, F. Chen, M.-J. Tsai, Unipolar resistive switching characteristics of ZnO thin films for nonvolatile memory applications, Appl. Phys. Lett., 92 (2008) 022110-022113.
[47] D. Adler, M.S. Shur, M. Silver, S.R. Ovshinsky, Threshold switching in chalcogenide-glass thin films, J. Appl. Phys., 51 (1980) 3289-3309.
[48] R.S. Potember, T.O. Poehler, D.O. Cowan, Electrical switching and memory phenomena in Cu-TCNQ thin films, Appl. Phys. Lett., 34 (1979) 405-407.
[49] F. Zahoor, T.Z. Azni Zulkifli, F.A. Khanday, Resistive random access memory (RRAM): an overview of materials, switching mechanism, performance, multilevel cell (MLC) storage, modeling, and applications, Nanoscale research letters, 15 (2020) 1-26.
[50] L. Zhao, Z. Jiang, H.-Y. Chen, J. Sohn, K. Okabe, B. Magyari-Köpe, H.-S.P. Wong, Y. Nishi, Ultrathin (~ 2nm) HfO x as the fundamental resistive switching element: Thickness scaling limit, stack engineering and 3D integration, in: 2014 IEEE International Electron Devices Meeting, IEEE, 2014, pp. 6.6. 1-6.6. 4.
[51] B. Govoreanu, G.S. Kar, Y. Chen, V. Paraschiv, S. Kubicek, A. Fantini, I. Radu, L. Goux, S. Clima, R. Degraeve, 10× 10nm 2 Hf/HfO x crossbar resistive RAM with excellent performance, reliability and low-energy operation, in: 2011 International Electron Devices Meeting, IEEE, 2011, pp. 31.36. 31-31.36. 34.
[52] X. Hong, D.J. Loy, P.A. Dananjaya, F. Tan, C. Ng, W. Lew, Oxide-based RRAM materials for neuromorphic computing, Journal of materials science, 53 (2018) 8720-8746.
[53] G. Wang, S. Long, M. Zhang, Y. Li, X. Xu, H. Liu, M. Wang, P. Sun, H. Sun, Q. Liu, Operation methods of resistive random access memory, Science China Technological Sciences, 57 (2014) 2295-2304.
[54] W.-Y. Chang, Y.-C. Lai, T.-B. Wu, S.-F. Wang, F. Chen, M.-J. Tsai, Unipolar resistive switching characteristics of ZnO thin films for nonvolatile memory applications, Applied Physics Letters, 92 (2008).
[55] D. Liu, N. Wang, G. Wang, Z. Shao, X. Zhu, C. Zhang, H. Cheng, Nonvolatile bipolar resistive switching in amorphous Sr-doped LaMnO3 thin films deposited by radio frequency magnetron sputtering, Applied Physics Letters, 102 (2013).
[56] H.Y. Lee, P.S. Chen, T.Y. Wu, Y.S. Chen, C.C. Wang, P.J. Tzeng, C.H. Lin, F. Chen, C.H. Lien, M.J. Tsai, Low power and high speed bipolar switching with a thin reactive Ti buffer layer in robust HfO2 based RRAM, in: Electron Devices Meeting, 2008. IEDM 2008. IEEE International, 2008, pp. 1-4.
[57] C. He, Z. Shi, L. Zhang, W. Yang, R. Yang, D. Shi, G. Zhang, Multilevel Resistive Switching in Planar Graphene/SiO2 Nanogap Structures, ACS Nano, 6 (2012) 4214-4221.
[58] L. Dongsoo, S. Dong-jun, C. Hye jung, J. Inhwa, R. Dong, W. Xiang, O. Seokjoon, M. Pyun, S. Sun-ok, H. Seongho, J. Minseok, H. Dae-Kyu, H.K. Park, M. Chang, M. Hasan, H. Hyunsang, Excellent uniformity and reproducible resistance switching characteristics of doped binary metal oxides for non-volatile resistance memory applications, in: Electron Devices Meeting, 2006. IEDM '06. International, 2006, pp. 1-4.
[59] W. Guan, S. Long, R. Jia, M. Liu, Nonvolatile resistive switching memory utilizing gold nanocrystals embedded in zirconium oxide, Appl. Phys. Lett., 91 (2007) 062111-062113.

[60] H.-S.P. Wong, H.-Y. Lee, S. Yu, Y.-S. Chen, Y. Wu, P.-S. Chen, B. Lee, F.T. Chen, M.-J. Tsai, Metal–oxide RRAM, Proceedings of the IEEE, 100 (2012) 1951-1970.
[61] I. Baek, D. Kim, M. Lee, H.-J. Kim, E. Yim, M. Lee, J. Lee, S. Ahn, S. Seo, J. Lee, Multi-layer cross-point binary oxide resistive memory (OxRRAM) for post-NAND storage application, in: IEEE InternationalElectron Devices Meeting, 2005. IEDM Technical Digest., IEEE, 2005, pp. 750-753.
[62] L.O. Chua, Memristor-The Missing Circuit Element, IEEE Transaction On Circuit Theory, vol ct-l 8, in, 1971.
[63] D.B. Strukov, G.S. Snider, D.R. Stewart, R.S. Williams, The missing memristor found, nature, 453 (2008) 80-83.
[64] J.J. Yang, M.D. Pickett, X. Li, A.A. OhlbergDouglas, D.R. Stewart, R.S. Williams, Memristive switching mechanism for metal//oxide//metal nanodevices, Nat Nano, 3 (2008) 429-433.
[65] X.L. Deng, S. Hong, I. Hwang, J.-S. Kim, J.H. Jeon, Y.C. Park, J. Lee, S.-O. Kang, T. Kawai, B.H. Park, Confining grains of textured Cu2O films to single-crystal nanowires and resultant change in resistive switching characteristics, Nanoscale, 4 (2012) 2029-2033.
[66] A. Chen, S. Haddad, Y.C. Wu, T.N. Fang, S. Kaza, Z. Lan, Erasing characteristics of Cu[sub 2]O metal-insulator-metal resistive switching memory, Appl. Phys. Lett., 92 (2008) 013503-013503.
[67] R. Waser, R. Dittmann, G. Staikov, K. Szot, Redox-Based Resistive Switching Memories – Nanoionic Mechanisms, Prospects, and Challenges, Adv. Mat., 21 (2009) 2632-2663.
[68] K. Kinoshita, T. Tamura, M. Aoki, Y. Sugiyama, H. Tanaka, Bias polarity dependent data retention of resistive random access memory consisting of binary transition metal oxide, Appl. Phys. Lett., 89 (2006) 103509-103503.
[69] M.H. Lee, C.S. Hwang, Resistive switching memory: observations with scanning probe microscopy, Nanoscale, 3 (2011) 490-502.
[70] S. Tsui, A. Baikalov, J. Cmaidalka, Y.Y. Sun, Y.Q. Wang, Y.Y. Xue, C.W. Chu, L. Chen, A.J. Jacobson, Field-induced resistive switching in metal-oxide interfaces, Appl. Phys. Lett., 85 (2004) 317-319.
[71] A. Sawa, T. Fujii, M. Kawasaki, Y. Tokura, Colossal Electro-Resistance Memory Effect at Metal/La$_{2}$CuO$_{4}$ Interfaces, Jpn. J. Appl. Phys., 44 L1241.
[72] L. Cario, C. Vaju, B. Corraze, V. Guiot, E. Janod, Electric-field-induced resistive switching in a family of Mott insulators: Towards a new class of RRAM memories, Advanced Materials, 22 (2010) 5193-5197.
[73] H.Y. Peng, G.P. Li, J.Y. Ye, Z.P. Wei, Z. Zhang, D.D. Wang, G.Z. Xing, T. Wu, Electrode dependence of resistive switching in Mn-doped ZnO: Filamentary versus interfacial mechanisms, Appl. Phys. Lett., 96 (2010) 192113-192113.
[74] S.E. Ahn, M.J. Lee, Y. Park, B.S. Kang, C.B. Lee, K.H. Kim, S. Seo, D.S. Suh, D.C. Kim, J. Hur, W. Xianyu, G. Stefanovich, H. Yin, I.K. Yoo, J.H. Lee, J.B. Park, I.G. Baek, B.H. Park, Write Current Reduction in Transition Metal Oxide Based Resistance Change Memory, Adv. Mat., 20 (2008) 924-928.
[75] I.H. Inoue, S. Yasuda, H. Akinaga, H. Takagi, Nonpolar resistance switching of metal/binary-transition-metal oxides/metal sandwiches: Homogeneous/inhomogeneous transition of current distribution, Phys. Rev. B, 77 (2008) 035105.
[76] K. Kinoshita, T. Tamura, M. Aoki, Y. Sugiyama, H. Tanaka, Lowering the Switching Current of Resistance Random Access Memory Using a Hetero Junction Structure Consisting of Transition Metal Oxides, Jpn. J. Appl. Phys., 45 L991.
[77] H. Méndez, I. Thurzo, D.R.T. Zahn, Experimental study of charge transport mechanisms in a hybrid metal/organic/inorganic device, Phys. Rev. B, 75 (2007) 045321.
[78] H. Kim, D.-H. Seo, S.-W. Kim, J. Kim, K. Kang, Highly reversible Co3O4/graphene hybrid anode for lithium rechargeable batteries, Carbon, 49 (2011) 326-332.
[79] F. Tong, K. Kim, D. Martinez, R. Thapa, A. Ahyi, J. Williams, D.-J. Kim, S. Lee, E. Lim, K.K. Lee, M. Park, Flexible organic/inorganic hybrid solar cells based on conjugated polymer and ZnO nanorod array, Semiconductor Science and Technology, 27 (2012) 105005.
[80] R. Zhu, C.-Y. Jiang, B. Liu, S. Ramakrishna, Highly Efficient Nanoporous TiO2-Polythiophene Hybrid Solar Cells Based on Interfacial Modification Using a Metal-Free Organic Dye, Adv. Mat., 21 (2009) 994-1000.

[81] J. Lee, B.-J. Jung, J.-I. Lee, H.Y. Chu, L.-M. Do, H.-K. Shim, Modification of an ITO anode with a hole-transporting SAM for improved OLED device characteristics, J. Mater. Chem., 12 (2002) 3494-3498.
[82] G.B. Murdoch, M. Greiner, M.G. Helander, Z.B. Wang, Z.H. Lu, A comparison of CuO and Cu[sub 2]O hole-injection layers for low voltage organic devices, Appl. Phys. Lett., 93 (2008) 083309-083303.
[83] C.R. Kagan, D.B. Mitzi, C.D. Dimitrakopoulos, Organic-Inorganic Hybrid Materials as Semiconducting Channels in Thin-Film Field-Effect Transistors, Science, 286 (1999) 945-947.
[84] F. Verbakel, S.C.J. Meskers, R.A.J. Janssen, Electronic memory effects in diodes from a zinc oxide nanoparticle-polystyrene hybrid material, Appl. Phys. Lett., 89 (2006) 102103-102103.
[85] V. Kannan, Y.S. Chae, C.V.V. Ramana, D.-S. Ko, J.K. Rhee, All-inorganic spin-cast quantum dot based bipolar nonvolatile resistive memory, J. Appl. Phys., 109 (2011) 086103-086103.
[86] G. Liu, Q.-D. Ling, E.Y.H. Teo, C.-X. Zhu, D.S.-H. Chan, K.-G. Neoh, E.-T. Kang, Electrical Conductance Tuning and Bistable Switching in Poly(N-vinylcarbazole)−Carbon Nanotube Composite Films, ACS Nano, 3 (2009) 1929-1937.
[87] S. Dong Ick, et al., Polymer–ultrathin graphite sheet–polymer composite structured flexible nonvolatile bistable organic memory devices, Nanotechnology, 22 (2011) 295203.
[88] H.Y. Jeong, J.Y. Kim, J.W. Kim, J.O. Hwang, J.-E. Kim, J.Y. Lee, T.H. Yoon, B.J. Cho, S.O. Kim, R.S. Ruoff, S.-Y. Choi, Graphene Oxide Thin Films for Flexible Nonvolatile Memory Applications, Nano Lett., 10 (2010) 4381-4386.
[89] C. Wu, F. Li, Y. Zhang, T. Guo, T. Chen, Highly reproducible memory effect of organic multilevel resistive-switch device utilizing graphene oxide sheets/polyimide hybrid nanocomposite, Appl. Phys. Lett., 99 (2011) 042108-042103.
[90] F. Li, D.I. Son, B.J. Kim, T.W. Kim, Nonvolatile electrical bistability and operating mechanism of memory devices based on CdSe/ZnS nanoparticle/polymer hybrid composites, Appl. Phys. Lett., 93 (2008) 021913-021913.
[91] D. Tyagi, H. Wang, W. Huang, L. Hu, Y. Tang, Z. Guo, Z. Ouyang, H. Zhang, Recent advances in two-dimensional-material-based sensing technology toward health and environmental monitoring applications, Nanoscale, 12 (2020) 3535-3559.
[92] X. Tong, E. Ashalley, F. Lin, H. Li, Z.M. Wang, Advances in MoS2-based field effect transistors (FETs), Nano-Micro Letters, 7 (2015) 203-218.
[93] H. Wang, N. Wang, T. Cheng, X. Wan, R. Sun, C.P. Wong, Halides-Assisted Low-Temperature Synthesis of Hexagonal Boron Nitride Nanosheets, Particle & Particle Systems Characterization, 36 (2019) 1900278.
[94] J. Chen, X. Huang, B. Sun, P. Jiang, Highly thermally conductive yet electrically insulating polymer/boron nitride nanosheets nanocomposite films for improved thermal management capability, ACS nano, 13 (2018) 337-345.
[95] G.U. Siddiqui, M.M. Rehman, Y.-J. Yang, K.H. Choi, A two-dimensional hexagonal boron nitride/polymer nanocomposite for flexible resistive switching devices, Journal of Materials Chemistry C, 5 (2017) 862-871.
[96] J. Li, Q. Wu, J. Wu, Synthesis of Nanoparticles via Solvothermal and Hydrothermal Methods 12, (2016).
[97] W.S. Hummers Jr, R.E. Offeman, Preparation of graphitic oxide, Journal of the american chemical society, 80 (1958) 1339-1339.
[98] S. Hellstrom, Basic models of spin coating, Submitted as coursework for Physics, 210 (2007).
[99] B.E. Warren, X-ray Diffraction, Courier Corporation, 1990.
[100] L. Whittig, W. Allardice, X-ray diffraction techniques, Methods of Soil Analysis: Part 1 Physical and Mineralogical Methods, 5 (1986) 331-362.
[101] B.D. Cullity, Elements of X-ray Diffraction, Addison-Wesley Publishing, 1956.
[102] J. Hanawalt, H. Rinn, L. Frevel, Chemical analysis by X-ray diffraction, Industrial & Engineering Chemistry Analytical Edition, 10 (1938) 457-512.
[103] B. Warren, X-ray diffraction methods, Journal of applied physics, 12 (1941) 375-384.

[104] M.J. Pelletier, Quantitative analysis using Raman spectrometry, Applied spectroscopy, 57 (2003) 20A-42A.
[105] I.R. Lewis, H. Edwards, Handbook of Raman spectroscopy: from the research laboratory to the process line, CRC press, 2001.
[106] P. Graves, D. Gardiner, Practical raman spectroscopy, Springer, 10 (1989) 978-973.
[107] J.R. Ferraro, Introductory raman spectroscopy, Elsevier, 2003.
[108] D. Titus, E.J.J. Samuel, S.M. Roopan, Nanoparticle characterization techniques, in: Green synthesis, characterization and applications of nanoparticles, Elsevier, 2019, pp. 303-319.
[109] N. Sangiorgi, L. Aversa, R. Tatti, R. Verucchi, A. Sanson, Spectrophotometric method for optical band gap and electronic transitions determination of semiconductor materials, Optical Materials, 64 (2017) 18-25.
[110] A. Mohammed, A. Abdullah, Scanning electron microscopy (SEM): A review, in: Proceedings of the 2018 International Conference on Hydraulics and Pneumatics—HERVEX, Băile Govora, Romania, 2018, pp. 7-9.
[111] M.A. Sutton, N. Li, D. Joy, A.P. Reynolds, X. Li, Scanning electron microscopy for quantitative small and large deformation measurements part I: SEM imaging at magnifications from 200 to 10,000, Experimental mechanics, 47 (2007) 775-787.
[112] A. Ul-Hamid, A beginners' guide to scanning electron microscopy, Springer, 2018.
[113] L.H. Schwartz, J.B. Cohen, L.H. Schwartz, J.B. Cohen, The nature of diffraction, Diffraction from Materials, (1987) 46-76.
[114] F. Lin, Preparation and characterization of polymer TiO 2 nanocomposites via in-situ polymerization, in, University of Waterloo, 2006.
[115] L.A. Bendersky, F.W. Gayle, Electron diffraction using transmission electron microscopy, Journal of research of the National Institute of Standards and Technology, 106 (2001) 997.
[116] H.H. Willard, L.L. Merritt Jr, J.A. Dean, F.A. Settle Jr, Instrumental methods of analysis, (1988).
[117] R. Jenkins, X-ray techniques: overview, Encyclopedia of analytical chemistry, (2000) 1-20.
[118] G. Friedbacher, H. Bubert, Surface and thin film analysis: a compendium of principles, instrumentation, and applications, John Wiley & Sons, 2011.
[119] D.E. Newbury, N.W. Ritchie, Performing elemental microanalysis with high accuracy and high precision by scanning electron microscopy/silicon drift detector energy-dispersive X-ray spectrometry (SEM/SDD-EDS), Journal of materials science, 50 (2015) 493-518.
[120] B. Singh, B. Mehta, D. Varandani, A.V. Savu, J. Brugger, CAFM investigations of filamentary conduction in Cu2O ReRAM devices fabricated using stencil lithography technique, Nanotechnology, 23 (2012) 495707.
[121] A. Chen, A review of emerging non-volatile memory (NVM) technologies and applications, Solid-State Electronics, 125 (2016) 25-38.
[122] R. Khosla, S.K. Sharma, Integration of ferroelectric materials: An ultimate solution for next-generation computing and storage devices, ACS Applied Electronic Materials, 3 (2021) 2862-2897.
[123] J. Boukhobza, S. Rubini, R. Chen, Z. Shao, Emerging NVM: A survey on architectural integration and research challenges, ACM Transactions on Design Automation of Electronic Systems (TODAES), 23 (2017) 1-32.
[124] J.S. Meena, S.M. Sze, U. Chand, T.-Y. Tseng, Overview of emerging nonvolatile memory technologies, Nanoscale research letters, 9 (2014) 1-33.
[125] Q. Cao, W. Lü, X.R. Wang, X. Guan, L. Wang, S. Yan, T. Wu, X. Wang, Nonvolatile multistates memories for high-density data storage, ACS Applied Materials & Interfaces, 12 (2020) 42449-42471.
[126] E.C. Ahn, H.-S.P. Wong, E. Pop, Carbon nanomaterials for non-volatile memories, Nature Reviews Materials, 3 (2018) 1-15.
[127] P. Feng, C. Chao, Z.-s. Wang, Y.-c. Yang, Y. Jing, Z. Fei, Nonvolatile resistive switching memories-characteristics, mechanisms and challenges, Progress in Natural Science: Materials International, 20 (2010) 1-15.

[128] R. Guo, L. You, Y. Zhou, Z.S. Lim, X. Zou, L. Chen, R. Ramesh, J. Wang, Non-volatile memory based on the ferroelectric photovoltaic effect, Nature communications, 4 (2013) 1-5.
[129] A. Rani, D.B. Velusamy, R.H. Kim, K. Chung, F.M. Mota, C. Park, D.H. Kim, Non-Volatile ReRAM Devices Based on Self-Assembled Multilayers of Modified Graphene Oxide 2D Nanosheets, Small, 12 (2016) 6167-6174.
[130] P. Noé, C. Vallée, F. Hippert, F. Fillot, J.-Y. Raty, Phase-change materials for non-volatile memory devices: from technological challenges to materials science issues, Semiconductor Science and Technology, 33 (2017) 013002.
[131] M. Ahmad, M. Rafiq, Z. Imran, K. Rasool, R. Shahid, Y. Javed, M. Hasan, Charge conduction and relaxation in MoS2 nanoflakes synthesized by simple solid state reaction, Journal of Applied Physics, 114 (2013) 043710.
[132] D.P. Sahu, S.N. Jammalamadaka, Remote control of resistive switching in TiO 2 based resistive random access memory device, Scientific reports, 7 (2017) 1-8.
[133] S. Long, L. Perniola, C. Cagli, J. Buckley, X. Lian, E. Miranda, F. Pan, M. Liu, J. Suñé, Voltage and power-controlled regimes in the progressive unipolar RESET transition of HfO2-based RRAM, Scientific reports, 3 (2013) 1-8.
[134] C. Pan, Y. Ji, N. Xiao, F. Hui, K. Tang, Y. Guo, X. Xie, F.M. Puglisi, L. Larcher, E. Miranda, Coexistence of grain-boundaries-assisted bipolar and threshold resistive switching in multilayer hexagonal boron nitride, Advanced functional materials, 27 (2017) 1604811.
[135] J. Park, K. Biju, S. Jung, W. Lee, J. Lee, S. Kim, S. Park, J. Shin, H. Hwang, Multibit Operation of $\hbox {TiO} _ {x} $-Based ReRAM by Schottky Barrier Height Engineering, IEEE Electron Device Letters, 32 (2011) 476-478.
[136] C.-H. Wang, Y.-H. Tsai, K.-C. Lin, M.-F. Chang, Y.-C. King, C.J. Lin, S.-S. Sheu, Y.-S. Chen, H.-Y. Lee, F.T. Chen, Three-Dimensional $\hbox {4F}^{2} $ ReRAM With Vertical BJT Driver by CMOS Logic Compatible Process, IEEE transactions on electron devices, 58 (2011) 2466-2472.
[137] S. Nilavazhagan, S. Muthukumaran, M. Ashokkumar, Structural, optical and morphological properties of La, Cu co-doped SnO2 nanocrystals by co-precipitation method, Optical Materials, 37 (2014) 425-432.
[138] H. Wang, P. Zhang, Z. Zang, High performance CsPbBr3 quantum dots photodetectors by using zinc oxide nanorods arrays as an electron-transport layer, Applied Physics Letters, 116 (2020) 162103.
[139] S. Wang, T. Wu, J. Qiu, R. Wang, Z. Zhu, X. Zhang, Y. Hua, Enhanced electron transfer dynamics in perylene diimide passivated efficient and stable perovskite solar cells, EcoMat, 3 (2021) e12146.
[140] Q. Zhuang, H. Wang, C. Zhang, C. Gong, H. Li, J. Chen, Z. Zang, Ion diffusion-induced double layer doping toward stable and efficient perovskite solar cells, Nano Research, (2022) 1-9.
[141] C. Zhang, H. Wang, H. Li, Q. Zhuang, C. Gong, X. Hu, W. Cai, S. Zhao, J. Chen, Z. Zang, Simultaneous passivation of bulk and interface defects through synergistic effect of anion and cation toward efficient and stable planar perovskite solar cells, Journal of Energy Chemistry, 63 (2021) 452-460.
[142] J.J. Yoo, G. Seo, M.R. Chua, T.G. Park, Y. Lu, F. Rotermund, Y.-K. Kim, C.S. Moon, N.J. Jeon, J.-P. Correa-Baena, Efficient perovskite solar cells via improved carrier management, Nature, 590 (2021) 587-593.
[143] M.-M. Bagheri-Mohagheghi, M. Shokooh-Saremi, Electrical, optical and structural properties of Li-doped SnO2 transparent conducting films deposited by the spray pyrolysis technique: a carrier-type conversion study, Semiconductor science and technology, 19 (2004) 764.
[144] N. Van Hieu, Comparative study of gas sensor performance of SnO2 nanowires and their hierarchical nanostructures, Sensors and Actuators B: Chemical, 150 (2010) 112-119.
[145] X. Li, J. Shan, W. Zhang, S. Su, L. Yuwen, L. Wang, Recent advances in synthesis and biomedical applications of two-dimensional transition metal dichalcogenide nanosheets, Small, 13 (2017) 1602660.
[146] J. Qiu, X. Guo, R. Chu, S. Wang, W. Zeng, L. Qu, Y. Zhao, F. Yan, G. Xing, Rapid-response, low detection limit, and high-sensitivity capacitive flexible tactile sensor based on three-dimensional

porous dielectric layer for wearable electronic skin, ACS applied materials & interfaces, 11 (2019) 40716-40725.
[147] T.J. Yoo, S.Y. Kim, M.G. Kwon, C. Kim, K.E. Chang, H.J. Hwang, B.H. Lee, A Facile Method for Improving Detectivity of Graphene/p-Type Silicon Heterojunction Photodetector, Laser & Photonics Reviews, 15 (2021) 2000557.
[148] Z. Sun, H. Chang, Graphene and graphene-like two-dimensional materials in photodetection: mechanisms and methodology, ACS nano, 8 (2014) 4133-4156.
[149] D. Castelló-Lurbe, H. Thienpont, N. Vermeulen, Predicting Graphene's Nonlinear-Optical Refractive Response for Propagating Pulses, Laser & Photonics Reviews, 14 (2020) 1900402.
[150] C. Ban, X. Wang, Z. Zhou, H. Mao, S. Cheng, Z. Zhang, Z. Liu, H. Li, J. Liu, W. Huang, A universal strategy for stretchable polymer nonvolatile memory via tailoring nanostructured surfaces, Scientific reports, 9 (2019) 1-7.
[151] H. Wang, H. Feng, J. Li, Graphene and graphene-like layered transition metal dichalcogenides in energy conversion and storage, Small, 10 (2014) 2165-2181.
[152] S. Yang, C. Jiang, S.-h. Wei, Gas sensing in 2D materials, Applied Physics Reviews, 4 (2017) 021304.
[153] C. Zhu, D. Du, Y. Lin, Graphene and graphene-like 2D materials for optical biosensing and bioimaging: A review, 2D Materials, 2 (2015) 032004.
[154] Y. Zhou, Controllable design, synthesis and characterization of nanostructured rare earth metal oxides, Physical Sciences Reviews, 5 (2020).
[155] B.M. Reddy, P. Bharali, P. Saikia, A Comprehensive Overview on Synthesis Techniques of Nanostructured Oxides, New Nanotechniques, 243-276.
[156] R. Kumar, E. Joanni, R.K. Singh, D.P. Singh, S.A. Moshkalev, Recent advances in the synthesis and modification of carbon-based 2D materials for application in energy conversion and storage, Progress in Energy and Combustion Science, 67 (2018) 115-157.
[157] S. Shamaila, A.K.L. Sajjad, S.A. Farooqi, N. Jabeen, S. Majeed, I. Farooq, Advancements in nanoparticle fabrication by hazard free eco-friendly green routes, Applied Materials Today, 5 (2016) 150-199.
[158] C. Aydın, Synthesis of SnO2: rGO nanocomposites by the microwave-assisted hydrothermal method and change of the morphology, structural, optical and electrical properties, Journal of Alloys and Compounds, 771 (2019) 964-972.
[159] Q. Feng, X. Li, J. Wang, Percolation effect of reduced graphene oxide (rGO) on ammonia sensing of rGO-SnO2 composite based sensor, Sensors and Actuators B: Chemical, 243 (2017) 1115-1126.
[160] N. Hidayah, W.-W. Liu, C.-W. Lai, N. Noriman, C.-S. Khe, U. Hashim, H.C. Lee, Comparison on graphite, graphene oxide and reduced graphene oxide: Synthesis and characterization, in: AIP Conference Proceedings, AIP Publishing LLC, 2017, pp. 150002.
[161] Z. Song, Z. Wei, B. Wang, Z. Luo, S. Xu, W. Zhang, H. Yu, M. Li, Z. Huang, J. Zang, Sensitive room-temperature H2S gas sensors employing SnO2 quantum wire/reduced graphene oxide nanocomposites, Chemistry of Materials, 28 (2016) 1205-1212.
[162] D. Zhang, H. Chang, R. Liu, Humidity-sensing properties of one-step hydrothermally synthesized tin dioxide-decorated graphene nanocomposite on polyimide substrate, Journal of Electronic Materials, 45 (2016) 4275-4281.
[163] H. Le Trung, N.K. Tran, H.C. Manh, H.N. Duc, H.T.T. Quynh, T.H. Pham, Hydrothermal synthesis, structure, and photocatalytic properties of SnO2/rGO nanocomposites with different GO concentrations, Materials Research Express, 5 (2018) 095506.
[164] P. Tyagi, A. Sharma, M. Tomar, V. Gupta, A comparative study of RGO-SnO2 and MWCNT-SnO2 nanocomposites based SO2 gas sensors, Sensors and Actuators B: Chemical, 248 (2017) 980-986.
[165] D. Nath, S. Mandal, D. Deb, J. Rakshit, P. Dey, J. Roy, Light tuning DC and AC electrical properties of ZnO-rGO based hybrid nanocomposite film, Journal of Applied Physics, 123 (2018) 095115.
[166] N. Jain, S. Sharma, N.K. Puri, Investigation of charge transport mechanism in hydrothermally synthesized reduced graphene oxide (rGO) incorporated zinc oxide (ZnO) nanocomposite films, Journal of Materials Science: Materials in Electronics, (2021) 1-17.

[167] B.K. Sahu, A. Pal, R. TS, A. Das, Single-Molecule Detection-Enabled Plasmonic Ag Nanogap for Unmasking Vibrational Properties in 0D SnO2, ACS Applied Nano Materials, (2022).
[168] J. Ding, H. Chen, D. Feng, H. Fu, Investigation on photoluminescence emission of (reduced) graphene oxide paper, in: IOP Conf. Ser.: Mater. Sci. Eng, 2018, pp. 012097.
[169] S. Saleh, A. Ibrahim, S. Mohamed, Structural and Optical Properties of Nanostructured Fe-Doped SnO_2, Acta Physica Polonica A, 129 (2016) 1220-1225.
[170] N. Jain, S. Sharma, N.K. Puri, Investigation of charge transport mechanism in hydrothermally synthesized reduced graphene oxide (rGO) incorporated zinc oxide (ZnO) nanocomposite films, Journal of Materials Science: Materials in Electronics, 33 (2022) 1307-1323.
[171] Y. Chen, Y. Niu, T. Tian, J. Zhang, Y. Wang, Y. Li, L.-C. Qin, Microbial reduction of graphene oxide by Azotobacter chroococcum, Chemical Physics Letters, 677 (2017) 143-147.
[172] N. Garino, A. Sacco, M. Castellino, J.A. Muñoz-Tabares, A. Chiodoni, V. Agostino, V. Margaria, M. Gerosa, G. Massaglia, M. Quaglio, Microwave-assisted synthesis of reduced graphene oxide/SnO2 nanocomposite for oxygen reduction reaction in microbial fuel cells, ACS Applied Materials & Interfaces, 8 (2016) 4633-4643.
[173] B. Babu, I.N. Reddy, K. Yoo, D. Kim, J. Shim, Bandgap tuning and XPS study of SnO2 quantum dots, Materials Letters, 221 (2018) 211-215.
[174] B. Singh, B. Mehta, Govind, X. Feng, K. Müllen, Electronic interaction and bipolar resistive switching in copper oxide-multilayer graphene hybrid interface: Graphene as an oxygen ion storage and blocking layer, Applied Physics Letters, 99 (2011) 222109.
[175] H. Jadhav, S. Suryawanshi, M. More, S. Sinha, Pulsed laser deposition of tin oxide thin films for field emission studies, Applied Surface Science, 419 (2017) 764-769.
[176] S. Li, W. Xie, S. Wang, X. Jiang, S. Peng, D. He, Facile synthesis of rGO/SnO 2 composite anodes for lithium ion batteries, Journal of Materials Chemistry A, 2 (2014) 17139-17145.
[177] B. Singh, B. Mehta, M. Singh, G. Gupta, L. Dössel, X. Feng, K. Müllen, Structural and electronic interaction at CuO-hexa-peri-hexabenzocoronene hybrid interface, Applied Physics Letters, 98 (2011) 072101.
[178] D. Yang, R. Yang, K. Wang, C. Wu, X. Zhu, J. Feng, X. Ren, G. Fang, S. Priya, S.F. Liu, High efficiency planar-type perovskite solar cells with negligible hysteresis using EDTA-complexed SnO2, Nature communications, 9 (2018) 1-11.
[179] Z. Wang, T. Han, T. Fei, S. Liu, T. Zhang, Investigation of microstructure effect on NO2 sensors based on SnO2 nanoparticles/reduced graphene oxide hybrids, ACS applied materials & interfaces, 10 (2018) 41773-41783.
[180] R. Meena, R.S. Dhaka, Dielectric properties and impedance spectroscopy of NASICON type Na3Zr2Si2PO12, Ceramics International, 48 (2022) 35150-35159.
[181] Y. Song, T.W. Noh, S.-I. Lee, J.R. Gaines, Experimental study of the three-dimensional ac conductivity and dielectric constant of a conductor-insulator composite near the percolation threshold, Physical Review B, 33 (1986) 904.
[182] R. Khan, Y. Yuan, Z. Iqbal, J. Yang, W. Wang, Z. Ye, J. Lu, Variation of structural, optical, dielectric and magnetic properties of SnO 2 nanoparticles, Journal of Materials Science: Materials in Electronics, 28 (2017) 4625-4636.
[183] S. Khan, T. Khan, R. Khan, M. Khan, S.A. Khattak, G. Khan, Investigation of structural, optical, electrochemical and dielectric properties of SnO 2/GO nanocomposite, Journal of Materials Science: Materials in Electronics, 30 (2019) 10202-10210.
[184] S. Mehraj, Influence of Fe ions on the structural and dielectric properties of SnO2 nanoparticles, Science of Advanced Materials, 4 (2012) 1258-1267.
[185] A. Ahmed, M.N. Siddique, T. Ali, P. Tripathi, Influence of reduced graphene oxide on structural, optical, thermal and dielectric properties of SnO2 nanoparticles, Advanced Powder Technology, 29 (2018) 3415-3426.
[186] N. Bhakta, P. Chakrabarti, XRD analysis, Raman, AC conductivity and dielectric properties of Co and Mn co-doped SnO 2 nanoparticles, Applied Physics A, 125 (2019) 1-11.

[187] M. Kamran, M. Anis-ur-Rehman, Resistive switching effect in RE-Doped cobalt ferrite nanoparticles, Ceramics International, 48 (2022) 16912-16922.
[188] M. Kamran, M. Anis-ur-Rehman, Enhanced transport properties in Ce doped cobalt ferrites nanoparticles for resistive RAM applications, Journal of Alloys and Compounds, 822 (2020) 153583.
[189] S. Sumi, P.P. Rao, M. Deepa, P. Koshy, Electrical conductivity and impedance spectroscopy studies of cerium based aeschynite type semiconducting oxides: CeTiMO 6 (M= Nb or Ta), Journal of Applied Physics, 108 (2010) 063718.
[190] S. Nasri, A. Oueslati, I. Chaabane, M. Gargouri, AC conductivity, electric modulus analysis and electrical conduction mechanism of RbFeP2O7 ceramic compound, Ceramics International, 42 (2016) 14041-14048.
[191] L.L. Zhang, X. Zhao, M.D. Stoller, Y. Zhu, H. Ji, S. Murali, Y. Wu, S. Perales, B. Clevenger, R.S. Ruoff, Highly conductive and porous activated reduced graphene oxide films for high-power supercapacitors, Nano letters, 12 (2012) 1806-1812.
[192] N. Sakhuja, R.K. Jha, R. Chaurasiya, A. Dixit, N. Bhat, 1T-phase titanium disulfide nanosheets for sensing H2S and O2, ACS Applied Nano Materials, 3 (2020) 3382-3394.
[193] U.B. Isyaku, M.H.B.M. Khir, I.M. Nawi, M. Zakariya, F. Zahoor, ZnO based resistive random access memory device: a prospective multifunctional next-generation memory, IEEE Access, (2021).
[194] G. Ahmed, M. Hanif, K. Mahmood, R. Yao, H. Ning, D. Jiao, M. Wu, J. Khan, Z. Liu, Lattice defects of ZnO and hybrids with GO: Characterization, EPR and optoelectronic properties, AIP Advances, 8 (2018) 025218.
[195] S. Zhu, B. Sun, G. Zhou, T. Guo, C. Ke, Y. Chen, F. Yang, Y. Zhang, J. Shao, Y. Zhao, In-Depth Physical Mechanism Analysis and Wearable Applications of HfO x-Based Flexible Memristors, ACS Applied Materials & Interfaces, 15 (2023) 5420-5431.
[196] S. Zhu, B. Sun, S. Ranjan, X. Zhu, G. Zhou, H. Zhao, S. Mao, H. Wang, Y. Zhao, G. Fu, Mechanism analysis of a flexible organic memristive memory with capacitance effect and negative differential resistance state, APL Materials, 7 (2019).
[197] J.H. Lee, C. Wu, S. Sung, H. An, T.W. Kim, Highly flexible and stable resistive switching devices based on WS2 nanosheets: poly (methylmethacrylate) nanocomposites, Scientific reports, 9 (2019) 19316.
[198] T.-J. Yen, A. Chin, V. Gritsenko, Improved device distribution in high-performance SiNx resistive random access memory via arsenic ion implantation, Nanomaterials, 11 (2021) 1401.
[199] S. Bhattacharjee, P.K. Sarkar, M. Prajapat, A. Roy, Electrical reliability, multilevel data storage and mechanical stability of MoS2-PMMA nanocomposite-based non-volatile memory device, Journal of Physics D: Applied Physics, 50 (2017) 265103.
[200] K. Komal, G. Gupta, M. Singh, B. Singh, Improved resistive switching of RGO and SnO2 based resistive memory device for non-volatile memory application, Journal of Alloys and Compounds, 923 (2022) 166196.
[201] L.-G. Wang, Z.-Y. Cao, X. Qian, L. Zhu, D.-P. Cui, A.-D. Li, D. Wu, Atomic layer deposited oxide-based nanocomposite structures with embedded CoPt x nanocrystals for resistive random access memory applications, ACS Applied Materials & Interfaces, 9 (2017) 6634-6643.
[202] R. Vartak, A. Rag, S. De, S. Bhat, Study of Ag/RGO/ITO sandwich structure for resistive switching behavior deposited on plastic substrate, Applied Nanoscience, 8 (2018) 1343-1351.
[203] R. Singh, R. Kumar, A. Kumar, D. Kumar, M. Kumar, Enhanced resistive switching in graphene oxide based composite thin film for nonvolatile memory applications, Materials Research Express, 6 (2019) 105621.
[204] Y. Li, S. Long, Q. Liu, H. Lü, S. Liu, M. Liu, An overview of resistive random access memory devices, Chinese Science Bulletin, 56 (2011) 3072-3078.
[205] C. Yang, B. Sun, G. Zhou, T. Guo, C. Ke, Y. Chen, J. Shao, Y. Zhao, H. Wang, Photoelectric Memristor-Based Machine Vision for Artificial Intelligence Applications, ACS Materials Letters, 5 (2023) 504-526.
[206] Z. Cao, B. Sun, G. Zhou, S.S. Mao, S.H. Zhu, J. Zhang, C. Ke, Y. Zhao, J. Shao, Memristor-based neural networks: A bridge from device to artificial intelligence, Nanoscale Horizons, (2023).

[207] Z. Zhang, Z. Wang, T. Shi, C. Bi, F. Rao, Y. Cai, Q. Liu, H. Wu, P. Zhou, Memory materials and devices: From concept to application, InfoMat, 2 (2020) 261-290.
[208] T. Shi, R. Wang, Z. Wu, Y. Sun, J. An, Q. Liu, A review of resistive switching devices: performance improvement, characterization, and applications, Small Structures, 2 (2021) 2000109.
[209] W. Banerjee, Challenges and applications of emerging nonvolatile memory devices, Electronics, 9 (2020) 1029.
[210] K. Ando, S. Fujita, M. Hayashikoshi, Y. Fujimori, Non-volatile Memories, Normally-Off Computing, (2017) 27-55.
[211] M.-J. Lee, C.B. Lee, D. Lee, S.R. Lee, M. Chang, J.H. Hur, Y.-B. Kim, C.-J. Kim, D.H. Seo, S. Seo, A fast, high-endurance and scalable non-volatile memory device made from asymmetric Ta2O5− x/TaO2− x bilayer structures, Nature materials, 10 (2011) 625-630.
[212] M.S. Islam, A.A.M. Mazumder, C. Zhou, C. Stampfl, J. Park, C.Y. Yang, Current prospects and challenges in negative-capacitance field-effect transistors, IEEE Journal of the Electron Devices Society, (2023).
[213] S. Salahuddin, S. Datta, Use of negative capacitance to provide voltage amplification for low power nanoscale devices, Nano letters, 8 (2008) 405-410.
[214] M. Hoffmann, S. Slesazeck, T. Mikolajick, Progress and future prospects of negative capacitance electronics: A materials perspective, APL Materials, 9 (2021) 020902.
[215] R. Galatage, S. Bentley, P.H. Suvarna, Z. Krivokapic, Negative capacitance matching in gate electrode structures, in, Google Patents, 2019.
[216] W. Choi, N. Choudhary, G.H. Han, J. Park, D. Akinwande, Y.H. Lee, Recent development of two-dimensional transition metal dichalcogenides and their applications, Materials Today, 20 (2017) 116-130.
[217] O. Lopez-Sanchez, D. Lembke, M. Kayci, A. Radenovic, A. Kis, Ultrasensitive photodetectors based on monolayer MoS2, Nature nanotechnology, 8 (2013) 497-501.
[218] H. Hwang, H. Kim, J. Cho, MoS2 nanoplates consisting of disordered graphene-like layers for high rate lithium battery anode materials, Nano letters, 11 (2011) 4826-4830.
[219] T.F. Jaramillo, K.P. Jørgensen, J. Bonde, J.H. Nielsen, S. Horch, I. Chorkendorff, Identification of active edge sites for electrochemical H2 evolution from MoS2 nanocatalysts, science, 317 (2007) 100-102.
[220] H. Qiu, L. Pan, Z. Yao, J. Li, Y. Shi, X. Wang, Electrical characterization of back-gated bi-layer MoS2 field-effect transistors and the effect of ambient on their performances, Applied Physics Letters, 100 (2012) 123104.
[221] K.F. Mak, C. Lee, J. Hone, J. Shan, T.F. Heinz, Atomically thin MoS 2: a new direct-gap semiconductor, Physical review letters, 105 (2010) 136805.
[222] Y. Liu, Y.-X. Yu, W.-D. Zhang, MoS2/CdS heterojunction with high photoelectrochemical activity for H2 evolution under visible light: the role of MoS2, The Journal of Physical Chemistry C, 117 (2013) 12949-12957.
[223] M.A. Andio, P.N. Browning, P.A. Morris, S.A. Akbar, Comparison of gas sensor performance of SnO2 nano-structures on microhotplate platforms, Sensors and Actuators B: Chemical, 165 (2012) 13-18.
[224] M. Periyasamy, A. Kar, Modulating the properties of SnO 2 nanocrystals: morphological effects on structural, photoluminescence, photocatalytic, electrochemical and gas sensing properties, Journal of Materials Chemistry C, 8 (2020) 4604-4635.
[225] P. Sun, Y. Cai, S. Du, X. Xu, L. You, J. Ma, F. Liu, X. Liang, Y. Sun, G. Lu, Hierarchical α-Fe2O3/SnO2 semiconductor composites: Hydrothermal synthesis and gas sensing properties, Sensors and actuators B: chemical, 182 (2013) 336-343.
[226] J. Yang, S. Wang, L. Zhang, R. Dong, Z. Zhu, X. Gao, Zn2SnO4-doped SnO2 hollow spheres for phenylamine gas sensor application, Sensors and Actuators B: Chemical, 239 (2017) 857-864.
[227] B. Luo, Y. Fang, B. Wang, J. Zhou, H. Song, L. Zhi, Two dimensional graphene–SnS 2 hybrids with superior rate capability for lithium ion storage, Energy & Environmental Science, 5 (2012) 5226-5230.

[228] S. Rani, M. Sharma, D. Verma, A. Ghanghass, R. Bhatia, I. Sameera, Two-dimensional transition metal dichalcogenides and their heterostructures: Role of process parameters in top-down and bottom-up synthesis approaches, Materials Science in Semiconductor Processing, (2021) 106313.
[229] T. Wang, S. Chen, H. Pang, H. Xue, Y. Yu, MoS2-based nanocomposites for electrochemical energy storage, Advanced science, 4 (2017) 1600289.
[230] K. Kalantar-zadeh, J.Z. Ou, T. Daeneke, A. Mitchell, T. Sasaki, M.S. Fuhrer, Two dimensional and layered transition metal oxides, Applied Materials Today, 5 (2016) 73-89.
[231] N. Chaudhary, M. Khanuja, S. Islam, Hydrothermal synthesis of MoS2 nanosheets for multiple wavelength optical sensing applications, Sensors and Actuators A: Physical, 277 (2018) 190-198.
[232] D. Zhang, Y.e. Sun, P. Li, Y. Zhang, Facile fabrication of MoS2-modified SnO2 hybrid nanocomposite for ultrasensitive humidity sensing, ACS applied materials & interfaces, 8 (2016) 14142-14149.
[233] X. Ni, C. Chen, Q. Wang, Z. Li, One-step hydrothermal synthesis of SnO2-MoS2 composite heterostructure for improved visible light photocatalytic performance, Chemical Physics, 525 (2019) 110398.
[234] K. Komal, G. Gupta, M. Singh, B. Singh, Improved resistive switching of RGO and SnO2 based resistive memory device for non-volatile memory application, Journal of Alloys and Compounds, (2022) 166196.
[235] V. Singh, B. Singh, MoS2-PVDF/PDMS Based Flexible Hybrid Piezo-Triboelectric Nanogenerator for Harvesting Mechanical Energy, Journal of Alloys and Compounds, (2023) 168850.
[236] Y. Zhang, W. Zeng, Y. Li, The hydrothermal synthesis of 3D hierarchical porous MoS2 microspheres assembled by nanosheets with excellent gas sensing properties, Journal of Alloys and Compounds, 749 (2018) 355-362.
[237] W. Ding, L. Hu, J. Dai, X. Tang, R. Wei, Z. Sheng, C. Liang, D. Shao, W. Song, Q. Liu, Highly ambient-stable 1T-MoS2 and 1T-WS2 by hydrothermal synthesis under high magnetic fields, ACS nano, 13 (2019) 1694-1702.
[238] U. Holzwarth, N. Gibson, The Scherrer equation versus the'Debye-Scherrer equation', Nature nanotechnology, 6 (2011) 534-534.
[239] K.C. Bogaert, Defect-driven processing of two-dimensional transition metal dichalcogenides, in, Massachusetts Institute of Technology, 2019.
[240] A. Konopatsky, V.V. Kalinina, D.V. Barilyuk, D.V. Leybo, A.T. Matveev, X. Fang, D.V. Shtansky, Carbothermal-Reduction-Assisted Cvd Synthesis of Layered Mos2 Nanosheets on Activated Carbon Support: Implication for Photocatalysis, Available at SSRN 4188529.
[241] G. Muthulakshmi, M.M. Ismail, R. Ramya, M. Arivanandhan, S. Arjunan, A. Bhaskaran, Facile preparation of SnO2/MoS2 nanocomposites with high electrochemical performance for energy storage applications, Inorganic Chemistry Communications, 143 (2022) 109802.
[242] J. Tauc, Optical properties of amorphous semiconductors, Amorphous and liquid semiconductors, (1974) 159-220.
[243] N. Sharma, K. Prabakar, S. Ilango, S. Dash, A. Tyagi, Optical band-gap and associated Urbach energy tails in defected AlN thin films grown by ion beam sputter deposition: Effect of assisted ion energy, Advanced Materials Proceedings, 2 (2017) 342-346.
[244] N. Ahmad, S. Khan, M.M.N. Ansari, Optical, dielectric and magnetic properties of Mn doped SnO2 diluted magnetic semiconductors, Ceramics International, 44 (2018) 15972-15980.
[245] P. Chetri, B. Saikia, A. Choudhury, Structural and optical properties of Cu doped SnO2 nanoparticles: an experimental and density functional study, Journal of Applied Physics, 113 (2013) 233514.
[246] J. Wang, S. Liu, X. Cao, Z. Wang, Y. Guo, X. Li, C. Liu, W. Jiang, H. Wang, N. Wang, One-pot synthesis and gas sensitivity of SnO2 nanoparticles prepared using two Sn salts of SnCl4· 5H2O and SnCl2· 2H2O, Applied Physics A, 126 (2020) 1-7.
[247] S. Wu, H. Cao, S. Yin, X. Liu, X. Zhang, Amino acid-assisted hydrothermal synthesis and photocatalysis of SnO2 nanocrystals, The Journal of Physical Chemistry C, 113 (2009) 17893-17898.

[248] S. Cui, Z. Wen, X. Huang, J. Chang, J. Chen, Stabilizing MoS2 nanosheets through SnO2 nanocrystal decoration for high-performance gas sensing in air, Small, 11 (2015) 2305-2313.
[249] E.H. Umukoro, N. Kumar, J.C. Ngila, O.A. Arotiba, Expanded graphite supported pn MoS2-SnO2 heterojunction nanocomposite electrode for enhanced photo-electrocatalytic degradation of a pharmaceutical pollutant, Journal of Electroanalytical Chemistry, 827 (2018) 193-203.
[250] R. Zhang, Y. Li, J. Qi, D. Gao, Ferromagnetism in ultrathin MoS 2 nanosheets: from amorphous to crystalline, Nanoscale research letters, 9 (2014) 1-5.
[251] E.G. da Silveira Firmiano, A.C. Rabelo, C.J. Dalmaschio, A.N. Pinheiro, E.C. Pereira, W.H. Schreiner, E.R. Leite, Supercapacitor electrodes obtained by directly bonding 2D MoS2 on reduced graphene oxide, Advanced Energy Materials, 4 (2014) 1301380.
[252] X. Liu, D. Cao, T. Yang, H. Li, H. Ge, M. Ramos, Q. Peng, A.K. Dearden, Z. Cao, Y. Yang, Insight into the structure and energy of Mo 27 S x O y clusters, RSC Advances, 7 (2017) 9513-9520.
[253] S. Kumari, R. Gusain, N. Kumar, O.P. Khatri, PEG-mediated hydrothermal synthesis of hierarchical microspheres of MoS2 nanosheets and their potential for lubrication application, Journal of Industrial and Engineering Chemistry, 42 (2016) 87-94.
[254] C.M. Lee, G.C. Park, S.M. Lee, J.H. Choi, S.H. Jeong, T.Y. Seo, S.-B. Jung, J.H. Lim, J. Joo, Effects of precursor concentration on morphology of MoS2 Nanosheets by hydrothermal synthesis, Journal of Nanoscience and Nanotechnology, 16 (2016) 11548-11551.
[255] S. Singh, R.M. Sattigeri, S. Kumar, P.K. Jha, S. Sharma, Superior Room-Temperature Ammonia Sensing Using a Hydrothermally Synthesized MoS2/SnO2 Composite, ACS omega, 6 (2021) 11602-11613.
[256] C. Prabukumar, M.M.J. Sadiq, D.K. Bhat, K.U. Bhat, SnO2 nanoparticles functionalized MoS2 nanosheets as the electrode material for supercapacitor applications, Materials Research Express, 6 (2019) 085526.
[257] J. Fierro, L.G. Tejuca, Non-stoichiometric surface behaviour of LaMO3 oxides as evidenced by XPS, Applied surface science, 27 (1987) 453-457.
[258] Y. Liang, B. Fang, Hydrothermal synthesis of SnO2 nanorods: Morphology dependence, growth mechanism and surface properties, Materials Research Bulletin, 48 (2013) 4118-4124.
[259] Y. Guo, J. Tan, J. Zhao, Microstructure and electrical properties of nano-scale SnO2 hydrothermally coated CCTO-based composite ceramics, Ceramics International, 48 (2022) 17795-17801.
[260] R. Yuan, W. Xia, M. Xu, Z. Miao, S. Wu, X. Zhang, J. He, Q. Wang, Rectifying resistance switching behaviors of SnO2 microsphere films modulated by top electrodes, Current Applied Physics, 20 (2020) 431-437.
[261] M.H. Boratto, R.A. Ramos Jr, M. Congiu, C.F. Graeff, L.V. Scalvi, Memristive behavior of the SnO2/TiO2 interface deposited by sol–gel, Applied Surface Science, 410 (2017) 278-281.
[262] C. Nieh, M. Lu, T. Weng, Y. Chen, Resistive memory of single SnO2 nanowire based switchable diodes, Applied Physics Letters, 104 (2014).
[263] S. Trivedi, U. Joshi, Resistive Switching Properties of Highly Transparent SnO [2]: Fe, (2017).
[264] K. Komal, M. Singh, B. Singh, One step hydrothermal synthesis of MoS2–SnO2 nanocomposite for resistive switching memory application, Journal of Materials Science: Materials in Electronics, 34 (2023) 1351.
[265] R. Singh, R. Kumar, A. Kumar, D. Kumar, M. Kumar, Electroforming free enhanced resistive switching in reduced graphene oxide films embedded with silver nanoparticles for nonvolatile memory applications, Semiconductor Science and Technology, 36 (2021) 125019.
[266] S. Choudhary, M. Soni, S.K. Sharma, Low voltage & controlled switching of MoS2-GO resistive layers based ReRAM for non-volatile memory applications, Semiconductor Science and Technology, 34 (2019) 085009.
[267] D. Wang, S. Zhao, L. Li, L. Wang, S. Cui, S. Wang, Z. Lou, G. Shen, All-Flexible Artificial Reflex Arc Based on Threshold-Switching Memristor, Advanced Functional Materials, 32 (2022) 2200241.

[268] N. Gergel-Hackett, B. Hamadani, B. Dunlap, J. Suehle, C. Richter, C. Hacker, D. Gundlach, A flexible solution-processed memristor, IEEE Electron Device Letters, 30 (2009) 706-708.
[269] H. Lian, X. Cheng, H. Hao, J. Han, M.-T. Lau, Z. Li, Z. Zhou, Q. Dong, W.-Y. Wong, Metal-containing organic compounds for memory and data storage applications, Chemical Society Reviews, 51 (2022) 1926-1982.
[270] Y. Chen, Y. Yan, J. Wu, C. Wang, J.Y. Lin, J.S. Zhao, C.S. Hwang, Electroforming-free, flexible, and reliable resistive random-access memory based on an ultrathin TaO x film, ACS applied materials & interfaces, 12 (2020) 10681-10688.
[271] Y. Huang, Y. Gu, S. Mohan, A. Dolocan, N.D. Ignacio, S. Kutagulla, K. Matthews, A. Londoño-Calderon, Y.F. Chang, Y.C. Chen, Reliability Improvement and Effective Switching Layer Model of Thin-Film MoS2 Memristors, Advanced Functional Materials, (2023) 2214250.
[272] M. Ahmadi, O. Zabihi, S. Jeon, M. Yoonessi, A. Dasari, S. Ramakrishna, M. Naebe, 2D transition metal dichalcogenide nanomaterials: advances, opportunities, and challenges in multi-functional polymer nanocomposites, Journal of Materials Chemistry A, 8 (2020) 845-883.
[273] H. Jeong, J. Kim, D.Y. Kim, J. Kim, S. Moon, O.F. Ngome Okello, S. Lee, H. Hwang, S.-Y. Choi, J.K. Kim, Resistive switching in few-layer hexagonal boron nitride mediated by defects and interfacial charge transfer, ACS applied materials & interfaces, 12 (2020) 46288-46295.
[274] I. Varun, A.K. Mahato, V. Raghuwanshi, S.P. Tiwari, Ultralow Current Switching in Flexible Hybrid PVP: MoS 2/HfO x Bilayer Devices, IEEE Transactions on Electron Devices, 67 (2020) 3472-3477.
[275] V.K. Nagareddy, M.D. Barnes, F. Zipoli, K.T. Lai, A.M. Alexeev, M.F. Craciun, C.D. Wright, Multilevel ultrafast flexible nanoscale nonvolatile hybrid graphene oxide–titanium oxide memories, Acs Nano, 11 (2017) 3010-3021.
[276] Y. Sun, D. Wen, Nonvolatile WORM and rewritable multifunctional resistive switching memory devices from poly (4-vinyl phenol) and 2-amino-5-methyl-1, 3, 4-thiadiazole composite, Journal of Alloys and Compounds, 806 (2019) 215-226.
[277] S. Bhattacharjee, U. Das, P.K. Sarkar, A. Roy, Stable charge retention in graphene-MoS2 assemblies for resistive switching effect in ultra-thin super-flexible organic memory devices, Organic Electronics, 58 (2018) 145-152.
[278] J. Jung, D. Shin, Y. Lee, J.J. Pak, Fabrication of solution-processed SnO2–Based flexible ReRAM using laser-induced graphene transferred onto PDMS, Current Applied Physics, 25 (2021) 70-74.
[279] M.J. Yun, K.H. Kim, D. Bea, J. Jung, S. Kim, H.-D. Kim, Improved Resistive Switching of SnO 2 Based Resistive Random Access Memory Devices Using Post Microwave Treatment, Journal of Electrical Engineering & Technology, 16 (2021) 1011-1017.
[280] P.S. Sabzevar, M. Bagheri-Mohagheghi, A. Shirpay, SnO2: rGO transparent semiconducting thin films under annealing by hydrazine—modification of optical gap and electrical resistance, Journal of Materials Science: Materials in Electronics, 34 (2023) 791.
[281] B. Sun, W. Zhao, Y. Liu, P. Chen, Resistive switching effect of Ag/MoS 2/FTO device, Functional Materials Letters, 8 (2015) 1550010.
[282] K. Komal, M. Singh, B. Singh, Flexible SnO2-MoS2 based memristive device exhibiting stable and enhanced memory phenomenon, Journal of Physics D: Applied Physics, (2023).
[283] H.-x. Zhang, B.-G. Shin, D.-E. Lee, K.-B. Yoon, Preparation of PP/2D-Nanosheet Composites Using MoS2/MgCl2-and BN/MgCl2-Bisupported Ziegler–Natta Catalysts, Catalysts, 10 (2020) 596.
[284] A. Ayeshamariam, S. Ramalingam, M. Bououdina, M. Jayachandran, Preparation and characterizations of SnO2 nanopowder and spectroscopic (FT-IR, FT-Raman, UV–Visible and NMR) analysis using HF and DFT calculations, Spectrochimica Acta Part A: Molecular and Biomolecular Spectroscopy, 118 (2014) 1135-1143.
[285] M.R. Shenoy, S. Ayyasamy, V. Bhojan, R. Swaminathan, N. Raju, P. Senthil Kumar, M. Sasikumar, G. Kadarkarai, S. Tamilarasan, S. Thangavelu, Visible light sensitive hexagonal boron nitride (hBN) decorated Fe 2 O 3 photocatalyst for the degradation of methylene blue, Journal of Materials Science: Materials in Electronics, 32 (2021) 4766-4783.

[286] K. Sharma, N.K. Puri, Enhanced electrochemical performance of hydrothermally exfoliated hexagonal boron nitride nanosheets for applications in electrochemistry, Journal of The Electrochemical Society, 168 (2021) 056512.
[287] G. Kesavan, P.K. Gopi, S.-M. Chen, V. Vinothkumar, Iron vanadate nanoparticles supported on boron nitride nanocomposite: electrochemical detection of antipsychotic drug chlorpromazine, Journal of Electroanalytical Chemistry, 882 (2021) 114982.
[288] L. An, C. Bai, Y. Bai, B. Zhang, Y. Yu, Y. Hu, Superhydrophobicity of polyvinylidene fluoride induced by integrating liquid-exfoliated hexagonal boron nitride nanosheets, High Performance Polymers, 32 (2020) 73-82.
[289] A. Sharma, S. Arya, D. Chauhan, P.R. Solanki, S. Khajuria, A. Khosla, Synthesis of Au–SnO2 nanoparticles for electrochemical determination of vitamin B12, Journal of Materials Research and Technology, 9 (2020) 14321-14337.
[290] R. Jerome, A.K. Sundramoorthy, Preparation of hexagonal boron nitride doped graphene film modified sensor for selective electrochemical detection of nicotine in tobacco sample, Analytica Chimica Acta, 1132 (2020) 110-120.
[291] P. Bamola, B. Singh, A. Bhoumik, M. Sharma, C. Dwivedi, M. Singh, G.K. Dalapati, H. Sharma, Mixed-phase TiO2 nanotube–nanorod hybrid arrays for memory-based resistive switching devices, ACS Applied Nano Materials, 3 (2020) 10591-10604.
[292] Y. Chen, X. Xu, C. Li, A. Bendavid, M.T. Westerhausen, C. Bradac, M. Toth, I. Aharonovich, T.T. Tran, Bottom-Up Synthesis of Hexagonal Boron Nitride Nanoparticles with Intensity-Stabilized Quantum Emitters, Small, 17 (2021) 2008062.
[293] P.K. Rastogi, K.R. Sahoo, P. Thakur, R. Sharma, S. Bawari, R. Podila, T.N. Narayanan, Graphene–hBN non-van der Waals vertical heterostructures for four-electron oxygen reduction reaction, Physical Chemistry Chemical Physics, 21 (2019) 3942-3953.

Bio-data

Km. Komal is a research scholar at Delhi Technological University, Delhi pursuing her research in the Applied Physics Department since July 2018. Prior to this, she completed her Master in Physics from School of Physical Sciences, Jawaharlal Nehru University, New Delhi, in the year 2018 and Bachelor of Science from Govt. L.R. College Sahibabad, Chaudhary Charan Singh University, Meerut in the year 2016. She has been awarded the Junior and Senior Research Fellowships from Council of Scientific and Industrial research, India from 2018-2020 and 2020-2023, respectively. She has been awarded the Commendable Research Award for excellence in Research by DTU in year 2023. Her present research interest includes structural, optical and electric properties of metal oxide-2D material based composites for non-volatile resistive memory device applications.